FLUCTUATIONS AND NOISE IN NANOELECTRICAL AND NANOMECHANICAL SYSTEMS

by

Peter Kirton

Thesis submitted to the University of Nottingham for the degree of Doctor of Philosophy, May 2012

Abstract

In this thesis we present a study of the fluctuations and noise which occur in a particular nanoelectrical device, the single electron transistor (SET). Electrical transport through the SET occurs through a combination of stochastic, incoherent tunnelling and coherent quantum oscillations, giving rise to a rich variety of transport processes. In the first section of the thesis, we look at the fluctuations in the electrical properties of a SET. We describe the SET as an open quantum system, and use this model to develop Born-Markov master equation descriptions of the dynamics close to three resonant transport processes: the Josephson quasiparticle resonance, the double Josephson quasiparticle resonance and the Cooper-pair resonances. We use these models to examine the noise properties of both the charge on the SET island and the current flowing through the SET. Quantum coherent oscillations of Cooper-pairs in the SET give rise to noise spectra which can be highly asymmetric in frequency. We give an explicit calculation of how an oscillator capacitively coupled to the SET island can be used to infer the quantum noise properties close to the Cooper-pair resonances. To calculate the current noise we develop a new technique, based on classical full counting statistics. We are able to use this technique to calculate the effect of the current fluctuations on an oscillator coupled to the current through the SET, the results of which are in good agreement with recent measurements. In the final part of the thesis we explore the coupled dynamics of a normal state SET capacitively coupled to a resonator in the presence of an external drive. The coupling between the electrical and mechanical degrees of freedom leads to interesting non-linear behaviour in the resonator. We are able to find regions where the resonator has two possible stable amplitudes of oscillation, which can lead to a bistability in the dynamics. We also look at the fluctuations in the energy of the system. We use numerical methods to simulate the dynamics of the system, and to obtain the probability distribution for the work done, whose form can be interpreted by the appropriate fluctuation relation.

ACKNOWLEDGEMENTS

The work presented in thesis would not have been possible without the help and support of a number of people.

I begin by thanking my supervisor, Andrew Armour. His patience and support over the last few years of study have provided an invaluable resource, without his aid this thesis would not exist. The collaboration developed with Fabio Pistolesi and Manuel Houzet provided me with many ideas, and solutions to problems. I am particularly grateful to Fabio, for his hospitality in both Grenoble and Bordeaux, at various times during my studies.

I would also like to thank all of the other PhD students and postdocs, for the tea breaks and cake, a special mention to Emma for the many shared meals and games of badminton. My appreciation goes to all the NUSCR members, both past and present, for giving me fun times away from physics.

My deepest gratitude goes to my family, my mum and brother, Neil for their love and support throughout my time in Nottingham. Finally, I give my eternal thanks to Lindsey, for being there for me whenever I needed her.

CONTENTS

Part I.

Single Electron Transistors

1

INTRODUCTION

Fluctuations and noise play an increasingly important role in the dynamics of systems as they become smaller. Noise not only provides an intrinsic problem to be minimised in an experiment, but measurement of noise can also provide a sophisticated way of uncovering the behaviour of a system [1, 2, 3]. Features in the noise, beyond those which are present in the mean dynamics, give information about the interactions within the system, and also the energy and time scales which are important to the dynamics [1, 4, 5].

In this thesis we examine the information we can gain by studying noise in *nanoelectrical systems*, small electrical circuits, in which the quantisation of charge is important [2]. We will focus our attention on one particular example, the single electron transistor (SET).

1.1 single electron transistors

The SET consists of a small metallic island coupled to leads via tunnel junctions. Current is transported through the device via individual electrons hopping on and off the island into the leads. Examples of such devices can be seen in Fig. 1.1. The SET was first proposed by Averin and Likharev in 1986 [6] and was demonstrated in 1987 by Fulton and Dolan [7]. It was shown in these early examples that the electrostatic energy of the island is highly sensitive to the charge on a nearby gate, and so changing the voltage applied to the gate can dramatically change the current through the SET.

It is also possible to make the leads and island of the SET from materials which, at sufficiently low temperatures, become superconducting [12]. In this case, the transport can become highly complex with a number of different processes which can contribute. To fully describe a superconducting SET (SSET) the use of quantum mechanics is essential. In such systems, the presence of steady state quantum coherence leads to interesting features in both the average current [13] and the noise spectrum [14, 4, 15] of the device. While transport in the normal state SET is purely due to the tunnelling of normal electrons, in the SSET a much richer variety of processes are possible. Different combinations of coherent Cooper-pair oscillations and inco-

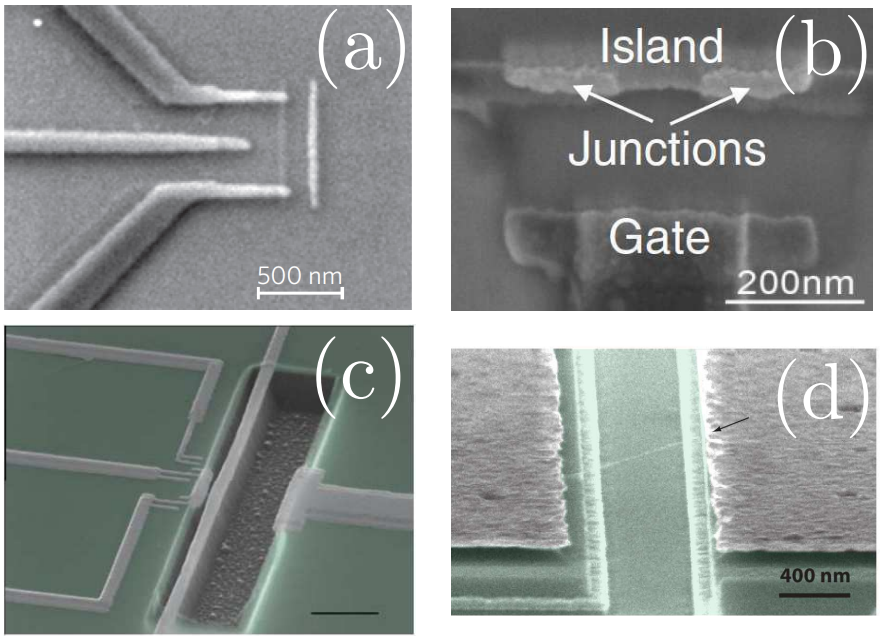

Figure 1.1.: Experimental realisations of single electron transistors, taken from (a) Ref. [8], (b) Ref. [9] and (c) Ref. [10]. In (d), from Ref. [11], we show a carbon nanotube (indicated by the arrow) with an embedded quantum dot, the dynamics are described in a very similar way to the SET.

herent quasiparticle tunnelling can become favourable, with a highly sensitive dependence on the choice of bias point [13].

The SET also provides a prototype for many other physical systems. Similar dynamics can occur in quantum dots [16, 17, 18], molecular transistors [19], and carbon nanotubes, which can support single electron transport [11, 20].

1.2 MEASUREMENT AND NOISE

The SET found uses as a detector, since it can easily be integrated with other systems and its current measured. The current through the SET depends strongly on the charge, Q_g, induced on the gate electrode: a change in Q_g by only $e/2$ can change the current, I, from its maximum value to zero. This means that the SET has a large *gain* $G = dI/dQ_g$ and so can be used as a highly sensitive electrometer [21] for detecting nearby charges. Because of this it was suggested as a read out device for qubits based on systems with charge coherence [22, 23].

The position of a nearby mechanical object, such as a nanomechanical beam, can also be measured with a high degree of accuracy by the SET [24, 25]. If the beam forms one plate of the gate capacitor, then, as the beam moves, it changes the capacitance, thus effectively changing

Q_g, this then leads to sensitive dependence of I on the position of the oscillator. An example of this kind of device is shown in Fig. 1.1 (c).

More recently, experiments have shown that a SET can be used to image *surface acoustic waves* (SAW) [26] in piezoelectric crystals. The displacement of the surface induces a polarisation in the substrate, which is detected as a change in the potential of the SET, and so measurement of the current through the SET allows the imaging of SAW [27].

The sensitivity of all these measurements is limited by two distinct sources of noise. Firstly, the intrinsic noise of the SET; the current through the SET fluctuates about its mean value. Charge is transferred one electron at a time, which creates *shot noise* in the current, and so limits the sensitivity of the measurement [1]. Secondly, the sensitivity is limited by the effect of *back-action* noise [3]. Since the SET and the measured system are coupled, fluctuations in the SET cause fluctuations in the measured system, thus creating uncertainty in the measurement. This back-action noise is a very general feature of quantum measurement, and absolute limits on sensitivity, imposed by quantum mechanics, can be calculated [3].

1.3 Fluctuations beyond measurement

Back-action noise can be seen from a different point of view. As well as being a nuisance in the context of sensitive measurement, the back-action can have dramatic effects on the measured system which is coupled to the SET and can, in fact, be used to manipulate its dynamics and can even be used for the dissipative generation of quantum states [28]. Recent experiments have used the back-action of SETs to *cool* an oscillator to a temperature lower than the thermal environment [10] and also to induce laser-like instabilities in a superconducting resonator [28], by pumping energy from the SET into the resonator. Other experiments have used the back-action effects of single electron tunnelling to induce non-linear behaviour in driven carbon nanotubes [11, 20]. Finally, the back-action caused by a conductor provides a 'fingerprint' of its noise properties. This means we can learn a lot about the intrinsic quantum dynamics of a conductor simply by measuring the effect it has on the dynamics of a simple system like a harmonic oscillator to which it is coupled [8, 29].

Fluctuations in the electrical properties of the SET can lead to fluctuations in the mechanical properties of a resonator coupled to the SET. This, in turn, leads to fluctuations in the *energy* of the resonator. Therefore, the thermodynamic quantities, such as the work done on the resonator by an external drive, do not have a definite value but can take on a range of values, and so have an associated probability distribution. These quantities can then, apparently, violate the second law of thermodynamics, for example, the work done can be negative

for some particular rare trajectories [30]. Quantifying the probability of such trajectories occurring led to the development of the so-called *fluctuation relations* [31, 32]. Very recently there has been interest in applying these relations to mesoscopic conductors [33, 34, 35]. The SET-resonator provides a particularly simple model system to study these fluctuation relations in an out-of- equilibrium system.

1.4 THIS THESIS

The structure of this thesis is as follows. In chapter 2 we provide a brief outline of the physics of the single electron transistor. We begin by describing the dynamics of SETs, both normal state and superconducting. We then develop the master equation formalism which we use throughout this thesis to describe the SSET, and outline the models which we use to describe transport through the SSET at three points where resonant transport occurs via different mechanisms: the Josephson quasiparticle (JQP) cycle, the double Josephson quasiparticle cycle (DJQP) and the Cooper-pair resonances (CPRs).

In chapter 3 we describe the formalism used for quantifying the noise properties of the SSET. This formalism is then used to calculate the island charge noise for the various transport mechanisms in the SSET outlined in chapter 2. We show that these calculations reveal features of the dynamics which cannot be seen by simply looking at the average behaviour of the system. For the CPRs, we develop the model further and look at how it could be experimentally feasible to probe the charge noise by weakly coupling an oscillator to the SSET island.

The focus of chapter 4 is on developing a method to calculate the quantum noise in the current through the SSET. Calculating the current noise is non-trivial: quantum coherence between states with Cooper-pairs in the leads and on the island means that the usual classical counting methods break down. A new technique, capable of solving this problem, is described in the first part of the chapter, which is then applied to the transport mechanisms in the SSET. We pay particular attention to the noise at the DJQP resonance, since we are able to provide an interpretation of a recent experiment, described in Ref. [8]. We also show how the quantum current noise gives detailed information about the charge transfer processes which occur in each of the junctions, beyond what was found for the charge noise.

In chapter 5 we look at a more complex system; an oscillator capacitively coupled to a normal state SET which is subject to a periodic driving force. Our simple model for the coupled dynamics of this system allows us to explore regions of interesting non-linear behaviour in the system. We are able to find regions where the resonator has two stable states which oscillate with different amplitudes. In this region, the steady state distribution of the oscillator can exhibit a bistability,

in which the system infrequently switches between the two states. We go on to present some preliminary results of the thermodynamics of this driven system. We investigate the distribution of work done by the external force, and find that, even though the mean work done is guaranteed to be positive, there are some trajectories in which the work done is negative. These trajectories allow us to examine the work fluctuation relations in this system.

The original material in this thesis is the result of collaboration with several individuals and some of it has been published elsewhere. The work presented in sections 2.5 and 3.7 has been published in Ref. [36], while the material in sections 4.2 and 4.3 form the basis of the preprint [37]. This work along with the remainder of the original material in chapter 4, was produced in collaboration with Fabio Pistolesi, Manuel Houzet and Andrew Armour. The material in chapter 5 resulted from a collaboration with Andrew Armour.

2

THE SET

Recently it has become possible to create mesoscopic devices in which electrons tunnel one-by-one through a series of junctions. Such devices rely on the quantisation of charge and energy to function, this means that quantum mechanics is fundamental to their behaviour. Single electron devices also have important technological applications in metrology and sensing; as discussed in chapter 1, they have been used as ultra-high precision measurement devices for quantities such as charge [38] and displacement [25, 39], and also there is a possibility of using these devices for determining a new current standard [40].

The particular example which we focus on this thesis is the single electron transistor (SET) [7] (described in detail in the following section). This device provides the prototypical example of a single electron transport device. The SET can be made from metal which is either in the normal state, or at low enough temperatures, in the superconducting state. For a normal state SET, the transport involves individual electrons. For a superconducting device, the current can be transmitted both by Cooper-pairs and, at high enough voltages, by quasiparticles. SETs support a wide range of different transport mechanisms, and can have rich and complex current-voltage characteristics.

In this chapter we will introduce several transport mechanisms which occur in SETs. We begin with a detailed description of the transport in a normal state SET in Sec. 2.1. Then, in Sec. 2.2, we give a general overview of the techniques used to describe the dynamics of the superconducting SET (SSET); we write down a Hamiltonian and show that, to correctly describe the transport, we need to include dissipation in our model. In the following sections we give detailed models for a variety of transport cycles in the SSET, in Sec. 2.3 we describe the Josephson quasiparticle resonance, in Sec. 2.4 we describe the double Josephson quasiparticle resonance and finally, in Sec. 2.5 we describe the Cooper-pair resonances.

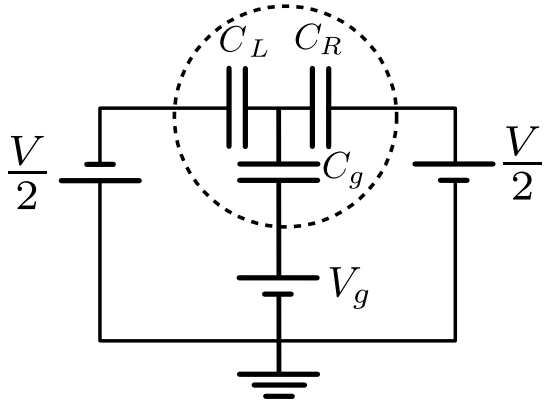

Figure 2.1.: A schematic diagram of the SET. The encircled region shows the SET island.

2.1 NORMAL STATE SETS

A normal state single electron transistor consists of a small island coupled to leads by tunnel junctions with capacitances $C_{L(R)}$. A schematic of the circuit is given in Fig. 2.1. The electrostatics of the system are controlled by two voltage sources; a source-drain bias, V, is applied symmetrically across the junctions, and a gate voltage, V_g, is applied to a gate capacitor, C_g. This then induces a polarisation charge on the island [41], which we write in terms of the effective number of electrons required to create it,

$$n_g = \frac{C_g V_g}{e}, \tag{2.1}$$

which controls the energy levels of the island. Since the device is not superconducting, transport is purely due to incoherent tunnelling of electrons. To make sure that these electrons travel one at a time through the transistor, we require the energy cost for adding extra electrons to the island to be the largest scale in the problem. This charging energy is given by [41],

$$E_C = \frac{e^2}{2C_\Sigma}, \tag{2.2}$$

where C_Σ is the total capacitance of the island $C_\Sigma = C_L + C_R + C_g$. To make sure that charging effects dominate over thermal fluctuations we need $E_C \gg k_B T$, and so the island needs to have a small capacitance, this means that the SET island needs to be physically small. The energy of the system with n excess electrons on the island (assuming $C_L = C_R$) is given by the Hamiltonian [42, 43],

$$H(n) = E_C(n - n_g)^2. \tag{2.3}$$

For certain choices of source-drain and gate voltage single electron transport occurs through the device. To quantify the conditions for

this we consider the change in electrostatic energy when an electron tunnels at each junction. We choose the direction of the source-drain voltage such that electron tunnelling occurs from left to right across the transistor. The change in electrostatic energy due to a forward tunnel event at the left and right junctions is given by [41],

$$\Delta E_L = (H(n) - H(n+1)) + \frac{eV}{2}, \tag{2.4}$$

$$\Delta E_R = -(H(n) - H(n+1)) + \frac{eV}{2}. \tag{2.5}$$

In each case, the first term is due to the electrostatic energy difference between the states before and after the tunnel event and the second term is the energy gained due to the source-drain voltage. We then substitute the Hamiltonians from Eqn. (2.3) into the expressions for ΔE and obtain,

$$\Delta E_L = E_C(2n + 1 - 2n_g) + \frac{eV}{2}, \tag{2.6}$$

$$\Delta E_R = -E_C(2n + 1 - 2n_g) + \frac{eV}{2}. \tag{2.7}$$

So, if we choose[1] $0 \leq n_g \leq 1$, then the lowest two island states are given by $n = 0, 1$. In the low temperature limit considered here, the only spontaneous changes which can occur are from higher to lower energy states, i.e. with $\Delta E > 0$. This allows us to set a bound on the source-drain voltage such that both the $n = 0, 1$ states are accessible by allowed transitions and all others are forbidden,

$$\max[(1-2n_g), (-1+2n_g)] \leq \frac{eV}{2E_C} \leq \min[(1+2n_g), (3-2n_g)]. \tag{2.8}$$

At voltages smaller than the lower bound, the system enters the region of *Coulomb blockade* [41], where only one state is available to the island and so no transport can occur: the system is stuck in a single state. At voltages above the upper bound, another channel of transport opens up, and three or more states are available for transport. This *Coulomb diamond* structure of available island states is shown in Fig. 2.2, where we show the various states available as a function of the gate and source-drain voltages.

We now limit ourselves to regions where single electron transport can take place (the green region of Fig. 2.2). To describe the dynamics of the island in this region we use the *orthodox model* of transport through the SET [44]. This states that the transition rate at each of the junctions is simply related to the free energy difference between the initial and final states. At zero temperature this is given by [44],

$$\Gamma_{L(R)} = \frac{\Delta E_{L(R)}}{e^2 R} \Theta(\Delta E_{L(R)}), \tag{2.9}$$

1 without loss of generality, since the replacement $n_g \to n_g \pm 1$ gives the same dynamics but with the island states shifted by $n \to n \pm 1$

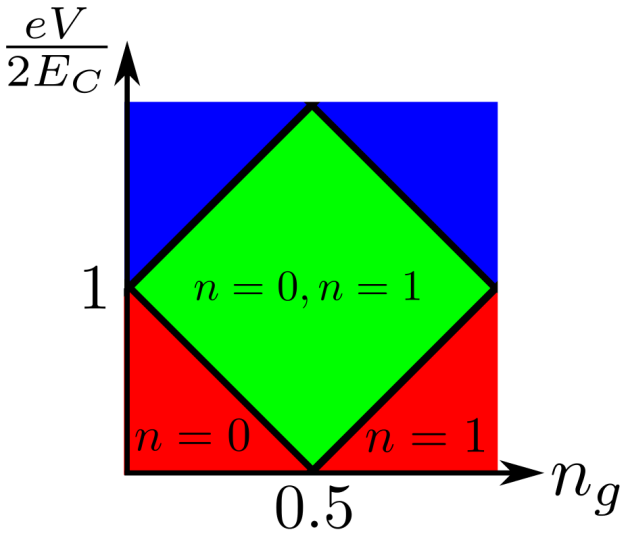

Figure 2.2.: A Coulomb diamond. The red regions are those where only one state is available to the island and no transport is available, the green region is where single electron transport can take place since two island states are available and the blue region shows where more than two states are available and more complicated transport occurs.

where $\Theta(\cdot)$ is the Heaviside step function which ensures the energy differences are positive, and R is the tunnel resistance of the junctions. We then assume that an ensemble of SETs can be described by probability functions $P_{0(1)}(t)$, which describe the probability of finding the island in the state $n = 0(1)$ at time t [44]. These evolve according to the master equations,

$$\dot{P}_0 = \Gamma_R P_1 - \Gamma_L P_0, \tag{2.10}$$

$$\dot{P}_1 = \Gamma_L P_0 - \Gamma_R P_1. \tag{2.11}$$

The master equations can then be used to calculate the average steady state current though the SET,

$$\langle I \rangle = e\Gamma_L P_0 = e\Gamma_R P_1, \tag{2.12}$$

which is given by,

$$\langle I \rangle = \frac{e\Gamma_L \Gamma_R}{\Gamma_L + \Gamma_R}. \tag{2.13}$$

We will come back to systems involving normal state SETs in chapter 5, but for the remainder of this chapter and chapters 3 and 4, we turn to the dynamics of *superconducting* SETs.

2.2 SUPERCONDUCTING SINGLE ELECTRON TRANSISTORS

Single electron transistors can also be made using superconducting material [45, 38, 21] for the leads and island so that, at low enough

temperatures, the main charge carriers through the device are Cooper-pairs. The tunnel junctions then become Josephson junctions which allow quantum coherence between states with a Cooper-pair on each side of the junction to develop. This then means that a full quantum mechanical description of the system is required.

A convenient set of basis states which describe the Hilbert space of the SSET island and leads consist of the states $|n, N_L\rangle$, where n labels the island charge state and N_L counts the number of electrons in the left hand lead of the SSET. We *choose* to count electron transport through the left-hand junction (we could equally have written the states with N_R), we include this degree of freedom which is absent in many models [14, 46, 47], since it gives more information about the current than just the island charge n, as we will see in chapter 4.

The Hamiltonian which describes the coherent evolution of the system contains two terms [41, 48, 4],

$$H_S = H_C + H_J, \tag{2.14}$$

where H_C describes the charging energy of the island, this is very similar to the classical Hamiltonian used to describe the normal state SET in Eqn. (2.3), and also includes a term which describes the energy gain from the source-drain voltage,

$$H_C = \sum_{n,N_L} \left[E_C(n - n_g)^2 + \left(N_L + \frac{n}{2} \right) eV \right] |n, N_L\rangle \langle n, N_L| . \tag{2.15}$$

The term $neV/2$ arises from the fact that electrons on the island have passed through one of the junctions and so enter the Hamiltonian with half the energy cost of those in the lead. The Josephson coupling is described by H_J, which couples states that differ by one Cooper-pair transition,

$$H_J = -\frac{E_J}{2} \sum_{n,N_L} \Big[|n, N_L\rangle \langle n + 2, N_L - 2| + |n, N_L\rangle \langle n - 2, N_L| \Big] + h.c., \tag{2.16}$$

where E_J is the Josephson energy of the junctions (taken to be equal), and *h.c.* is the Hermitian conjugate. The first term in this expression (and its conjugate) describes Josephson oscillations at the left hand junction, which change the value of the counting variable, N_L, while the second term describes oscillations at the right junction, which do not change N_L.

As with the normal state SET, the choice of n_g and V have a strong affect on the transport mechanisms available. Experimental results for the current through a SSET as a function of both drain-source and gate voltage are reproduced in Fig. 2.3 (from [13]). We see a variety of features which can be attributed to the various transport mechanisms, which we will describe in detail in the remainder of

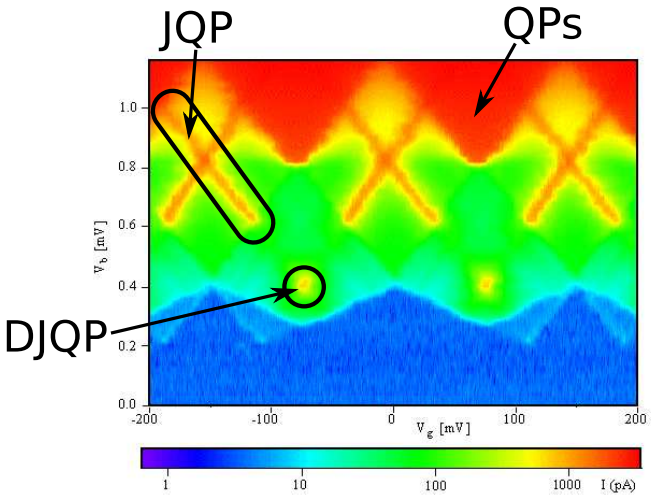

Figure 2.3.: Current-voltage characteristics of an SSET. The various resonant transport mechanisms discussed in the main text are labelled. Adapted from [13]

this chapter. At high source-drain voltage we see the current gets very large. In this region, labelled QPs, *quasiparticle tunnelling* (described in the next section) can occur at both junctions, this leads to behaviour which is very similar to a normal state SET. At lower voltages than this we see lines of high current, these can be attributed to Josephson quasiparticle (JQP) resonances. At even lower voltages, at the points where two JQP lines would cross we see large peaks which are due to *double* Josephson quasiparticle (DJQP) resonances.

The presence of a steady state dc current through the SSET cannot be explained without some form of dissipation, a simple Hamiltonian description is not adequate. If the SSET island was completely isolated from its environment, then the dynamics would simply evolve coherently under the action of the Hamiltonian, and the equation of motion for the *density operator* [49] would simply be,

$$\dot{\rho} = -i[H_S, \rho], \tag{2.17}$$

where, for simplicity, we now work with units where $\hbar = e = k_B = 1$ (unless otherwise stated). The long time behaviour of such an equation simply contains oscillations between states linked by the Josephson Hamiltonian, and so only describes an ac current. To describe the dissipative dynamics, we need to introduce dissipation to our system induced by coupling to an external bath.

2.2.1 *Coupling to an environment*

In general an *open quantum system* [50] can be described by partitioning the universe into the *system* which is the part that contains the

degrees of freedom we are interested in, and the *bath* which contains everything else. The complete Hamiltonian can then be written as,

$$H = H_S + H_B + H_{SB}, \tag{2.18}$$

where H_S contains operators which act only on the Hilbert space of the system, H_B is the Hamiltonian of just the bath and H_{SB} describes the interaction between the two subsystems. The complete evolution of the full density operator of the system and bath is then given by the coherent master equation,

$$\dot{\rho} = -i[H, \rho]. \tag{2.19}$$

This equation is usually too complicated to directly solve, and so approximations are made. In this thesis, we always work with systems which can be described by a *Born-Markov* master equation [50]. This relies on two approximation schemes for the above equation. Firstly, in the Born approximation, we assume that the coupling Hamiltonian between the system and bath is weak, in the sense that we can use perturbation theory in this Hamiltonian. Secondly, we use the Markov approximation, which requires the relaxation timescale of the bath to be much faster than any of the dynamics of the system. This allows us to ignore any *memory* effects of the bath, and assume the evolution equation for the system is local in time. After these approximations, we end up with an equation for the reduced density operator of the system, $\rho_S = \mathrm{Tr}_B[\rho]$, where Tr_B is the partial trace over bath degrees of freedom. This equation of motion is given by [50],

$$\dot{\rho_S} = -i[H_S, \rho_S] + \mathcal{L}_B \rho_S, \tag{2.20}$$

where $\mathcal{L}_B$ is a *superoperator* [50] which contains all the remaining information about the interaction with the bath.

In the following sections, we outline the form of the Born-Markov master equation descriptions, which we will use in the following chapters to describe the various current carrying processes in the SSET. We will give brief overviews of the derivations for the JQP and DJQP cycles, since complete derivations are available in the literature, but, for the Cooper-pair resonances a master equation description is not available elsewhere, and so the description we provide contains rather more detail.

2.3 JOSEPHSON QUASIPARTICLE RESONANCE

We begin with the Josephson quasiparticle (JQP) resonance. Solving the coherent equations above shows that, even at zero applied bias, it is possible for ac Josephson oscillations to occur in the SSET. However, this does not on its own lead to dc current. For this to occur we need dissipation, provided in the case of the JQP resonance by a bath

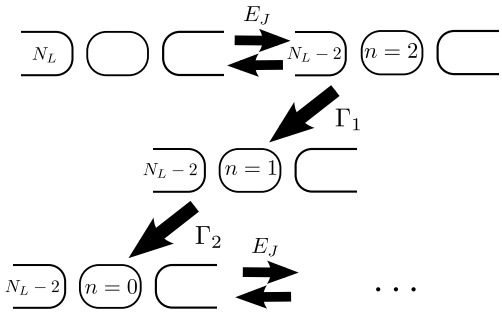

Figure 2.4.: The JQP cycle. Cooper-pair tunnelling at the left junction is followed by two quasiparticle decays at the right junction.

of *quasiparticles*, collective excitations which, for the purposes of this thesis, behave exactly as electrons in a normal conductor. For quasiparticle transport to occur, the applied bias needs to be high enough to overcome the gap in the density of states, $V > 2\Delta$, where Δ is the superconducting gap. When this condition is met, the transport can involve a mixture of both resonant Cooper-pair transport and quasiparticle decays. Under certain conditions, this combination of coherent and incoherent effects can lead to the *JQP cycle* [51, 12, 52]; the steps involved are shown schematically in Fig. 2.4. We choose the left-hand junction to be resonant for a Cooper-pair transition, while quasiparticle decays occur at the right-hand junction, the results presented are equally valid for the reverse situation. The JQP resonance is referred to as a *cycle*, since the number of Cooper-pairs on the island returns to its initial state ($n = 0$ in Fig. 2.4), but the counting variable N_L decreases by 2 each cycle, and so a dc current results.

Resonant Cooper-pair oscillations can occur when two states for which the number of Cooper-pairs on the island differ by one are degenerate in charging energy. Labelling these states as $|0, N_L\rangle$ and $|2, N_L - 2\rangle$, the resonance condition becomes [53, 4],

$$V = 4E_C(1 - n_g). \tag{2.21}$$

This is derived by setting the charging energies of the two states equal, $\langle 0, N_L| H_C |0, N_L\rangle = \langle 2, N_L - 2| H_C |2, N_L - 2\rangle$, with H_C defined in Eqn. (2.15). In Fig. 2.3, we see the JQP features as lines of enhanced current. Here we focus on one of these features described by the expression above. There are, of course, a whole set of resonance points at which the JQP cycle takes place, for example, when the states $|n, N_L\rangle$ and $|n + 2, N_L - 2\rangle$ are resonant, along the line $V = 4E_C(1 - n_g + n)$, which, together with the resonances at the right hand junction, gives the pattern of lines seen in Fig. 2.3. All of the results presented here are valid for any of these other JQP cycles, with trivial shifts in the definitions of n and N_L. This leads us to naturally

introduce a parameter which describes how far the system is detuned from the JQP resonance [15]

$$\delta = 4E_C(1 - n_g) - V. \tag{2.22}$$

For the JQP cycle to occur, we need to provide enough energy to allow the quasiparticle decays to occur. To be able to break up Cooper-pairs on the SSET island we need the applied voltage to be able to overcome the superconducting gap, Δ. This condition can be derived in the same way as we did in Sec. 2.1, for the normal state SET, including an extra energy cost, 2Δ, to be overcome [54, 4]. This leads to the following result for the two decays to be energetically favourable,

$$V \geq 2\Delta - E_C \qquad n = 2 \to 1, \tag{2.23}$$

$$V \geq 2\Delta + E_C \qquad n = 1 \to 0, \tag{2.24}$$

since the condition for the $n = 1 \to 0$ transition is always more stringent, we only need to make sure the voltage is high enough to satisfy this, as then $n = 2 \to 1$ will automatically be satisfied. There is also an upper limit to the voltage at which the JQP can be seen. For drain-source voltages, $V > 4\Delta$, quasiparticle tunnelling is favourable at both junctions, and so incoherent transport dominates, and the SSET behaves as a normal state SET. This can be seen in the experimental results in Fig. 2.3, in the region labelled QPs, where the Coulomb diamond structure can be clearly seen.

We now calculate the rates for the quasiparticle decays, $\Gamma_{1(2)}$ (as labelled in Fig. 2.4). To do this, we employ a slightly more sophisticated approach than we did for the normal state SET in Sec. 2.1. The tunnel rates depend on the density of states available for the particle to tunnel into, and the energy which it gains by tunnelling. The rates, calculated using Fermi's golden rule, are given by [54],

$$\Gamma_{1(2)} = \frac{1}{R}\int_{-\infty}^{\infty} \varrho(\epsilon)\varrho\left(\epsilon + E_{1(2)}\right) f(\epsilon)\left[1 - f\left(\epsilon + E_{1(2)}\right)\right] d\epsilon, \tag{2.25}$$

where $f(\epsilon)$ is the Fermi occupation at a given energy, which, at $T = 0$, is simply $f(\epsilon) = \Theta(-\epsilon)$ with $\Theta(\cdot)$ the Heaviside step function. This expression is only valid when the junction resistances are small enough to use perturbation theory, which is the same condition on that used in the Born approximation for the master equation. The energy gained in each quasiparticle decay, $E_{1(2)}$, is given by [15],

$$E_1 = V + E_C + \frac{\delta}{2}, \tag{2.26}$$

$$E_2 = V - E_C + \frac{\delta}{2}. \tag{2.27}$$

We have also introduced the density of states at energy ϵ, which, for a superconductor, is [54],

$$\varrho(\epsilon) = \Theta(\epsilon^2 - \Delta^2)\sqrt{\frac{\epsilon^2}{\epsilon^2 - \Delta^2}}. \tag{2.28}$$

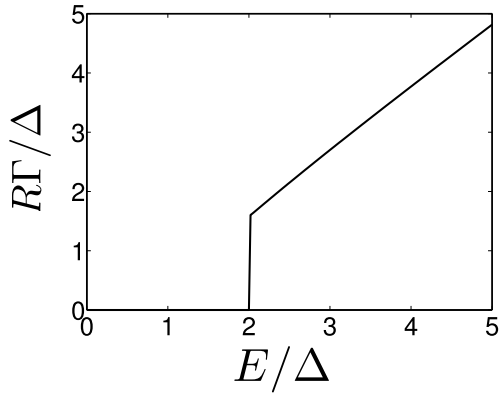

Figure 2.5.: Dependence of quasiparticle rate on the energy difference for the transition, $\Gamma(E)$.

In Fig. 2.5 we show the dependence of the quasiparticle rate on energy. We see that the rate is zero for applied bias below the threshold, $V < 2\Delta$, and increases, to a very good approximation, linearly above this. The energy dependence of the rates close to resonance is rather weak, and so from now on we simply use the on-resonance values for the decay rates [4, 15, 47].

2.3.1 *Master equation*

We now sketch the derivation of a Born-Markov master equation, which can describe the full quantum dynamics of the SSET tuned close to the JQP. We do not give a full details of derivation here, a more complete derivation can be found, for example, in Refs. [53, 48, 4, 15]. The Hamiltonian is, in this case, given by [53, 48],

$$H = H_S + H_{qp} + H_T, \tag{2.29}$$

where H_{qp} describes the bath provided by the quasiparticles, and H_T is the tunnel Hamiltonian which couples the SSET island to the bath, these are the bath and coupling Hamiltonians for our system (as in Eqn. (2.18)). We assume that the quasiparticle bath is weakly coupled to the system Hamiltonian, which is equivalent to assuming that the junction resistances are large, $R \gg R_Q$, where $R_Q = e^2/h$ is the quantum of resistance, and that the decay time of the bath is short compared to all other timescales (this is equivalent to requiring that E_C is the dominant energy scale [55]). This results in a standard Born-Markov master equation for the evolution of σ, the reduced density matrix of the SSET [56, 4, 57, 47],

$$\dot{\sigma} = -i[H_S, \sigma] + \mathcal{L}_{qp}\sigma, \tag{2.30}$$

where we only include the terms relevant to the JQP in Josephson part of H_S, since all of the other terms are far from resonance [53, 48, 4],

$$H_J = -\frac{E_J}{2}\sum_{N_L} |0, N_L\rangle \langle 2, N_L - 2| + h.c.. \tag{2.31}$$

The dissipative part of the evolution is given by [53, 48, 4],

$$\begin{aligned}\mathcal{L}_{qp}\sigma = \sum_{N_L} \Gamma_1 \big[&|1, N_L\rangle \langle 2, N_L| \sigma |2, N_L\rangle \langle 1, N_L| \\ &-1/2 \{|2, N_L\rangle \langle 2, N_L|, \sigma\}\big] \\ +\Gamma_2 \big[&|0, N_L\rangle \langle 1, N_L| \sigma |1, N_L\rangle \langle 0, N_L| \\ &-1/2 \{|1, N_L\rangle \langle 1, N_L|, \sigma\}\big].\end{aligned} \tag{2.32}$$

For the purposes of calculating the average current and charge noise (as we will go on to do in the following chapter), we can trace out the counting degree of freedom, N_L, and introduce the reduced density operator,

$$\rho_{ij} = \sum_{N_L} \langle i, N_L| \sigma |j, N_L + q\rangle, \tag{2.33}$$

where q is chosen to pick out the relevant coherences, i.e. for ρ_{00} we use $q = 0$, but for ρ_{20} we need to use $q = 2$. This leaves us with a simple equation which only describes the evolution of the degree of freedom corresponding to the charge on the island [14, 46, 47]. We notice that the only coherences which couple to the diagonal elements of the density matrix are those between the states which are linked by the resonant Josephson transition, $|0, N_L\rangle$ and $|2, N_L - 2\rangle$. Therefore, we only need to consider the evolution of five elements of ρ which are given by,

$$\dot{\rho}_{00} = \Gamma_2\rho_{11} - iJ(\rho_{02} - \rho_{20}), \tag{2.34}$$

$$\dot{\rho}_{11} = \Gamma_1\rho_{22} - \Gamma_2\rho_{11}, \tag{2.35}$$

$$\dot{\rho}_{22} = -\Gamma_1\rho_{22} + iJ(\rho_{02} - \rho_{20}), \tag{2.36}$$

$$\dot{\rho}_{02} = -iJ(\rho_{00} - \rho_{22}) + \left(i\delta - \frac{\Gamma_1}{2}\right)\rho_{02}, \tag{2.37}$$

$$\dot{\rho}_{20} = iJ(\rho_{00} - \rho_{22}) + \left(-i\delta - \frac{\Gamma_1}{2}\right)\rho_{20}, \tag{2.38}$$

where $J = E_J/2$. This set of equations can be converted into a matrix equation,

$$\frac{d|\rho\rangle\rangle}{dt} = \mathcal{M}|\rho\rangle\rangle, \tag{2.39}$$

where we now work in *Liouville space* [49, 58, 59, 60] in which operators in Hilbert space are described by vectors such as,

$$|\rho\rangle\rangle = (\rho_{00}, \rho_{11}, \rho_{22}, \rho_{02}, \rho_{20})^T, \tag{2.40}$$

and the evolution is described by a *superoperator* which in Liouville space is the matrix $\mathcal{M}$. This has the form,

$$\mathcal{M} = \begin{pmatrix} 0 & \Gamma_2 & 0 & -iJ & iJ \\ 0 & -\Gamma_2 & \Gamma_1 & 0 & 0 \\ 0 & 0 & -\Gamma_1 & iJ & -iJ \\ -iJ & 0 & iJ & i\delta - \Gamma_1/2 & 0 \\ iJ & 0 & -iJ & 0 & -i\delta - \Gamma_1/2 \end{pmatrix}. \tag{2.41}$$

We can then find the unique stationary state density matrix as the eigenvector of $\mathcal{M}$ with eigenvalue 0,

$$\mathcal{M}|0\rangle\rangle = 0, \tag{2.42}$$

where $|0\rangle\rangle$ is the vector representation of the stationary state density matrix normalised correctly so that $\rho_{00} + \rho_{11} + \rho_{22} = 1$.

2.3.2 *Average current*

The average current at the JQP can then be calculated in a similar way as for a normal SET, if we count the number of particles which go through the right-hand (incoherent) junction then we find that the stationary state current is simply,

$$\langle I \rangle = \Gamma_1 \rho_{22} + \Gamma_2 \rho_{11}, \tag{2.43}$$

where the density matrix elements are evaluated in the steady state. This gives the simple expression [51, 4],

$$\langle I \rangle = \frac{2E_J^2 \Gamma_1}{4\delta^2 + \Gamma_1^2 + E_J^2 \left(2 + \frac{\Gamma_1}{\Gamma_2}\right)}, \tag{2.44}$$

which is a Lorentzian as a function of detuning, δ. We note that, around the resonance, the energy dependence of the quasiparticle rates, $\Gamma_{1(2)}$, is rather weak, and the main voltage dependence of the current is due to the detuning parameter, δ. In the following chapters, to simplify our model, we will ignore the difference between the two quasiparticle rates, since this does not significantly alter the results [15, 57, 47].

2.4 DOUBLE JOSEPHSON QUASIPARTICLE RESONANCE

At the point in the V-n_g plane where two JQP lines would cross transport in the SSET becomes dominated by the double Josephson quasiparticle resonance (DJQP) [14, 55, 15, 57], as has been observed by a variety of experimental setups [61, 13, 62, 8]. A schematic of the cycle can be seen in Fig. 2.6. The cycle consists of two resonant Josephson

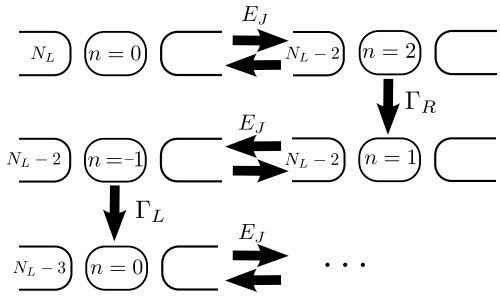

Figure 2.6.: The DJQP cycle. Quasiparticle decays and Cooper-pair tunnelling occurs at both junctions.

transitions, one at each junction, linked by incoherent quasiparticle decays. The DJQP occurs at lower voltages than the JQP cycle, because the limiting quasiparticle decay, $n = 1 \rightarrow 0$, is not involved. The signature of the DJQP can be seen in the experimental results reproduced in Fig. 2.3, where at voltages below the JQP lines a large peak is seen in the current.

The description of the DJQP follows a natural extension to that presented in the previous section for the JQP resonance. The condition for resonant Cooper-pair transport at each junction is given by [14, 15],

$$4E_C(n_g - 1) + V = 0, \tag{2.45}$$

$$4E_C n_g - V = 0, \tag{2.46}$$

which implies that the DJQP occurs when $n_g = 0.5$, $V = 2E_C$. It then follows that the DJQP is only seen in the vicinity of a point in Fig. 2.3, whereas the JQP resonance was a line. We can then identify two detuning parameters, one for each junction as,

$$\delta_L = 4E_C(n_g - 1) + V, \tag{2.47}$$

$$\delta_R = 4E_C n_g - V. \tag{2.48}$$

The quasiparticle rates can be calculated in exactly the same way as for the JQP in Eqn. (2.25). This leads to the result that, for the relevant quasiparticle transitions to be energetically favourable, we require,

$$V \geq 2\Delta - E_C. \tag{2.49}$$

Combining these results, on resonance, we need system parameters such that $3E_C \geq 2\Delta$, to ensure that all of the conditions are met to observe the DJQP. We find at the centre of the DJQP resonance the two quasiparticle rates are the same, $\Gamma_L = \Gamma_R$, since the two quasiparticle processes have the same energy gain at this point [15]. Since the energy dependence of the rates is weak (as for the JQP), we will simplify our model by using the on-resonance values, and set $\Gamma_L = \Gamma_R = \Gamma$ [14, 55, 15].

2.4.1 *Master equation*

The master equation for the DJQP can be derived in exactly the same way as for the JQP [14, 55, 57, 15] (making the same Born-Markov approximations), to find the form [14],

$$\dot{\sigma} = -i[H_S, \sigma] + \mathcal{L}_{qp}\sigma, \tag{2.50}$$

where the Josephson part of the Hamiltonian includes the transitions at both junctions, since they are both resonant at some point in the cycle [55],

$$H_J = -\frac{E_J}{2}\sum_{N_L}(|0, N_L\rangle\langle 2, N_L - 2| + |-1, N_L\rangle\langle 1, N_L| + h.c.). \tag{2.51}$$

The dissipative part of the master equation describes the quasiparticle decays and can be written as [48, 55],

$$\begin{aligned}\mathcal{L}_{qp}\sigma = \sum_{N_L}\Gamma\Big[&|1, N_L\rangle\langle 2, N_L|\,\sigma\,|2, N_L\rangle\langle 1, N_L| \\ &-\frac{1}{2}\{|2, N_L\rangle\langle 2, N_L|, \sigma\}\Big] \\ +\Gamma\Big[&|0, N_L\rangle\langle -1, N_L - 1|\,\sigma\,|-1, N_L - 1\rangle\langle 0, N_L| \\ &-\frac{1}{2}\{|-1, N_L\rangle\langle -1, N_L|, \sigma\}\Big].\end{aligned} \tag{2.52}$$

We can again, as with the JQP, trace out the degree of freedom associated with N_L, by defining the same quantity as in Eqn. (2.33), which then leaves us with an equation of the same form as Eqn. (2.39), but now the density matrix vector contains the eight elements,

$$|\rho\rangle\rangle = (\rho_{00}, \rho_{22}, \rho_{02}, \rho_{20}, \rho_{-1-1}, \rho_{11}, \rho_{-11}, \rho_{1-1})^T. \tag{2.53}$$

We include the evolution of the four charge states involved in the cycle, $(\rho_{00}, \rho_{22}, \rho_{-1-1}, \rho_{11})$, and also four coherences, $(\rho_{02}, \rho_{20}, \rho_{-11}, \rho_{1-1})$, two for the resonant Cooper-pair tunnelling at each junction. The evolution matrix is given by [55],

$$\mathcal{M} = \begin{pmatrix} 0 & 0 & -iJ & iJ & \Gamma & 0 & 0 & 0 \\ 0 & -\Gamma & iJ & -iJ & 0 & 0 & 0 & 0 \\ -iJ & iJ & G_L^- & 0 & 0 & 0 & 0 & 0 \\ iJ & -iJ & 0 & G_L^+ & 0 & 0 & 0 & 0 \\ 0 & 0 & 0 & 0 & -\Gamma & 0 & -iJ & iJ \\ 0 & \Gamma & 0 & 0 & 0 & 0 & iJ & -iJ \\ 0 & 0 & 0 & 0 & -iJ & iJ & G_R^- & 0 \\ 0 & 0 & 0 & 0 & iJ & -iJ & 0 & G_R^+ \end{pmatrix}, \tag{2.54}$$

where $G^{\pm}_{L(R)} = \pm i\delta_{L(R)} - \Gamma/2$, and we have chosen the order of the basis in such a way that it emphasises the block structure. The top left 4×4 block of $\mathcal{M}$ describes the coherent Josephson oscillations at the left junction, while the bottom right block describes the oscillations at the right junction. These blocks are linked by the two Γ terms which correspond to the incoherent decays which link the two sets of oscillations.

2.4.2 *Average current*

Calculating the average current at the DJQP is slightly more complicated than for the JQP, since both junctions involve the coherent transport of Cooper-pairs, and so rate equation arguments are not so simple to apply: there is no simple rate associated with the Josephson transitions. To overcome this problem, we note that the average current is simply accounted for by counting charges through the device and so an incoherent model of the transport is sufficient [55]. To produce this model, we adiabatically eliminate the coherences from the evolution matrix, by substituting the steady state values for the coherences into the evolution equations for the populations. This then gives an effective incoherent model for just the evolution of the probabilities. This is described by the matrix [55],

$$\mathcal{M}_{\text{inc}} = \begin{pmatrix} -\gamma_L & \gamma_L & \Gamma & 0 \\ \gamma_L & -(\gamma_L + \Gamma) & 0 & 0 \\ 0 & 0 & -(\gamma_R + \Gamma) & \gamma_R \\ 0 & \Gamma & \gamma_R & -\gamma_R \end{pmatrix}, \tag{2.55}$$

where,

$$\gamma_{L(R)} = \frac{E_J^2 \Gamma}{4\delta^2_{L(R)} + \Gamma^2}, \tag{2.56}$$

describe an effective incoherent rate for Cooper-pair tunnelling at the left (right) junction, and we use the basis $|\rho\rangle\rangle = (P_0, P_2, P_{-1}, P_1)^T$, with P_i the probability of being in the island state $n = i$. We can then use rate arguments to find the current as,

$$\langle I \rangle = 2\gamma_L(P_0 - P_2) + \Gamma_L P_{-1}. \tag{2.57}$$

where the P's are evaluated using the stationary state of the evolution matrix, $\mathcal{M}_{\text{inc}}$. This gives the result [13, 55]

$$\langle I \rangle = \frac{3E_J^2\Gamma}{2\Gamma^2 + 4E_J^2 + 4(\delta_L^2 + \delta_R^2)} \tag{2.58}$$

We see that, for given system parameters E_J and Γ, the current is a Lorentzian peak with a maximum at zero detuning, $\delta_L = \delta_R = 0$, as

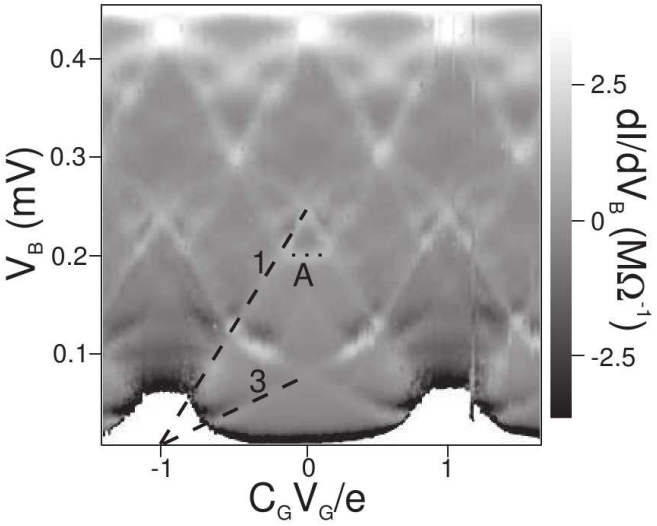

Figure 2.7.: Experimental results showing the low voltage Cooper-pair resonances, as the diamond shaped pattern. Reproduced from Ref. [65].

with the JQP, but now we have two detunings and so the DJQP feature is seen as a 2D Lorentzian peak as a function of the two voltages. This peak can clearly be seen in the experimental results of Fig. 2.3, at the points where pairs of JQP lines would intersect.

2.5 COOPER-PAIR RESONANCES

We now turn to a slightly more complex transport process in the SSET, the *Cooper-pair resonances* [52, 63, 45, 64, 65, 66] (CPRs). These are features which occur at voltages much lower than the JQP and DJQP, where transport is dominated by the coherent transfer of one or more Cooper-pairs across both junctions of the SSET. At these low voltages, there is not enough energy provided to break the superconducting gap thus the bath which causes dissipation and decoherence is not provided by quasiparticles (as it was for the other resonances), but instead is the electromagnetic environment in which the circuit is embedded. These features have been observed in measuremnts of the current through the SSET at low voltages. One set of results is shown in Fig. 2.7 (reproduced from Ref. [65]), the highlighted series of lines which depend on gate and drain source voltage are due to the CPRs.

In this section, we develop a detailed model of the SSET close to the CPRs, including the electromagnetic environment for the transistor, which requires a different treatment from that used for the JQP and DJQP resonances. We note that, throughout this section, we will go back to using dimensionful units, since we will often refer to experiments to pick realistic parameter values.

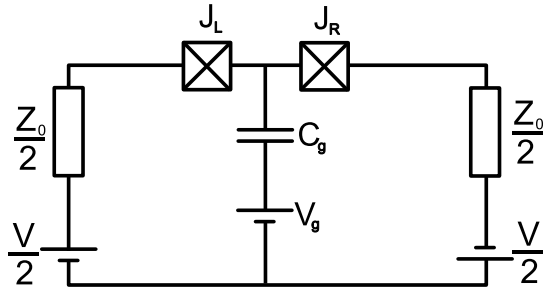

Figure 2.8.: Circuit diagram of the SSET. The SSET island is linked to the leads by the Josephson junctions, $J_{L(R)}$, and is coupled to the voltage gate by the capacitance C_g. The bias voltage, V, and impedances in the circuit, Z_0, are taken to be distributed symmetrically.

2.5.1 *Model System*

The SSET, including the embedded environment, is shown schematically in Fig. 2.8. For simplicity, we assume that the drain-source bias, V, is applied symmetrically and take the junctions to have equal capacitances, C_J, and Josephson energies, E_J. A voltage, V_g, is applied to the gate which has capacitance, C_g (assumed to be much less than C_J). The electromagnetic environment of the SSET is modelled by the impedance Z_0, distributed symmetrically between the leads. Since the transport involves only Cooper-pairs, we use the slightly different definition of the charging energy of the island, $E_C = 4e^2/2C_\Sigma$, which we assume is the dominant scale in the system, so that $E_C \gg k_B T, E_J$. We again describe the state of the SSET by $|n, N_L\rangle$, but now n counts the number of excess *Cooper-pairs* on the island, and N_L the number of Cooper-pairs in the left hand lead [52, 45, 64].

The full Hamiltonian of the system can be written as,

$$H = H_S + H_{\text{int}} + H_{\text{env}}, \tag{2.59}$$

where H_{env} is the Hamiltonian of the electromagnetic environment, and the SSET Hamiltonian, H_S, consists of two parts $H_S = H_C + H_J$. The charging Hamiltonian of the island is,

$$H_C = \sum_{n=0,1} \sum_{N_L} [E_C(n - n_g)^2 + 2eV(N_L + n)] \, |n, N_L\rangle \, \langle n, N_L| \,, \tag{2.60}$$

where $n_g = C_g V_g / 2e$ is the number of Cooper-pairs equivalent to the induced polarisation charge. The sum runs over $n = 0, 1$, since we have chosen $0 < n_g < 1$ such that these are the only available states for the island, at low temperature, as with the normal state SET.

It is useful to introduce the new counting variable $k = (N_R - N_L)/2$, with N_R the number of Cooper-pairs in the right reservoir [45]. This takes into account transitions at both junctions, and makes it easier to visualise the state of the system. We can then label the state with the complete basis set $\{|n, k\rangle\}$.

The states $\{|n,k\rangle\}$ can be separated into two ladders: $\{|0,k\rangle, |1,k+1/2\rangle\}$ and $\{|0,k+1/2\rangle, |1,k\rangle\}$, where k is now an integer. Josephson coupling links together adjacent members of the same ladder, but does not connect states from different ladders. Since the drain-source voltage $V \ll 2\Delta$, we may assume that quasiparticle tunnelling (which can link the ladders) is negligible, hence we need only consider one of the sets of states. Choosing the ladder $\{|0,k\rangle, |1,k+1/2\rangle\}$, the Josephson coupling between states is given by [45, 66],

$$H_J = -\frac{E_J}{2}\sum_k (|0,k\rangle\langle 1,k+1/2| + |0,k\rangle\langle 1,k-1/2| + h.c.). \quad (2.61)$$

We assume that the dominant source of dissipation and decoherence of the SSET is the electromagnetic environment, modelled by the impedances in the leads connecting it to the voltage sources. The impedances lead to fluctuations in the drain-source voltage, $\delta\hat{V}$, which couple to the system operator, $\hat{k}$, and give rise to the interaction Hamiltonian (a detailed derivation of this is given in appendix A),

$$H_{\text{int}} = -2e\hat{k}\delta\hat{V}. \quad (2.62)$$

The effects of $\delta\hat{V}$ on the SSET are determined by the equilibrium spectrum of the voltage fluctuations, which takes the form [41, 45, 67, 66, 2],

$$\begin{aligned} S_V(\omega) &= 4e^2\int_{-\infty}^{\infty}\langle\delta\hat{V}(t)\delta\hat{V}(0)\rangle e^{i\omega t}\,dt \\ &= \frac{8e^2\hbar\omega}{1-e^{-\hbar\omega/k_BT}}\text{Re}[Z_T], \end{aligned} \quad (2.63)$$

where $Z_T = (Z_0^{-1} - i\omega C_J^2/C_\Sigma)^{-1}$ is the total effective impedance seen at the junctions. At the low frequencies which turn out to be relevant for the system dynamics, $\omega \ll (\text{Re}[Z_T]C_J)^{-1}$, we can ignore the second term in the definition of Z_T above and take $\text{Re}[Z_T] = \text{Re}[Z_0]$. We further assume that the embedding circuit provides a low, real (Ohmic) impedance, to ensure weak coupling to the environment, which allows us to use the Born approximation later. This amounts to assuming that $Z_0 = R \ll R_Q$, where R_Q is the quantum of resistance, such as would be generated by a transmission line [3]. Our description can easily be extended to take into account a finite impedance in series with the gate voltage [66], but since we take the limit $C_g \ll C_J$, this has a much weaker influence, and so we neglect it here (see appendix A for details).

The voltage dependence of the charging energy leads to resonances where the eigenvalues of the charging Hamiltonian, H_C (Eqn. 2.60), become degenerate. The charging energies of the states $|0,k\rangle$ and $|1,k+p+1/2\rangle$, where $p = 0,1,2,\ldots$, become degenerate at particular values of the drain-source voltage, $V = V_{\text{res}}^{(p)}$, are given by $(2p+$

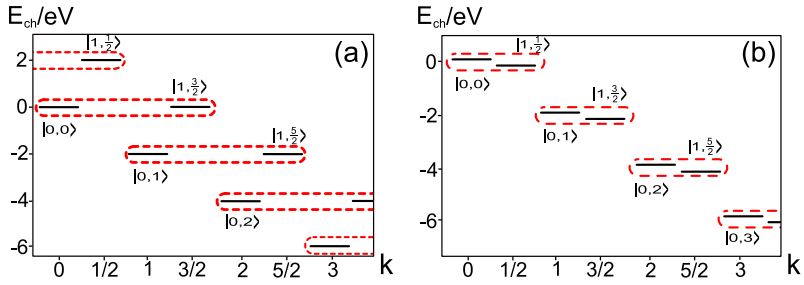

Figure 2.9.: Energy levels of H_C, (a) with $V = V_{\rm res}^{(1)}$ at the $p = 1$ resonance and (b) with $V \gtrsim V_{\rm res}^{(0)}$ for $p = 0$. The dashed lines enclose the doublets: the energy levels which are almost degenerate near the given resonance.

$1)eV_{\rm res}^{(p)} = E_C(1 - 2n_g)$. The energy levels near the $p = 0$ and $p = 1$ resonances are illustrated in Fig. 2.9.

The dynamics of the system around the resonances can be thought of as follows. Since $E_J \ll E_C$ for most choices of operating point, the charging energy dominates, however, close to degeneracies in the charging energy, the Josephson coupling becomes important, and the pairs of states, $|0, k\rangle$ and $|1, k + p + 1/2\rangle$, become strongly mixed, forming doublets. The interaction with the environment can then cause the system to decay into the neighbouring doublets with lower energy. Taken together, the coherent evolution and decay form a cascade in which k increases systematically, and hence a dc current flows. Away from the resonances, the coherent evolution is suppressed, and decay processes cannot take the system to ever higher k values, so the current is also suppressed. Thus, the degeneracies in the charging energy lead to resonances in the current [52, 63, 45, 68, 66]. The one exception to this picture arises for the $p = 0$ resonance, where one can see from Fig. 2.9(b) that, for voltages above resonance, $V > E_C|1 - 2n_g|/e$, the system can move indefinitely to larger values of k, via incoherent decay processes alone. Hence in this case the resonance becomes strongly broadened on one side [45, 66].

2.5.2 *Master equations*

Having seen how and where the Cooper-pair resonances arise, we now proceed to derive a quantitative description of the charge dynamics of the SSET that includes the dissipation and decoherence induced by the electromagnetic environment. As a first step, we use a unitary transformation method to derive an effective Hamiltonian which provides a systematic way of accounting for the coherent effect of the Josephson coupling between resonant states. We then proceed to derive the master equation for the SSET, tracing out the environment using the Born-Markov approximations. The resulting master

equation can then be used to derive a much simpler equation that describes just the SSET island charge.

2.5.2.1 *Effective Hamiltonian*

Close to the p-th Cooper-pair resonance, and provided that the voltage, V, is not too small, the eigenvalues of the SSET charging Hamiltonian are grouped into doublets, $\{|0,k\rangle, |1,k+p+1/2\rangle\}$, with the spacing between members of a given doublet much less than the spacing between the doublets. If the voltage drops below a certain threshold, the resonances start to overlap, since the various values of $V_{\text{res}}^{(p)}$ get very close together at low voltages, and the simple picture presented above breaks down. When all of these conditions are met, the main effect of the Josephson Hamiltonian is to introduce couplings between states within each doublet. Since the full system Hamiltonian cannot be diagonalised exactly, we treat the Josephson coupling as a perturbation, and use a unitary transformation to derive an effective Hamiltonian which takes into account the mixing it induces between states within a doublet [69].

In the full Hamiltonian, the Josephson terms link states which are far from resonance, these terms taken together form an effective link between the states in the same doublet. We therefore want to find a transformation to the Hamiltonian which makes this structure obvious. We seek a unitary transformation, U, such that the transformed Hamiltonian, $H_S' = UH_SU^\dagger$, is block diagonal in the space of the doublets. This transformation is found as a perturbation series in E_J, and we keep only the leading order contributions and those which occur at the correct order to describe the resonant coupling (details are given in appendix B). This results in an effective system Hamiltonian which is block-diagonal in the pairs of nearly-resonant states $\{|0,k\rangle, |1,k+p+1/2\rangle\}$. Each block takes the form,

$$H_k' = \begin{pmatrix} \bar{E} - \Delta E & J_p \\ J_p & \bar{E} + \Delta E \end{pmatrix}, \tag{2.64}$$

where $\bar{E} = -2eVk$ is the average charging energy of the resonant states, and J_p is the high order coupling between the states. For $p \geq 1$,

$$J_p = (-1)^p \frac{J^q}{\left(2eV_{\text{res}}^{(p)}\right)^{2p} (p!)^2}, \tag{2.65}$$

where $q = 2p+1$ and $J = E_J/2$. For the case $p = 0$, $J_p = J$. This term links the two resonant states by Josephson transitions at the junctions since there are q such Josephson event this occurs at order q in the perturbation theory. The splitting between resonant states, ΔE, is given by,

$$\Delta E = \frac{E_C(1-2n_g) - qeV}{2} + \frac{J^2}{eV_{\text{res}}^{(p)}} \frac{2q}{q^2-1}. \tag{2.66}$$

The first term is the electrostatic energy difference between the states, and the second term is a correction which arises at second order in the perturbation calculation[2]. For $p = 0$, the second order correction is given by $J^2/(eV_{\text{res}}^{(0)})$.

The block Hamiltonians are diagonalised by a rotation, $U_\alpha = \mathrm{e}^{-i\sigma_y \alpha}$, where σ_y is the usual Pauli matrix, to give the eigenstates of the doublets,

$$|a,k\rangle = \cos\alpha\,|0,k\rangle + \sin\alpha\,|1,k+{}^{(2p+1)}/_{2}\rangle\,, \tag{2.67a}$$

$$|b,k\rangle = -\sin\alpha\,|0,k\rangle + \cos\alpha\,|1,k+{}^{(2p+1)}/_{2}\rangle\,. \tag{2.67b}$$

The corresponding eigenenergies are, $E_{a,k} = \bar{E} - \Delta E'$, $E_{b,k} = \bar{E} + \Delta E'$, where α is defined by,

$$\sin 2\alpha = \frac{-J_p}{\Delta E'}, \tag{2.68a}$$

$$\cos 2\alpha = \frac{\Delta E}{\Delta E'}, \tag{2.68b}$$

and the energy level splitting is,

$$\Delta E' = \mathrm{sgn}(\Delta E)\sqrt{\Delta E^2 + J_p^2}, \tag{2.69}$$

which changes sign at the resonance.

Note that the description of the system in terms of doublets is only valid within a region around each resonance. The requirement that the spacing between energy levels in the doublet should be much smaller than the spacing between the doublets means that we must have $|\Delta E'| \ll eV$.

2.5.2.2 *Born-Markov description*

We now use the block-diagonal form of the Hamiltonian to derive the master equation for the SSET. To do this we need to calculate the different decay mechanisms which link the various states of the system. We will find that there are two important types of decay: firstly the inter-doublet decays which link states in different doublets and also the intra-doublet decays which link states within the same doublet.

We assume that the interaction between the SSET and the bath is weak [67], $R \ll R_Q$, and that the bath has a sufficiently dense spectrum of levels that the standard Born and Markov approximations can be made [69].

2 We evaluate J_p and the second order correction to ΔE using the resonance value for the voltage, $V = V_{\text{res}}^{(p)}$, as these terms only give a significant contribution in the vicinity of the resonances when the electrostatic part of ΔE is small. Making this approximation simplifies the calculation of the perturbation series.

Written in terms of the eigenstates of the system Hamiltonian, the Born-Markov master equation for the components of the SSET density operator, σ, takes the form [69],

$$\frac{d\tilde{\sigma}_{\mu\nu}}{dt} = \sum_{\mu'\nu'}^{\text{sec}} \mathscr{R}_{\mu\nu\mu'\nu'}\tilde{\sigma}_{\mu'\nu'}. \tag{2.70}$$

The tilde denotes the interaction picture, and the sum is over only the secular[3] terms, for which $\omega_{\mu\nu} = \omega_{\mu'\nu'}$, with $\omega_{\mu\nu}$ the frequency difference between eigenstates μ and ν. The coupling tensor, $\mathscr{R}_{\mu\nu\mu'\nu'}$, which describes how different states couple to each other in the master equation, is given by,

$$\begin{aligned}\mathscr{R}_{\mu\nu\mu'\nu'} = &-\int_0^\infty d\tau \\ &\times \left[g(\tau) \left(\delta_{\nu\nu'} \left[\sum_n k'_{\mu n} k'_{n\mu'} e^{i\omega_{\mu' n}\tau} \right] - k'_{\mu\mu'} k'_{\nu'\nu} e^{i\omega_{\mu'\mu}\tau} \right) \right. \\ &\left. + g(-\tau) \left(\delta_{\mu\mu'} \left[\sum_n k'_{\nu' n} k'_{n\nu} e^{i\omega_{n\nu'}\tau} \right] - k'_{\mu\mu'} k'_{\nu'\nu} e^{i\omega_{\nu\nu'}\tau} \right) \right],\end{aligned} \tag{2.71}$$

where $\hat{k}' = U\hat{k}U^\dagger$, and $g(\tau) = 4(e/\hbar)^2\langle \delta\hat{V}(\tau)\delta\hat{V}(0)\rangle$ is the correlation function of the electromagnetic environment whose properties were specified in Eqn. (2.63).

The transformed operator $\hat{k}'$ (given explicitly in appendix B) takes the form of a power series in J,

$$\hat{k}' = \hat{k}^{(0)} + \hat{k}^{(1)} + \hat{k}^{(2)} + \ldots, \tag{2.72}$$

where the term $\hat{k}^{(n)}$ is n^{th} order in J. We proceed by expanding the terms of the form $k'_{\mu\mu'}k'_{\nu\nu'}$ in $\mathscr{R}$ up to second order in J. The zeroth order term, $k^{(0)}_{\mu\mu'}k^{(0)}_{\nu\nu'}$, is diagonal in the charge state basis and generates dephasing of the charge states. For states within the same doublet, this leads to dissipative transitions between the eigenstates (intra-doublet transitions). The next non-zero contribution comes from terms of the form $k^{(1)}_{\mu\mu'}k^{(1)}_{\nu\nu'}$, which link states from a given doublet with states in the nearest neighbour and next-nearest neighbour doublets, leading to inter-doublet transitions. The same generic description applies to all the resonances with $p \geq 1$, but, for the $p = 0$ case, the states in a given doublet only couple to one other doublet leading to a slightly different form for the master equation, as we discuss below.

3 Secular terms are those for which $|\omega_{\mu\nu} - \omega_{\mu'\nu'}| \ll 1/\Delta t$ where Δt is the coarse-graining timescale (much larger than the correlation time of the environment, but much shorter than the timescale over which $\tilde{\sigma}$ evolves) over which the master equations are valid. Only terms where $\omega_{\mu\nu} = \omega_{\mu'\nu'}$ are included since the smallest Bohr frequency in the system is $J_p/\hbar$ which we can safely assume is much larger than $1/\Delta t$.

To calculate the inter-doublet terms, we note that close to resonance, the inter-doublet transitions occur on a much larger energy scale than the spacing between levels in the doublet, $peV \gg \Delta E'$. This allows us to simplify the calculation by ignoring the J_p terms in the block-diagonal Hamiltonian (Eqn. (2.64)), and treat the charge states, $|n,k\rangle$, as the eigenstates of the system. Thus, using the charge state basis, the inter-doublet contributions take the form,

$$\left.\frac{d\tilde{\sigma}_{0k,0k'}}{dt}\right|_{\text{inter}} = \Gamma_L\tilde{\sigma}_{1k+1/2,1k'+1/2} + \Gamma_R\tilde{\sigma}_{1k-1/2,1k'-1/2} - \Gamma_{\Delta k}\tilde{\sigma}_{0k,0k'}, \tag{2.73a}$$

$$\left.\frac{d\tilde{\sigma}_{1k+1/2,1k'+1/2}}{dt}\right|_{\text{inter}} = -(\Gamma_L+\Gamma_R+\Gamma_{\Delta k})\tilde{\sigma}_{1k+1/2,1k'+1/2}, \tag{2.73b}$$

$$\left.\frac{d\tilde{\sigma}_{0k,1k'+1/2}}{dt}\right|_{\text{inter}} = -\left(\frac{\Gamma_L+\Gamma_R}{2}+\Gamma_{\Delta k}\right)\tilde{\sigma}_{0k,1k'+1/2}, \tag{2.73c}$$

$$\left.\frac{d\tilde{\sigma}_{1k+1/2,0k'}}{dt}\right|_{\text{inter}} = -\left(\frac{\Gamma_L+\Gamma_R}{2}+\Gamma_{\Delta k}\right)\tilde{\sigma}_{1k+1/2,0k'}, \tag{2.73d}$$

where we have assumed $k_{\text{B}}T \ll peV$, and the dephasing rate is given by,

$$\Gamma_{\Delta k} = \frac{S_V(0)}{2\hbar^2}\Delta k^2, \tag{2.74}$$

with $\Delta k = k_1 - k_2$ for $\tilde{\sigma}_{ik_1,jk_2}$. The transition rates at the centre of the resonance[4] are given by,

$$\Gamma_L = \left(\frac{J}{4peV_{\text{res}}^{(p)}}\right)^2 \frac{S_V(\omega_p)}{\hbar^2}, \tag{2.75}$$

$$\Gamma_R = \left(\frac{J}{4(p+1)eV_{\text{res}}^{(p)}}\right)^2 \frac{S_V(\omega_{p+1})}{\hbar^2}, \tag{2.76}$$

with $\omega_p = 2peV_{\text{res}}^{(p)}/\hbar$. For the $p = 0$ case, there is only one decay channel linking different doublets, and the associated energy difference is $2eV$. Thus, provided $2eV \gg k_{\text{B}}T, \Delta E'$, the same set of inter-doublet terms is obtained, but with $\Gamma_L = 0$.

To calculate the terms in the master equation describing the intra-doublet transitions, we need to use the full eigenstates of the system (Eqn. (2.67)), and take account of the effects of the J_p terms in the Hamiltonian. The energy differences between the states within a doublet can be much smaller than those between the doublets, and so, in this case, we include the effects of a finite temperature by keeping

4 All of our calculations are performed in the vicinity of the resonances and so we generally evaluate $\Gamma_{L,R}$ using the resonance value for the voltage, $V = V_{\text{res}}^{(p)}$, as within the range of voltages over which the doublet picture is valid these quantities are typically very slowly varying.

the finite temperature part of the voltage fluctuation spectrum in Eqn. (2.63). This leads to the intra-doublet equations,

$$\left.\frac{d\tilde{\sigma}_{ak,ak}}{dt}\right|_{\text{intra}} = \gamma_{ba}\tilde{\sigma}_{bk,bk} - \gamma_{ab}\tilde{\sigma}_{ak,ak}, \tag{2.77a}$$

$$\left.\frac{d\tilde{\sigma}_{bk,bk}}{dt}\right|_{\text{intra}} = \gamma_{ab}\tilde{\sigma}_{ak,ak} - \gamma_{ba}\tilde{\sigma}_{bk,bk}, \tag{2.77b}$$

$$\left.\frac{d\tilde{\sigma}_{ak,bk}}{dt}\right|_{\text{intra}} = -\left(\frac{\gamma_{ab}+\gamma_{ba}}{2}\right)\tilde{\sigma}_{ak,bk}, \tag{2.77c}$$

$$\left.\frac{d\tilde{\sigma}_{bk,ak}}{dt}\right|_{\text{intra}} = -\left(\frac{\gamma_{ab}+\gamma_{ba}}{2}\right)\tilde{\sigma}_{bk,ak}, \tag{2.77d}$$

where γ_{ij} gives the transition rate between the states, $|i,k\rangle$ and $|j,k\rangle$, within the k-th doublet. These have the form,

$$\gamma_{ij} = \left(\frac{2p+1}{2}\right)^2 c^2 s^2 \frac{S_V(\omega_{ij})}{\hbar^2}, \tag{2.78}$$

where $s = \sin\alpha$, $c = \cos\alpha$ and $\omega_{ab} = -\omega_{ba} = -2\Delta E'/\hbar$.

Finally, we transform the inter-doublet contributions, Eqn. (2.73), into the eigenstate basis, and combine them with the intra-doublet terms, Eqn. (2.77), to obtain the full master equations of the system. For sufficiently weak dissipation, $\Gamma_{L(R)} \ll |\omega_{ab}|$, it is possible to simplify the master equation significantly by making a further rotating wave approximation (RWA). In this approximation, we only keep terms which couple a population to a population or terms which couple a coherence to another coherence with the same energy spacing [69]. After this approximation the master equation takes the form,

$$\begin{aligned}\frac{d\tilde{\sigma}_{ak,ak'}}{dt} &= \Gamma^p_{aa}\tilde{\sigma}_{ak_1,ak'_1} + \Gamma^p_{ba}\tilde{\sigma}_{bk_1,bk'_1} \\ &+ \Gamma^{p+1}_{aa}\tilde{\sigma}_{ak_2,ak'_2} + \Gamma^{p+1}_{ba}\tilde{\sigma}_{bk_2,bk'_2} + \gamma^{\Delta k}_{ba}\tilde{\sigma}_{bk,bk'} \\ &- (\Gamma^p_{ab} + \Gamma^p_{aa} + \Gamma^{p+1}_{ab} + \Gamma^{p+1}_{aa} + \gamma^{\Delta k}_{ab} + \Gamma_{\Delta k})\tilde{\sigma}_{ak,ak'},\end{aligned} \tag{2.79a}$$

$$\begin{aligned}\frac{d\tilde{\sigma}_{bk,bk'}}{dt} &= \Gamma^p_{ab}\tilde{\sigma}_{ak_1,ak'_1} + \Gamma^p_{bb}\tilde{\sigma}_{bk_1,bk'_1} \\ &+ \Gamma^{p+1}_{ab}\tilde{\sigma}_{ak_2,ak'_2} + \Gamma^{p+1}_{bb}\tilde{\sigma}_{bk_2,bk'_2} + \gamma^{\Delta k}_{ab}\tilde{\sigma}_{ak,ak'} \\ &- (\Gamma^p_{ba} + \Gamma^p_{bb} + \Gamma^{p+1}_{ba} + \Gamma^{p+1}_{bb} + \gamma^{\Delta k}_{ba} + \Gamma_{\Delta k})\tilde{\sigma}_{bk,bk'},\end{aligned} \tag{2.79b}$$

$$\begin{aligned}\frac{d\tilde{\sigma}_{ak,bk'}}{dt} &= -\left(\frac{\Gamma^p_{aa}+\Gamma^p_{bb}}{2}\right)\tilde{\sigma}_{ak_1,bk'_1} - \left(\frac{\Gamma^{p+1}_{aa}+\Gamma^{p+1}_{bb}}{2}\right)\tilde{\sigma}_{ak_2,bk'_2} \\ &- \left(\frac{\Gamma_L+\Gamma_R}{2} + \gamma^{\Delta k}_{\text{coh}} + \Gamma_{\Delta k}\right)\tilde{\sigma}_{ak,bk'},\end{aligned} \tag{2.79c}$$

where $k_1 = k - p$, $k_2 = k - p - 1$ and Γ_{ij}^p are the transition rates between the states $|i, k+p\rangle \to |j, k\rangle$, which are given by,

$$\Gamma_{aa}^p = \Gamma_{bb}^p = \Gamma_L c^2 s^2, \tag{2.80a}$$
$$\Gamma_{aa}^{p+1} = \Gamma_{bb}^{p+1} = \Gamma_R c^2 s^2, \tag{2.80b}$$
$$\Gamma_{ba}^p = \Gamma_L c^4, \tag{2.80c}$$
$$\Gamma_{ba}^{p+1} = \Gamma_R c^4, \tag{2.80d}$$
$$\Gamma_{ab}^p = \Gamma_L s^4, \tag{2.80e}$$
$$\Gamma_{ab}^{p+1} = \Gamma_R s^4. \tag{2.80f}$$

We have also defined,

$$\gamma_{ij}^{\Delta k} = \begin{cases} \gamma_{ij} & \Delta k = 0, \\ \left(\frac{2p+1}{2}\right)^2 \frac{S_V(0)}{\hbar^2} c^2 s^2 & \Delta k \neq 0, \end{cases} \tag{2.81}$$

$$\gamma_{\text{coh}}^{\Delta k} = \begin{cases} \frac{\gamma_{ab}+\gamma_{ba}}{2} & \Delta k = 0, \\ \left[\left(\frac{2p+1}{2}\right)(c^4 + s^4) + \Delta k \cos 2\alpha\right] \left(\frac{2p+1}{2}\right) \frac{S_V(0)}{\hbar^2} & \Delta k \neq 0. \end{cases} \tag{2.82}$$

For the RWA to be valid, the incoherent decay rates must be much smaller than the Bohr frequency associated with the doublets, which, for $p \geq 1$, results in the condition $\Gamma_L \ll 2|J_p|/\hbar$ (since Γ_L is the largest decay rate). From Eqs. (2.65) and (2.75), we find that, $\hbar\Gamma_L/|J_p| \propto (R/R_Q)(eV_{\text{res}}^{(p)}/J)^{2p-1}$. By tuning the gate voltage, $V_{\text{res}}^{(p)}$ can take on any value in the range $0 < (2p+1)eV_{\text{res}}^{(p)} < E_C$, thus, for a given value of R, the requirement that the RWA is valid puts a limit (which becomes stricter as p increases) on the maximum voltage that can be considered. Our interest here is in the regime where the SSET charge dynamics are largely coherent, leading to sharp resonances in the current, and hence we naturally focus on the regime where the RWA is valid. Since these conditions can only be met in practice [66, 63, 65] for the lower values of p, we will concentrate on the $p = 0, 1$ resonances.

The master equations bear a strong resemblance to those which describe the radiative cascade of quantum optics [69]. In the radiative cascade, a laser field drives a two-level atom, and when the field is treated quantum mechanically, the eigenstates of the system are atom-field hybrids (dressed states). Decay processes lead to a cascade in which photons are emitted, and the laser state moves progressively towards lower photon numbers. Analogously, in the SSET, the states $\{|a, k\rangle, |b, k\rangle\}$ are like the atom-laser dressed states, with the island charge states playing the role of the atom, and k like the state of the laser. In this case, decay processes generate a cascade, in which the system evolves towards states of ever increasing k.

2.5.2.3 *Effective two-level system*

Although the full master equation for the SSET is rather complicated, it is possible to derive a much simpler set by tracing over the charges that have passed through the SSET. We define the full set of reduced coherences,

$$\rho_{ij}^{q}(t) = \sum_{k} \langle i, k+q | \, \sigma(t) \, | j, k \rangle \,, \tag{2.83}$$

and, carrying out the trace over k, we obtain a much simpler matrix equation,

$$\frac{d|\rho^q\rangle\rangle}{dt} = (2iqeV + \mathcal{M}^q)|\rho^q\rangle\rangle, \tag{2.84}$$

where $|\rho^q\rangle\rangle = (\rho^q_{aa}, \rho^q_{bb}, \rho^q_{ab}, \rho^q_{ba})^T$. Within the RWA the form of the evolution matrix, $\mathcal{M}^q$, is given by,

$$\mathcal{M}^q = \begin{pmatrix} -(\Gamma_q + \Gamma_a^q) & \Gamma_b^q & 0 & 0 \\ \Gamma_a^q & -(\Gamma_q + \Gamma_b^q) & 0 & 0 \\ 0 & 0 & -(i\omega_{ab} + \Gamma_{\mathrm{coh}}^q) & \\ 0 & 0 & 0 & -(-i\omega_{ab} + \Gamma_{\mathrm{coh}}^q) \end{pmatrix}, \tag{2.85}$$

where $\Gamma_q = \Gamma_{\Delta k = q}$ and the other rates are given by,

$$\Gamma_a^q = (\Gamma_L + \Gamma_R)\cos^4\alpha + \gamma_{ba}^q, \tag{2.86}$$

$$\Gamma_b^q = (\Gamma_L + \Gamma_R)\sin^4\alpha + \gamma_{ab}^q, \tag{2.87}$$

$$\Gamma_{\mathrm{coh}}^q = \frac{(\Gamma_L + \Gamma_R)(1 + 2c^2s^2)}{2} + \gamma_{\mathrm{coh}}^q + \Gamma_q. \tag{2.88}$$

By taking $q = 0$, we obtain the equation which describes the evolution of the island charge. This is equivalent to the evolution matrices presented earlier for the JQP and DJQP. The resulting master equation describes a two-level system (TLS) which is both driven and damped.

The full density operator, σ, does not have a steady state, the system cascades to increasing values of k, as charge tunnels though the transistor. The reduced equations derived above, however, do have a well defined steady state. All of the reduced coherences, where $q \neq 0$, are zero in the steady state, $\rho_{ij}^{q\neq 0} = 0$. The $q = 0$ case has the steady state: $\rho_{aa(bb)} = \Gamma_{b(a)}/(\Gamma_a + \Gamma_b)$, and $\rho_{ab} = 0$. Note that here, and in what follows we drop the superscripts on ρ and Γ for the case $q = 0$.

2.5.3 *Average current*

We now go on to calculate the steady state average current, $\langle I \rangle$, through the transistor. The current is determined by the rate of change of the number of Cooper-pairs which have crossed the device,

$$\langle I \rangle = 2e\frac{d\langle \hat{k}' \rangle}{dt} = 2e \, \mathrm{Tr}[\hat{k}'\dot{\sigma}]. \tag{2.89}$$

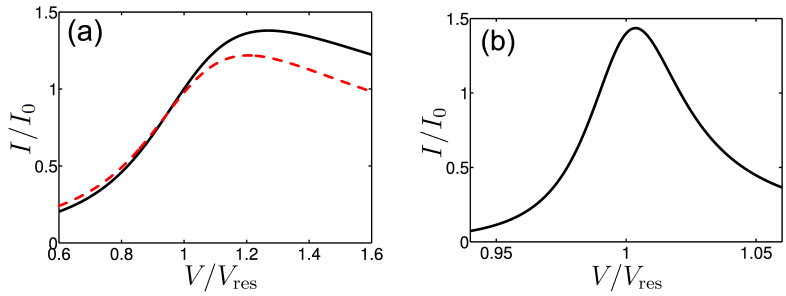

Figure 2.10.: Current-voltage characteristics of the SSET in the vicinity of (a) the $p = 0$ resonance (b) the $p = 1$ resonance. The current is scaled by $I_0 = e(\Gamma_L + \Gamma_R)$ in each case. The values of the other parameters are given in the text. In (a) we also show in the dashed, red line the current calculated using the full voltage dependence of the decay rate Γ_R and the Hamiltonian.

We calculate only the dominant term, which comes from the lowest order part of the $\hat{k}'$ expansion, $\hat{k}^{(0)} = \hat{k}$, as the next lowest order contribution (from $\hat{k}^{(1)}$) vanishes and we neglect higher order contributions. In this basis, the density matrix is diagonal, and so we do not need to eliminate the coherences as we did for the DJQP. We can ignore the contributions from the intra-doublet rates, since these are in thermal equilibrium, and do not give any contribution to the average dc current. This means that, in terms of the inter-doublet rates, we have,

$$\begin{aligned}\langle I\rangle = 2e\Big(p\left[(\Gamma^p_{aa}+\Gamma^p_{ab})\rho_{aa}+(\Gamma^p_{bb}+\Gamma^p_{ba})\rho_{bb}\right]\\ +(p+1)\left[(\Gamma^{p+1}_{aa}+\Gamma^{p+1}_{ab})\rho_{aa}+(\Gamma^{p+1}_{bb}+\Gamma^{p+1}_{ba})\rho_{bb}\right]\Big),\end{aligned} \tag{2.90}$$

which can be more compactly written by transforming the decays to the charge basis,

$$\langle I\rangle = 2e\left(\rho_{aa}s^2+\rho_{bb}c^2\right)\left(p\Gamma_L+(p+1)\Gamma_R\right). \tag{2.91}$$

Within the regime where the RWA is valid, this matches the results obtained previously [70, 45, 64] using a rate equation approach and Fermi's golden rule.

The current near the $p = 0$ and $p = 1$ resonances is shown in Fig. 2.10, for the typical parameter values [66, 63, 65] $E_C = 4E_J = 100\,\mu$eV, $T = 30$ mK, a resistance for the embedding circuit $R = 50\,\Omega$, and we have set $n_g = 0.1$. The full lines in Fig. 2.10 show the current calculated with the decay rates, J_p and ΔE, given by their on-resonance values. As the $p = 0$ resonance is very broad (in comparison to the $p = 1$ resonance), we have also calculated the current including the full voltage dependence of the relevant decay rate and the Hamiltonian (dashed curve in Fig. 2.10(a)).

The two resonances show rather different characteristics. The current around the $p = 0$ resonance is broad and highly asymmetric. This is because, in this case, purely dissipative processes can generate

a dc current for $V > V_{\text{res}}$ (incoherent Cooper-pair tunnelling [2]), as can be seen from the energy level diagram in Fig. 2.9(b). The current for the $p = 1$ resonance is much closer to the standard Lorentzian form of a resonance, the small amount of asymmetry still present arises from the intra-doublet transitions. For $V < V_{\text{res}}$, relaxation between the levels of the doublets (controlled by $\gamma_{ab(ba)}$) hinders current flow, whilst for $V > V_{\text{res}}$ it helps it. This leads to a small asymmetry in the current as a function of voltage which is only removed when the temperature is sufficiently high such that $\gamma_{ab} \simeq \gamma_{ba}$, and a Lorentzian shape is recovered.

Extending our calculation to include the regime where the RWA is no longer valid, we find that the current peaks at the resonances become suppressed. This is because, outside of the RWA, the system is unable to build up the coherence between charge states necessary for current to flow. This is consistent with Ref. [66], where this effect was studied in detail.

2.6 SUMMARY

In this chapter, we have described the main transport mechanisms which lead to dc current, in both the normal and superconducting SET. For the normal SET, we saw that it was enough to use a classical master equation description to give access to the full dynamics. For the SSET, we needed to develop a full quantum description, including both the coherent Hamiltonian evolution, as well as environment induced dissipation. The dominant environment is different for the different current carrying processes, for the JQP and DJQP quasiparticles are present and generate dissipation and decoherence, for the CPRs dissipation is induced by fluctuations in applied voltage source due to impedances in the circuit.

In the following chapters, we will show how the master equations we have just described can be used to investigate the fluctuations in both the charge on the SSET island and the current through the transistor.

Part II.

Quantum Noise

3

CHARGE NOISE

As we have seen in the previous chapter, quantities such as the average current through the SSET, or the average charge on the island, do not give any insights into the quantum mechanics of the transport. Effective classical tunnelling models are enough to give results, and the Cooper-pair transport can be modelled as a classical stochastic process. In this chapter and the next, we will consider the *quantum noise spectra* [71, 3] of the SSET, and show how information contained in the noise can give more information about the underlying quantum mechanics of the transport. This chapter focuses on the noise in the charge on the SSET island, in the following chapter we will look at the noise in the current travelling through the SSET. We will show how these quantities can give definite signatures of the quantum mechanical nature of the dynamics. We will also describe the quantum mechanical nature of the processes used to observe such quantities.

In Sec. 3.1 we outline exactly what we mean by quantum noise and describe how quantum noise differs from classical noise. Then in Sec. 3.2 we show one way of experimentally accessing the quantum noise, by coupling the system of interest to a harmonic oscillator. We return to the SSET in Sec. 3.3, and discuss possible systems which can be used to measure both the island charge and current noise. The remainder of the chapter focuses on charge noise. In Sec. 3.4, we begin by giving an outline of the technique which we use for calculating the charge noise. This is followed in Secs. 3.5 and 3.6 by reviews of previous calculations of the charge for the SSET close to the JQP and DJQP resonances. Finally, in Sec. 3.7, we give a new calculation of the noise close to the Cooper-pair resonances, discuss how this differs from the other resonances, and analyse the back-action when an oscillator is coupled to the SSET.

3.1 QUANTUM NOISE

A fundamental part of the study of noisy classical processes involves the calculation of two-time correlation functions of some observable F, $\langle F(t)F(0)\rangle$ [3]. These quantities allow us access to information about the nature of the fluctuations which are not available from just

the steady state mean dynamics $\langle F \rangle$. An equivalent way of looking at these two-time correlation functions is through their Fourier transform, the *noise spectral density*, defined as,

$$S_F^{\text{clas}}(\omega) = \int_{-\infty}^{\infty} \mathrm{e}^{i\omega t} \langle \delta F(t) \delta F(0) \rangle \, dt, \tag{3.1}$$

where the average is taken over the stationary state probability distribution, and $\delta F = F - \langle F \rangle$ quantifies fluctuations away from the mean. For a *classical* quantity F, $\langle \delta F(t) \delta F(0) \rangle = \langle \delta F(0) \delta F(t) \rangle$: the order we do the measurements in doesn't matter, furthermore $\langle \delta F(t) \delta F(0) \rangle$ must be a *real* quantity [72]. This then allows us to write the spectral density as,

$$S_F^{\text{clas}}(\omega) = \int_{0}^{\infty} 2 \cos \omega t \langle \delta F(t) \delta F(0) \rangle \, dt, \tag{3.2}$$

which is *symmetric* in frequency, $S_F^{\text{clas}}(\omega) = S_F^{\text{clas}}(-\omega)$ [3].

Similarly, the study of *quantum noise* is concerned with the two time correlation functions of quantum mechanical *operators*, $\langle \hat{F}(t) \hat{F}(0) \rangle$. It is again convenient to work with the *quantum noise spectral density*, which is defined in an analogous way to the classical quantity [71, 3],

$$S_F(\omega) = \int_{-\infty}^{\infty} \mathrm{e}^{i\omega t} \langle \delta \hat{F}(t) \delta \hat{F}(0) \rangle \, dt, \tag{3.3}$$

where the average is now taken over the stationary density matrix, and we have defined the operator, $\delta \hat{F} = \hat{F} - \langle \hat{F} \rangle$. Since $\hat{F}(t)$ and $\hat{F}(0)$ do not necessarily commute, we have, $\langle \hat{F}(t) \hat{F}(0) \rangle \neq \langle \hat{F}(0) \hat{F}(t) \rangle$. In fact, the situation is complicated even further: the product of two Hermitian operators is, in general, no longer Hermitian, and so $\langle \hat{F}(t) \hat{F}(0) \rangle$ can be complex, and therefore is *unobservable* [3]. The spectral density, however, is real. As long as the average is taken in the stationary state, we may write, for some Hermitian Hamiltonian, H, which describes the full unitary evolution of the system and environment,

$$\langle \hat{F}(t) \hat{F}(0) \rangle = \mathrm{Tr}[\mathrm{e}^{iHt} \hat{F} \mathrm{e}^{-iHt} \hat{F} \rho] = \mathrm{Tr}[\hat{F} \mathrm{e}^{-iHt} \hat{F} \mathrm{e}^{iHt} \rho] = \langle \hat{F}(0) \hat{F}(t) \rangle^*. \tag{3.4}$$

Here we have used the cyclic property of the trace [71],

$$\mathrm{Tr}[ABC] = \mathrm{Tr}[CAB] = \mathrm{Tr}[BCA], \tag{3.5}$$

and the fact that, in the steady state, $[\rho, H] = 0$, along with the assumption that our observable $F = F^\dagger$ is Hermitian. This allows us to write the noise spectrum as,

$$S_F(\omega) = 2\mathrm{Re} \int_{0}^{\infty} \mathrm{e}^{i\omega t} \langle \delta \hat{F}(t) \delta \hat{F}(0) \rangle \, dt, \tag{3.6}$$

which is real and so, in principle, can be observed, but the quantum noise spectrum is *not* symmetric in frequency. Measurement of an asymmetric noise spectrum is a signature of quantum dynamics [3].

As a simple example of the difference between quantum and classical noise, consider the position noise spectrum of a harmonic oscillator in thermal equilibrium with an external bath [3],

$$S_x(\omega) = 2\mathrm{Re}\int_0^\infty \mathrm{e}^{i\omega t}\langle \delta\hat{x}(t)\delta\hat{x}(0)\rangle\, dt. \tag{3.7}$$

The two time correlation function can be calculated as,

$$\langle \hat{x}(t)\hat{x}(0)\rangle = \langle \hat{x}(0)\hat{x}(0)\rangle \cos\omega_0 t + \langle \hat{p}(0)\hat{x}(0)\rangle \frac{\sin\omega_0 t}{\omega_0}, \tag{3.8}$$

where ω_0 is the frequency of the oscillator and $\hat{p}$ is the operator for the oscillator's momentum. We use units with $\hbar = M = 1$, with M the mass of the oscillator. We have changed to using $\hat{x}$ instead of $\delta\hat{x}$, since in thermal equilibrium, $\langle \hat{x}\rangle = 0$. In the classical limit, $\langle \hat{p}\hat{x}\rangle = 0$, since the position and velocity of a thermal oscillator are uncorrelated. In the quantum case, since $\hat{x}$ and $\hat{p}$ do not commute, we find [3], $\langle \hat{p}(0)\hat{x}(0)\rangle = -i/2$. Using this, and the fact that the stationary state of a harmonic oscillator in thermal equilibrium at temperature T, is given by the Bose distribution, $n_B(\omega_0)$, we find that the two-time correlation function is,

$$\langle \hat{x}(t)\hat{x}(0)\rangle = \frac{1}{2\omega_0}\left[n_B(\omega_0)\mathrm{e}^{i\omega_0 t} + (n_B(\omega_0)+1)\mathrm{e}^{-i\omega_0 t}\right], \tag{3.9}$$

which gives the noise spectrum,

$$S_x(\omega) = \frac{\pi}{\omega_0}\left[n_B(\omega_0)\delta(\omega+\omega_0) + (n_B(\omega_0)+1)\delta(\omega-\omega_0)\right]. \tag{3.10}$$

This expression is asymmetric at low temperatures, $T \ll \omega_0$, and becomes symmetric in the high temperature limit, where $n_B(\omega_0) \approx n_B(\omega_0)+1$. Thus, as expected, it is only necessary to use a quantum mechanical description when $T \ll \omega_0$ for a harmonic oscillator [3].

Even though the quantum noise spectrum is real, and so there is no formal reason why it should not be observable, it is not immediately obvious how to measure it. It is necessary to find a detector which can distinguish between the noise power at positive and negative frequencies. In the following section, we will show how this is possible using an auxiliary quantum system coupled to the device of interest.

3.2 LINEAR RESPONSE

In the previous section, we outlined a definition of the quantum noise spectrum. We showed that the spectrum is real, and so now the obvious question to ask is, how do we go about measuring such a quantity? To do this we must couple the system to an external device

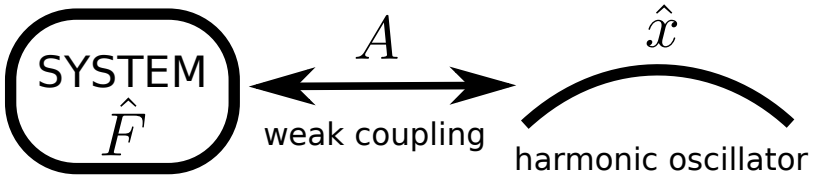

Figure 3.1.: Schematic representation of the system-oscillator coupling Hamiltonian, Eqn. (3.11).

known as a *quantum spectrum analyser* [3]; a quantum mechanical system which can distinguish between noise at positive and negative frequencies. Examples of such systems which have been used in recent experiments include quantum two level systems [73, 74, 3], Josephson junctions [75, 9] and quantum harmonic oscillators [76, 10, 8, 3].

In this section, we will give an overview of a calculation showing how a quantum harmonic oscillator can be used as a quantum spectrum analyser, closely following the approach outlined in Ref. [3]. The harmonic oscillator will be the most relevant example when we return to consider the SSET in the remainder of the chapter, since the noise has been measured in this way in a number of experiments [10, 8]. The calculation for a two-level system follows along similar lines [3].

We examine the behaviour of a harmonic oscillator weakly coupled to an operator in our system, the set-up is shown schematically in Fig. 3.1. To calculate the dynamics we use the ideas of *linear response theory* [77, 3]. We consider the case of linear coupling between the system operator $\hat{F}$ and the position of the oscillator, which gives the coupling Hamiltonian the form,

$$H_{\text{int}} = A\hat{F}\hat{x}, \tag{3.11}$$

where $\hat{x} = \hat{a} + \hat{a}^\dagger$ is the dimensionless position operator for the oscillator and A is the coupling strength. In the weak coupling limit we may use perturbation theory to obtain expressions for the transition rates between eigenstates of the harmonic oscillator, induced by the interaction with the system, by using Fermi's golden rule. These are given by [3],

$$\Gamma_{n\to n+1} = A^2(n+1)S_F(-\omega_0) = (n+1)\Gamma_\uparrow, \tag{3.12}$$

$$\Gamma_{n\to n-1} = A^2 n S_F(\omega_0) = n\Gamma_\downarrow, \tag{3.13}$$

where $\Gamma_{i\to j}$ is the transition rate between the Fock states, $|i\rangle$ and $|j\rangle$, of the oscillator, ω_0 is the frequency of the oscillator, and $S_F(\omega)$ is the quantum noise spectrum of the system. We have defined the rates, $\Gamma_\uparrow = A^2 S_F(-\omega_0)$ and $\Gamma_\downarrow = A^2 S_F(\omega_0)$, for compactness.

We see from these expressions that fluctuations in the system operator $\hat{F}$ at the frequency of the oscillator cause transitions between eigenstates. We also see that the rates to go up an energy level and to

drop down an energy level are proportional to the noise at negative and positive frequencies respectively, and so we begin to see how the dynamics of the oscillator can measure the quantum noise.

To proceed, we use these rates to construct a simple master equation for the probability that the oscillator is in state $|n\rangle$,

$$\dot{P}(n) = n\Gamma_{\uparrow}P(n-1) + (n+1)\Gamma_{\downarrow}P(n+1) - (n\Gamma_{\downarrow} + (n+1)\Gamma_{\uparrow})P(n), \quad (3.14)$$

which then has the stationary state distribution,

$$P_{\text{st}}(n) = \exp\left(-\frac{n\omega_0}{T_{BA}(\omega_0)}\right)\left[1 - \exp\left(-\frac{\omega_0}{T_{BA}(\omega_0)}\right)\right]^{-1}. \quad (3.15)$$

We can map this onto the distribution which would be measured in an oscillator in thermal equilibrium, as long as we identify the (frequency dependent) effective temperature due to the *back-action* of the system on the oscillator as,

$$T_{BA}(\omega) = \frac{\omega}{\ln\left(\frac{S_F(\omega)}{S_F(-\omega)}\right)}. \quad (3.16)$$

This can equally be written as an effective Bose occupation number for the oscillator,

$$n_{BA}(\omega) = \frac{1}{\exp\left(\frac{\omega}{T_{BA}(\omega)}\right) - 1} = \left[\frac{S_F(\omega)}{S_F(-\omega)} - 1\right]^{-1}. \quad (3.17)$$

The back-action arises because of the coupling between the system and the oscillator. This means that the dynamics of the system have an effect on the oscillator, in principle we also expect the dynamics of the oscillator to effect the system, but as we only consider the lowest order contributions, this effect is ignored within the linear response formalism [77, 3].

More information can be gained by looking at how the oscillator reaches this steady state. We can write an equation for the average energy of the oscillator,

$$\langle E\rangle = \sum_0^{\infty} \omega_0\left(n + \frac{1}{2}\right)P(n), \quad (3.18)$$

which is given by,

$$\langle \dot{E}\rangle = \gamma_{BA}(\omega_0)\left[\omega_0\left(n_{BA} + \frac{1}{2}\right) - \langle E\rangle\right] \quad (3.19)$$

where the effective damping rate is given by the asymmetric part of the noise,

$$\gamma_{BA}(\omega) = A^2(S_F(\omega) - S_F(-\omega)). \quad (3.20)$$

We note that the energy equation (3.19) has the expected stationary solution for a harmonic oscillator with an average of n_{BA} quanta, $\langle E \rangle = \omega_0 (n_{BA} + 1/2)$.

If the oscillator is also in contact with another thermal bath which forms the rest of its environment (excluding the coupled system), then these results can be generalised [78, 79, 80]. If the external environment can be characterised by a thermal occupation number n_{ext} and a damping rate γ_{ext}, then the total effective damping and occupation number of the oscillator are found to be,

$$\gamma_{\text{eff}} = \gamma_{BA} + \gamma_{\text{ext}}, \tag{3.21}$$

$$n_{\text{eff}} = \frac{\gamma_{BA} n_{BA} + \gamma_{\text{ext}} n_{\text{ext}}}{\gamma_{BA} + \gamma_{\text{ext}}}. \tag{3.22}$$

We see from these that, if the back-action damping is positive and the back-action temperature is smaller than the external temperature $n_{BA} < n_{\text{ext}}$, then the system can be used to *cool* the oscillator to temperatures lower than its thermal environment [15, 57, 10]. The effective damping can also become *negative* if the noise satisfies $S_F(\omega) < S_F(-\omega)$, this can lead to instabilities in which the oscillator undergoes self-sustained oscillations [15, 46] (we will not consider this behaviour in detail here).

The effective damping rate and temperature of the oscillator are linearly independent quantities, and thus, if both can be measured, the noise spectrum at $\pm\omega_0$ can be constructed. Hence, a harmonic oscillator can be used to measure the quantum noise spectrum at its natural frequency [8, 3].

3.3 NOISE IN THE SSET

We return now to think about the SSET. Recent experiments have probed the dynamics of SSET-resonator systems in which the resonator is coupled to either the island charge [10] or the current [8] of the SSET. The charge noise, with $\hat{F} = \hat{n}$, can be probed by coupling a nanomechanical beam to the gate of the SSET, the position of the beam then changes the gate capacitance, affecting the charge on the island. The coupling Hamiltonian is then as in Eqn. (3.11), with the system operator being the island charge. It is also possible to probe the noise in the current through the SSET [8]. In this type of experiment a harmonic oscillator, made from an LC circuit, is coupled directly into the current travelling through one of the leads of the SSET, this then creates a coupling Hamiltonian as in Eqn. (3.11), but now the relevant operator is, $\hat{F} = \hat{I}$, the current through the SSET.

The charge noise is the simplest of these quantities to analyse. The dynamics of $\hat{n}$ is entirely contained within the evolution of the simple reduced density operator, ρ (when the counting variable, N_L, has been traced out, see Sec. 2.3), and so it is a *system operator*, with respect to this simple master equation. This fact allows us to use the

quantum regression theorem (detailed in the following section) to calculate the noise. The current noise is a more complex quantity, since the current is not represented by a system operator, and more complex techniques need to be developed, we will describe these fully in chapter 4.

3.4 CALCULATING THE CHARGE NOISE - THE QUANTUM REGRESSION THEOREM

We have seen in the previous chapter how the dynamics of open quantum systems can be described by a master equation within the Born-Markov approximations. In general, this allows us to write the evolution of the density operator as,

$$\frac{d|\sigma\rangle\rangle}{dt} = \mathcal{L}|\sigma\rangle\rangle, \tag{3.23}$$

where $\mathcal{L}$ is a superoperator which fully describes both the coherent and incoherent dynamics of the system. In this section we will show it is possible to calculate the charge noise spectra of the SSET from an equation of this form. To do this, we need to develop a technique for calculating the two-time correlation functions. A convenient basis for the Hilbert space of the SSET, as seen in the previous chapter, is $\{|n, N_L\rangle\}$, where N_L counts the number of charges in the left-hand reservoir, and n is the excess island charge.

Since the charge noise does not depend on the counting variable, N_L, we can simply trace it out to obtain a finite equation of motion as in the previous chapter. We define,

$$\rho = \mathrm{Tr}_{N_L}[\sigma], \tag{3.24}$$

which then has the equation of motion in Liouville space,

$$\frac{d|\rho\rangle\rangle}{dt} = \mathcal{M}|\rho\rangle\rangle. \tag{3.25}$$

We now go on to show how this equation of motion can be used to calculate the charge noise spectrum,

$$S_n(\omega) = \int_{-\infty}^{\infty} \mathrm{e}^{i\omega t}\langle \delta\hat{n}(t)\delta\hat{n}(0)\rangle \, dt. \tag{3.26}$$

To be able to calculate the spectrum, it is simplest to start by calculating $\langle \hat{n}(t)\hat{n}(0)\rangle$, and simply subtract the average part, $\langle \hat{n}(0)\rangle^2$, at the end. To do this we use the *quantum regression theorem* [81, 82], this states that, for a Markovian master equation, a two-time correlation function has the same evolution equation as the mean value and so can be written, for the system operator $\hat{F}$ [83, 71] as,

$$\langle \hat{F}(t)\hat{F}(0)\rangle = \mathrm{Tr}[\hat{F}\mathrm{e}^{\mathcal{M}t}\hat{F}\rho_{\mathrm{st}}], \tag{3.27}$$

where $t > 0$. From this, we can write the correlation function of the island charge in Liouville space,

$$\langle \hat{n}(t)\hat{n}(0)\rangle = \langle\langle 0|\check{n}e^{\mathcal{M}t}\check{n}|0\rangle\rangle. \tag{3.28}$$

where we use $\check{n}$ to differentiate the Liouville space superoperator from the Hilbert space operator, $\hat{n}$. We have also introduced the row vector, $\langle\langle 0|$, which is the left eigenvector of $\mathcal{M}$ with eigenvalue 0. This corresponds to the trace operation in Hilbert space, i.e. $\langle\langle 0|$ is a vector which has 1 in elements which corresponding to diagonal elements of the density matrix, and zero for coherences, this then ensures that $\langle\langle 0|\rho\rangle\rangle = 1$ for all valid density matrices, $|\rho\rangle\rangle$.

The time evolution operator is only defined for $t > 0$, and so, to find the negative time part required in the definition of the noise spectrum, we use the relation, $\langle \hat{n}(0)\hat{n}(t)\rangle = \langle \hat{n}(t)\hat{n}(0)\rangle^*$ (discussed in Sec. 3.1). We can calculate the exponential in the evolution by introducing the set of left and right eigenvectors which diagonalise $\mathcal{M}$, defined by,

$$\mathcal{M}|\lambda_i\rangle\rangle = \lambda_i|\lambda_i\rangle\rangle, \qquad \langle\langle\lambda_i|\mathcal{M} = \langle\langle\lambda_i|\lambda_i, \tag{3.29}$$

this then lets us write the exponential,

$$e^{\mathcal{M}t} = \sum_i e^{\lambda_i t}|\lambda_i\rangle\rangle\langle\langle\lambda_i|, \tag{3.30}$$

where we have assumed the set of eigenvectors, $\{|\lambda_i\rangle\rangle\}$, form an orthonormal basis and we have neglected the possibility of degeneracy. These results together allow us to Fourier transform Eqn. 3.28 and find an expression for the charge noise,

$$S_n(\omega) = -2\sum_{i\neq 0} \mathrm{Re}\left(\frac{\langle\langle 0|\check{n}|\lambda_i\rangle\rangle\langle\langle\lambda_i|\check{n}|0\rangle\rangle}{i\omega + \lambda_i}\right). \tag{3.31}$$

We do not include the $i = 0$ term in the sum which corresponds to the eigenvector $|0\rangle\rangle$. It is given by,

$$\mathrm{Re}\left(\frac{\langle\langle 0|\check{n}|0\rangle\rangle\langle\langle 0|\check{n}|0\rangle\rangle}{i\omega}\right), \tag{3.32}$$

and so this is the $\delta(\omega)$ contribution of $\langle\hat{n}\rangle^2$ which is subtracted from the definition of the noise in Eqn. (3.3).

In the remainder of this chapter, we present a series of calculations of this charge noise spectrum for the various resonances in the SSET introduced in chapter 2. We begin by looking at the JQP and DJQP, the charge noise at these resonances has been previously calculated using slightly different methods [4, 14, 57, 15] and so we give a review of the results and do not discuss in detail the effects of the noise on an oscillator. However, the results for the Cooper-pair resonances are

new and so we give much more detail. We also give a full analysis of the behaviour of an oscillator in the linear response regime; we give explicit calculations of the damping and effective temperature of the oscillator for two very different frequency regimes, those typical of a nanomechanical resonator and also an LC oscillator. We choose to focus on the CPRs, since the transport at these resonances is fully coherent: it is entirely due to Cooper-pair oscillations, no quasiparticles are involved. This suggests that the CPRs might be a good candidate for a very low noise process which could cool an oscillator to temperatures lower than those found by coupling to the JQP or DJQP [15].

3.5 JOSEPHSON QUASIPARTICLE RESONANCE

We begin by calculating the charge noise spectrum for the SSET close to the JQP resonance, the Born-Markov model for this system was outlined in Sec. 2.3. To calculate the charge noise, we need the terms which make up Eqn. (3.31); the full eigenspectrum of the evolution matrix, along with the superoperator for the charge. To find the $\check{n}$ superoperator we need to find a representation of the Hilbert space operator, $\hat{n}$, in Liouville space. We know that $\hat{n}$ acts as,

$$\hat{n}\rho = \begin{pmatrix} 0 & 0 & 0 \\ 0 & 1 & 0 \\ 0 & 0 & 2 \end{pmatrix} \begin{pmatrix} \rho_{00} & 0 & \rho_{20} \\ 0 & \rho_{11} & 0 \\ \rho_{02} & 0 & \rho_{22} \end{pmatrix} = \begin{pmatrix} 0 & 0 & 2\rho_{20} \\ 0 & \rho_{11} & 0 \\ 0 & 0 & 2\rho_{22} \end{pmatrix}. \quad (3.33)$$

We then wish to find the superoperator which acts in the same way as this, i.e. we need to find the superoperator $\check{n}$, such that $\check{n}|\rho\rangle\rangle$ gives the same result as Eqn. (3.33) in the basis $|\rho\rangle\rangle = (\rho_{00}, \rho_{11}, \rho_{22}, \rho_{02}, \rho_{20})^T$ defined in Sec. 2.3. The $\check{n}$ superoperator is therefore given by the diagonal Liouville space matrix,

$$\check{n} = \mathrm{diag}[0, 1, 2, 0, 2]. \quad (3.34)$$

Diagonalising the 5×5 matrix, $\mathcal{M}$, for the JQP (Eqn. (2.41)) is analytically quite complicated, and so we turn to exact numerical diagonalisation, except for a few limits where the analytic result is simple enough to be informative.

3.5.1 *Zero frequency spectrum*

We begin by examining the noise at $\omega = 0$. This represents the average of the fluctuations over time since it is given by

$$S_n(0) = \int_{-\infty}^{\infty} \langle \delta\hat{n}(t)\delta\hat{n}(0)\rangle \, dt \quad (3.35)$$

and so gives information about the overall nature of the fluctuations.

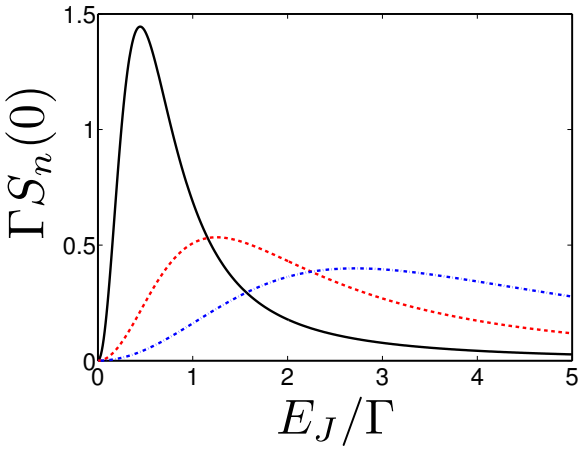

Figure 3.2.: Zero frequency charge noise $S_n(0)$ as a function of E_J/Γ for various detunings, close to the JQP resonance. The solid, black line is $\delta = 0$, the dashed, red line is $\delta = \Gamma$ and the dotted, blue line is $\delta = 2\Gamma$.

We show results for the dimensionless zero frequency charge noise, $\Gamma S_n(0)$, in Fig. 3.2, where we show the variation as a function of E_J/Γ, for various detunings δ. We see in the two extreme limits, $E_J/\Gamma \ll 1$, and $E_J/\Gamma \gg 1$, the noise vanishes. In the $E_J/\Gamma \ll 1$ limit, this is because the system is always stuck in the $n = 0$ island state, with very rapid incoherent transitions taking the system instantly through the states $n = 2$ and $n = 1$, this means that the island charge does not fluctuate. In the opposite limit, $E_J/\Gamma \gg 1$, the system has two states in which it spends a large amount of time: the rapid Cooper-pair oscillations mean the system is in a state $|n\rangle \propto |0\rangle + |2\rangle$, an infrequent quasiparticle decay can then take the system to the definite island state $n = 1$. Both of these states have the same expectation value of island charge $\langle \hat{n} \rangle$, and so fluctuations between them do not cause noise in n, hence the zero frequency noise again vanishes. Between these limits, where $E_J \approx \Gamma$, the noise shows a maximum at the point where the island charge fluctuates rapidly. Detuning the Cooper-pair resonance by choosing $\delta \neq 0$ smears out the charge noise profile, the maximum noise is reduced. These results agree with those calculated elsewhere [4, 15].

3.5.2 *Finite frequency noise*

We can also evaluate the noise at frequencies away from zero. We show results in both the coherent ($E_J \gg \Gamma$) and incoherent ($\Gamma \ll E_J$) transport limits in Figs. 3.3 (a) and (b) respectively. We begin by discussing the coherent limit. In this case, the picture to have in mind of the dynamics is that a large number of Josephson oscillations occur between infrequent quasiparticle events. After the first quasiparti-

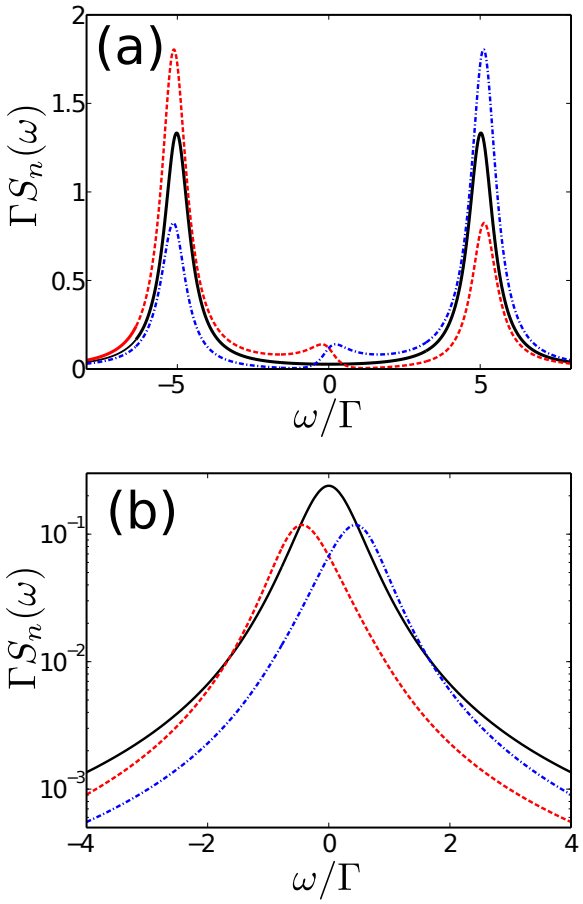

Figure 3.3.: Charge noise spectrum near the JQP. In (a) we show the coherent limit where $E_J = 5\Gamma$, the parameters are $\delta = 0$ (solid, black line), $\delta = \Gamma$ (dashed, red line) and $\delta = -\Gamma$ (dotted, blue line). In (b) we show the incoherent spectrum, $E_J = 0.1\Gamma$, the parameters are $\delta = 0$ (solid, black line), $\delta = 0.5\Gamma$ (dashed, red line) and $\delta = -0.5\Gamma$ (dotted, blue line).

cle tunnels off the island we have to wait a long time, stuck in the island state $n = 1$, until another quasiparticle tunnels off and the Cooper-pair oscillations can start again. The large amount of coherent oscillations lead to correlations in the charge state of the island at the oscillation frequency which give the large spectral peaks seen in Fig. 3.3 (a). In the small detuning limit, $\delta \ll \Gamma$, the heights of the peaks are given by,

$$\Gamma S_n(\pm E_J) = \frac{4}{3}\left(1 \mp \frac{2\delta}{E_J}\right), \tag{3.36}$$

we see that detuning from resonance introduces asymmetry to the heights of the peaks as shown in the figure. When the detuning is positive, $\delta > 0$, resonant oscillation requires the emission of energy to the environment, and so the negative frequency peak is enhanced. The converse is true for $\delta < 0$, enhancing the positive frequency peak.

The asymmetry in $S_n(\omega)$ leads to a non-zero value for the damping of an oscillator weakly coupled to the island charge, as we can see from the results of Sec. 3.2 and, in particular, Eqn. (3.20) [15]. When the positive frequency peak is larger, the damping is positive and the SSET cools the oscillator [10]. When the negative peak is larger the damping is negative and the SSET pumps energy into the oscillator [46, 47]. The physics behind this process is very similar to that used in sideband cooling of trapped ions in which the absorption spectra of the ions shows very similar asymmetries [84].

In the incoherent limit, there is a different picture of the dynamics, in this case a very slow Josephson oscillation is immediately interrupted by two fast quasiparticle decays, which take the system back to the initial island charge state $n = 0$. This means that we now do not see side-peaks in the spectrum since there are no correlations at the frequency of the Cooper-pair oscillations. We only see incoherent correlations which occur around $\omega = 0$. Detuning the system still introduces an asymmetry, as this moves the maximum in the noise to $\omega \approx -\delta$.

The evolution between these two regimes can be seen in Fig. 3.4, where we show the frequency dependent noise as a function of E_J/Γ for both the on resonance system, (a), and when the system is detuned from resonance, (b). We see that the single incoherent peak at small E_J/Γ splits into two resonant peaks as the Cooper-pair oscillation frequency is increased above Γ. When the detuning is non-zero, the symmetry of the spectrum disappears, and the negative frequency peak dominates the spectrum, as explained above. In the incoherent limit, the negative frequency peak is the only one present, the positive frequency peak only starts to appear at larger values of E_J/Γ, when the coherent oscillations have a significant effect.

3.6 DOUBLE JOSEPHSON QUASIPARTICLE RESONANCE

We now go on to present results for the charge noise near the DJQP resonance, using the model described in detail in Sec. 2.4. The charge noise is calculated in exactly the same way as for the JQP, but now the time evolution is given by the 8×8 matrix from Eqn. (2.54), and the superoperator for the island charge is given by,

$$\check{n} = \mathrm{diag}[0, 2, 0, 2, -1, 1, -1, 1], \tag{3.37}$$

where the basis for the density matrix in Liouville space is $|\rho\rangle\rangle = (\rho_{00}, \rho_{22}, \rho_{02}, \rho_{20}, \rho_{-1-1}, \rho_{11}, \rho_{-11}, \rho_{1-1})^T$, as in Sec. 2.4. Using these results, and the general expression, Eqn. (3.31), we are able to find the charge noise spectrum. Again, analytic diagonalisation is complex, except for a few specific limits where the results are simple enough to be useful. So we mostly use numerical techniques to find the eigenvectors of $\mathcal{M}$.

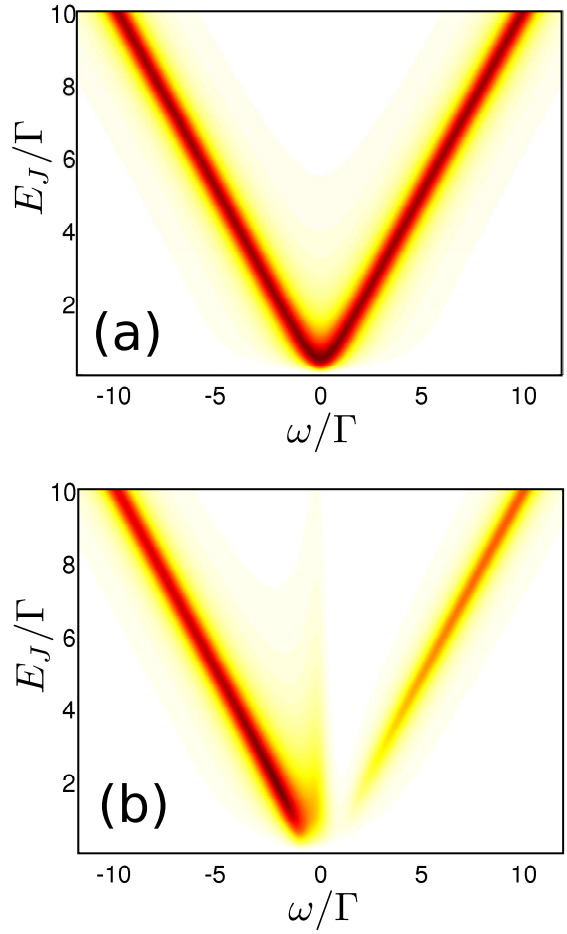

Figure 3.4.: Frequency dependent charge noise spectrum near the JQP as a function of E_J/Γ for (a) $\delta = 0$ and (b) $\delta = \Gamma$.

3.6.1 *Zero frequency*

We again start by examining the fluctuations at $\omega = 0$. The results for this quantity are shown in Fig. 3.5 for various values of detuning. We can find an analytic expression for the noise in this limit, and for zero detuning, we find,

$$\Gamma S_n(0) = \frac{1}{2}\left(1 + \frac{\Gamma^4 + 4\Gamma^2 E_J^2}{2\Gamma^2 E_J^2 + 4E_J^4}\right). \tag{3.38}$$

In the limit $E_J \ll \Gamma$, which is considered in Ref. [14], we obtain consistent results. At $\delta_L = \delta_R = 0$, the noise is a decreasing function of E_J/Γ, which diverges at $E_J \to 0$, and has the limit $\Gamma S_n(0) \to 1/2$ for large E_J/Γ.

The behaviour is different to that found for the JQP in Fig. 3.2, the noise does not vanish in the extreme limits of $E_J/\Gamma \to 0, \infty$. In the limit $E_J/\Gamma \ll 1$, the dynamics are well modelled by the incoherent model presented in Sec. 2.4.2. There is a slow Cooper-pair transition

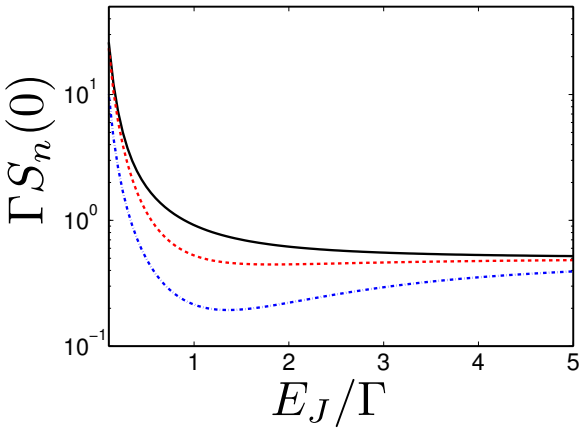

Figure 3.5.: Zero frequency charge noise $S_n(0)$ as a function of E_J/Γ for various detunings close to the DJQP resonance. The solid, black line is $\delta_L = 0$, the dashed, red line is $\delta_L = \Gamma$ and the dotted, blue line is $\delta_L = 2\Gamma$. All results are at $\delta_R = 0$.

from state $n = 0$ to $n = 2$, at a rate $\gamma = E_J^2/\Gamma$, followed by an instant quasiparticle decay to state $n = 1$. There is then another slow Cooper-pair transition to the state $n = -1$, and another instant quasiparticle decay back to $n = 0$. This means that the system fluctuates between the island states $n = 0$ and $n = 1$, at a switching rate given by γ, which goes to zero in this limit, giving rise to a divergence in the noise. In the coherent limit $E_J/\Gamma \gg 1$, the Cooper-pair oscillations build up coherence, as for the JQP, and so the system spends its time in either the state $|n\rangle \propto |0\rangle + |2\rangle$ or $|n\rangle \propto |-1\rangle + |1\rangle$ which have different values of $\langle n\rangle$, and so again fluctuations between these states cause the noise to be finite. Detuning from resonance decreases the noise for all values of E_J/Γ, the suppression is maximised when the timescales for the incoherent and coherent processes match (around the dip in Fig. 3.5).

3.6.2 *Finite frequency*

We now go on to consider the finite frequency noise. We first look at the spectrum in the coherent transport limit, where $E_J \gg \Gamma$, shown in Fig. 3.6 (a). The structure consists of three peaks, one centred at $\omega = 0$ and the others at $\omega = \pm E_J$. The height of the central peak is approximately $1/2$, with only a weak dependence on detuning, the heights of the side-peaks are given by,

$$\Gamma S_n(\pm E_J) = 4\left(1 \mp \frac{\delta_L + \delta_R}{E_J}\right), \tag{3.39}$$

where we have assumed small detuning $\delta_L, \delta_R \ll \Gamma$. The side-peaks arise in a very similar way to those at the JQP, the island charge is highly correlated on the timescale of the Cooper-pair oscillation. De-

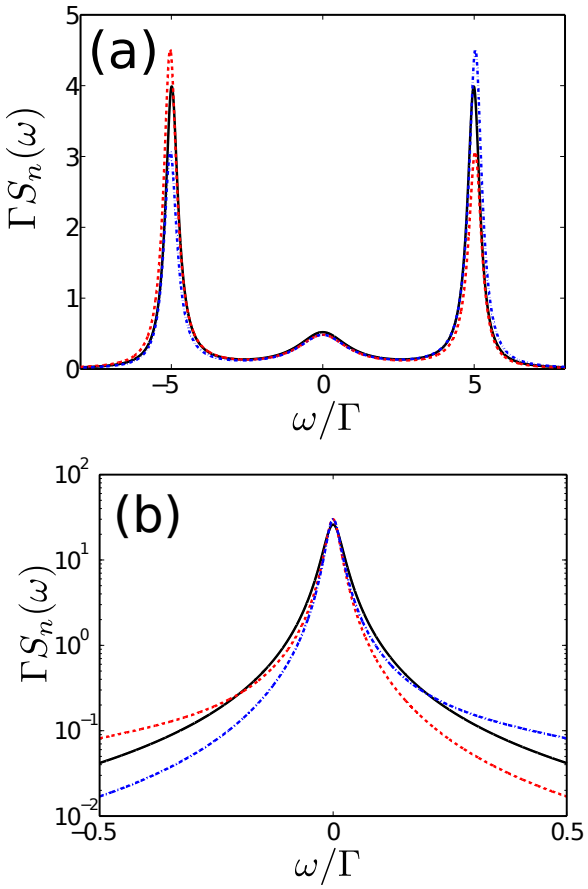

Figure 3.6.: Charge noise spectrum near the DJQP. In (a) we show the coherent limit where $E_J = 5\Gamma$, the parameters are $\delta_L + \delta_R = 0$ (solid, black line), $\delta_L + \delta_R = \Gamma$ (dashed, red line) and $\delta_L + \delta_R = -\Gamma$ (dotted, blue line). In (b) we show the incoherent spectrum, $E_J = 0.1\Gamma$, the parameters are $\delta_L + \delta_R = 0$ (solid, black line), $\delta_L + \delta_R = 0.5\Gamma$ (dashed, red line) and $\delta_L + \delta_R = -0.5\Gamma$ (dotted, blue line).

tuning the system from resonance again changes the relative heights of the sidepeaks, if $\delta_L + \delta_R > 0$ the negative frequency peak is enhanced, whereas the converse happens if $\delta_L + \delta_R < 0$. As with the JQP resonance, we can think of this in terms of the SSET's preference to absorb or emit energy to undergo resonant oscillations. If the resonances are detuned such that the Cooper-pairs need to absorb energy to move between the island and the lead, then the negative frequency part of the spectrum is increased; the opposite occurs if the detuning is such that the Cooper-pairs need to emit energy. The only difference between this and the results for the JQP is that it is now the sign of $\delta_L + \delta_R$, which determines the relative heights, since it is the average preference for absorbing/emitting energy of both junctions which matters.

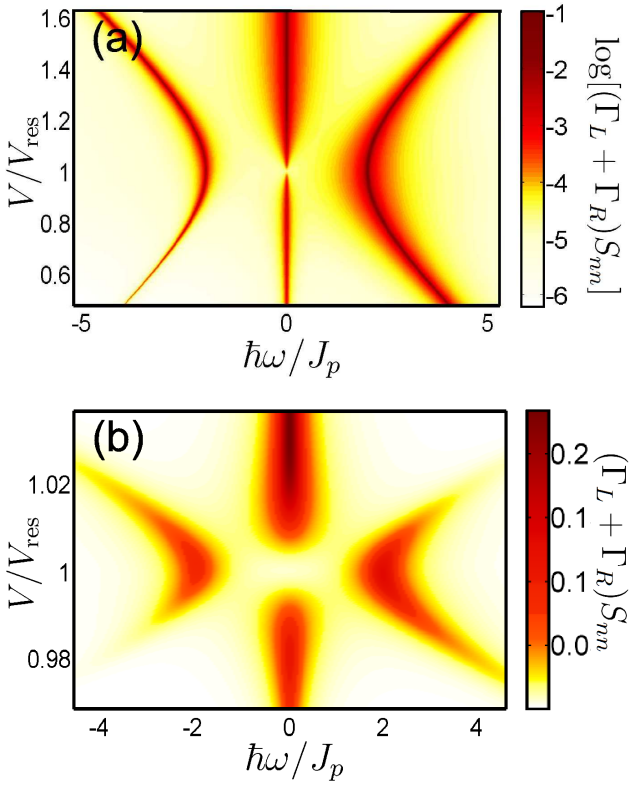

Figure 3.7.: Charge noise spectrum as a function of frequency and voltage around the (a) $p = 0$ and (b) $p = 1$ Cooper-pair resonances. The resonances occur at the point where the central peak disappears.

In the incoherent limit the spectrum is very different, the sidepeaks are suppressed because of the lack of coherence, and we are just left with a large central peak (the zero frequency noise is much larger at low values of E_J/Γ). Detuning from resonance still introduces asymmetry to the spectrum, but this much less pronounced than in the coherent case, due to the lack of sidepeaks.

3.7 COOPER-PAIR RESONANCES

We now turn to consider the charge noise properties of the SSET close to the Cooper-pair resonances. Near the Cooper-pair resonances the island charge operator is more complicated than for the JQP and DJQP. The full representation of the operator $\hat{n}'$ can be written as a series expansion in terms of powers of the Josephson coupling J (as we did for $\hat{k}'$), $\hat{n}' = \hat{n}^{(0)} + \hat{n}^{(1)} + \ldots$, as described in appendix B. In the small J/eV limit for which our model is valid (see Sec. 2.5) the dominant contribution to the spectrum comes from the zeroth order terms in the expansion, $\hat{n}^{(0)} = \hat{n}$, and so we consider these terms first. The higher order terms in $\hat{n}'$ give rise to weaker features in the spectrum, which we go on to calculate in Sec. 3.7.2.

For the Cooper-pair resonances it is possible to find an exact expression for the charge noise since the eigenbasis evolution matrix (the $q = 0$ case of Eqn. (2.85)) is straightforward to exactly diagonalise and we are able to find the full set of left and right eigenvectors normailsed such that $\langle\langle\lambda|\lambda\rangle\rangle = 1$,

$$|0\rangle\rangle = \frac{1}{\Gamma_{\text{pop}}}\begin{pmatrix}\Gamma_b\\ \Gamma_a\\ 0\\ 0\end{pmatrix}, \qquad \langle\langle 0| = (1,1,0,0), \tag{3.40}$$

$$|-(\Gamma_{\text{pop}}\rangle\rangle = \frac{1}{2}\begin{pmatrix}1\\ -1\\ 0\\ 0\end{pmatrix}, \quad \langle\langle -\Gamma_{\text{pop}}| = \frac{2}{\Gamma_{\text{pop}}}(\Gamma_a, -\Gamma_b, 0, 0), \tag{3.41}$$

$$|-i\omega_{ab} - \Gamma_{\text{coh}}\rangle\rangle = \begin{pmatrix}0\\ 0\\ 1\\ 0\end{pmatrix}, \quad \langle\langle -i\omega_{ab} - \Gamma_{\text{coh}}| = (0,0,1,0), \tag{3.42}$$

$$|i\omega_{ab} - \Gamma_{\text{coh}}\rangle\rangle = \begin{pmatrix}0\\ 0\\ 0\\ 1\end{pmatrix}, \qquad \langle\langle i\omega_{ab} - \Gamma_{\text{coh}}| = (0,0,0,1), \tag{3.43}$$

where $\Gamma_{\text{pop}} = \Gamma_a + \Gamma_b$.

We also need the superoperator representation of the charge operator. This can be found by noting that the charge operator in Hilbert space is given by,

$$\hat{n}\rho = \begin{pmatrix}n_{aa} & n_{ab}\\ n_{ba} & n_{bb}\end{pmatrix}\begin{pmatrix}\rho_{aa} & \rho_{ab}\\ \rho_{ba} & \rho_{bb}\end{pmatrix}, \tag{3.44}$$

where we note that in the eigenstate basis the charge operator is not diagonal as it was for the JQP and DJQP. We can then construct the Liouville space representation

$$\check{n} = \begin{pmatrix}n_{aa} & 0 & 0 & n_{ab}\\ 0 & n_{bb} & n_{ba} & 0\\ 0 & n_{ab} & n_{aa} & 0\\ n_{ba} & 0 & 0 & n_{bb}\end{pmatrix}, \tag{3.45}$$

where we use the basis $|\rho\rangle\rangle = (\rho_{aa}, \rho_{bb}, \rho_{ab}, \rho_{ba})^T$, as in Sec. 2.5. This superoperator is then used to construct the charge noise spectrum using Eqn. (3.31),

$$S_n(\omega) = 2\rho_{aa}\rho_{bb}(n_{aa} - n_{bb})^2 \frac{\Gamma_{\text{pop}}}{\omega^2 + \Gamma_{\text{pop}}^2} + 2n_{ab}^2 \left(\frac{\rho_{bb}\Gamma_{\text{coh}}}{(\omega - \omega_{ab})^2 + \Gamma_{\text{coh}}^2} + \frac{\rho_{aa}\Gamma_{\text{coh}}}{(\omega - \omega_{ba})^2 + \Gamma_{\text{coh}}^2} \right). \quad (3.46)$$

Examples of the spectrum as a function of frequency and voltage around the $p = 0$ and $p = 1$ resonances are shown in Fig. 3.7. In both cases the spectrum consists of three Lorentzians and has a similar general form to that seen at the JQP and DJQP resonances. This triplet structure is exactly what is expected for a coherent TLS in the presence of dissipation [69, 80] and is very similar to the Mollow triplet observed in the resonance fluorescence cascade [69]. The central peak around zero frequency arises due to incoherent fluctuations between eigenstates, its height is determined by $|n_{aa} - n_{bb}|$, the difference in average charge between the $|a\rangle$ and $|b\rangle$ eigenstates. This peak disappears when the system is tuned to resonance since the eigenstates are equal mixtures of charge states.

The sidepeaks arise at $\omega = \pm\omega_{ab}$ due to coherent oscillations between the eigenstates. The heights of the sidepeaks are controlled by the steady state populations of the eigenstates, which is what provides the asymmetry between the negative and positive frequency peaks, and the width is given by the rate at which the coherences decay, Γ_{coh} (see Eqn. (2.88)). Note that the spacing of the sidepeaks is much larger for $p = 0$, the splitting is typically of order $J_{p=0} \sim 25\,\text{GHz}$, compared to $J_{p=1} \sim 1\,\text{GHz}$ for the $p = 1$ resonance. This means that finite temperature effects are not as important in the $p = 0$ resonance. When the systems is tuned directly to resonance the spectrum is not perfectly symmetric, as it was for the other resonances, this effect is purely because of the presence of the incoherent intradoublet transitions which mean that the populations of the eigenstates are not equal on resonance.

3.7.1 *Coupling to an oscillator*

We now calculate the effective temperature and damping experienced by an oscillator coupled to the SSET tuned near to the CPRs. We will explore the back-action effect of the SSET on resonators in two different regimes of frequency, $\Omega = 100\,\text{MHz}$ and $\Omega = 4\,\text{GHz}$, corresponding to different physical realisations of the resonator. The 100 MHz frequency is typical of a nanomechanical resonator [25], whilst the 4 GHz frequency matches that of superconducting striplines [85] or LC resonators [8]. We focus on the $p = 1$ resonance from now on

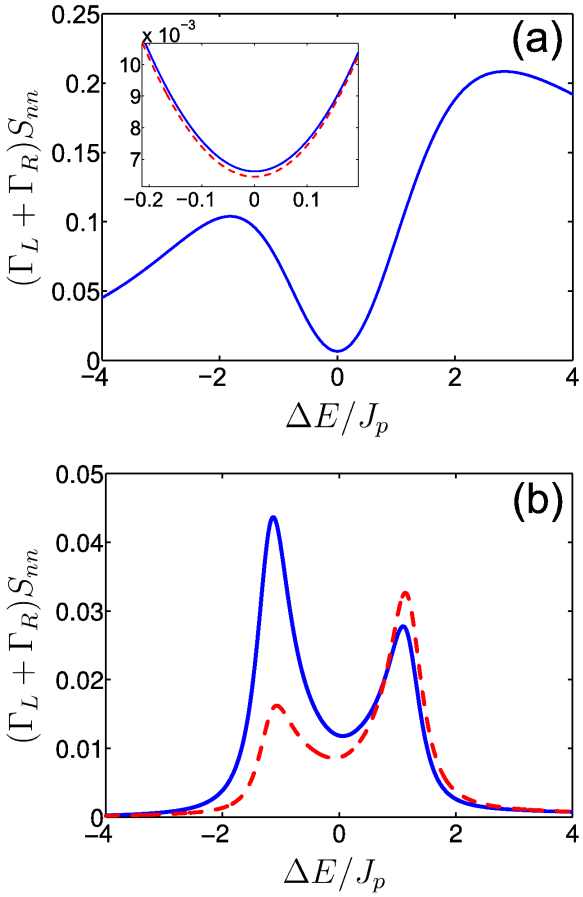

Figure 3.8.: Charge noise, S_n, as a function of ΔE for (a) $\Omega = 100\,\text{MHz}$ and (b) $\Omega = 4\,\text{GHz}$ oscillator. Solid (blue) lines are $S_n(\Omega)$, dashed (red) lines are $S_n(-\Omega)$. The inset in (a) shows the region around the minimum where the difference between the two curves is most pronounced.

since the sidepeaks of the $p = 0$ resonance are too wide to have any significant effect, even for a high frequency LC oscillator.

Figure 3.8 shows the charge noise as a function of the detuning from resonance for $\Omega = \pm 100\,\text{MHz}$ and $\Omega = \pm 4\,\text{GHz}$. At 100 MHz the spectrum is very symmetric, $S_{nn}(\Omega) \approx S_n(-\Omega)$ because the sidepeaks have very little weight at this frequency. In this case maximum asymmetry is achieved at the centre of the resonance ($\Delta E = 0$), when the spacing of the outer peaks is minimized. In contrast, at 4 GHz, the spectrum is highly asymmetric as here the sidepeaks cross through this frequency.

The curves for $S_n(\pm\Omega)$ are not simply reflections of each other, as would be expected for a classically driven TLS [80], or other resonances in the SSET such as the JQP and DJQP [15, 57]. This asymmetry occurs for the same reason that the current peak is not a simple Lorentzian; the intra-doublet decay rates are not symmetric between $\pm\Delta E$. Similar effects are seen in a driven TLS [86], when the

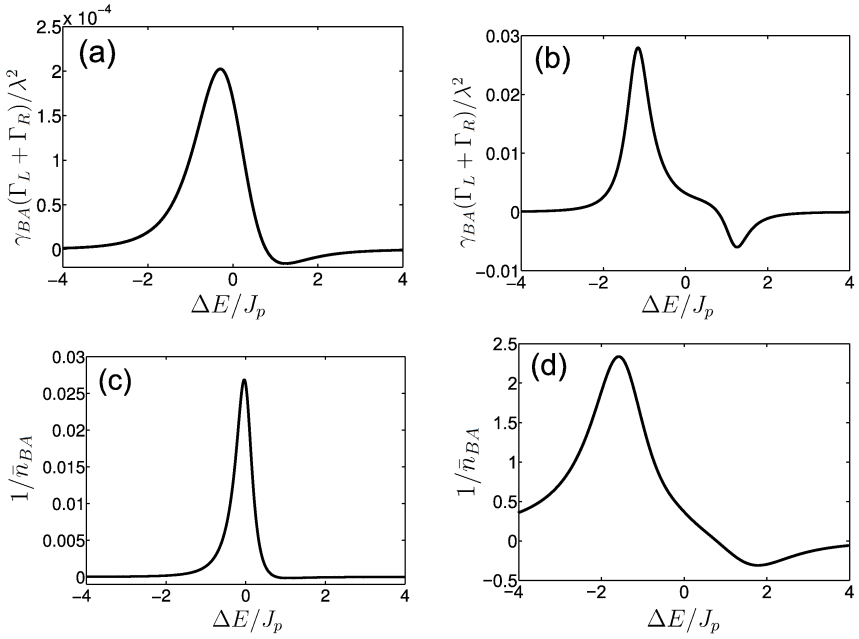

Figure 3.9.: Back-action damping, γ_{BA}, [(a)-(b)] and effective occupation number, n_{BA}, [(c)-(d)] of an oscillator weakly coupled to the SSET. (a) and (c) are for $\Omega = 100\,\text{MHz}$, (b) and (d) for $\Omega = 4\,\text{GHz}$.

temperature dependence of the relaxation rate is taken into account. The behaviour of the driven TLS, where $S_n(\Omega, \Delta E) = S_n(-\Omega, -\Delta E)$, is recovered in the high temperature limit where the intra-doublet transition is saturated, $\gamma_{ab} = \gamma_{ba}$. We can understand how the intra-doublet decays lead to this asymmetric behaviour in terms of effective temperatures. The intra-doublet decays drive the eigenstate populations towards an equilibrium distribution which corresponds to the temperature of the bath, this is constant and always positive. However, the inter-doublet rates drive the SSET to an equilibrium point whose effective temperature varies strongly with ΔE and, in particular, changes sign when $\Delta E = 0$. The competition between these two behaviours causes the asymmetry in this system [15, 57].

In Fig. 3.9 we plot the back-action damping, γ_{BA}, calculated using Eqn. (3.20) from the charge noise for $\Omega = 100\,\text{MHz}$ and $\Omega = 4\,\text{GHz}$. The size of the damping depends on the asymmetry of the noise spectrum. The small asymmetry in the low frequency noise spectrum gives the damping a very small magnitude, but for the high frequency resonator it is much larger. The lack of symmetry in the noise spectrum, $S_n(\Omega, \Delta E) \neq S_n(-\Omega, -\Delta E)$, leads to quite different magnitudes for the damping at $\pm\Delta E$, with the anti-damping peak suppressed by the intra-doublet decays for both the high and low frequency cases.

When a resonator is coupled to the SSET its steady state is determined by a combination of the back-action of the SSET and the influ-

ence of the rest of the resonator's surroundings which are in thermal equilibrium at a temperature T_{ext}, and give rise to a damping rate γ_{ext}. The overall occupation number of the resonator, n_{eff}, is given by Eqn. (3.22). At a given external temperature, the SSET can be used to cool the resonator provided provided $n_{BA} < n_{\text{ext}}$, where n_{ext} is the occupation number which corresponds to T_{ext}. Such cooling is important when attempting to reach the vibrational ground state of nanomechanical resonators with frequencies in the MHz range, as even at temperatures below 100 mK they will still contain a large number of thermal quanta [10, 78, 79, 80].

Figures 3.9(c) and 3.9(d) show the behaviour of n_{BA} (plotted as $1/n_{BA}$ to emphasize the behaviour near minimas) around the resonance at 100 MHz and 4 GHz. For $\Omega = 100\,\text{MHz}$, the minimum in n_{BA} occurs when the system is tuned directly to resonance, where the central peak in the noise spectrum vanishes. For the typical device parameters we have chosen (given in Sec. 2.5.3), we find a minimum of $n_{BA} \approx 37$, which corresponds through the expression $n_{BA} = (\exp(\hbar\Omega/k_B T_{BA}) - 1)^{-1}$ to an effective temperature $T_{BA} \approx 29\,\text{mK}$, only slightly lower than the bath temperature, $T = 30\,\text{mK}$. This result is, however, dependent on T through the intra-doublet rates and the relative cooling potential does improve at higher bath temperatures, for example $T_{BA} \approx 37\,\text{mK}$ for $T = 50\,\text{mK}$ and $T_{BA} \approx 50\,\text{mK}$ for $T = 80\,\text{mK}$.

The cooling potential of the CPRs is less than was found for the JQP or DJQP resonances [15], where it was found that, in principle, these resonances are capable of cooling a MHz oscillator from around 500mK to as low as 50mK. The main problem with using the SSET tuned to a Cooper-pair resonance to cool a mechanical resonator is the spacing of the peaks in the noise spectrum. For effective cooling, we need the frequency of the resonator to match the separation of the peaks. This cannot be achieved at low frequencies in this device since the minimum intra-doublet spacing (and hence minimum peak splitting) $2J_p/\hbar$ is in the GHz range. Trying to engineer a device where this splitting was much smaller would lead to a deterioration in the effectiveness of the cooling because of the effect of thermal noise on the SSET itself: the asymmetry in the peaks would be reduced and they would also be broadened (this would take the system outside both the regime where the RWA is valid and also the resolved sideband limit where optimal cooling can be achieved [78, 79]). In contrast, for a driven TLS [80], the potential for cooling is much greater as it is possible to tune the drive (which corresponds to the Josephson coupling in our system) and it is the *difference* between this frequency and the level separation of the TLS (both of which can be much greater than $k_{\text{B}}T/\hbar$) that sets the spacing of the sidepeaks in the corresponding noise spectrum.

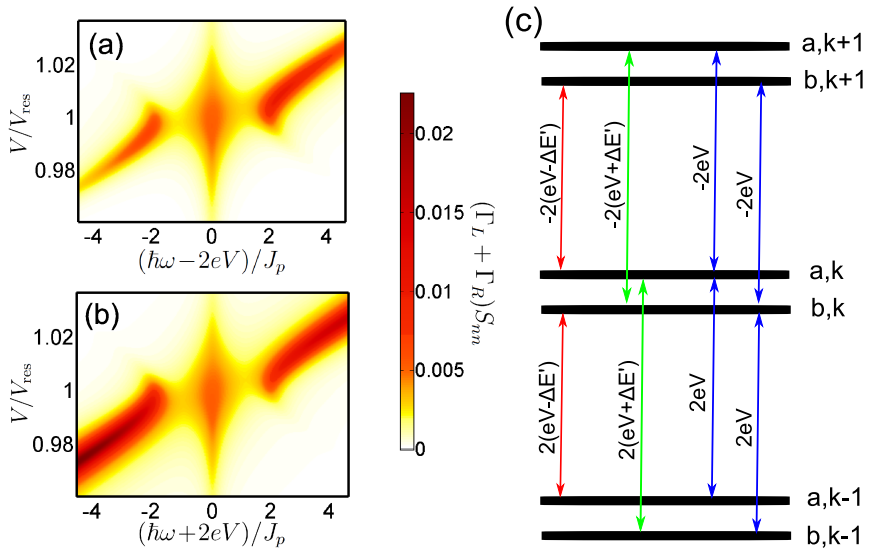

Figure 3.10.: $S_{n^{(1)}}(\omega)$ in the vicinity of the $p = 1$ resonance (a) and (b) show the spectrum at frequencies around $\hbar\omega = \pm 2eV$ respectively. A schematic illustration of the processes giving rise to the spectral features is shown in (c). This illustrates the inter-doublet transitions and the corresponding frequencies of the features they give rise to.

3.7.2 *Higher order spectral features*

The full charge noise spectrum close to the CPRs also contains contributions at other frequencies far from $\omega = 0$. These arise from the higher order contributions in the perturbative expansion of $\hat{n}'$. In this section we investigate the most significant of these high order terms, which arises from the $\langle \hat{n}^{(1)}(t)\hat{n}^{(1)}(0)\rangle$ term in the expansion. The form of $n^{(1)}$ is calculated in appendix B,

$$\hat{n}^{(1)} = -\sum_k \frac{J}{2peV} |0,k\rangle \langle 1,k+1/2| + \frac{J}{2(p+1)eV} |0,k\rangle \langle 1,k-1/2| + h.c., \quad (3.47)$$

for $p \geq 1$, in the case $p = 0$ the first term is not present. When this is transformed to the eigenstate basis it contains terms proportional to $|i,k\rangle \langle j,k+q|$, with $q = \pm p, \pm(p+1)$, for $p = 0$ only terms $q = \pm 1$ are present. As an example we calculate the corresponding spectrum,

$$S_{n^{(1)}}(\omega) = \int_{-\infty}^{\infty} \langle \hat{n}^{(1)}(t)\hat{n}^{(1)}(0)\rangle e^{i\omega t} dt, \quad (3.48)$$

for the $p = 1$ resonance (note that in the steady state $\langle \hat{n}^{(1)}\rangle = 0$ and so we do not need to work with the operator $\delta\hat{n}^{(1)}$). To do this we use a slightly different technique. The states linked by $\hat{n}^{(1)}$ are not present in our definition of ρ and so we need to use a different set of

reduced master equations. For the $p = 1$ resonance these correspond to Eqn. (2.84) with the values of $q = \pm 1, \pm 2$, which include the correct coherences. We can then construct the relevant two-time correlation using the regression theorem.

We find that the spectrum consists of triplets of peaks centred on the frequencies $\hbar\omega = 2qeV$, with the sidepeaks separated by the intra-doublet level spacing in each case. The triplets with $q = \pm 1$ and $q = \pm 2$ simply differ by a constant prefactor and a slight modification to the decay rates, and so we concentrate here on just the $q = \pm 1$ case. The spectrum around $\hbar\omega = \pm 2eV$ is shown in Figs. 3.10(a) and 3.10(b). The peaks in this part of the spectrum arise from first order Josephson coupling between states at the relevant frequency differences. We show the relevant transitions and their frequencies in Fig. 3.10(c). Since this spectrum occurs at higher order in the perturbation theory the magnitude of $S_{n^{(1)}n^{(1)}}$ is much smaller than it was for the zeroth order spectrum (Fig. 3.7). The central peak in both Figs. 3.10(a) and 3.10(b) is the same, because the transitions which give rise to these peaks always link corresponding states within the two doublets (i.e. an a state with an a state or a b state with a b) for both the positive and negative frequency processes as shown in Fig. 3.10(c). However, the sidepeaks of the two triplets are quite different. The weights of the sidepeaks are proportional to $|n^q_{ij}|^2\rho_{ii}$, where $n^q_{ij} = \sum_k \langle i, k+q| \, n^{(1)} \, |j,k\rangle$, and $i(j)$ is the initial (final) state for the relevant transition. This means that each of the four sidepeaks has a different combination of matrix element and population.

Far from the resonance, only one of the three peaks is present in each triplet. In this region the eigenstates are very close to the charge states, and since the Josephson effect only couples the states $|0,k\rangle$ and $|1,k+1/2\rangle$, we find that each state is only coupled to one other. Very close to the resonance all of the peaks appear, the eigenstates are mixtures of charge states, and so transitions between all of the states in the doublets can occur.

The features seen in this part of the spectrum arise because the system is not as simple as a true TLS, they arise from couplings between different doublets and hence require more than two energy levels. The frequencies at which the features in this part of the spectrum occur, $\sim 100\,\mathrm{GHz}$, are much larger than the range that can be probed with a stripline resonator. However, it might be possible to observe the noise at this frequency in a different kind of experiment, in which the SSET is instead coupled to another mesoscopic conductor, such as a SIS junction, which is sensitive to fluctuations at such high frequencies [65, 87].

3.8 SUMMARY

In this chapter we have described an efficient technique for calculating the charge noise spectrum in systems described by a Born-Markov master equation. We have presented results for the three transport cycles in the SSET which we introduced in chapter 2. The charge noise gives much more information about the dynamics than can be obtained from mean quantities. All of the resonances show the same basic behaviour. In the coherent limit, there are three peaks, one at $\omega = 0$ which is due to incoherent fluctuations, and two at $\omega = \pm J$ where here J is the relevant oscillation frequency. The relative heights of the side-peaks are controlled by which way the system is detuned from resonance. The ability to change the symmetry of the spectrum by changing the operating point allows the SSET to both extract energy from or pump energy into a harmonic oscillator weakly coupled to the gate of the SSET. We examined this behaviour in detail for two different experimentally interesting frequencies for the case of the Cooper-pair resonances. It turned out that the frequency scale set by the Josephson coupling means that the cooling potential of the CPRs is not as good as it is for the JQP or DJQP. We also found that for the Cooper-pair resonances there are further sets of peaks in the spectrum at higher frequencies, which arise because of the terms at higher order in the expansion of $\hat{n}'$.

4

CURRENT NOISE

Much recent attention has focused on the way in which the counting statistics of transferred charge through a conductor can give insights into its dynamics [2]. Transport of electrons through even a classical tunnel junction is *stochastic* in nature, this leads to the idea that examining the distribution of these tunnel events can give a detailed understanding of the dynamics of the transport [1, 2, 5]. Previous work using Born-Markov master equations has concentrated on systems in which the transport can be described by a classical stochastic process [88, 89, 58, 90] in which the variable, N, that counts the number of charges passing through a particular point in the circuit is a definite quantity. In the few results where this is not the case, the calculated quantity has always been the *symmetrised* noise [4, 55].

In this chapter we develop a method for calculating the unsymmetrised noise in the current through the SSET, which is closely related to the second moment of the classical distribution, and show how this can be used to predict the back-action on an oscillator (as discussed in Sec. 3.2). This requires a more sophisticated technique than those already available; the current through the SSET unavoidably involves quantum coherence, the counting variable can be in a superposition involving a Cooper-pair on both the left and right sides of the junction. We show how it is possible to develop a simple expression for the current noise in systems which involve quantum coherent oscillations and apply this to the different transport mechanisms in the SSET, paying particular attention to the noise at DJQP which has been measured recently in the experiment of Ref. [8].

The outline of this chapter is as follows. Firstly, in Sec. 4.1, we explain the differences between quantum and classical current noise and discuss why unsymmetrised noise is difficult to calculate in the presence of quantum coherence. In Sec. 4.2 we outline our new technique for calculating the unsymmetrised current noise. We then use this technique to calculate the noise close to the DJQP resonance in Sec. 4.3, these results are compared to those obtained in a recent experiment, Ref. [8]. In Secs. 4.4 and 4.5 we give results for the current noise close to the JQP and CPRs respectively.

In a classical device the charge transferred, and therefore the current, is fully described by its probability distribution. For example, consider counting the particles tunnelling through one junction of the normal state SET[1]. The particles involved in the transport have either passed through the junction or not, and so one can write down a full *classical* probability distribution, $P(N,t)$, which contains all of the information about the statistics of N [2]. It is usual to write this quantity in terms of a moment generating function [2],

$$P(\chi,t) = \sum_N \mathrm{e}^{i\chi N} P(N,t), \tag{4.1}$$

where all of the information about transferred charge is now encoded in the counting field χ. This then allows easy calculation of all the moments of the distribution [2],

$$\langle N^m \rangle = \frac{\partial^m}{\partial(i\chi)^m} P(\chi,t)\bigg|_{\chi=0}. \tag{4.2}$$

The current and higher order moments can then be calculated as, for example, $\langle I \rangle = \langle \dot{N} \rangle$. This type of expression can even be used to calculate the noise when the *internal* dynamics are quantum mechanical [88, 89, 58, 90], in this case it is possible to define a probability distribution by tracing out the internal degrees of freedom,

$$P(N,t) = \mathrm{Tr}_{\mathrm{int}}[\rho(N,t)], \tag{4.3}$$

following this, the standard classical techniques can be used.

It is also possible to generalise these techniques to calculate the finite frequency noise [58, 90]. Previous studies have devoted much attention to calculating either the zero-frequency [91, 92, 93] or finite frequency *symmetrised* [94, 55, 4, 92, 95] noise. The symmetrised noise is of interest because it is this quantity which is measured by a device that is insensitive to differences between positive and negative frequency fluctuations [74, 3] such as a normal state SET [96, 97] or quantum point contact [98]. It is given by,

$$S_I^{\mathrm{sym}}(\omega) = \frac{1}{2}\int_{-\infty}^{\infty} \mathrm{e}^{i\omega t} \langle \{\delta\hat{I}(t), \delta\hat{I}(0)\} \rangle \, dt, \tag{4.4}$$

where $\{A,B\} = AB + BA$ is the anti-commutator. From the results of Sec. 3.1, we see that for systems which can be described by a classical distribution (ignoring any effects of non-Markovian transport [99, 90, 100]) the current noise spectrum must be symmetric [88, 2]. However this is not the case for systems involving Josephson junctions, such as the SSET. In these systems, the counting variable can be in a *coherent*

1 We only consider the regime where the system is described by a Markovian master equation.

superposition, Cooper-pairs can be in a quantum state in which they are both on the left and right side of the junction.

Here we focus on calculating the quantum current noise (as defined in Sec. 3.1). Recent experimental progress has made it possible to observe the *asymmetric* parts of the noise by coupling the current to a quantum spectrometer, using the ideas of linear response outlined in Sec. 3.2. This type of measurement has been performed in a variety of systems where quantum effects are important, such as in superconducting tunnel junctions [101, 75], quantum point contacts [102, 103], a carbon nanotube quantum dot in the Kondo regime [104], as well as in various transport processes in the SSET [9, 65, 8]. To this end, here we concentrate on developing a simple and efficient method for calculating the asymmetric part of the noise which occurs within the Born-Markov approximations. Previous studies have calculated the non-Markovian asymmetric noise [99, 90, 100], however these effects only become relevant at much higher frequencies than are typically observed in experiments involving SSETs[2]. The technique which we develop here is able to explicitly calculate the asymmetric noise in systems with steady state coherence, induced in the SSET by the presence of the Josephson junctions, this was not considered in the previous non-Markovian calculations.

4.2 CALCULATING THE CURRENT NOISE

In this section we present a technique for calculating the noise in fluctuations of the current for a device whose dynamics are described by a generic Born-Markov master equation as in Eqn. (3.23). In Liouville space this equation has the form,

$$\frac{d|\sigma(t)\rangle\rangle}{dt} = \mathcal{L}|\sigma(t)\rangle\rangle. \tag{4.5}$$

To calculate the charge noise the procedure from here was simple: the dynamics of the island charge are contained within the reduced density operator, ρ (see Eqn. (3.24)), and the regression theorem then gives the two-time correlation function which can be used to find the noise spectrum (see Sec. 3.4).

For the current noise we cannot simply trace out the dependence on the counting variable, N, as we did for the charge noise. When considering the current, it is the counting variable which contains all of the relevant information. This means we still have the problem that $\mathcal{L}$, which describes the evolution of the full density matrix, σ, is infinite and does not have a well defined steady state. Motivated

2 For the SSET the Markov approximation starts to break down at frequencies $\omega > E_C$ [55] which is much higher than, for example, the frequency of the oscillator used to measure the noise in Ref. [8] or even the typical frequency of the Josephson oscillations.

by the classical techniques discussed in the previous section, we introduce the Fourier transformed density operator, which is similar to Eqn. (4.1),

$$\rho_{ij,q}(\chi) = \sum_N \langle i, N| \, \mathrm{e}^{i\chi\hat{N}} \sigma \, |j, N+q\rangle = \sum_N \mathrm{e}^{i\chi N} \, \langle i, N| \, \sigma \, |j, N+q\rangle \, , \quad (4.6)$$

where the second equality comes from the fact that $|i, N\rangle$ is an eigenstate of $\hat{N}$. Here q is chosen appropriately for the coherences present in the problem. The density matrix has elements which are labelled with i and j and q is simply used as a label which allows us to keep track of the coherence in N. We have introduced χ, a counting field, which includes all of the information about $\hat{N}$. This is very similar to the way in which counting fields are introduced for *classical* problems [2], but to include quantum coherence we make sure that χ is the conjugate field to the *operator* $\hat{N}$. We note that our choice of the definition of $\rho_{ij,q}(\chi)$ is, in some sense, arbitrary: we could equally have defined, for example, $\rho_{ij,q}(\chi) = \sum_N \langle i, N| \, \sigma \mathrm{e}^{i\chi\hat{N}} \, |j, N+q\rangle$, and obtained the same final results, as long as we were consistent throughout.

We can write an evolution equation for the Liouville space representation of this Fourier transformed density operator,

$$\frac{d|\rho(\chi,t)\rangle\rangle}{dt} = \mathcal{M}(\chi)|\rho(\chi,t)\rangle\rangle. \quad (4.7)$$

The superoperator $\mathcal{M}$ can then be calculated from the full evolution using the definition of ρ,

$$\dot{\rho}_{ij,q}(\chi) = [\mathcal{M}(\chi)\rho(\chi)]_{ij,q} = \sum_N \mathrm{e}^{i\chi N} \, \langle i, N| \, \mathcal{L}\sigma \, |j, N+q\rangle \, . \quad (4.8)$$

When $\chi = 0$, the evolution superoperator, $\mathcal{M}(\chi)$, reduces to the evolution for the internal charge dynamics of the island, which we used in chapters 2 and 3.

Given $\rho(\chi, t)$, one can obtain the (time dependent) average of any operator and, in particular, of $\hat{N}$,

$$\langle \hat{N}(t) \rangle \equiv \mathrm{Tr}[\hat{N}(t)\sigma] = \langle\langle 0| \frac{\partial|\rho(\chi,t)\rangle\rangle}{\partial i\chi}\bigg|_{\chi=0}, \quad (4.9)$$

where $\langle\langle 0|$ is the vector equivalent to the trace operation in Hilbert space, as introduced in Sec. 3.4. This then gives motivation for the definition of $\rho(\chi)$ in Eqn. (4.6), we introduced the Fourier transformed density operator to allow the simple calculation of quantities like the one above.

This then gives a simple way of calculating the particle current by taking a time derivative $\langle \hat{I}(t) \rangle \equiv \pm d\langle \hat{N}(t) \rangle / dt$,

$$\langle \hat{I}(t) \rangle = \pm \, \langle\langle 0| \left(\mathcal{M}(\chi) \frac{\partial \mathrm{e}^{\mathcal{M}(\chi)t}}{\partial i\chi} + \mathcal{M}'(\chi) \mathrm{e}^{\mathcal{M}(\chi)t} \right) |\rho_0\rangle\rangle \bigg|_{\chi=0} , \quad (4.10)$$

where the choice of sign arises from the particular counting variable, N, chosen. For example, if $N = N_L$ counts the number of particles in the left reservoir of the SSET, then a *decrease* in N represents a positive current, whereas if $N = N_R$ is the number of particles in the right reservoir, then an *increase* in N is a positive current. In this expression, $|\rho_0\rangle\rangle$, is the initial density matrix, and a prime indicates a derivative with respect to $i\chi$. The first term of (4.10) vanishes, since $\langle\langle 0|\mathcal{M}(0) = 0$. This relation follows from the conservation of probability, $\langle\langle 0|\rho(0,t)\rangle\rangle = 1$, and the equation of motion for $|\rho(0,t)\rangle\rangle$, given by Eqn. (4.7),

$$\frac{d\langle\langle 0|\rho(0,t)\rangle\rangle}{dt} = \langle\langle 0|\mathcal{M}(0)|\rho(0,t)\rangle\rangle = 0, \tag{4.11}$$

which must be true for all $|\rho\rangle\rangle$, and so we find $\langle\langle 0|\mathcal{M}(0) = 0$.

For the second term of Eqn. (4.10), as we have already seen for the charge degree of freedom, the process is stationary: $|\rho\rangle\rangle$ has a well defined steady state. This implies that $\lim_{t\to\infty} e^{\mathcal{M}(0)t}|\rho_0\rangle\rangle = |0\rangle\rangle$ for any initial vector $|\rho_0\rangle\rangle$. The resulting simple expression for the stationary current is then,

$$\langle\hat{I}\rangle = \pm\langle\langle 0|\mathcal{M}'(0)|0\rangle\rangle\,, \tag{4.12}$$

which, as we will show later, gives the same result as the simple counting methods shown in chapter 2.

We can now go on to consider the current-current correlation function,

$$S_I(t_1,t_2) \equiv \langle\hat{I}(t_1)\hat{I}(t_2)\rangle - \langle\hat{I}(t_1)\rangle\langle\hat{I}(t_2)\rangle. \tag{4.13}$$

The first term can be written, using our definition of the current operator, $\hat{I}(t) = d\hat{N}(t)/dt$, as follows,

$$\langle\hat{I}(t_1)\hat{I}(t_2)\rangle = \frac{\partial}{\partial t_1}\frac{\partial}{\partial t_2}\mathrm{Tr}[\hat{N}(t_1)\hat{N}(t_2)\sigma(t=0)]\,. \tag{4.14}$$

To find the noise spectrum we need to calculate this quantity for both $t_1 > t_2$ and $t_1 < t_2$, but since the quantum regression theorem[3] [69] (see the previous chapter) only gives forward time evolution we first define for $t_1 > t_2$,

$$f(t_1,t_2) = \langle\hat{N}(t_1)\hat{N}(t_2)\rangle. \tag{4.15}$$

We can then calculate the $t_1 < t_2$ part by using the relation $\langle\hat{N}(t_2)\hat{N}(t_1)\rangle = f(t_1,t_2)^*$, as we did for the charge noise. The correlation function is then,

$$S_I(t_1,t_2) = \partial_{t_1}\partial_{t_2}[\Theta(t_1-t_2)f(t_1,t_2) + \Theta(t_2-t_1)f(t_1,t_2)^*] - \langle\hat{I}(t_1)\rangle\langle\hat{I}(t_2)\rangle, \tag{4.16}$$

3 We are able to use the regression theorem since we have included the counting variable as a system operator in our Born-Markov description.

with $\Theta(t)$ the Heaviside step function. We can now use the regression theorem to obtain the correlator $f(t_1, t_2)$ for $t_1 > t_2$,

$$f(t_1, t_2) = \mathrm{Tr}\left[\check{N} e^{\mathcal{L}(t_1 - t_2)} \check{N} e^{\mathcal{L} t_2} \sigma(t = 0)\right], \tag{4.17}$$

where $\check{N}$ is the superoperator representation of the counting operator $\hat{N}$, constructed in the same way as the island charge superoperator $\check{n}$ in the previous chapter (see, for example, Eqn. (3.33)).

Finally, we express (4.17) as a scalar product in Fourier space, by converting the $\check{N}$ superoperators to χ derivatives,

$$f(t_1, t_2) = \langle\langle 0| \frac{\partial}{\partial i\chi} \left[e^{\mathcal{M}(\chi)(t_1 - t_2)} \frac{\partial}{\partial i\chi} e^{\mathcal{M}(\chi) t_2} \right] |\rho_0\rangle\rangle . \tag{4.18}$$

Performing the time and χ derivatives (see appendix C), we find that $S_I(t_1, t_2)$ only depends on the time difference, $t = t_1 - t_2$, in the stationary limit, $t_2 \to \infty$ and the correlation function reads,

$$\begin{aligned} S_I(t) = \delta(t) \mathrm{Re}\langle\langle 0|\mathcal{M}''|0\rangle\rangle + \langle\langle 0|\mathcal{M}' e^{\mathcal{M} t} \mathcal{M}'|0\rangle\rangle \\ + \langle\langle 0|\mathcal{M}' e^{-\mathcal{M} t} \mathcal{M}'|0\rangle\rangle^* - \langle I\rangle^2, \end{aligned} \tag{4.19}$$

where the $\chi = 0$ argument is omitted for brevity.

This expression can then be Fourier transformed and simplified by introducing the set of orthonormal eigenvectors of $\mathcal{M}(0)$, as we did for the charge noise, and we find the compact expression,

$$S_I(\omega) = \mathrm{Re}\langle\langle 0|\mathcal{M}''|0\rangle\rangle - 2 \sum_{i \neq 0} \mathrm{Re}\left(\frac{\langle\langle 0|\mathcal{M}'|\lambda_i\rangle\rangle \langle\langle \lambda_i|\mathcal{M}'|0\rangle\rangle}{i\omega + \lambda_i} \right) . \tag{4.20}$$

Given the full χ dependent evolution matrix $\mathcal{M}(\chi)$ and its eigenbasis, we now have simple expressions for both the charge and current noise.

At first sight, Eqn. (4.20) looks rather similar to expressions obtained by calculating probabilities for given numbers of charges, N, to have passed into the leads, such as in Refs. [105, 58, 60]. However, there is a crucial difference: these calculations assume that there is no coherence between states with different N. Our choice of basis for σ allows us to express the counting operator $\hat{N}$ as a simple derivative with respect to $i\chi$, leading to the expression (4.20), which takes fully into account coherence in N. Including such coherences is inherently problematic for methods based on the counting statistics of charges in the leads, as discussed in Refs. [55, 106]. The presence of steady state coherence leads to issues when defining a classical counting variable at $t = 0$, since it is not in a definite state [55]; we have overcome this by using the full evolution of the density operator which keeps track of the coherence in a consistent way.

In the following sections we go on to calculate these evolution matrices and, from these, the noise spectrum for the different transport

processes in the SSET, as introduced in chapter 2. We also note that this technique is able to shed light on the problems encountered in calculating the current noise through a double quantum dot coupled to a thermal bath, encountered in Ref. [107]. In this system it was found, using the previously available techniques, that the noise in the current between the dots, where quantum coherence is vital for the transport, violates charge conservation. Using our technique, this problem does not arise. These results are presented in appendix D.

4.3 DOUBLE JOSEPHSON QUASIPARTICLE RESONANCE

We begin by calculating the quantum current noise around the DJQP resonance, described in detail in section 2.4. A recent experiment that probed the asymmetry in the current noise [8] provides motivation for us to study the full quantum problem, and go beyond the semi-classical symmetric results which already exist in certain limits [14, 55]. The previous calculations were only able to obtain the noise in the limits where the off-diagonal elements of the steady state density matrix are suppressed, since, in this case, it is possible to use the classical expressions to find the symmetrised noise.

To calculate the full quantum noise, we need to construct an explicit form for the evolution matrix, $\mathcal{M}(\chi)$, used in the expression for the noise Eqn. (4.20). Since the SSET has two junctions, there are two possible counting variables to use, N_L, the number of particles in the left reservoir, and N_R, the number in the right reservoir. In the calculations we give throughout the remainder of this chapter we will use N_L unless otherwise mentioned. The calculations involving N_R follow the same procedures.

There are eight elements in the Fourier transformed density matrix for the DJQP, each corresponds to one of the elements in the reduced density matrix we used for the island charge (see Eqn. (2.54). We then wish to find evolution equations for each of these which will form the Liouville space vector,

$$|\rho(\chi)\rangle\rangle = (\rho_{00,0}, \rho_{22,0}, \rho_{02,-2}, \rho_{20,2}, \rho_{-1-1,0}, \rho_{11,0}, \rho_{-11,0}, \rho_{1-1,0})^T, \quad (4.21)$$

we see that the label q keeps track of the coherence. All of the terms which are diagonal or only involve coherence at the right-hand junction have $q = 0$, while the two terms which involve coherence have $q = \pm 2$. As an example, we start by calculating the evolution equation for $\rho_{00,0}(\chi)$. The full evolution of the density matrix is given by Eqn. (2.50). From this and the description in Sec. 2.4, we find that the relevant expression in the evolution of σ is given by,

$$\begin{aligned}\langle 0, N_L| \dot{\sigma} |0, N_L\rangle = \Gamma_L \langle 1, N_L + 1| \rho |1, N_L + 1\rangle \\ + iJ(\langle 2, N_L - 2| \rho |0, N_L\rangle - \langle 0, N_L| \rho |2, N_L - 2\rangle), \quad (4.22)\end{aligned}$$

which, when we Fourier transform, yields,

$$\dot{\rho}_{00,0}(\chi) = \sum_{N_L} \langle 0, N_L | \, \mathrm{e}^{i\chi \hat{N}_L} \dot{\rho} \, | 0, N_L \rangle$$

$$= \sum_{N_L} \mathrm{e}^{i\chi N_L} [\Gamma \, \langle 1, N_L + 1 | \, \rho \, | 1, N_L + 1 \rangle$$
$$+ iJ(\langle 2, N_L - 2 | \, \rho \, | 0, N_L \rangle - \langle 0, N_L | \, \rho \, | 2, N_L - 2 \rangle)]. \quad (4.23)$$

The first term is straightforward, this only involves diagonal elements and represents the incoherent, classical quasiparticle decay at the left junction and is given by,

$$\sum_{N_L} \langle 1, N_L + 1 | \, \rho \, | 1, N_L + 1 \rangle$$
$$= \sum_{N_L} \mathrm{e}^{i\chi(N_L - 1)} \, \langle 1, N_L | \, \rho \, | 1, N_L \rangle = \mathrm{e}^{-i\chi} \rho_{11,0}(\chi), \quad (4.24)$$

where we have simply shifted the sum over N_L by one to make sure that we obtain something which matches with the definition of one of the elements of ρ. The other terms involve coherence and so we have to make sure that we shift each term by an appropriate amount so that we can again match with the relevant definition of ρ,

$$\sum_{N_L} \mathrm{e}^{i\chi N_L} (\langle 2, N_L - 2 | \, \rho \, | 0, N_L \rangle - \langle 0, N_L | \, \rho \, | 2, N_L - 2 \rangle)$$
$$= \mathrm{e}^{2i\chi} \rho_{20,2} - \rho_{02,-2}. \quad (4.25)$$

We note here that it is in the definition of these coherent terms that we make sure Eqn. (4.9) is satisfied and we ensure χ is conjugate to the operator $\hat{N}$.

We can perform a similar calculation to obtain the evolution of the off diagonal elements, for example,

$$\langle 0, N_L | \, \dot{\sigma} \, | 2, N_L - 2 \rangle = iJ(\langle 2, N_L - 2 | \, \sigma \, | 2, N_L - 2 \rangle - \langle 0, N_L | \, \sigma \, | 0, N_L \rangle)$$
$$- \left(i\delta_L + \frac{\Gamma_R}{2} \right) \langle 0, N_L | \, \sigma \, | 2, N_L - 2 \rangle \, , \quad (4.26)$$

which gives,

$$\dot{\rho}_{02,-2}(\chi) = \sum_{N_L} \langle 0, N_L | \, \mathrm{e}^{i\chi \hat{N}_L} \dot{\sigma} \, | 2, N_L - 2 \rangle$$
$$= iJ \left(\mathrm{e}^{2i\chi} \rho_{22,0} - \rho_{00,0} \right) - \left(i\delta_L + \frac{\Gamma_R}{2} \right) \rho_{02,-2}. \quad (4.27)$$

The other required terms are obtained in a similar way. Combining these results with those for the evolution of the other elements, we are able to find the evolution matrix in Fourier space as,

$$\mathcal{M}(\chi) = \begin{pmatrix} 0 & 0 & -iJ & iJe^{2i\chi} & \Gamma_L e^{-i\chi} & 0 & 0 & 0 \\ 0 & -\Gamma_R & iJe^{-2i\chi} & -iJ & 0 & 0 & 0 & 0 \\ -iJ & iJe^{2i\chi} & G_L^- & 0 & 0 & 0 & 0 & 0 \\ iJe^{-2i\chi} & -iJ & 0 & G_L^+ & 0 & 0 & 0 & 0 \\ 0 & 0 & 0 & 0 & -\Gamma_L & 0 & -iJ & iJ \\ 0 & \Gamma_R & 0 & 0 & 0 & 0 & iJ & -iJ \\ 0 & 0 & 0 & 0 & -iJ & iJ & G_R^- & 0 \\ 0 & 0 & 0 & 0 & iJ & -iJ & 0 & G_R^+ \end{pmatrix}. \tag{4.28}$$

This matrix contains all of the information describing the internal (charge) dynamics of the system. The matrix has precisely the same form as Eqn. (2.54) if we take $\chi = 0$, but it now also contains information about how charge passes through the transistor in the phase χ. We have been able to represent the evolution of the system in the full (infinite) Hilbert space of $|n, N_L\rangle$ in this finite evolution matrix.

As a simple example, we will use $\mathcal{M}(\chi)$ to calculate the average current, and show that this agrees with the result calculated using the rate equation approach of Sec. 2.4.2. We use Eqn. (4.12). This requires $\mathcal{M}'(0)$ (obtained from Eqn. (4.28)) and the following quantities,

$$\langle\langle 0| = (1,1,0,0,1,1,0,0), \tag{4.29}$$

$$|0\rangle\rangle = \frac{1}{4E_J^2 + 2\Gamma^2 + 4(\delta_L^2 + \delta_R^2)} \begin{pmatrix} E_J^2 + 4\delta_L^2 + \Gamma^2 \\ E_J^2 \\ -2E_J\delta_L + iE_J\Gamma \\ -2E_J\delta_L - iE_J\Gamma \\ E_J^2 \\ E_J^2 + 4\delta_R^2 + \Gamma^2 \\ 2E_J\delta_R + iE_J\Gamma \\ 2E_J\delta_R - iE_J\Gamma \end{pmatrix}, \tag{4.30}$$

where we have again simplified the result by assuming $\Gamma_L = \Gamma_R = \Gamma$ (see Sec. 2.4). When multiplied out this gives an expression for the average current,

$$\langle I\rangle = \frac{3E_J^2\Gamma}{2\Gamma^2 + 4E_J^2 + 4(\delta_L^2 + \delta_R^2)}, \tag{4.31}$$

which is the same as that found in Eqn. (2.58).

We could equally have defined a counting variable, N_R, which counts the charges in the right-hand reservoir. This gives an evolution in which the phase variable appears in the bottom right part of the matrix,

$$\mathcal{M}(\chi) = \begin{pmatrix} 0 & 0 & -iJ & iJ & \Gamma_L & 0 & 0 & 0 \\ 0 & -\Gamma_R & iJ & -iJ & 0 & 0 & 0 & 0 \\ -iJ & iJ & G_L^- & 0 & 0 & 0 & 0 & 0 \\ iJ & -iJ & 0 & G_L^+ & 0 & 0 & 0 & 0 \\ 0 & 0 & 0 & 0 & -\Gamma_L & 0 & -iJ & iJe^{-2i\chi} \\ 0 & \Gamma_R e^{i\chi} & 0 & 0 & 0 & 0 & iJe^{2i\chi} & -iJ \\ 0 & 0 & 0 & 0 & -iJ & iJe^{-2i\chi} & G_R^- & 0 \\ 0 & 0 & 0 & 0 & iJe^{2i\chi} & -iJ & 0 & G_R^+ \end{pmatrix}, \tag{4.32}$$

which naturally leads to the same average current as Eqn. (4.28).

These matrices can now be used to calculate the current noise. As for the charge noise, we use a combination of exact numerical diagonalisation and analytic limiting cases to analyse the behaviour.

A useful dimensionless quantity to consider when discussing the current noise is the *Fano Factor* [1] defined as,

$$F(\omega) = \frac{S_I(\omega)}{\langle I \rangle}, \tag{4.33}$$

this quantity allows us to easily compare our results to those obtained for an uncorrelated Poissonian system, which has $F(\omega) = 1$ [2]. Systems with noise such that $F(\omega) > 1$ are said to be *super-Poissonian*, this is usually a sign that the transport is bunched at the frequency ω. If the noise has $F(\omega) < 1$, the transport is usually anti-bunched and this is referred to as *sub-Poissonian* noise. Quantum mechanical processes can lower the Fano factor below what is classically expected [2].

4.3.1 *Zero frequency noise*

We begin by calculating the zero-frequency Fano factor through the left-hand junction. This quantity has already been calculated using semi-classical approaches [14, 55]. By charge conservation arguments this quantity must be the same at both junctions of the SSET [108]. It is possible to find a simple analytic expression for the Fano factor given by,

$$F(0) = \frac{3}{2}\left(1 - \frac{2E_J^2(3\Gamma^2 - \delta^2)}{(\Gamma^2 + \delta^2 + 2E_J^2)^2}\right), \tag{4.34}$$

where $\delta = \delta_L + \delta_R$. This matches the result obtained in Refs. [14, 55].

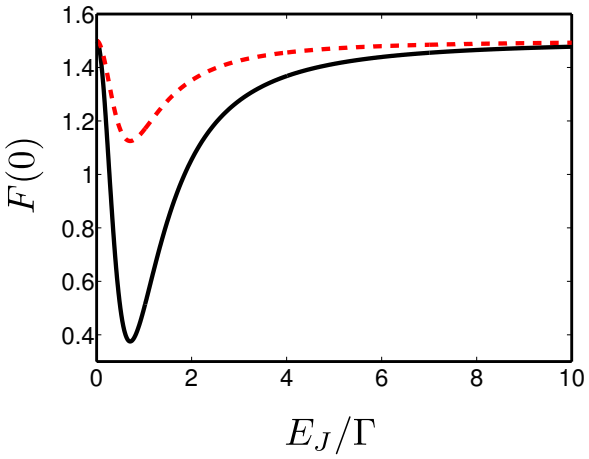

Figure 4.1.: The zero frequency Fano factor as a function of the ratio E_J/Γ. The black line shows the full quantum result, the red, dashed line shows the results of an incoherent calculation.

For given system parameters, Γ and E_J, the noise is minimised by choosing $\delta = 0$; detuning from resonance enhances the noise. We show the on-resonance Fano factor as a function of E_J/Γ in the black solid line of Fig. 4.1. In the two limits $E_J \gg \Gamma$ and $E_J \ll \Gamma$, the noise goes to $F(0) \to 3/2$, this can be thought of in terms of the effective charge transferred: in each cycle $3/2$ electrons are transferred per junction [55]. There is a dip in the noise around $E_J \approx \Gamma$, with a minimum of $3/8$ when $E_J = \Gamma/\sqrt{2}$ [55]. This can be compared to the results obtained for a normal state SET, where the minimum noise of $F(0) = 1/2$ is found when the timescales for tunnelling at both junctions match, $\Gamma_L = \Gamma_R$. This causes the noise to be sub-Poissoinain, since when an event occurs at one junction, it is unlikely to followed immediately by another. We see the same behaviour in the SSET when the timescales for Josephson oscillations, E_J, and incoherent tunnelling, Γ, are of the same order.

We can also calculate the zero frequency noise for the incoherent model presented in Sec. 2.4.2 (in particular using the evolution matrix $\mathcal{M}_{\text{inc}}$ from Eqn. (2.55)), from this we find the result (at zero detuning),

$$F_{\text{inc}} = \frac{3}{2}\left(1 - \frac{2E_J^2\Gamma^2}{(\Gamma^2 + 2E_J^2)^2}\right), \tag{4.35}$$

this is shown as the red, dashed line in Fig. 4.1. This has the same qualitative form as the full calculation, but $F(0) < F_{\text{inc}}(0)$ for all choices of E_J/Γ: coherence *suppresses* the noise below what is expected for classical charge transport. A process which is quantum coherent is more ordered than a classical incoherent process and so is less noisy [55].

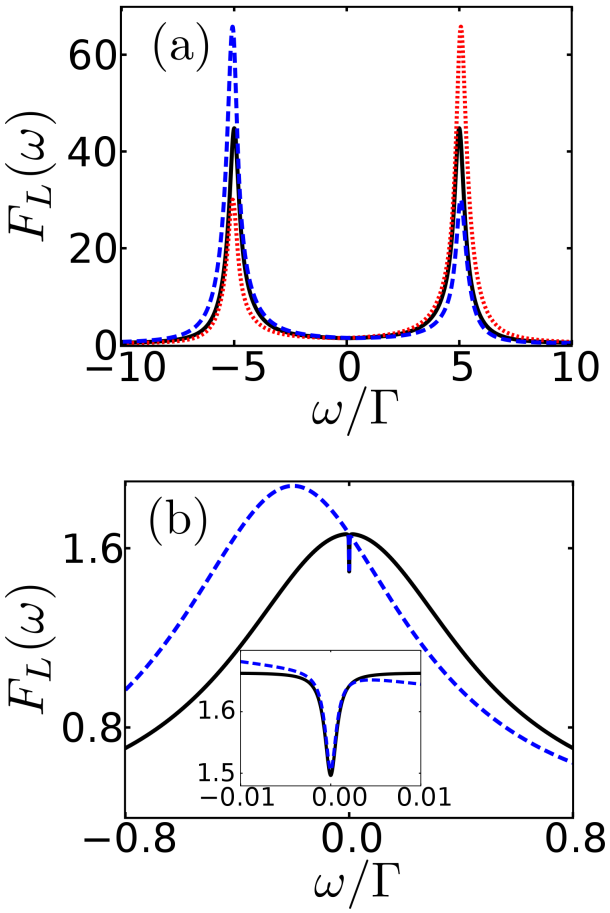

Figure 4.2.: Frequency dependent Fano factor, $F_L(\omega)$. (a) Weak quasiparticle tunnelling regime $E_J/\Gamma = 5$: $\delta_L = 0$ (black solid line), $\delta_L = \Gamma$ (blue dashed line) and $\delta_L = -\Gamma$ (red dotted line). (b) Strong quasiparticle tunnelling regime $E_J/\Gamma = 0.02$: $\delta_L = 0$ (black solid line) and $\delta_L = 0.2\Gamma$ (blue dashed line). In all cases, $\delta_R = 0$ and $\Gamma_L = \Gamma_R = \Gamma$, neglecting the voltage dependence of the rates.

4.3.2 *Frequency dependent noise*

The key advantage of our technique over those presented elsewhere [4, 55] is that it allows us to calculate the full *unsymmetrised* frequency dependent current noise. We now consider the noise through the left junction, $S_L(\omega)$, and the associated Fano factor, $F_L(\omega)$, for a given set of system parameters. We note that, at finite frequencies, we need to distinguish between the noise through the left and right junctions since there is, in general, no simple relation between the two quantities away from $\omega = 0$. However, since the junctions of the SSET at the DJQP resonance are symmetric, provided one assumes (as we do here) that the junctions are identical, the symmetries inherent in the DJQP cycle mean that we obtain the same noise spectrum at each junction, but with the replacement $\delta_L \leftrightarrow \delta_R$.

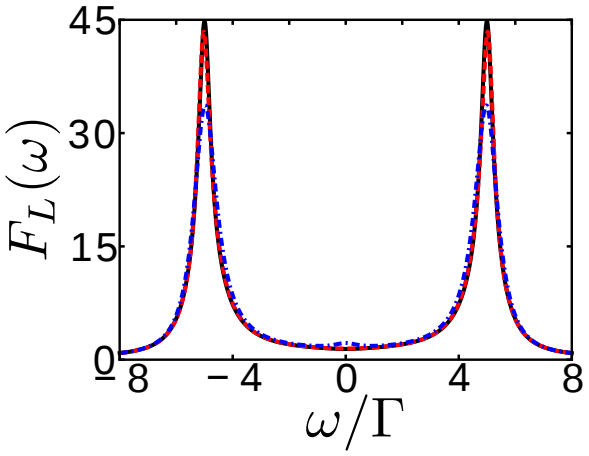

Figure 4.3.: The effect of changing δ_R on the Fano factor in the left-hand junction $F_L(\omega)$. The parameters are the same as in Fig. 4.2, with $\delta_L = 0$. The black, solid line shows $\delta_R = 0$, the red, dashed line $\delta_R = \Gamma$ and the blue, dotted line shows $\delta_R = -5\Gamma$.

Figure 4.2 shows the frequency dependent Fano factor for the left junction. We can distinguish two different behaviours corresponding to weak ($E_J/\Gamma \gg 1$) and strong ($E_J/\Gamma \ll 1$) quasiparticle tunnelling. For $E_J/\Gamma \gg 1$, shown in Fig. 4.2(a), coherent Cooper-pair oscillations lead to strong peaks in the spectrum at $\omega \simeq \pm E_J$. The dynamics in this regime can be thought of as a series of Josephson oscillations, interrupted by very infrequent quasiparticle decays [55], and so the current is highly correlated at the frequency of the Josephson oscillations, leading to the large super-Poissonian peaks seen in the spectrum. We can obtain an analytic expression for the noise at the resonant frequency, and find, at linear order in δ_L and for $\delta_R = 0$, that the peaks have heights,

$$F_L(\pm E_J) = \frac{16E_J(E_J \mp 2\delta_L)}{9\Gamma^2}, \tag{4.36}$$

and width $\propto \Gamma$, since the resonance is broadened by the quasiparticle decays. For $\delta_L < 0$, the positive frequency part of $F_L(\omega)$ is enhanced, since resonant oscillation in the SSET involves absorption of energy. This leads to an enhancement of the noise at the resonant frequency: energy exchange with the environment is necessary for the oscillations to occur. The opposite process occurs for $\delta_L > 0$, resonant oscillation in this case requires the SSET to emit energy into the environment. The value of δ_R influences the magnitude of $F_L(\omega)$, but not its asymmetry, as shown in Fig. 4.3. Detuning the resonance at the right hand junction affects the flow of current, but not the relative probabilities of energy absorption and emission at the left junction.

For $E_J/\Gamma \ll 1$, as in Fig. 4.2(b), there are no peaks in $F_L(\omega)$. The quasiparticle decays occur on a timescale much shorter than the Cooper-pair oscillations, so the current does not feature coherent oscillations

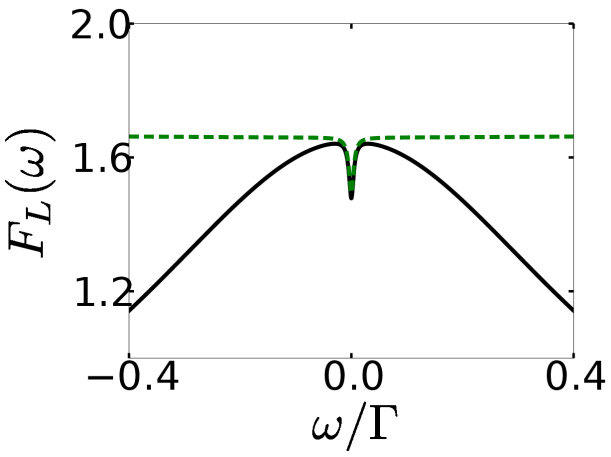

Figure 4.4.: Frequency dependent noise spectrum using the same parameters as Fig. 4.2(b). Comparison of the results of an incoherent model (green, dashed line) and the full quantum calculation (black, solid line).

and the peaks are absent. The only feature in the spectrum is a dip around $\omega = 0$, with $F_L = 3/2$ for $|\omega| \ll E_J^2/\Gamma$ (as was seen in the zero frequency calculation), this then increases to $F_L = 5/3$ on a scale determined by $E_J^2/\Gamma \ll |\omega| \ll \Gamma$. This dip has the same origin as the Lorentzian dip seen in the finite frequency spectrum of the normal state SET. In that system, the frequency dependent noise is given by,

$$F(\omega) = 1 - \frac{2\Gamma_L\Gamma_R}{\Gamma_T^2 + \omega^2}, \tag{4.37}$$

where $\Gamma_{L(R)}$ is the decay rate at the left(right)-hand junction, and $\Gamma_T = \Gamma_L + \Gamma_R$. This corresponds to a Lorentzian dip around zero frequency which occurs because the large charging energy of the system means that it is unlikely that two tunnel events occur in the same junction on timescales shorter than the decay time of system. For the DJQP, the same thing happens, an event at the left junction needs to wait for an event at the right junction before another can occur at the left junction, leading to the same dip around $\omega = 0$.

For high frequencies, $\omega \gg E_J, \Gamma$, we find $F_L(\omega) \to 1/3$, independent of all system parameters (though the Born-Markov approach breaks down eventually in the limit of very high frequencies $\omega \gg E_C$). This sub-Poissonian noise arises because Cooper-pairs contribute to the current, but not to the high frequency noise. To illustrate this, we make a comparison with the results of the incoherent model, based on Eqn. (2.55), in Fig. 4.4. This model is derived by assuming that

the Cooper-pair transitions are simply quasiparticle transitions with charge $2e$, resulting in the evolution matrix,

$$\mathcal{M}_{\text{inc}} = \begin{pmatrix} -\gamma_L & \gamma_L e^{2i\chi} & \Gamma e^{-i\chi} & 0 \\ \gamma_L e^{-2i\chi} & -(\gamma_L + \Gamma) & 0 & 0 \\ 0 & 0 & -(\gamma_R + \Gamma) & \gamma_R \\ 0 & \Gamma & \gamma_R & -\gamma_R \end{pmatrix}, \tag{4.38}$$

from which we can calculate the current noise using Eqn. (4.20).

We see that the two curves match exactly at low frequencies, the dip is well described by a model of incoherent transport, but at high frequencies the incoherent model predicts $F_L(\omega) \to 5/3$. In the quantum calculation at high frequencies, only the quaisparticles contribute, and so only 1 out of 3 charge carriers per cycle contribute to the noise. In the incoherent model, the Cooper-pairs are treated as quasiparticles with charge $2e$, and so we obtain the same result as in a tunnel junction in which quasiparticles of charge e and $2e$ carry current.

4.3.3 *Coupling to an oscillator*

An oscillator coupled to the current travelling through one of the leads is able to probe the asymmetric current noise spectrum through the effective damping and temperature. In this section we will use the linear response formalism, outlined in Sec. 3.2, to describe the back-action on an oscillator which the current noise gives rise to. These results will then be compared to the results of a recent experiment, Ref. [8].

The oscillator is coupled to the current through one of the leads of the SSET. However, this current is not just the tunnel current through one of the junctions, but is given by a combination of the particle current through the junction and the displacement current due to accumulated charge on the capacitor plates. The full current in one of the leads therefore involves the tunnel current through both junctions and is given by the Ramo-Shockley theorem [2],

$$\hat{I}(t) = \frac{C_L}{C_\Sigma}\hat{I}_L(t) + \frac{C_R}{C_\Sigma}\hat{I}_R(t), \tag{4.39}$$

where $\hat{I}_{L(R)}$ is the particle current through the left (right) lead. We need to calculate the noise in this quantity, not just the noise in particle currents, as we did above. We can then use this to construct the current-current correlation function in the lead as,

$$\begin{aligned}\langle \hat{I}(t)\hat{I}(0)\rangle = \frac{C_L^2}{C_\Sigma^2}\langle \hat{I}_L(t)\hat{I}_L(0)\rangle + \frac{C_R^2}{C_\Sigma^2}\langle \hat{I}_R(t)\hat{I}_R(0)\rangle \\ + \frac{C_L C_R}{C_\Sigma^2}(\langle \hat{I}_L(t)\hat{I}_R(0)\rangle + \langle \hat{I}_R(t)\hat{I}_L(0)\rangle).\end{aligned} \tag{4.40}$$

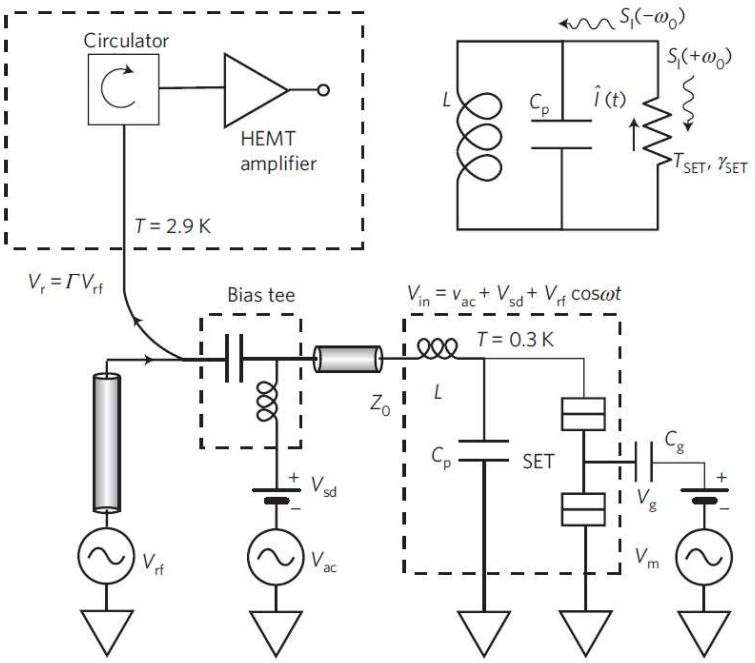

Figure 4.5.: Experimental set-up of Ref. [8]. Reproduced from Ref. [8]. The top-right hand corner shows the effective circuit, the SSET is coupled to an LC oscillator formed from the inductor, L and the capacitor, C_p.

The cross terms can then be written in terms of the charge noise by noting that $\dot{\hat{n}} = \hat{I}_L - \hat{I}_R$. The noise measured by coupling a detector to one of the leads is then given by,

$$S_I(\omega) = \frac{C_L}{C_\Sigma} S_L(\omega) + \frac{C_R}{C_\Sigma} S_R(\omega) - \frac{C_L C_R}{C_\Sigma^2} \omega^2 S_n(\omega), \tag{4.41}$$

where S_n is the charge noise spectrum (examined in detail in the previous chapter). For simplicity, we assume that the SSET is symmetric $C_L = C_R = C$, and that the gate capacitance is small, $C_g \ll C$, this allows us to write,

$$S_I(\omega) = \frac{S_L(\omega)}{2} + \frac{S_R(\omega)}{2} - \frac{\omega^2 S_n(\omega)}{4}, \tag{4.42}$$

which is a reasonable approximation for most experimental set-ups.

An experiment was recently performed on a SSET close to the DJQP [8], where the damping and effective temperature of an oscillator coupled to the current flowing through one of the leads was measured, it is this experiment which we now focus our attention on. The experimental set up is reproduced in Fig. 4.5, we see that the system consists of a SSET, with an LC oscillator coupled to one of the leads. The interaction Hamiltonian for this system is given by [8],

$$H_{\text{int}} = -\hat{I}(t)\hat{\Phi}, \tag{4.43}$$

Physical quantity	Experimental value
Charging energy	$E_C = 237\,\mu\text{eV}$
Josephson energy	$E_J = 51\,\mu\text{eV}$
Superconducting gap	$\Delta = 190\,\mu\text{eV}$
Normal state junction resistances	$R_J = 27\,\text{k}\Omega$
Oscillator frequency	$\omega_0/2\pi = 1.04\,\text{GHz}$
Oscillator-SSET coupling strength	$A = 2.28 \times 10^{18}\,\text{C}^{-1}$

Table 4.1.: Parameter values for the experiment in Ref. [8].

where Φ is the flux in the inductor L, which plays the role of the position of the oscillator.

The damping rate and steady state thermal occupation of the oscillator are then measured, and their value without the SSET coupled subtracted (to remove other environmental effects). The noise properties of the SSET at the frequency of the oscillator are then inferred, using linear response, as we showed in the previous chapter. In this section, we compare our analytical calculations to the experimental results.

To calculate $S_I(\omega)$, we use the results for $S_L(\omega)$, presented in the previous section, along with those for $S_n(\omega)$, from the previous chapter. This just leaves us with $S_R(\omega)$ to calculate, this is done using the same procedure as for $S_L(\omega)$ along with the evolution matrix at the right hand junction from Eqn. 4.32.

The relevant parameters for the experiment in Ref. [8] can be found in table 4.1. The junctions are taken to be symmetric, and the coupling strength is calculated as [8],

$$A = \frac{1}{\sqrt{2\hbar\omega_0 C_p}}. \tag{4.44}$$

These parameters allow us to calculate a value of $E_J/\Gamma \simeq 0.5$ at resonance, where Γ is calculated using the full expressions given in Sec. 2.3. Using these parameters we are able to use our model to predict the noise and, from this, the damping and effective steady state temperature of the oscillator, deducing the effect of coupling to the SSET.

We begin by considering the damping rate. We split the damping into its three constituent parts, the particle current contributions,

$$\gamma_{L(R)} = A^2(S_{L(R)}(\omega_0) - S_{L(R)}(-\omega_0)), \tag{4.45}$$

shown in Figs. 4.6(a) and 4.6(b) respectively and the charge noise contribution,

$$\gamma_n = A^2\omega_0^2(S_n(\omega_0) - S_n(-\omega_0)), \tag{4.46}$$

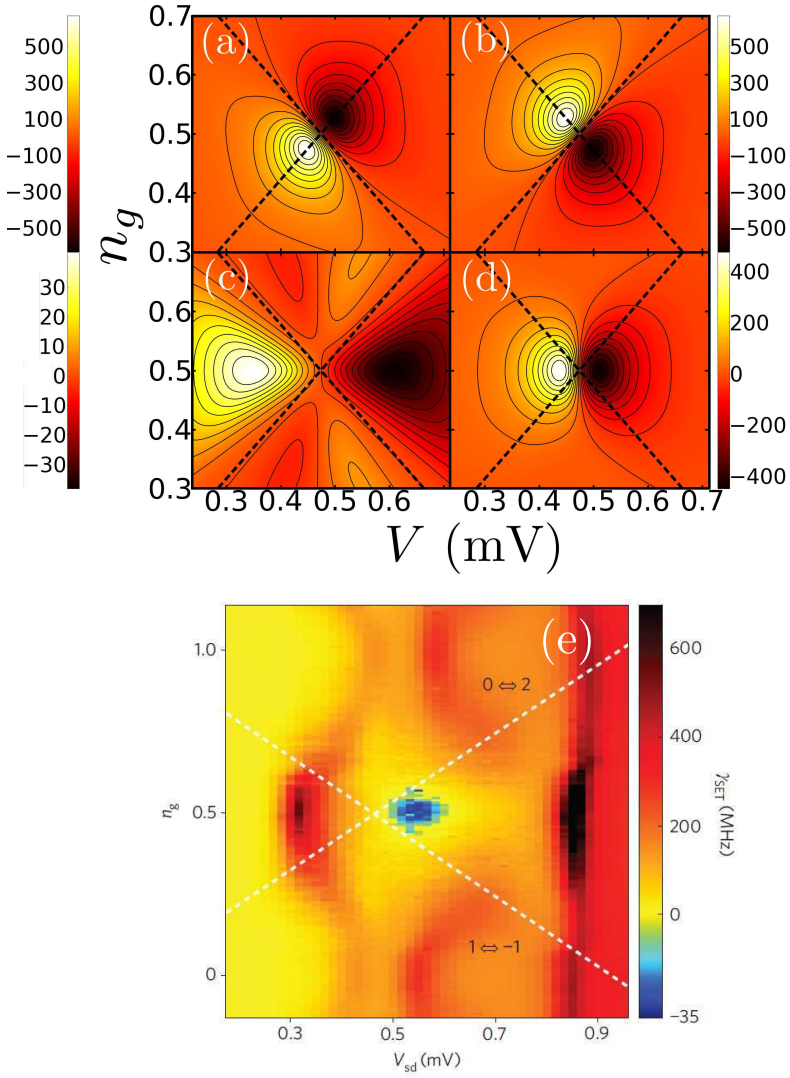

Figure 4.6.: Contributions to the damping (in MHz) from particle currents in (a) left, γ_L, and (b) right, γ_R, junctions; (c) contribution from the charge noise, γ_n and (d) total damping, γ_{BA}. Dashed lines indicate the two Cooper-pair resonances which overlap at the DJQP resonance. For comparison, in (e) we reproduce the measured results, from Ref. [8], for the effective damping rate of the oscillator due to the SSET.

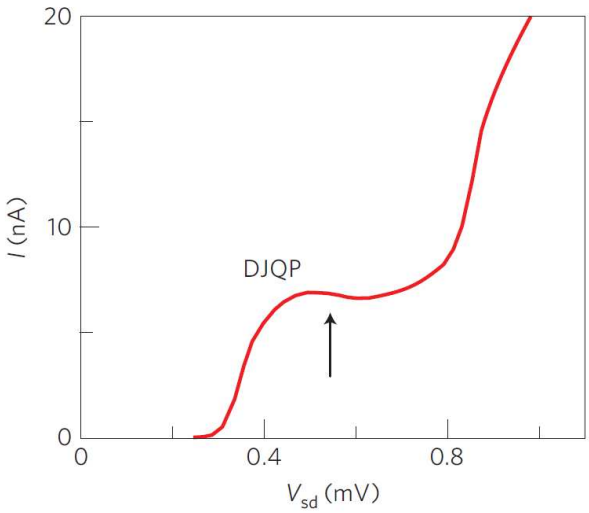

Figure 4.7.: Current-voltage characteristics of the SSET, around the DJQP, as measured in Ref. [8]. Reproduced from Ref. [8].

shown in Fig. 4.6(c) along with the total damping rate,

$$\gamma_{BA} = \frac{\gamma_L + \gamma_R}{2} - \frac{\gamma_n}{4}, \tag{4.47}$$

in Fig. 4.6(d).

The particle current contributions are (almost [4]) antisymmetric about lines where the corresponding junction has a Cooper-pair resonance. Regions of positive (negative) damping arise when a resonance is detuned, so energy is on average, absorbed (emitted) from the resonator by the SSET. The charge noise contribution has a different symmetry, as both Cooper-pair resonances affect the island charge (discussed in detail in the previous chapter). The overall damping, shown in Fig. 4.6(d), is dominated by γ_L and γ_R; the influence of γ_n is weak because the frequency scale for the SSET is set by E_J, which is much larger than ω_0, as can be seen from Eqn. (4.47).

For comparison we reproduce the results of Ref. [8] in Fig. 4.6(e). The asymmetry which we have calculated, shown in Fig. 4.6(d), is very similar to that observed in the experiment. We can also make a simple comparison by computing the maximum and minimum values of γ_{BA}, which occur for $n_g = 0.5$, and bias voltages below and above the centre of the DJQP resonance (see Fig. 4.6(d)). We obtain maximum and minimum damping rates with the same magnitude, 475 MHz, but opposite sign, in accord with the symmetry of the problem. Measured maximum and minimum damping rates [8] were ≈ 550 MHz and ≈ -35 MHz respectively.

4 There is a perfect antisymmetry when the voltage dependence of the quasiparticle rates is neglected; including this dependence, as is the case in Fig. 4.6 where we use the full energy dependent rates discussed in Sec. 2.3, leads to small deviations.

Our calculation fits with the experiment on the low bias side, though agreement is less good on the high bias side. The difference is probably due to the low resistance junctions ($R_J = 27\,\mathrm{k}\Omega \sim R_Q$) used [8, 10, 62], which allow higher-order processes (beyond the DJQP cycle), whose contribution to the current (and hence to the damping) increases with the bias voltage. We can see this by looking at the measured I-V characteristic of the device (reproduced here in Fig. 4.7), where we see that the current does not have the simple Lorentzian shape associated with the DJQP (see Sec. 2.4.2), but also has a background which seems to increase approximately linearly with bias voltage. The contribution of this background is small for voltages below the DJQP, but is large above the resonance.

We next look at the effective back-action temperature of the oscillator, which can be found from the noise using the expression Eqn. (3.16). We are again able to split this expression up into the parts due to the separate contributions from the particle currents in each junction, and the charge noise, as we did for the damping. These results are presented in Fig. 4.8. We see that the symmetry of each part is the same as that found for the damping, with regions of positive and negative T, corresponding to the positive and negative damping regions. The experimentally measured results for this quantity are reproduced in Fig. 4.8(e). We see that our results are able to reproduce the same basic form as the experimental results, but for this quantity we do not find such good quantitative agreement, even on the low bias side of the resonance. We calculate that the minimum positive temperature (i.e. at the point with the strongest cooling) is 420mK, whereas in the experiment it is measured as being as low as 100 ± 40mK. This difference cannot be explained by the same mechanisms as the damping, since the low temperature occurs on the low voltage side of resonance, where the background current is small. However, in the experiment, the effective temperature is a *derived* quantity which relies on accurate measurement of the damping as well as the symmetrised noise. The processes needed for measuring these additional quantities can introduce a lot of extra sources of potential error, and even a very small difference in the values can result in a large difference in the inferred temperature.

4.4 JOSEPHSON QUASIPARTICLE RESONANCE

We now go on to discuss the asymmetric quantum current noise near to the JQP resonance. The evolution matrix at the JQP resonance can be calculated in a very similar way to the DJQP, using the model

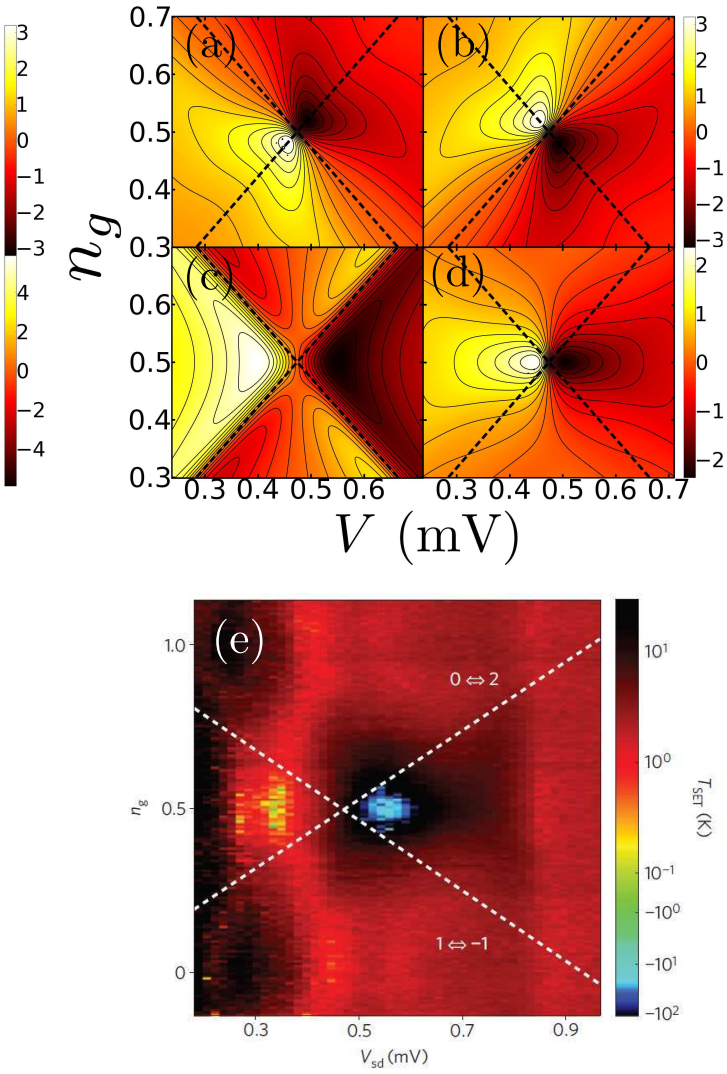

Figure 4.8.: Contributions to the inverse temperature (in K^{-1}) from particle currents in (a) left, $1/T_L$, and (b) right, $1/T_R$, junctions; (c) contribution from the charge noise, $1/T_n$ and (d) total inverse temperature, $1/T_{BA}$. Dashed lines indicate the two Cooper-pair resonances, which overlap at the DJQP resonance. For comparison, in (e) we reproduce the measured results, from Ref. [8], for the effective temperature of the oscillator due to the SSET.

presented in Sec. 2.3. If we count charges travelling through the left (coherent) junction then we obtain,

$$\mathcal{M}(\chi) = \begin{pmatrix} 0 & \Gamma_2 & 0 & -iJ & iJe^{2i\chi} \\ 0 & -\Gamma_2 & \Gamma_1 & 0 & 0 \\ 0 & 0 & -\Gamma_1 & iJe^{-2i\chi} & -iJ \\ -iJ & 0 & iJe^{2i\chi} & i\delta - \Gamma_1/2 & 0 \\ iJe^{-2i\chi} & 0 & -iJ & 0 & -i\delta - \Gamma_1/2 \end{pmatrix}, \quad (4.48)$$

where the basis for the matrix is given by,

$$|\rho(\chi)\rangle\rangle = (\rho_{00,0}, \rho_{11,0}, \rho_{22,0}, \rho_{02,-2}, \rho_{20,2})^T. \quad (4.49)$$

Again, q labels the coherence, as for the DJQP. The eigenvectors necessary for calculating the current from Eqn. (4.12) are,

$$\langle\langle 0| = (1,1,1,0,0), \quad (4.50)$$

$$|0\rangle\rangle = \frac{1}{E_J^2\left(2+\frac{\Gamma_1}{\Gamma_2}\right)+\Gamma_1^2+4\delta^2} \begin{pmatrix} E_J^2+4\delta^2+\Gamma_1^2 \\ E_J^2\frac{\Gamma_1}{\Gamma_2} \\ E_J^2 \\ 2\delta E_J - iE_J\Gamma_1 \\ 2\delta E_J + iE_J\Gamma_1 \end{pmatrix}, \quad (4.51)$$

where we recall, $E_J = 2J$. This gives the same result for the average current as obtained by counting methods in Sec. 2.3.2,

$$\langle I\rangle = \frac{2E_J^2\Gamma_1}{4\delta^2+\Gamma_1^2+E_J^2\left(2+\frac{\Gamma_1}{\Gamma_2}\right)}. \quad (4.52)$$

If we count at the right-hand junction we obtain a very different form for the evolution matrix,

$$\mathcal{M}(\chi) = \begin{pmatrix} 0 & \Gamma_2 e^{i\chi} & 0 & -iJ & iJ \\ 0 & -\Gamma_2 & \Gamma_1 e^{i\chi} & 0 & 0 \\ 0 & 0 & -\Gamma_1 & iJ & -iJ \\ -iJ & 0 & iJ & i\delta - \Gamma_1/2 & 0 \\ iJ & 0 & -iJ & 0 & -i\delta - \Gamma_1/2 \end{pmatrix}, \quad (4.53)$$

where at the right junction the basis is,

$$|\rho(\chi)\rangle\rangle = (\rho_{00,0}, \rho_{11,0}, \rho_{22,0}, \rho_{02,0}, \rho_{20,0})^T. \quad (4.54)$$

Since the transport is incoherent at this junction q is always zero. We see that counting at the right junction attaches phases to the incoherent decay terms $\Gamma_{1(2)}$ since it is these which are responsible for the current through the right-hand junction. Even though this evolution matrix has a completely different form, the charge conservation

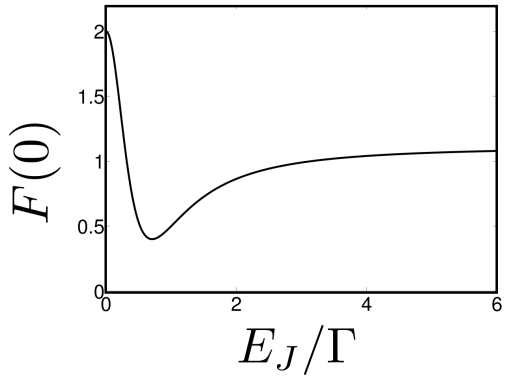

Figure 4.9.: Zero frequency Fano factor $F(0)$ for the JQP resonance as a function of E_J/Γ at zero detuning $\delta = 0$.

enforced on the system ensures that the average current at the right-hand junction is exactly the same as at the left-hand one.

It is again possible to obtain exact numerical results in the same way as for the DJQP, by diagonalising the χ-dependent evolution matrices for either the left or right junctions given above. As we will show, the finite frequency noise is very different in each junction because of the different transport mechanisms. Transport through the left junction is entirely coherent and inherently quantum mechanical, whereas transport through the right junction is stochastic and classical. In contrast to the average current and zero frequency noise, which are the same at both junctions, the finite frequency noise is able to give signatures of this different behaviour.

Throughout the remainder of this section, we will assume $\Gamma_1 = \Gamma_2 = \Gamma$, for simplicity, as we did for the charge noise in the previous chapter.

4.4.1 *Zero-frequency noise*

At $\omega = 0$ we can extract an analytic form for the Fano factor $F(\omega) = S(\omega)/\langle I \rangle$,

$$F(0) = 2\left(1 - \frac{4E_J^2(E_J^2 + 2\Gamma^2)}{(3E_J^2 + \Gamma^2 + 4\delta^2)^2}\right), \tag{4.55}$$

which is the same as was found using a variety of other techniques in Refs. [53, 4, 93]. We show $F(0)$ as a function of E_J/Γ at $\delta = 0$ in Fig. 4.9. In the incoherent limit, $E_J, \delta \ll \Gamma$, we find the Fano factor, $F(0) \to 2$, this can be understood [4] since, in this limit, the Cooper-pair effectively breaks up on the island instantly and the quasiparticles tunnel straight away. This then leads to an effective charge transferred of $2e$ each cycle, and so the noise is twice the Poissonian value. In the strong Josephson limit, $E_J \gg \Gamma, \delta$, we find the noise

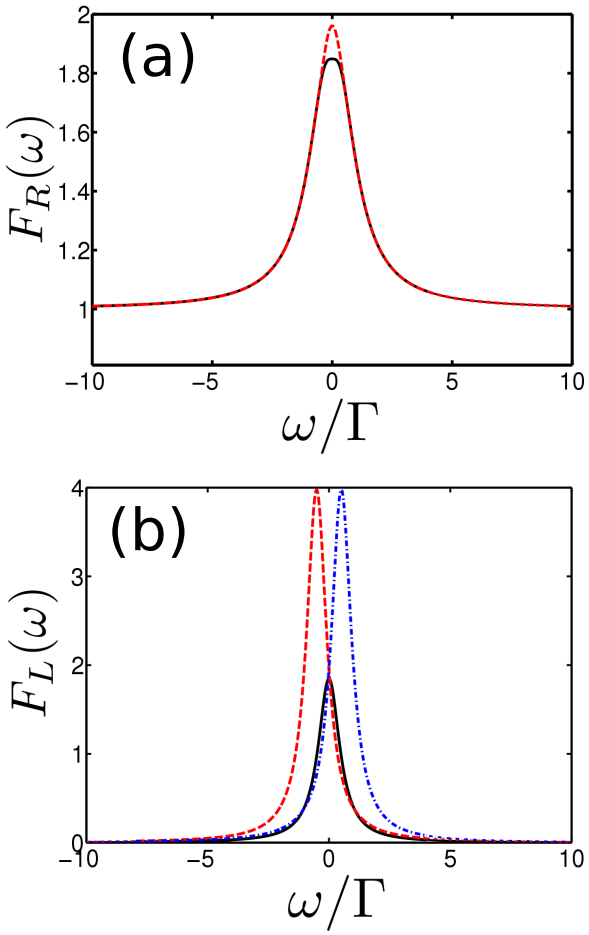

Figure 4.10.: Finite frequency Fano factor for (a) the right junction and (b) the left junction in the incoherent ($E_J = 0.1\Gamma$) limit. The detunings are $\delta = 0$ (solid black curve), $\delta = 0.5\Gamma$ (dashed red curve) and $\delta = -0.5\Gamma$ (dotted, blue curve). The $\delta = -0.5\Gamma$ case is not shown for the right-hand junction, since this is the same as the $\delta = 0.5\Gamma$ result.

is suppressed to $F(0) \to 10/9$, which is much closer to the Poissonian limit. As with the DJQP, we find a minimum in the noise when the timescales for Cooper-pair oscillations and quasiparticle decays match, $E_J = \Gamma/\sqrt{2}$, $F(0) = 2/5$. The presence of this dip is understood in the same way as for the DJQP (see Sec. 4.3.1).

4.4.2 *Finite frequency noise*

Our technique also gives access to the finite frequency quantum current noise. We begin by examining the incoherent limit $E_J \ll \Gamma$. In Fig. 4.10 we plot results for the Fano factor of (a) the right junction and (b) the left junction for various detunings. We see that the noise in the right junction is always symmetric in frequency, and changing the detuning only has a small effect around $\omega = 0$. The transport at

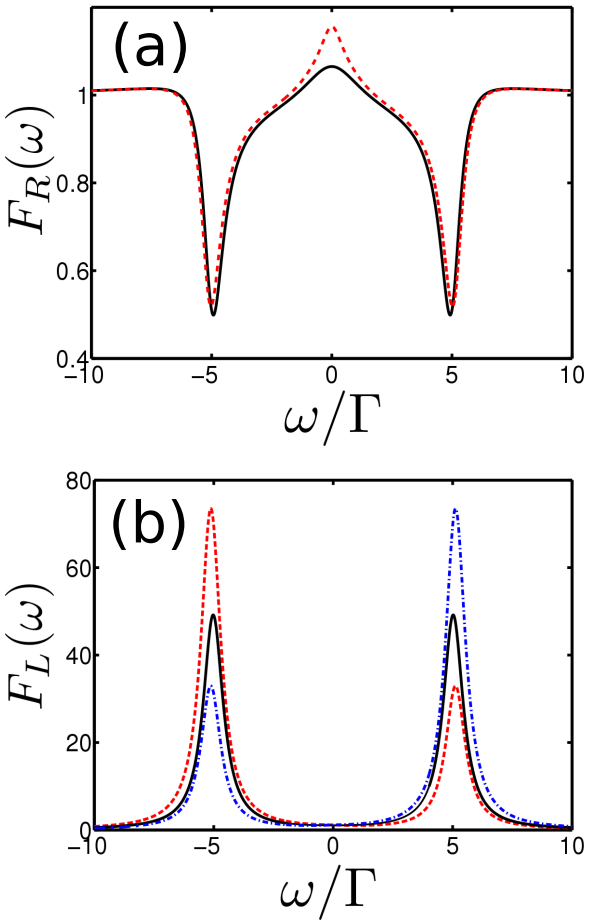

Figure 4.11.: Finite frequency Fano factor for (a) the right junction and (b) the left junction in the coherent ($E_J = 5\Gamma$) limit. The detunings are $\delta = 0$ (solid black curve), $\delta = \Gamma$ (dashed red curve) and $\delta = -\Gamma$ (dotted, blue curve). The $\delta = -\Gamma$ case is not shown for the right-hand junction, since this is the same as the $\delta = \Gamma$ result.

this junction is purely due to the incoherent tunnelling of quasiparticles, there is no way for emission/absorption asymmetry to arise, and the spectrum is always symmetric. This is no longer the case for the left-hand junction, where the transport is purely due to coherent Cooper-pair oscillations. We now see results which are reminiscent of those at the DJQP, where detuning from resonance introduces a large asymmetry to the spectrum. This detuning only affects the Cooper-pair transport, it can only affect the noise at frequencies close to the relevant eigenvalue of the evolution, $|\omega| \sim \sqrt{E_J^2 + \delta^2}$, far from this the noise must be detuning independent.

In Fig. 4.11, we plot similar results for the coherent transport limit $E_J \gg \Gamma$. We see that, as with the DJQP, the spectrum at the left junction develops peaks at the frequency of the Cooper-pair oscillations, which become asymmetric depending on the choice of the detuning parameter, δ. The spectrum for the right hand junction is very different. We see dips at the frequency of the Cooper-pair oscillations, the current in the incoherent junction has weaker correlations at this frequency. While the large amount of Josephson oscillations are occurring at the left junction (which cause the peaks in $F_L(\omega)$), the current though the right-hand lead becomes more *ordered*. Quasiparticle decays can only happen when the Cooper-pair has a high probability of being on the island which is controlled by the frequency of the coherent oscillations.

The high frequency behaviour also shows significant differences between the two junctions, we find, for frequencies $\omega \gg E_J, \Gamma, \delta$, that the noise in the right-hand junction is Poissonian, $F_R(\omega) \to 1$, whereas the noise in the left junction vanishes, $F_L(\omega) \to 0$. This can be understood in the same way that we understood high frequency result of $1/3$ obtained for the DJQP. In the left junction only Cooper-pair oscillations which have a distinct frequency are present, at high frequencies these make no contribution to the noise and so it vanishes, whereas in the right junction only quasiparticle decays are present, these are Poissonaian and so contribute at all frequencies, giving purely Poissonian noise at high frequencies. We note that all of these results, when symmetrised, match exactly with the semi-analytic results presented in Ref. [4].

4.5 COOPER-PAIR RESONANCES

We are able to calculate the current noise around the Cooper-pair resonances in an analogous way. We work using slightly different equations of motion than for the charge noise. Previously, we were able to write evolution in the eigenstate basis $|\rho\rangle\rangle = (\rho_{aa}, \rho_{bb}, \rho_{ab}, \rho_{ba})^T$, where exact diagonalisation is possible. However, in the eigenstate basis the transfer of charge is complicated by the fact that, in this basis, the decays are not between states with definite charge, and

so attaching the relevant phases in the evolution matrix is complicated. To simplify this process, we instead work in the basis where the transferred charge is an easy to identify quantity, the *charge basis*. The charge basis for the p^{th} resonance at the left-hand junction is,

$$|\rho(\chi)\rangle\rangle = (\rho_{00,0}, \rho_{11,0}, \rho_{01,-(p+1)}, \rho_{10,p+1})^T. \tag{4.56}$$

Full expressions for the counting variables, $\hat{N}'_L$ and $\hat{N}'_R$, can be written as power series in J, as we did for $\hat{n}' = \hat{n}^{(0)} + \hat{n}^{(1)} + \dots$ (see appendix B), since they are given by,

$$\hat{N}'_L = -\hat{k}' - \frac{\hat{n}'}{2}, \qquad\qquad \hat{N}_R = \hat{k}' - \frac{\hat{n}'}{2}. \tag{4.57}$$

However, in this section we will ignore any terms which arise at high order, and only deal with the leading order contributions from $\hat{n}^{(0)}$ and $\hat{k}^{(0)}$, since these are the dominant contributions.

We introduce the counting field, χ, to the evolution described by the $q = 0$ case of the matrix in Eqn. (2.85). This equation describes the full evolution within each doublet, including the evolution of the coherences. It is rotated back to the charge basis by using the inverse of the transformation in Eqn. (2.67), which gives,

$$\mathcal{M} = \begin{pmatrix} -A & \Gamma_L + \Gamma_R + B & C & C^* \\ A & -(\Gamma_L + \Gamma_R + B) & -C & -C^* \\ D & E & F & G \\ D^* & E^* & G & F^* \end{pmatrix}, \tag{4.58}$$

where we have defined the quantities,

$$A = c^4\gamma_{ab} + s^4\gamma_{ba}, \tag{4.59}$$
$$B = c^4\gamma_{ba} + s^4\gamma_{ab}, \tag{4.60}$$
$$C = iJ_p/\hbar + cs(s^2 - c^2)\gamma_{\text{coh}}, \tag{4.61}$$
$$D = iJ_p/\hbar + sc[2(s^2\gamma_{ba} - c^2\gamma_{ab}) + (c^2 - s^2)\gamma_{\text{coh}}], \tag{4.62}$$
$$E = -iJ_p/\hbar + sc[2(c^2\gamma_{ba} - s^2\gamma_{ab}) + (s^2 - c^2)\gamma_{\text{coh}}], \tag{4.63}$$
$$F = -2i\Delta E/\hbar - \left(\frac{\Gamma_L + \Gamma_R}{2}\right) - (1 + 2s^2c^2)\gamma_{\text{coh}}, \tag{4.64}$$
$$G = -2s^2c^2\gamma_{\text{coh}}, \tag{4.65}$$

with $c = \cos\alpha$ and $s = \sin\alpha$. We have used the non-RWA versions of the inter-doublet transition rates, $\Gamma_{L(R)}$, from Eqns. (2.75)-(2.76), since these are simpler in the charge basis. The extra elements arise from rotating the intra-doublet rates, from Eqn. (2.78), to the charge basis.

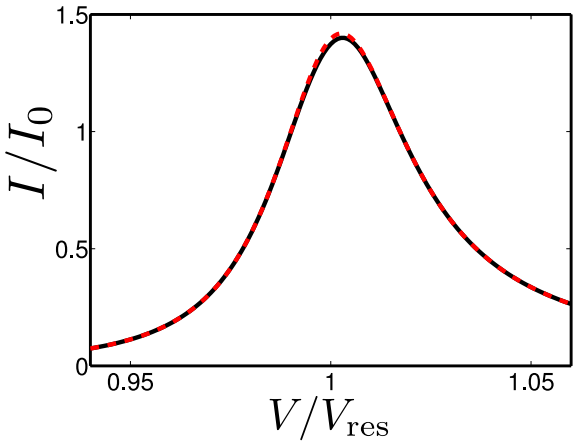

Figure 4.12.: Current close to the $p = 1$ resonance. The black solid line shows the calculation based on the evolution matrix, Eqn. (4.58), while the red, dashed line shows the analytic result from Eqn. (2.91). The parameters are the same as in Fig. 2.10 (b).

We can now attach counting fields to these terms in the same way as we did for JQP and DJQP. This results in the following evolution matrices where we count at the left and right junctions,

$$\mathcal{M}_L(\chi) = \begin{pmatrix} -A & \Gamma_L e^{-i\chi} + \Gamma_R + Be^{-i(p+1)\chi} & C & C^* e^{-i(p+1)\chi} \\ Ae^{i(p+1)\chi} & -(\Gamma_L + \Gamma_R + B) & -Ce^{i(p+1)\chi} & -C^* \\ D & Ee^{-i(p+1)\chi} & F & Ge^{-i(p+1)\chi} \\ D^* e^{i(p+1)\chi} & E^* & Ge^{i(p+1)\chi} & F^* \end{pmatrix}, \tag{4.66}$$

$$\mathcal{M}_R(\chi) = \begin{pmatrix} -A & \Gamma_L + \Gamma_R e^{i\chi} + Be^{-ip\chi} & C & C^* e^{-ip\chi} \\ Ae^{ip\chi} & -(\Gamma_L + \Gamma_R + B) & -Ce^{ip\chi} & -C^* \\ D & Ee^{-ip\chi} & F & Ge^{-ip\chi} \\ D^* e^{ip\chi} & E^* & Ge^{ip\chi} & F^* \end{pmatrix}, \tag{4.67}$$

noting that the only differences between the two matrices are whether a phase is attached to the Γ_R or Γ_L term and for $\mathcal{M}_R$ we make the replacement $(p+1) \to p$. Transitions between resonant states transport $p+1$ Cooper-pairs through the left junction, but only p through the right junction, since one remains on the island. The changes made to the basis now make it harder to exactly diagonalise the evolution matrix, Eqn. (4.58), and so we use numerical diagonalisation to find the current and noise.

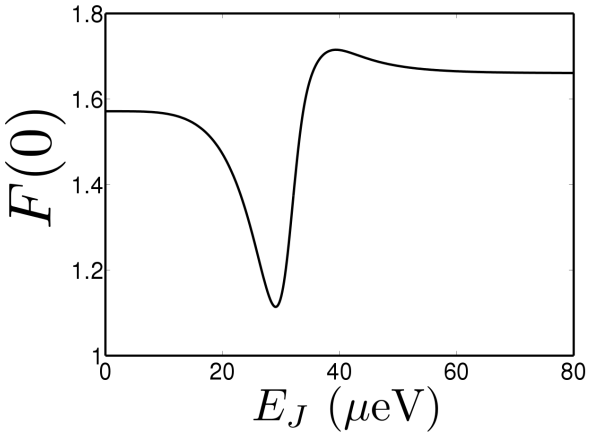

Figure 4.13.: Zero frequency Fano factor, $F(0)$, for the $p = 1$ Cooper-pair resonance, as a function of E_J. All other parameters are as in Fig. 2.10 (b) and are kept constant.

To check these expressions we first compare the average current calculated using the analytic expression, Eqn. (2.91), and that calculated using the above matrices. In Fig. 4.12, this is shown close to the $p = 1$ resonance, for the same parameters as Fig. 2.10 (b). We see that the two approaches give very similar results, except for very close to the resonance, where the conditions on the RWA, which was used to find the analytic equation, are at their weakest. The current is independent of whether we use $\mathcal{M}_L$ or $\mathcal{M}_R$, as required by charge conservation.

4.5.1 *Zero-frequency noise*

We now go on to look at the behaviour of the zero-frequency current noise. It is more difficult to choose parameters for the Cooper-pair resonances than for the JQP and DJQP, since there is no obvious single parameter which can describe the behaviour of the system such as E_J/Γ. For the CPRs, both the inter-doublet and intra-doublet decay rates, Γ and γ, as well as the coherent oscillation frequency, J_p, depend on E_J; the incoherent decays are actually environment induced transitions between states linked by a Josephson oscillation [45]. We plot the zero frequency noise as a function of E_J, keeping all other parameters constant in Fig. 4.13. The noise has a dip which looks very much like those seen for the JQP and DJQP resonances. However this dip is *not* due to timescale matching: we are always in the limit $J_p \ll \Gamma$. The dip occurs as we cross the resonance; the results are taken at constant n_g and V, and so we cross the resonance at a particular value of E_J. This can be seen more clearly in Fig. 4.14, where we show the zero-frequency Fano factor as a function of both E_J and n_g. We also plot the position of the resonance, defined as the maximum in the current, as the black, dashed curve and the location of the min-

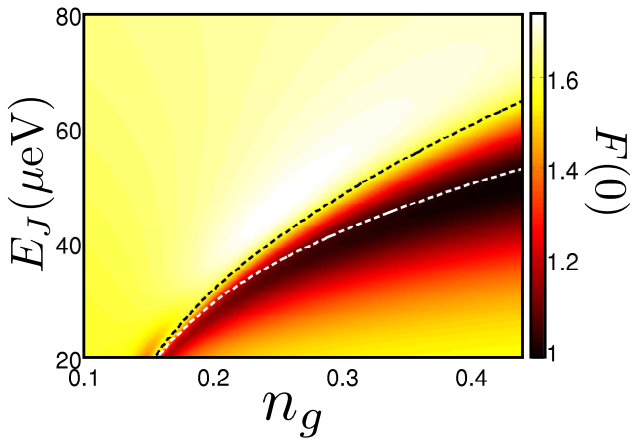

Figure 4.14.: Zero frequency Fano factor, $F(0)$, for the $p = 1$ Cooper-pair resonance as a function of E_J and n_g. All other parameters are as in Fig. 2.10 (b) and are kept constant. The black, dashed line shows the resonance (where $\Delta E = 0$) and the white, dashed line shows the charge degeneracy point (where $n_{aa} = n_{bb}$).

imum in the zero frequency charge noise (where $\rho_{aa} = \rho_{bb}$, see the discussion in Sec. 3.7) as a white, dashed line. The minimum in the Fano factor corresponds to the same point as the minimum in the zero frequency charge noise. At this point the transport is more ordered. Fluctuations between eigenstates within the same doublet do not cause charge fluctuations in the counting variable, the eigenstates are equal mixtures of the two charge states which make up a doublet. It is only the decays described by the inter-doublet transitions which cause the current to fluctuate.

4.5.2 *Finite-frequency noise*

We show the finite frequency Fano factor around the $p = 1$ resonance in Fig. 4.15 at both the left (a) and right (b) junctions, using the same parameters as we did for the charge noise, shown in Fig. 3.7. We are able to obtain an approximate description of the noise spectrum around the peaks by performing a coherent calculation, outlined in appendix E. The resulting spectra are given by,

$$S_i(\omega) = \left|I_{ab}^{(i)}\right|^2 \left[\frac{\rho_{aa}\Gamma_{\mathrm{coh}}}{(\omega-\omega_{ab})^2+\Gamma_{\mathrm{coh}}^2} + \frac{\rho_{bb}\Gamma_{\mathrm{coh}}}{(\omega-\omega_{ba})^2+\Gamma_{\mathrm{coh}}^2}\right], \quad (4.68)$$

where $i = L, R$ labels the junction and the matrix elements are,

$$I_{ab}^{(L)} = -\frac{2eiJ_p(p+1)}{\hbar}, \qquad I_{ab}^{(R)} = \frac{2eiJ_p p}{\hbar}. \quad (4.69)$$

We see that this spectrum has many similarities to the charge noise spectrum discussed in Sec. 3.7, except, in this case, the central peak

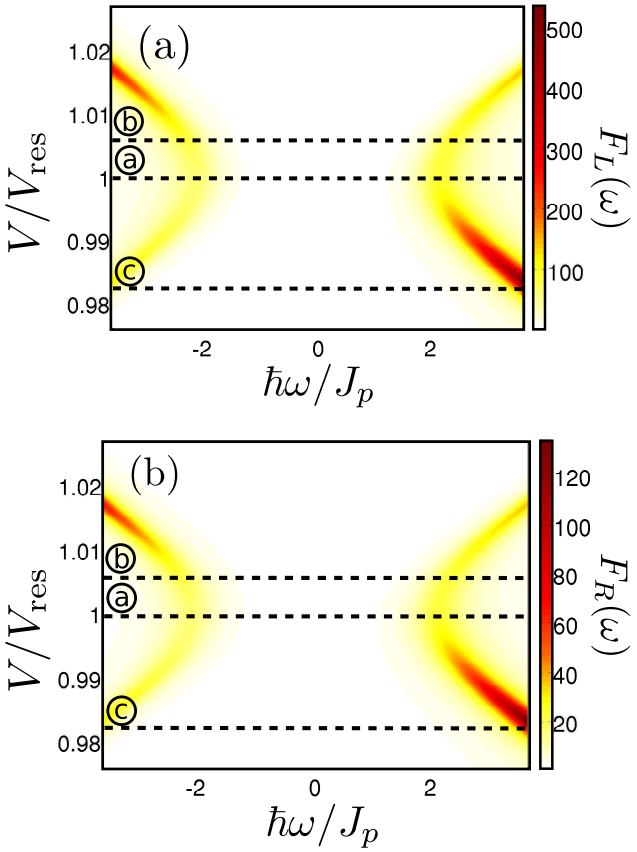

Figure 4.15.: Frequency dependent Fano factor in the vicinity of the $p = 1$ Cooper-pair resonance. The parameters are the same as in Fig. 3.7 (b). The dashed lines show the locations of the constant voltage sweeps presented in Fig. 4.16

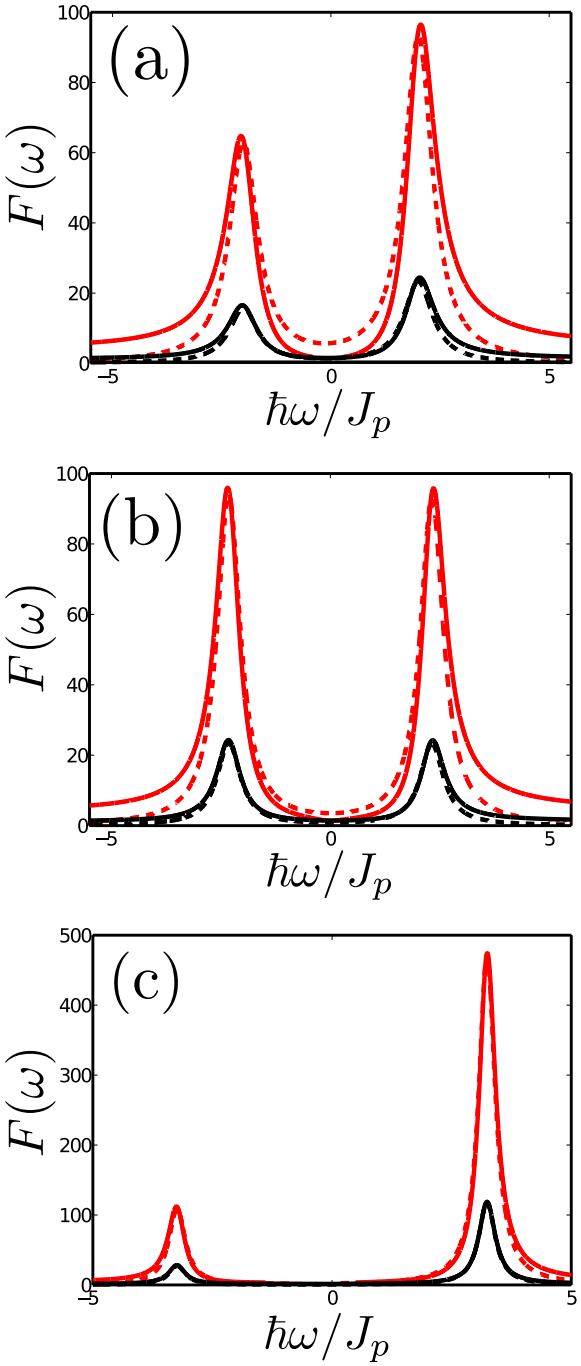

Figure 4.16.: Frequency dependent Fano factor close to the $p = 1$ Cooper-pair resonance. The red lines show $F_L(\omega)$, while the black lines show $F_R(\omega)$. The solid curves are the full spectrum, while the dashed lines show the coherent part from Eqn. (4.68). In (a) we show the spectrum directly on resonance, where the current is maximised, (b) shows the spectrum at the charge degeneracy point where $\rho_{aa} = \rho_{bb}$, (c) shows the spectrum when the system is further detuned from resonance. The location of these slices are shown as the dashed lines in Fig. 4.15.

is not present. The peaks are located at $\omega = \pm\omega_{ab}$, the frequency of the coherent oscillation. In Fig. 4.16, we show slices through the spectrum at three different values of $V/V_{\rm res}$. The numerical results are plotted as solid lines, while the dashed lines show the result of the coherent calculation. Figure 4.16 (a) shows that the spectrum is not symmetric at the centre of the resonance, but instead the symmetric point occurs at a higher voltage, at the same point as for the charge noise, when $\rho_{aa} = \rho_{bb}$, shown in Fig. 4.16 (b). This is an effect of the intra-doublet transitions, as discussed in Sec. 3.7. The heights of the peaks are well approximated by the analytic expression, the small discrepancy seen in Fig. 4.16 (a) and (b) is because these results are taken close to the resonance, in the regime where the RWA starts to break down. Further away from resonance, as shown in Fig. 4.16 (c), the coherent model exactly captures the nature of the peaks.

The noise in the left-hand junction is always larger than that in the right-hand junction, except at $\omega = 0$ when they must be equal. From the coherent calculation we find,

$$\frac{F_L(\pm\omega_{ab})}{F_R(\pm\omega_{ab})} = \frac{(p+1)^2}{p^2}. \tag{4.70}$$

At the left-hand junction each coherent oscillation involves $p+1$ Cooper-pairs, while at the right only p Cooper-pairs are involved, this leads to the much larger coherent peaks in $F_L(\omega)$.

In the high frequency limit, we find that the spectrum becomes symmetric, as is the case for the other resonances. All of the quantum oscillations which give rise to the asymmetry do not contribute at high frequencies. Exact, analytic forms for the high frequency noise can be found as,

$$F_L(\infty) = 1 + \frac{(p+1)^2(A\rho_{00} + B\rho_{11}) - [(p-1)\Gamma_L + (p+1)\Gamma_R]\rho_{11}}{\langle \hat{I} \rangle}, \tag{4.71}$$

$$F_R(\infty) = 1 + \frac{p^2(A\rho_{00} + B\rho_{11}) - p(\Gamma_L + \Gamma_R)\rho_{11}}{\langle \hat{I} \rangle}, \tag{4.72}$$

where the density matrix elements are evaluated in the steady state. The noise in the left junction is again always higher than the right. If we look at the difference in the noise at the two junctions we find,

$$F_L(\infty) - F_R(\infty) = \frac{\left[(p+1)^2 - p^2\right](A\rho_{00} + B\rho_{11}) + (\Gamma_L - \Gamma_R)\rho_{11}}{\langle \hat{I} \rangle}. \tag{4.73}$$

The incoherent dynamics consist of the intra-doublet decays, which take the system between eigenstates within the doublet and the inter-doublet decays, which take the system from the $n = 1$ to the $n = 0$ island state via a decay at either the left or right junction. These two

effects give different contributions to Eqn. (4.73) above. The intra-doublet decays give rise to the first term: these decays carry $p+1$ Cooper-pairs at the left junction and p at the right junction. The difference in the inter-doublet decays at the left and right junctions gives rise to the other term.

4.6 SUMMARY AND FUTURE WORK

In this chapter we have presented a new technique for calculating the current-current correlation function, which is valid for systems with steady state quantum coherence. We have shown how the technique is particularly suited to calculating the quantum current noise in systems with Josephson junctions such as the SSET. The current noise spectrum shows similar features for all of the current resonances which we study. Peaks occur in the noise spectrum at the relevant Josephson frequency when the transport is coherent. The asymmetry of these peaks is controlled by the detuning from resonance. The zero-frequency noise shows a dip when the timescales for the coherent and incoherent processes match (this is not possible for the CPRs). The high frequency noise contains information about only the incoherent decay process; the coherent processes have a definite frequency associated with them, and so make no contribution in the limit $\omega \to \infty$.

Close to the DJQP resonance, we were able to use our technique to closely match the results of the experiment in Ref. [8], using no fitting parameters. This allowed us to confirm their interpretation of the results as being due to the asymmetry in the emission/absorption rates of the SSET.

The technique developed in this chapter opens up many opportunities for further investigation. In the first instance, it would be interesting to develop a more complete calculation of the back-action damping and temperature of an oscillator coupled to the current at the JQP and CPRs. An interesting comparison could then be made with the corresponding results for a gate coupled oscillator [15].

When a resonator is coupled to the gate of the SSET, the current noise also contains important information about its dynamics. Applying our method to a model including the SSET and resonator would allow us to calculate the quantum current noise in such a system for the first time. In Ref. [95], it was found that the classical current noise spectrum contains peaks at the frequency of the oscillator, it would be interesting to look at the asymmetry in the quantum noise of these peaks. It is likely that the asymmetry is related to the distribution of energy in the oscillator, and so could be used as a way of measuring the dynamical state of the oscillator.

It would be interesting to think about higher order unsymmetrised current correlations, such as the third order cumulant or skewness of the distribution,

$$S^{(3)}(\omega_1, \omega_2) = \int_{-\infty}^{\infty} \int_{-\infty}^{\infty} \mathrm{e}^{i\omega_1 t_1} \mathrm{e}^{i\omega_2 t_2} \langle \delta\hat{I}(t_2)\delta\hat{I}(t_1)\delta\hat{I}(0)\rangle dt_1 dt_2. \quad (4.74)$$

It should be possible to generalise our technique to calculate this quantity, but at present it is unclear exactly what the unsymmetrised skewness, means or how it could be measured in an experiment [109].

Part III.

Classical Dynamics

5

THE DRIVEN SET RESONATOR

IN THIS CHAPTER, we turn to a look at a system which involves mechanical as well as electrical degrees of freedom. We will examine the dynamics of the normal state SET capacitively coupled to a harmonic oscillator in the presence of an external drive. We use a very simple model to describe the system, but our approach is easy to generalise to more complex systems. Effects like those we describe could occur in a range of systems. From carbon nanotubes with embedded quantum dots [11, 20], to nanomechanical shuttles in which the central nanoparticle or quantum dot is allowed to oscillate [17], from resonators coupled to quantum dots [16, 18], to molecular devices, in which a molecular orbital acts as a resonator [19] as well as the SET-resonators [25, 10] which we explicitly study here.

The model we use is an extension of the one presented in Refs. [110, 111, 112, 113], for undriven SET-resonator systems. The oscillator acts as a movable plate for the gate capacitor, thus the current through the SET is dependent on the position of the oscillator. However, the charge on the island of the SET also exerts a fluctuating electrostatic force on the resonator and so the dynamics of the resonator are influenced by the charge travelling through the transistor. It is these fully coupled dynamics which lead to the complex behaviour of the system. It has been shown that for weak SET-resonator coupling the SET damps the resonator's motion driving it into a thermal state [110], but for stronger coupling the dynamics become more complex [112, 114, 113] and no simple picture for the behaviour of the resonator exists. We present a generalisation of the existing models to take into account a periodic driving force applied to the resonator, this could be provided by, for example, an rf field [11], ultrasonic waves [16] or using an AFM in self-oscillation mode [18].

The back-action of the SET on the oscillator can act like a thermal bath provided the oscillator's position does not affect the charge dynamics too strongly. This picture can break down in three ways. Firstly, if the back-action damping is negative, the SET emits energy into the oscillator which can be driven into a limit cycle with large amplitude oscillations [46]. Secondly, if the electromechanical coupling is too strong then fluctuations in the system's trajectory can cause the dynamics to become non-linear [112, 114]. Finally, recent ex-

periments [11, 20] have found that by driving the mechanical motion strongly, it is possible to induce non-linear behaviour due to charge transport. In this chapter we will explore how the interplay between an external drive and electrical transport can lead to non-linear behaviour in the SET-resonator system.

Previous work [115, 116] has studied the electronic properties of similar systems in the presence of a driving force. These pieces of work were only interested in the electrical transport properties, and did not consider the behaviour of the oscillator, which we focus on here.

Beyond the non-linear dynamics, it is also interesting to look at some of the thermodynamic properties of the system. In small systems thermodynamic quantities, such as the work done by an external force, do not have well defined values. Fluctuations in the dynamics lead the thermodynamic quantities to have distributions, the nature of which can give insights into the behaviour of the system [30]. Exact results for these distributions are available for a harmonic oscillator in contact with a true thermal bath [117, 30]. This gives us a sensitive test of how far the analogy of the SET acting on the resonator as a thermal bath [110, 113] can go.

The structure of this chapter is as follows. In Sec. 5.1 we outline the model of the driven SET-resonator which we use. We derive classical master equations which describe the evolution of the probability distributions of both the SET and resonator. In Sec. 5.2 we present solutions to the master equations in the regime where the driving force is not strong enough to cause the dynamics to become non-linear. In this section we also briefly review the results previously obtained for the undriven system. In Sec. 5.3 we show how it is possible to go beyond the linear theory, and give calculations of the frequency shift and damping of the oscillator due to the SET in the non-linear region. We show how these results predict that the system can have more than one stable solution, with different amplitudes of oscillation. This then leads to Sec. 5.4 where we examine the nature of the bistability which can exist when fluctuations are able to drive transitions between the stable states. Finally, in Sec. 5.5, we present some preliminary results examining the thermodynamic properties of the system. We examine the distributions of the work done by the driving force, and show how these can give important information about the dynamics of the resonator.

5.1 MODEL

The SET-resonator system is sketched schematically in Fig. 5.1. The SET island is coupled to the left and right leads by tunnel junctions with equal capacitances, C_J, and a bias, V is applied symmetrically across the SET. A gate electrode is used to tune the operating point

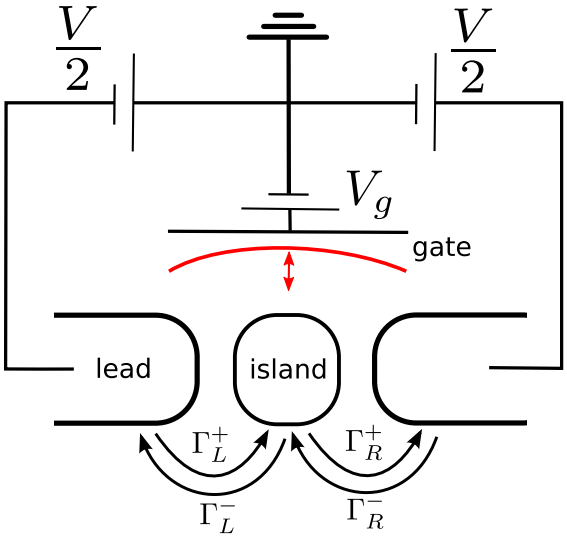

Figure 5.1.: Circuit diagram of the SET resonator system. The SET is coupled by tunnel junctions to two leads. A gate capacitor is used to tune the operating point, one plate of which is mechanically compliant to provide electro-mechanical coupling.

of the island. The island capacitor consists of one plate which is mechanically compliant, giving rise to a position dependent capacitance $C_g(x)$. This means that, as the plate moves the operating point of the SET changes and, as the charge on the island fluctuates, the electrostatic force on the plate changes, giving rise to electro-mechanical coupling. As long as the displacement of the resonator is small compared to its equilibrium displacement, $x \ll d$, we can make the linear approximation for the dependence of the gate capacitance on the position of the oscillator [110],

$$C_g(x) = C_g^0 \left(1 - \frac{x}{d}\right), \tag{5.1}$$

where C_g^0 is the capacitance when the oscillator is in its equilibrium position.

The dynamics of the SET are determined by the relative sizes of the energy scales in the system. These are the charging energy of the island, $E_C = e^2/2C_\Sigma$ (where $C_\Sigma = 2C_J + C_g(x)$ is the total capacitance of the island), the thermal energy $k_B T$ and the energy scale of the drain-source voltage eV. We choose to work in a regime where the charging energy is the dominant energy scale. At low enough temperatures, and if the island is small enough, then the charging energy can dominate over thermal effects. The voltages are tuned such that only the two island states $n = N, N+1$ are available, as described in Sec. 2.1.

5.1.1 *Equations of motion*

We begin by writing down the Hamiltonian for the SET-resonator system. This consists of three parts, one for each subsystem and one for the external drive, $F(t)$, and is given by,

$$H(n) = E_C[n - n_g(x)]^2 + \frac{p^2}{2m} + \frac{m\omega_0^2 x^2}{2} - xF(t), \tag{5.2}$$

where $n_g(x) = C_g(x)V_g/e$ is the, position dependent, polarisation charge induced by the gate, m the mass of the resonator, and ω_0 its natural frequency. The first term is the electrostatic energy introduced in Sec. 2.1. and the other terms are simply the Hamiltonian of a harmonic oscillator in the presensce of an external drive. Since constants can be removed from the Hamiltonian without changing the dynamics, and we only wish to keep terms at linear order in x/d we may rewrite this as [110],

$$H(n) = E_C\left[n^2 - 2nn_g^0\left(1 - \frac{x}{d}\right)\right] + \frac{p^2}{2m} + \frac{m\omega_0^2 x^2}{2} - xF(t), \tag{5.3}$$

where $n_g^0 = C_g^0 V_g/e$. For $n = N$ we obtain,

$$H(N) = E_C(N^2 - 2Nn_g^0) + \frac{p^2}{2m} + \frac{m\omega_0^2 x^2}{2} - (x - \Delta x)F(t), \tag{5.4}$$

where we have made a shift in the origin of position, $x \to x + \Delta x$, with,

$$\Delta x = \frac{-2E_C N n_g^0}{dm\omega_0^2}. \tag{5.5}$$

For the state $n = N + 1$, we find,

$$\begin{aligned} H(N+1) = {} & E_C[(N+1)^2 - 2(N+1)n_g^0] + \frac{p^2}{2m} \\ & + \frac{m\omega_0^2(x - x_0)^2}{2} - \frac{m\omega_0^2 x_0^2}{2} - (x - \Delta x)F(t), \end{aligned} \tag{5.6}$$

where $x_0 = -2N_g E_C/m\omega_0^2 d$ is the change in the equilibrium displacement of the resonator when the SET changes between the charge states $n = N$ and $n = N + 1$ [110].

We can then use Hamilton's equations to write down the equations of motion for the position and velocity of the resonator from the above Hamiltonians,

$$\dot{x} = \frac{\partial H}{\partial p} = \frac{p}{m} = v, \tag{5.7}$$

$$\dot{v} = \frac{\dot{p}}{m} = -\frac{1}{m}\frac{\partial H}{\partial x} = -\omega_0^2(x - nx_0) + \frac{F(t)}{m}, \tag{5.8}$$

where we now redefine $n \to n - N$, so that the two states available are $n = 0, 1$. Equations (5.7) and (5.8) are, in a sense, *stochastic* differential equations [118], they do not have a unique solution since the evolution of n is not deterministic. From these equations, we see that an effect of the SET is to change the equilibrium point of the harmonic oscillator, depending on the charge state of the island. The force on the oscillator due to the SET is not entirely random, as in the Langevin equation for an oscillator in a thermal bath [72], since it also has a systematic component: it is driven by fluctuations on the SET island which are not completely uncorrelated events.

We next need to calculate the rates at which electrons tunnel through the SET. The voltage applied across the SET makes if favourable for electrons to tunnel from left to right across the transistor, these are the only processes allowed at zero external temperature without the oscillator (see Sec. 2.1). As we will see, the position of the oscillator is able to affect these rates: processes which are forbidden for the uncoupled SET are possible and processes which are allowed in the uncoupled system can become suppressed. This means that we need to allow not only for the possibility of electrons tunnelling from left to right through the transistor, but also from right to left. There are then four possible processes which can change the charge state of the island: if the island is empty, then electrons can tunnel from the left or right leads onto the island, and if the island is occupied, the electron can tunnel off into either the left or right lead. We denote these four rates by $\Gamma^{\pm}_{L(R)}$ where $+(-)$ represents transitions which go in the same (opposite) direction to the applied bias, and $L(R)$ denotes transitions at the left (right) junction. These are shown schematically in Fig. 5.1.

At zero temperature, the rates are calculated within the *orthodox model* [44]. They are simply related to the energy differences between the relevant states, as for the uncoupled system presented in Sec. 2.1,

$$\Gamma^{\pm}_{L(R)} = \Theta(\Delta E^{\pm}_{L(R)}) \frac{\Delta E^{\pm}_{L(R)}}{R_J e^2} \tag{5.9}$$

where $\Theta(\cdot)$ is the Heaviside step function, R_J is the junction resistance, and the ΔE terms are the free energy difference associated with each of the transitions. The free energy differences can be calculated from the Hamiltonian as,

$$\Delta E^{\pm}_{L} = \pm E_L \pm m\omega_0^2 x_0 x, \tag{5.10}$$

$$\Delta E^{\pm}_{R} = \pm E_R \mp m\omega_0^2 x_0 x, \tag{5.11}$$

where,

$$E_L = E_C \left(1 - 2n_g^0\right) + \frac{eV}{2}, \tag{5.12}$$

$$E_R = -E_C(1 - 2n_g^0) + \frac{eV}{2}. \tag{5.13}$$

The extra term, $eV/2$, is due to the change of energy in the leads, because of the tunnelling of an electron [41]. This term is then positive if the electron is travelling with the bias, and is negative if the electron tunnels in the opposite direction to the bias. We see that these rates are the same as those in Sec, 2.1, but with the addition of an extra position dependent term [110].

We can simplify the description by introducing a set of scaling parameters, which allow us to write the equations in a dimensionless form [110]. We scale time as $t = \tau\tilde{t}$, where τ is the electron tunnel time, $\tau = (\Gamma_L^+ + \Gamma_R^+)^{-1} = 2R_J e^2/eV$, and length is scaled by $x = x_0\tilde{x}$, this then gives the dimensionless form of Hamilton's equations,

$$\dot{\tilde{x}} = \tilde{v}, \qquad \dot{\tilde{v}} = -\epsilon^2(\tilde{x} - n) + f(t), \tag{5.14}$$

where $\epsilon = \omega_0\tau$ is the dimensionless oscillator frequency, and $f(t) = F(t)\tau^2/mx_0$ is the dimensionless driving force. The dimensionless tunnel rates are then given by $\Gamma = \tilde{\Gamma}/\tau$, which gives,

$$\tilde{\Gamma}_L^{\pm} = \Theta(\pm\Delta_L \pm \kappa\tilde{x})(\pm\Delta_L \pm \kappa\tilde{x}), \tag{5.15}$$

$$\tilde{\Gamma}_R^{\pm} = \Theta(\pm\Delta_R \mp \kappa\tilde{x})(\pm\Delta_R \mp \kappa\tilde{x}), \tag{5.16}$$

where $\kappa = m\omega_0^2 x_0/eV$, is the strength of the dimensionless coupling between the SET and resonator and $\Delta_{L(R)} = E_{L(R)}/eV$ which satisfies $\Delta_L + \Delta_R = 1$ [110]. From now we will always use the dimensionless forms of quantities, and so will drop the tilde.

We now see how it is possible for the position of the oscillator to change which tunnel processes are allowed in the SET, and even block transport completely, through the so-called *distortion blockade* [112, 114]. We see that, if the oscillator's position is such that $x > x_{\max}$, where $x_{\max} = \Delta_R/\kappa$, then the only possible allowed processes are those in which an electron tunnels onto the island Γ_L^+, Γ_R^- and so transport through the SET stops. The same occurs when $x < x_{\min}$, with $x_{\min} = -\Delta_L/\kappa$, when the only allowed processes are those in which an electron tunnels off the island.

It is possible to use the above expression for the Hamiltonians and tunnel rates to find classical master equations, which describe the evolution of probability distributions for the state of the SET and the resonator. These take the form of classical Liouville equations, which include both the Hamiltonian evolution and the dissipative parts due to electron tunnelling [110],

$$\dot{P}_0(x, v; t) = \{H_0, P_0\} + (\Gamma_R^+ + \Gamma_L^-)P_1 - (\Gamma_L^+ + \Gamma_R^+)P_0, \tag{5.17}$$

$$\dot{P}_1(x, v; t) = \{H_1, P_1\} - (\Gamma_R^+ + \Gamma_L^-)P_1 + (\Gamma_L^+ + \Gamma_R^+)P_0, \tag{5.18}$$

where $P_{0(1)}(x, v; t)$ is the probability that, at time t, the SET is in the state $n = 0(1)$, with the resonator position and velocity given by x and v respectively. The Hamiltonians for $n = 0(1)$, $H_{0(1)}$ are the di-

mensionless form of Eqns. (5.4)-(5.6). The evolution under the Hamiltonian is given by a *Poisson bracket* [118], defined by,

$$\{H, P\} = \frac{\partial H}{\partial x}\frac{\partial P}{\partial p} - \frac{\partial H}{\partial p}\frac{\partial P}{\partial x}. \tag{5.19}$$

In the following section, we show how it is possible to find exact solutions to these master equations in the limit where the decay rates are linear functions of position.

5.2 LINEAR THEORY

It is possible to make progress analytically when the electron transition rates have a linear dependence on the position coordinate, i.e. when the dynamics of the system never take it into a region where the $\Theta(\cdot)$ functions are important. This occurs as long as the condition $\kappa|x| \ll \Delta_{L,R}$ is true for all trajectories explored by the system. This amounts to ignoring all effects of the distortion blockade, and is equivalent to taking the limits $x_{\min} \to -\infty$, $x_{\max} \to \infty$ [110, 113]. When this is the case, the only rates which are non-zero are those in which electron tunnel from left to right, $\Gamma^{+}_{L(R)}$. This allows us to substitute both the Hamiltonians and the correct decay rates into Eqns. (5.17) and (5.18) to obtain,

$$\dot{P}_0 = [\epsilon^2 x - f(t)]\frac{\partial P_0}{\partial v} - v\frac{\partial P_0}{\partial x} + (\Delta_R - \kappa x)P_1 - (\Delta_L + \kappa x)P_0, \tag{5.20}$$

$$\dot{P}_1 = [\epsilon^2 (x-1) - f(t)]\frac{\partial P_1}{\partial v} - v\frac{\partial P_1}{\partial x} - (\Delta_R - \kappa x)P_1 + (\Delta_L + \kappa x)P_0. \tag{5.21}$$

These can be added together to give the Fokker-Planck equation for the full probability distribution of the resonator, independent of the state of the SET [110],

$$\dot{P}(x, v; t) = [\epsilon^2 x - f(t)]\frac{\partial P}{\partial v} - \epsilon^2\frac{\partial P_1}{\partial v} - v\frac{\partial P}{\partial x}. \tag{5.22}$$

The master equations can be used to find equations of motion for all moments of the position and velocity of the resonator, solving these provides a full dynamical description of the resonator,

$$\frac{\partial}{\partial t}\langle x^n v^m\rangle = \iint dx\, dv x^n v^m \dot{P}(x, v; t). \tag{5.23}$$

We then integrate by parts to find the relevant parts of Eqn. (5.22) [110, 113],

$$\iint dx\, dv x^n v^m \frac{\partial P}{\partial x} = -n\langle x^{n-1} v^m\rangle, \tag{5.24}$$

$$\iint dx\, dv x^n v^m \frac{\partial P}{\partial v} = -m\langle x^n v^{m-1}\rangle, \tag{5.25}$$

which allow us to find a closed set of expressions for the first moments [110],

$$\langle \dot{x} \rangle = \langle v \rangle, \tag{5.26}$$

$$\langle \dot{v} \rangle = \epsilon^2(\langle P_1 \rangle - \langle x \rangle) + f(t), \tag{5.27}$$

$$\langle \dot{P_1} \rangle = \Delta_L - \langle P_1 \rangle + \kappa \langle x \rangle, \tag{5.28}$$

where $\langle P_1 \rangle = \int\int dx dv P_1$.

5.2.1 *Undriven system*

We briefly review the results previously [110, 112, 113] obtained when no drive is present, $f(t) = 0$. In this case the set of equations for the first moments, Eqns. (5.26)-(5.28), have the unique steady state solution,

$$\langle x \rangle_{ss} = \frac{\Delta_L}{1-\kappa}, \qquad \langle v \rangle_{ss} = 0, \qquad \langle P_1 \rangle_{ss} = \frac{\Delta_L}{1-\kappa}. \tag{5.29}$$

We can then simplify the analysis by shifting the equations of the first moments by their steady state values [110], to give,

$$\delta \dot{x} = \delta v, \qquad \delta \dot{v} = \epsilon^2(\delta P - \delta x), \qquad \delta \dot{P_1} = \kappa \delta x - \delta P_1, \tag{5.30}$$

where we define the shifted variables as, e.g., $\delta x = \langle x \rangle - \langle x \rangle_{ss}$. We can then Fourier transform these equations, to obtain a single equation for δx_ω [110],

$$\delta x(\omega)(-\omega^2 + \omega_{\text{eff}}^2 + i\omega\gamma_{\text{eff}}) = 0, \tag{5.31}$$

where $\delta x(\omega)$ is the Fourier transform of the position co-ordinate,

$$\delta x(\omega) = \int_{-\infty}^{\infty} \mathrm{e}^{i\omega t} \delta x(t) dt. \tag{5.32}$$

We have also defined the quantities,

$$\omega_{\text{eff}}^2 = \epsilon^2 \left(1 - \frac{\kappa}{1+\omega^2}\right), \qquad \gamma_{\text{eff}} = \frac{\epsilon^2 \kappa}{1+\omega^2}. \tag{5.33}$$

The physical motivation for these definitions is that Eqn. (5.31) has many similarities to the equation of motion of a classical damped, harmonic oscillator. The quantities in Eqn. (5.31) then represent the natural frequency and damping rate of this oscillator. However, written in this form, ω_{eff} and γ_{eff} are frequency dependent, and so the dynamics cannot be exactly mapped to a harmonic oscillator without further approximation. This is because the full dynamics are *non-Markovian*, the motion of the oscillator depends on the charge state, which depends on the resonator position in the past. However, in the weak coupling limit, $\kappa \ll 1$, we can make the approximation that the response of

the resonator is strongly peaked around $\omega = \epsilon$ [110]. Hence, we can exactly map the system onto the equation for a damped harmonic oscillator with the replacement $\omega \to \epsilon$ in Eqn. (5.33),

$$\delta\ddot{x} + \gamma_{\text{eff}}\delta\dot{x} + \omega_{\text{eff}}^2\delta x = 0. \tag{5.34}$$

Since γ_{eff} is always positive for the normal state SET [15], and can be quite large, we do not add any extrinsic damping, γ_{ext}, arising from the resonator's couplings to its thermodynamic surroundings (e.g. via the clamping points of the beam). We always assume the dynamics are such that the back-action effects dominate, $\gamma_{\text{eff}} \gg \gamma_{\text{ext}}$ [110, 112, 10, 18]. This is often the case in experiments, for example it was found that $\gamma_{\text{eff}}/\gamma_{\text{ext}} \sim 20$ in Ref. [18] and $\gamma_{\text{eff}}/\gamma_{\text{ext}} \sim 50$ in Ref. [10].

It is also possible to analyse the charge dynamics of the SET. For example, we can calculate the average dimensionless current passing through the SET. In the steady state this is found as,

$$\langle I \rangle = (\Delta_L + \kappa\langle x \rangle)\langle P_0 \rangle = (\Delta_R - \kappa\langle x \rangle)\langle P_1 \rangle. \tag{5.35}$$

If we choose the tunnel rates, $\Delta_{L(R)}$, such that the SET is at the *charge degeneracy point* so that average charge on the island $\langle P_0 \rangle = \langle P_1 \rangle = 0.5$, we find that the current is maximised, and is given by $\langle I \rangle = 0.25$. This amounts to choosing,

$$\Delta_L = \frac{1}{2}(1 - \kappa). \tag{5.36}$$

This value for the detuning keeps the system as far from the Coulomb blockade boundaries (see Sec. 2.1) as possible, and so ensures that the linear approximation works over the largest range of parameters [110, 112, 113]. This is therefore the value used for all of the results presented in the remainder of this chapter.

We can verify that Eqn. (5.34), the damped harmonic oscillator equation, gives an accurate representation of the resonator's dynamics by comparing the solution to that obtained via numerical simulation of the full system dynamics. The numerical calculations are based on Monte-Carlo simulations of individual trajectories, full details of which can be found in appendix F. In Fig. 5.2, we show a comparison of position of the oscillator as a function of time, calculated as both the solution to Eqn. (5.34), and the average over many runs of the numerics, using initial conditions $\langle x \rangle = \langle v \rangle = \langle P_1 \rangle = 0$. We see that the analytics give a good approximation to the numerical results, and so the approximations made are consistent, at least for the mean dynamics. Since the dynamics are not deterministic, it is necessary to obtain information about the full probability distribution, $P(x, v)$, to fully understand the behaviour of the system. The average position and velocity do not give the complete picture, because of this we now turn to examine the variances in the distributions of the oscillator variables.

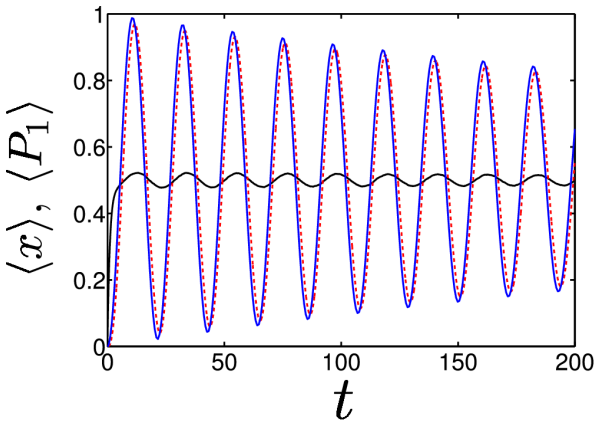

Figure 5.2.: Average over many trajectories taken by the SET, the red, dashed line is the position of the oscillator, the black, solid line is the average charge on the island, $\langle P_1 \rangle$. We also show as a blue, solid line the analytic solution to the damped, SHO equation for $\langle x \rangle$. The parameters used are $\kappa = 0.05$, $\epsilon = 0.3$.

The mean dynamics in the weak coupling limit are well described by mapping the problem onto that of a classical damped harmonic oscillator. This leads us to ask if the complete dynamics can be approximated by a harmonic oscillator in a thermal environment. If this is the case, we expect that the distributions of position and velocity should be Gaussian, and so the mean and variance of position and velocity are enough to completely describe the distributions. We find equations for the second cumulants of the system, following the same procedure as for the means [110],

$$\dot{\delta x^2} = 2\delta xv, \tag{5.37}$$
$$\dot{\delta v^2} = 2\epsilon^2(\delta v_1 - \delta xv), \tag{5.38}$$
$$\dot{\delta xv} = \epsilon^2(\delta x_1 - \delta x^2) + \delta v^2, \tag{5.39}$$
$$\dot{\delta x_0} = \delta v_N - \kappa\delta x^2 + \Delta_R\delta x_1 - \Delta_L\delta x_0, \tag{5.40}$$
$$\dot{\delta x_1} = \delta v_1 + \kappa\delta x^2 - \Delta_R\delta x_1 + \Delta_L\delta x_0, \tag{5.41}$$
$$\dot{\delta v_0} = -\epsilon^2\delta x_0 - \kappa\delta xv + \Delta_R\delta v_1 - \Delta_L\delta v_0 - \epsilon^2\langle P_0\rangle\langle P_0\rangle, \tag{5.42}$$
$$\dot{\delta v_1} = -\epsilon^2\delta x_1 + \kappa\delta xv - \Delta_R\delta v_1 + \Delta_L\delta v_0 + \epsilon^2\langle P_0\rangle\langle P_1\rangle, \tag{5.43}$$

where we have defined, for example, $\delta x^2 = \langle x^2\rangle - \langle x\rangle^2$ and $\delta x_0 = \langle x_0\rangle - \langle x\rangle\langle P_0\rangle$, with $\langle x_0\rangle = \int\int dxdvP_0x$. These have the steady state values [110],

$$\delta xv = \delta v_1 = \delta v_0 = 0, \tag{5.44}$$
$$\delta x_1 = -\delta x_0 = \langle P_1\rangle\langle P_0\rangle, \tag{5.45}$$
$$\delta x^2 = \frac{\langle P_1\rangle\langle P_0\rangle}{\kappa}, \tag{5.46}$$
$$\delta v^2 = \epsilon^2(1-\kappa)\delta x^2. \tag{5.47}$$

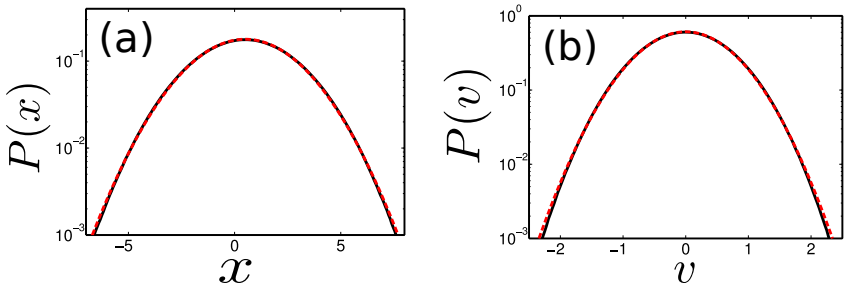

Figure 5.3.: Distribution of the position and velocity of the resonator x and v in the steady state for weak electro-mechanical coupling $\kappa = 0.05$. The solid black lines are the numerical results, the dashed red lines show the Gaussian approximation calculated using the analytic results for the mean and variance discussed in the main text.

We can then compare these results with those of a harmonic oscillator in contact with a thermal bath, where it can be shown that the system obeys equipartition of energy with $\delta v^2 = \omega^2 \delta x^2$ [72]. This is also true for these results with the frequency given by the renormalised oscillator frequency $\omega_{\text{eff}} = \epsilon\sqrt{1-\kappa}$, which is valid in the limit $\epsilon \ll 1$. This then lets us identify the effective temperature of the SET as,

$$T_{\text{eff}} = \frac{\omega_{\text{eff}}^2 \langle P_1 \rangle \langle P_0 \rangle}{\kappa}. \tag{5.48}$$

We can use these results to fully describe the distribution of the position and velocity of the resonator, assuming it is Gaussian, and compare them to the numerical results. The distribution of both the position and velocity are shown in Fig. 5.3, we see that, to a very good approximation, over three orders of magnitude the numerical results coincide with those predicted by the above expressions.

The probability distribution function for the resonator is, to a very good approximation, thermal at low coupling strengths [110, 113]. We can understand this result by considering the *central limit theorem*. Although the electron tunnelling events are not Gaussian (for a tunnel junction the distribution is Poissonian), in the weak coupling limit a large number of (independent) events are needed to have an appreciable effect on the resonator. We find, from the central limit theorem, that the distribution of a large number of events is Gaussian independent of the distribution of the individual events. This gives rise to the observed thermal properties of the resonator when it is weakly in contact with the SET. In the limit of large κ this picture breaks down. Each electron tunnel event has a significant effect on the dynamics, and so the central limit theorem no longer applies. This effect is examined in detail in Refs. [112, 114, 113], and we do not discuss it further here.

5.2.2 *Driven Dynamics*

We now examine the effects of including an external driving force. We will concentrate on the case of a periodic applied drive, with drive strength f_0 and frequency ω_D,

$$f(t) = f_0 \sin \omega_D t. \tag{5.49}$$

The presence of the drive means that the first moments of the distribution do not have a stationary solution, but in the long time limit they must oscillate at the same frequency as the drive. Therefore, so we make the following ansatz for the fluctuating part of the position,

$$\delta x = C e^{-i\omega_D t} + C^* e^{i\omega_D t}, \tag{5.50}$$

where we have again defined $\delta x = x - \langle x \rangle_{ss}$ with $\langle x \rangle_{ss}$ the steady state undriven solution from Eqn. (5.29). This is still the relevant quantity since the force has zero average, $\int f(t)\, dt = 0$, when the integral is over a complete period. This gives rise to the equations for the shifted quantities,

$$\delta \dot{x} = \delta v, \quad \delta \dot{v} = \epsilon^2(\delta P - \delta x) + f(t), \quad \delta \dot{P} = \kappa \delta x - \delta P. \tag{5.51}$$

We are able to substitute the ansatz, Eqn. (5.50), into the expression for $\delta \dot{P}$, and find that in Fourier space this becomes,

$$\delta P(\omega) = \kappa \left[C \frac{\delta(\omega + \omega_D)}{1 + i\omega} + C^* \frac{\delta(\omega - \omega_D)}{1 - i\omega} \right], \tag{5.52}$$

which can be converted back to the time domain to find,

$$\delta P(t) = \frac{\kappa}{1 + \omega_D^2} (\delta x - \delta v). \tag{5.53}$$

This allows us to write an expression for $\delta \dot{v}$,

$$\delta \dot{v} = -\epsilon^2 \left(1 - \frac{\kappa}{1 + \omega_D^2} \right) \delta x - \frac{\epsilon^2 \kappa}{1 + \omega_D^2} \delta v + f(t), \tag{5.54}$$

which is exactly the equation of a driven harmonic oscillator with renormalised frequency and damping due to the SET. These are given by,

$$\omega_{\text{eff}}^2 = \epsilon^2 \left(1 - \frac{\kappa}{1 + \omega_D^2} \right), \qquad \gamma_{\text{eff}} = \frac{\epsilon^2 \kappa}{1 + \omega_D^2}. \tag{5.55}$$

These results are very similar to those in the undriven case, Eqn. (5.33), but now it is the frequency of the drive which enters these expressions in place of the natural frequency of the oscillator.

We can exactly solve the effective equation of motion for the damped, driven, harmonic oscillator,

$$\delta \ddot{x} + \gamma_{\text{eff}} \delta \dot{x} + \omega_{\text{eff}}^2 \delta x = f(t), \tag{5.56}$$

which allows us to find the coefficients from our ansatz, Eqn. (5.50),

$$C = \frac{if_0(\omega_{\text{eff}}^2 - \omega_D^2) - f_0\gamma_{\text{eff}}\omega_D}{2(\omega_{\text{eff}}^2 - \omega_D^2)^2 + 2\gamma_{\text{eff}}^2\omega_D^2}. \tag{5.57}$$

We can check this result by looking at the response of the system to an applied drive. In Fig. 5.4 we plot the amplitude of the position oscillation of the resonator,

$$A_x = 2|C|, \tag{5.58}$$

to various drive frequencies, for parameters such that the response is always linear, $\kappa = 0.05$, $\epsilon = 0.3$, $f_0 = 0.01$. The horizontal, red line shows the critical amplitude, A_c, above which the system starts to go non-linear. At charge degeneracy, this can be written simply in terms of the distance between the points where the tunnel rates become non-linear,

$$A_c = \frac{x_{\text{max}} - x_{\text{min}}}{2} = \frac{1}{2\kappa}. \tag{5.59}$$

For the coupling strength used in the figure, this means that the linear theory is valid for $A_x < 10$. As can be seen in Fig. 5.4 the response of the system to this drive strength is always much less than the critical amplitude, and so the linear theory matches the numerical results. We see that the response is a Lorentzian, centred around the renormalised frequency of the oscillator (the ω_D dependence of ω_{eff} and γ_{eff} is negligible), this is the expected result for a linear harmonic oscillator.

If we look at the behaviour of the second moments, we find that the system shows slightly different behaviour to thermal harmonic oscillator. In a truly thermal environment, there is no dependence of the temperature on the co-ordinates of the oscillator. For the SET-resonator this is no longer the case, as we explain below.

To analyse the effective temperature of the system, we need to examine the variance of the position and velocity distribution, as we did for the undriven system. We can obtain a set of ODEs for the second moments using the same techniques as before, finding exactly the same set of equations as (5.37)-(5.43). Although the equations are the same, the results are slightly different: the term $\langle P_0\rangle\langle P_1\rangle$ in these equations oscillates due to the drive at frequency $2\omega_D$[1] even in the steady state. This produces oscillations in the variances of the position and momentum of the resonator: the behaviour is like a thermal environment with a position dependent temperature.

An example of the full position distribution over one period of the drive is shown in Fig. 5.5 (a). The mean is well described by the linear analytic result from Eqn. (5.50). The oscillations in the variance occur

1 At charge degeneracy we find $\langle P_1\rangle = 1/2 + A\sin(\omega_D t + \phi)$ so $\langle P_0\rangle\langle P_1\rangle = 1/4 + A^2\sin^2(\omega_D t + \phi)$, away from charge degeneracy there are also oscillations at ω_D.

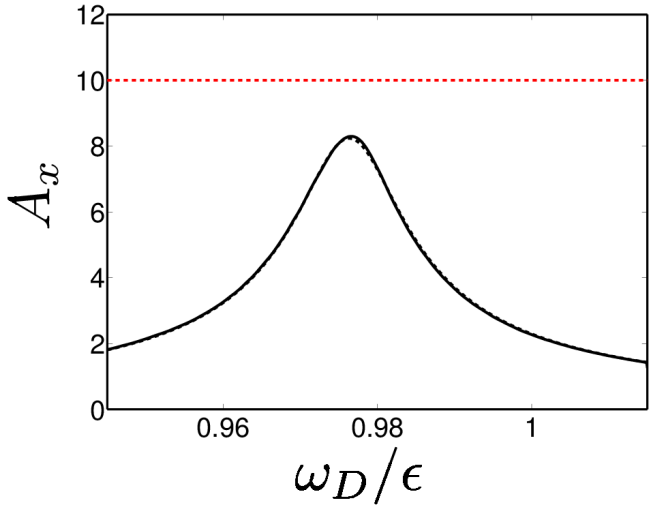

Figure 5.4.: Amplitude of the position oscillations, A_x, as a function of drive frequency, ω_D. The solid, black line is the numerical result, the dashed, black line the analytic result from Eqn. (5.58). The red, dashed line shows the limit above which the linear theory does not hold (see text). The parameters used are $f_0 = 0.01$, $\epsilon = 0.3$, $\kappa = 0.05$.

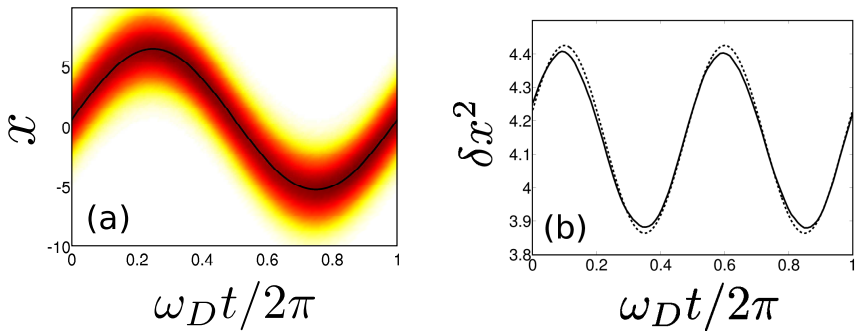

Figure 5.5.: Oscillations in both the mean and variance of the position distribution over a period of the drive. The parameters are $\epsilon = 0.3$, $\kappa = 0.05$, $f_0 = 0.05$ and $\omega_D = 0.002\pi$. In (a) we show the full position distribution, the solid, black line shows the analytic solution for the mean. In (b) we show the variance, the solid line is the numerical result, the dashed line shows the solution to Eqns. (5.37)-(5.43).

because of the oscillations in $\langle P_0 \rangle \langle P_1 \rangle$, as described above. This can be thought of as a change in the effective temperature of the bath at each point in the cycle since $T_{\text{eff}} \propto \langle P_0 \rangle \langle P_1 \rangle$ as in Eqn. (5.48). These oscillations cannot be seen if the drive is faster than the relaxation. We require $\omega_D \ll \gamma_{\text{eff}}$, since, if the drive is too fast, then the oscillator simply feels the average of the temperature over a single period. It is not able to respond quickly enough to changes in its environment. In Fig. 5.5, we have $\omega_D/\gamma_{\text{eff}} \sim 1.39$, and so the oscillations are visible, but they are not as large as the variation in temperature which the oscillator feels throughout the cycle. It is not practical to simulate the dynamics in the regime where the oscillator is driven slowly enough such that it is always in thermal equilibrium; for weak coupling, γ_{eff} is very small. However, we are able to examine this regime by solving the set of coupled ODEs (Eqns. (5.37)-(5.43)), which, as we can see from Fig. 5.5 (b), give a good approximation to the numerical results. In Fig. 5.6, we plot the variance over a single period for drive frequencies $\omega_D/2\pi = 0.01$ (black), $\omega_D/2\pi = 0.001$ (blue), and $\omega_D/2\pi = 0.0001$ (green), along with the variances corresponding to the maximum and minimum temperatures (red, dashed lines) experienced by the oscillator during the cycle. The damping rate $\gamma_{\text{eff}} = 0.0009$ and so the green curve satisfies the condition $\omega_D \ll \gamma_{\text{eff}}$, and so we see the variance oscillates between the extremes of temperature experienced during the cycle. In this case, the oscillator is in the *adiabatic limit*, the oscillations are slow enough that the system is always in equilibrium with an effective bath, whose temperature varies sinusoidally as $\langle P_0 \rangle \langle P_1 \rangle$.

5.3 BEYOND LINEAR RESPONSE

It is possible, by increasing the drive strength slightly, to drive the resonator into regions where the linear theory breaks down. If any part of the trajectory enters the region where tunnelling in the SET is forbidden, then the dynamics can become much more complicated. In this section we will examine the response of the oscillator to a stronger drive, and develop ways of analytically describing the dynamics.

5.3.1 *Non-linear damping and frequency shift*

Increasing the drive strength above that used in Fig. 5.4 means that the simple linear expressions for damping and frequency shift in Eqn. (5.55) are no longer valid. When the system is outside of the linear response region, the effective damping and frequency shift of the oscillator will be modified. The simplest way to calculate such a modification is to calculate the fraction of time that the oscillator spends in the region where $x_{\text{min}} < x < x_{\text{max}}$ and modify the effective cou-

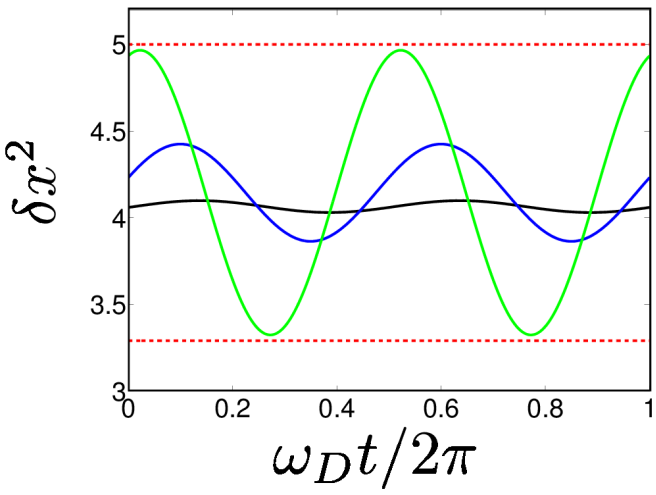

Figure 5.6.: Oscillations of the variance of the position distribution over one period of the drive for different drive frequencies. The black curve is $\omega_D = 0.02\pi$, the blue is $\omega_D = 0.002\pi$ and the green is $\omega_D = 0.0002\pi$. The red, dashed lines show the variance which corresponds to the maximum and minimum temperature experienced during the cycle.

pling strength by this factor. This method is inspired by the approach in Ref. [113], used to calculate the renormalised frequency at strong coupling strengths.

To make progress, we first assume that the position of the oscillator is harmonic, and oscillates at the frequency of the drive (we ignore the phase difference between the position and the drive since it does not feature in what follows),

$$\delta x(t) = A_x \sin(\omega_D t). \tag{5.60}$$

Outside the linear region, when one of the Heaviside functions in the decay rates is important, transport through the SET stops [112, 114]. This means that the oscillator effectively becomes decoupled from its environment, and so is not damped or frequency shifted by the SET in the parts of its trajectory outside of the linear boundary. This leads us to introduce the amplitude dependent effective coupling,

$$\kappa_A = \frac{\omega_D \kappa}{2\pi} \int_0^{\frac{2\pi}{\omega_D}} \Theta\left(\Delta_L + \kappa x(t)\right) \Theta\left(\Delta_R - \kappa x(t)\right)\right) \, dt, \tag{5.61}$$

where $x(t) = \delta x(t) + \langle x \rangle_{ss}$. This expression renormalises the linear coupling strength by the fraction of the drive period which the mean spends in the damped region. We can find the result of the integral at charge degeneracy as,

$$\kappa_A = \begin{cases} \kappa & A_x < \frac{1}{2\kappa} \\ \frac{2\kappa}{\pi} \sin^{-1}\left(\frac{1}{2\kappa A_x}\right) & A_x \geq \frac{1}{2\kappa} \end{cases}. \tag{5.62}$$

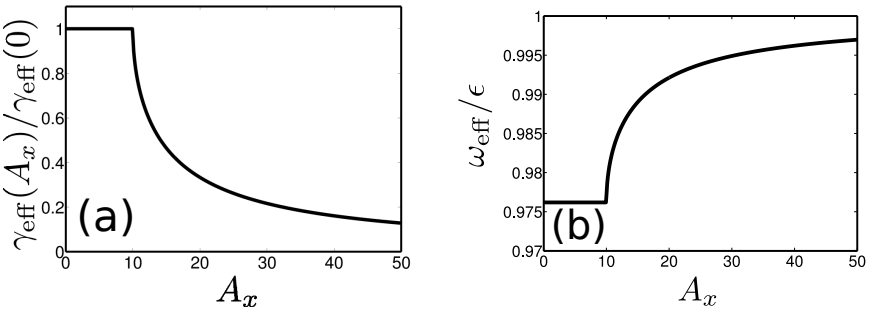

Figure 5.7.: Amplitude dependent (a) damping and (b) frequency of the oscillator using the simple model of Eqn. (5.63). Parameters are $\epsilon = 0.3$, $\kappa = 0.05$ and $\omega_D = 0.29$.

This expression can be then be used to find approximate, amplitude dependent, expressions for the damping and frequency shift,

$$\omega_{\rm eff}^2(A_x) = \epsilon^2\left(1 - \frac{\kappa_A}{1+\omega_D^2}\right), \qquad \gamma_{\rm eff}(A_x) = \frac{\epsilon^2\kappa_A}{1+\omega_D^2}. \tag{5.63}$$

Examples of these functions are shown in Fig. 5.7. In the region where the amplitude is still in the linear region, $A_x < A_c$, the damping and frequency shift remain at their linear values. Above A_c we see the damping decrease towards zero and the frequency move towards ϵ. In the limit $A_x \to \infty$, the system spends less and less time inside the damped region. This limit is, of course, not experimentally relevant, since when the back-action damping becomes too small, $\gamma_{\rm eff} < \gamma_{\rm ext}$, the dynamics become dominated by the external damping provided by the true thermal environment.

The oscillations will only be stable when they occur at certain values of A_x. To predict these values, we need to derive an equation of motion for A_x [47]. This is given by,

$$\dot{A}_x = \frac{1}{A_x}\left[(x - \langle x\rangle_{\rm ss})\dot{x} + \frac{v\dot{v}}{\omega_D^2}\right]. \tag{5.64}$$

We can derive the terms on the right hand side of Eqn. (5.64) by using the fact that the resonator position obeys the effective equation,

$$\ddot{x} + \gamma_{\rm eff}(A_x)\dot{x} + \omega_{\rm eff}^2(A_x)x^2 = f_0 \sin\omega_D t, \tag{5.65}$$

where the amplitude dependent damping and frequency are calculated from Eqn. (5.63). This can be solved using the same ansatz, Eqn. (5.50), as for the linear case, but now $C(A_x)$ is a function of amplitude. To make progress with Eqn. (5.64), we need to make some simplifying assumptions. If we assume that the dynamics of A_x are *slow* on the timescale of the force (we will verify these conditions self-consistently later), we can introduce the quantity [47],

$$\tilde{A}_x = \frac{\omega_D}{2\pi}\int_0^{\frac{2\pi}{\omega_D}} A_x\, dt, \tag{5.66}$$

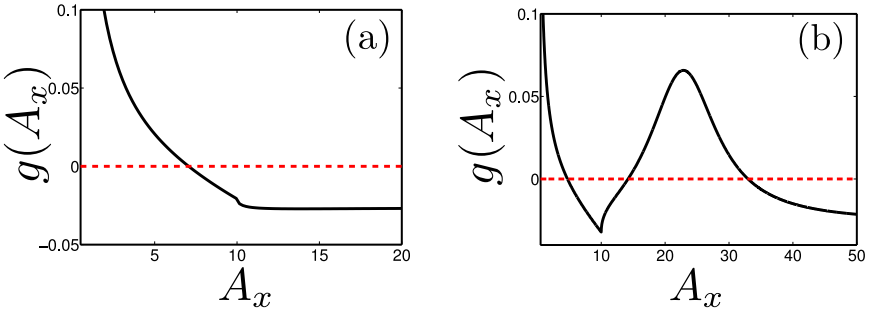

Figure 5.8.: Self-consistency condition for $f_0 = 0.015$, $\epsilon = 0.3$, $\kappa = 0.05$, for two different drive frequencies (a) $\omega_D = 0.29$: we see only one crossing in the linear region, (b) $\omega_D = 0.298$: there are three solutions, one in the linear region, one unstable and one high amplitude stable solution. The solid, black lines show $g(A_x)$ from Eqn. (5.69), while the dashed, red lines are constant at 0, to make the crossing points apparent.

which has the equation of motion,

$$\frac{d\tilde{A}_x}{dt} = -\frac{\gamma_{\text{eff}}(\tilde{A}_x)\tilde{A}_x}{2} - \frac{f_0 \text{Re}[C(\tilde{A}_x)]}{\omega_D \tilde{A}_x}. \tag{5.67}$$

We then find $C(\tilde{A}_x)$ from the solutions to Eqn. (5.65) and obtain the simplified evolution equation,

$$\frac{d\tilde{A}_x}{dt} = g(\tilde{A}_x), \tag{5.68}$$

where,

$$g(A) = -\frac{\gamma_{\text{eff}}(A)}{2}\left[A - \frac{f_0^2}{A\left[(\omega_{\text{eff}}^2(A) - \omega_D^2)^2 + \gamma_{\text{eff}}^2(A)\omega_D^2\right]}\right]. \tag{5.69}$$

The slow dynamics condition above is then equivalent to $|g(A)| \ll \omega_D A$, which is automatically satisfied close to a fixed point, and for a fast enough driving force.

For the oscillations at a given amplitude, A_x, to be stable, there are two conditions which must be met. Firstly, we require that the amplitude corresponds to a fixed point, i.e. $g(A_{\text{fp}}) = 0$. Secondly, we require that amplitudes in the vicinity of these fixed points decay to the fixed point solution. This is equivalent to the condition [119, 47],

$$\left.\frac{dg}{dA_x}\right|_{A_x = A_{\text{fp}}} < 0. \tag{5.70}$$

From Eqn. (5.69), we find that the possible stable amplitudes are given by[2],

$$A_x = \frac{f_0}{\sqrt{(\omega_{\text{eff}}^2(A_x) - \omega_D^2)^2 + \gamma_{\text{eff}}^2(A_x)\omega_D^2}}. \tag{5.71}$$

This equation can have either 1 or 3 solutions depending on the choice of parameters, examples of both cases are shown in Fig. 5.8. The stability of these solutions can be deduced from the gradient of the black curves at the crossing point as described above. We see that, in the case with only one crossing point, the system is in the linear regime, and the stable solution is simply the linear one. In the case with three crossing points, the central one gives an unstable solution, the small amplitude result is in the linear region and the large amplitude solution is a new stable fixed point for the system, where the damping and frequency shift are reduced from the linear values. This behaviour, where the system has multiple stable solutions with different amplitudes, is found in many other driven non-linear systems, such as the Duffing oscillator [119]. The Duffing oscillator can be seen as a harmonic oscillator with a position dependent spring constant,

$$k(x) = k_0 + \alpha x^2. \tag{5.72}$$

In this system, at large enough drive strength, there are regions where two stable amplitude solutions exist [119]. The non-linearity we find, although similar to that of the Duffing oscillator, is different in detail. In particular, for a Duffing oscillator, one finds a quadratic amplitude dependence of the resonant frequency, which is very different from the form found in Fig. 5.7, for the SET-resonator.

We can use the non-linear damping and frequency shift, along with the conditions on stability of the solutions to Eqn. (5.71), to find the response of the system, A_x, as a function of drive frequency. An example of the resulting curve can be seen in Fig. 5.9. At low frequencies, below the blue shaded region and at frequencies $\omega_D > \epsilon$, the non-linear results exactly match the linear theory. The response is below A_c, and Eqn. (5.71) has only one stable solution; therefore there are no modifications to the linear results.

In the blue shaded region, (a), in Fig. 5.9, the amplitudes grow beyond A_c, and so the linear and non-linear calculations give different results. The linear calculation leads to a Lorentzian peak centred around $\omega_{\text{eff}}(0)$. However, in the non-linear case, the frequency shift becomes smaller (leading to a larger effective frequency) for $A_x > A_c$. In the blue shaded region, this means that the drive frequency is further from resonance than in the linear case, and hence the amplitude is smaller.

2 In the limit $A \to \infty$, we find $\gamma_{\text{eff}}(A) \to 0$, but this only decays as $1/A$ and so $\gamma_{\text{eff}}(A)A$ is still finite.

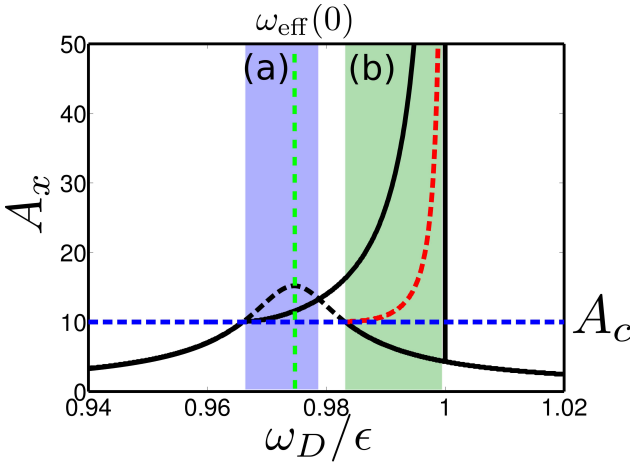

Figure 5.9.: The solutions to the self-consistency expression, Eqn. (5.71), as a function of drive frequency, for $f_0 = 0.02$, $\epsilon = 0.3$ and $\kappa = 0.05$. The black solid lines show the stable solutions, the red dashed line is the unstable solution. We also show the linear result as the black dashed line, the amplitude at which the linear theory fails, A_c, as the horizontal blue dashed line, and the linear response frequency, $\omega_{\text{eff}}(0)$, as the vertical dashed green line. The shaded regions (a) and (b) are discussed in the text.

In the green shaded region, (b), for drive frequencies close to (but below) ϵ, a high amplitude solution exists because of a positive feedback mechanism. In this regime, as the amplitude grows beyond A_c, the reduction in the effective frequency brings the system closer to resonance with the drive. Hence, increasing the amplitude further (an effect which is further enhanced by the reduction in γ_{eff} with increasing A_x) causes the system to eventually stabilise. This is because, when the amplitude and $\omega_{\text{eff}}(A_x)$ become sufficiently large the system moves significantly away from resonance.

When the drive frequency becomes larger than ϵ, the high amplitude solution no longer exists. If the damping and frequency shift were not amplitude dependent the system would simply oscillate at a slightly lower A_x, due to being more detuned from resonance. In fact, as this happens the effective frequency shifts further away (ω_{eff} decreases with decreasing amplitude), reducing the amplitude of the oscillations further: the system spirals back down to the linear branch.

We can better understand this behaviour by introducing an effective potential landscape for the system. We define the potential from the equation of motion for A_x, Eqn. (5.68),

$$U(A_x) = -\int_0^{A_x} g(a)\, da. \tag{5.73}$$

This potential then, naturally, has a gradient of zero at the solutions to the self-consistency expression, Eqn. (5.71), the stable fixed points correspond to minima in this potential. We note that the potential has

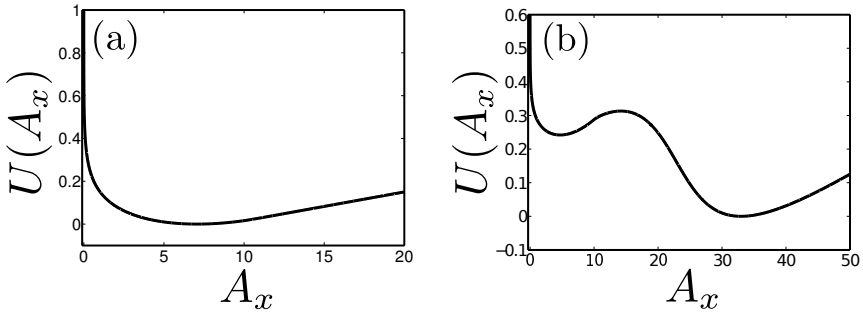

Figure 5.10.: Examples of the potential landscape, calculated from Eqn. (5.73). The parameters are the same as those in Fig. 5.8

a divergence at $A_x = 0$, as can be seen from the second term in Eqn. (5.69), because of this we shift the potential by an arbitrary constant, so that the minimum is $U(A_x) = 0$.

Example potential landscapes with one and two minima are shown in Fig. 5.10, these correspond to the same parameters as Fig. 5.8. The unstable solution is located at the maximum between the potential wells of the stable solutions. As we increase ω_D and sweep through the resonance, the large amplitude solution appears as a second minimum, as seen in Fig. 5.10 (b).

We can compare the predicted stable amplitudes to our numerical results for systems which enter the non-linear region. We expect the dynamics to be much more complicated than for the linear case, since the system has two stable solutions with different amplitude oscillations. We show numerical results as the solid blue and green curves in Fig. 5.11. The results for the high amplitude state are qualitatively the same as those calculated above, but there is some quantitative difference because of the simple model we used to calculate the renormalised damping and frequency shift. The green and blue numeric curves differ only in their initial conditions, the results in green show a sweep through frequency from low to high, whereas the blue curve shows a sweep from high to low frequency. The initial conditions for each data point are the final results of the previous one. The direction of sweep has a large effect on the results observed in the region where two solutions are predicted. If the fluctuations about the mean are not large enough to escape the potential well which the system is initially in, then it remains in that state. This means that when we sweep down from large frequencies, the oscillator cannot enter the high amplitude branch until the barrier between the two states becomes small enough. We see that the blue curve jumps to the high amplitude before the low amplitude state ceases to exist. At some point these fluctuations are able to overcome the potential barrier, and the system transitions to the high amplitude state which has a deeper potential well (see Fig. 5.10 (b)), and so the system cannot escape back to the low amplitude state.

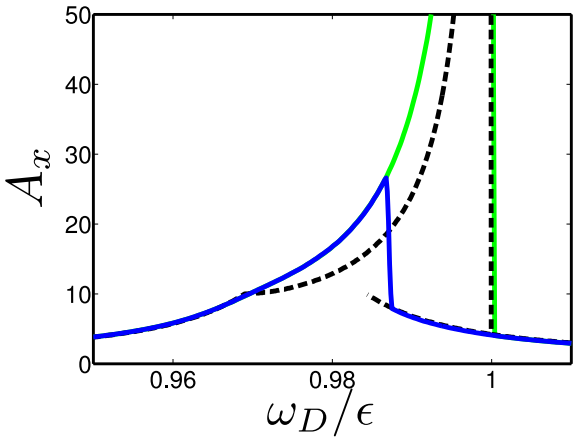

Figure 5.11.: Comparison of the numerical results to those obtained from the self-consistency expression. The solid green and blue lines show the numerical results for forward and backward frequency sweeps respectively. The black, dashed line shows the stable analytic solutions. The parameters are the same as Fig. 5.9.

We can produce a more complex model and obtain a better result for the damping and frequency shift, by following the technique outlined in Refs. [47, 18]. We assume that a constant amplitude solution to the full non-linear expression exists, and use this to map the equations onto that of damped, driven harmonic oscillator. We can then identify the terms which correspond to an amplitude dependent damping and frequency shift.

We begin with the set of coupled equations for the first moments, including the non-linear rates but decoupling the second moments which are present, so that, for example, we assume $\langle x_1 \rangle = \langle x \rangle \langle P_1 \rangle$ [47]. This approximation has been found to give good agreement for the mean dynamics of various systems [120, 47, 121, 93]. We write the equations of motion as,

$$\ddot{x} - \epsilon^2(P - x) = f(t), \tag{5.74}$$

$$\dot{P} = \Gamma_L(x)(1 - P) + \Gamma_R(x)P, \tag{5.75}$$

where we have dropped the angle brackets for compactness and written $P = \langle P_1 \rangle$. We may then numerically solve the expression for $P(t)$, Eqn. (5.75), using the ansatz for $x(t)$ in Eqn. (5.60). We wish to map the equation for $\ddot{x}$ onto that for a damped, driven harmonic oscillator. Making a comparison between Eqn. (5.74) and the driven oscillator equation we identify,

$$-\epsilon^2 P = \gamma_{\text{eff}}\dot{x} + \epsilon^2 \Delta\omega^2_{\text{eff}} x, \tag{5.76}$$

where we have defined the frequency shift,

$$\omega^2_{\text{eff}} = \epsilon^2(1 + \Delta\omega^2_{\text{eff}}). \tag{5.77}$$

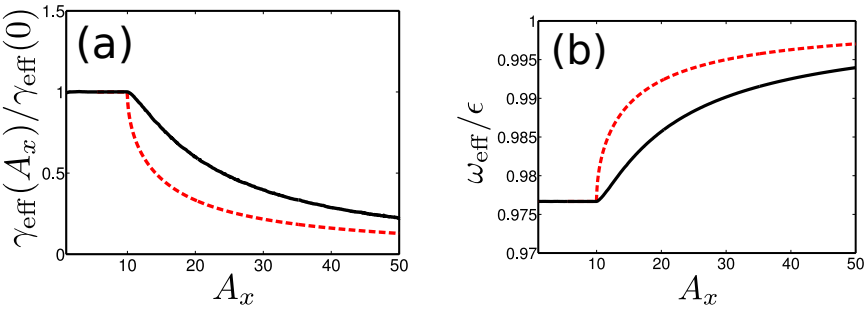

Figure 5.12.: Amplitude dependent (a) damping and (b) frequency of the oscillator. Solid, black lines show the solution using Eqn. (5.78), red, dashed lines show the results using Eqn. (5.63). Parameters as in Fig. 5.7.

We can then multiply Eqn. (5.76) by either $\cos\omega_D t$ or $\sin\omega_D t$, and integrate over one period of the drive to find the damping and frequency shift [46],

$$\gamma_{\rm eff} = -\frac{\epsilon^2}{\pi A}\int_0^{\frac{2\pi}{\omega_D}} P(t)\cos\omega_D t\, dt, \tag{5.78a}$$

$$\omega_{\rm eff}^2 = \epsilon^2\left(1 - \frac{\omega_D}{\pi A}\int_0^{\frac{2\pi}{\omega_D}} P(t)\sin\omega_D t\, dt\right). \tag{5.78b}$$

These expressions then give a simple physical interpretation of the damping and frequency shift, the damping is due to the *out of phase* (with respect to x) component of the average island charge, while the frequency shift is due to the *in phase* component [46, 18].

It is possible to again extract the amplitude dependent damping and frequency shift, which can be used in the self-consistency expression, Eqn. 5.71, to find the amplitude of the stable solutions. In Fig. 5.12, we plot the amplitude dependence of the damping and frequency shift calculated using this method, along with the simple results calculated previously using Eqn. (5.63). We see that the corrected damping and frequency shift is always larger than the simple estimates. This is because the damping does not just switch on and off as the resonator travels through the non-linear boundary, it becomes reduced when the mean is close to $x_{\rm min}$ or $x_{\rm max}$, as some trajectories are in the uncoupled region. Therefore, the previous calculation was always an underestimate.

We can again use this result to compare with our numerical response curve. To simplify the numerics, we neglect the dependence of $\gamma_{\rm eff}$ and $\omega_{\rm eff}$ on ω_D. The results of this calculation are then shown in the dashed, black curve in Fig. 5.13, we see that this now gives very good agreement with the numerics (shown as the green, solid curve). For simplicity, we have only shown the high amplitude stable branch and the numeric sweep from low to high frequency. The amplitude

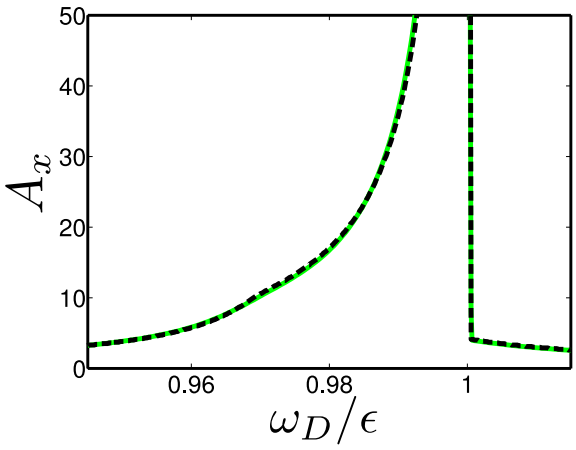

Figure 5.13.: Comparison of the numerical results (solid, green curve) with those obtained using the more complex expressions in Eqn. (5.78) (black, dashed curve). Same parameters as Fig. 5.9.

of the oscillations is greater than that calculated using Eqn. (5.63), since, although the damping felt by the oscillator is larger, so is the frequency shift, this means that the oscillator is closer to resonance and so has a larger response.

5.4 BISTABILITY

In the previous section, we saw how it was possible for the system to end up in a different state depending on the initial conditions used for the numerics, but the stationary state was always either the high or low amplitude solution. For weaker drive, it should be possible to find *bistable behaviour*, where it is possible for fluctuations to drive the system both from the high amplitude state to the linear state and back again. The stationary solution should then contain components of both solutions. This type of behaviour is common to a wide range of damped, driven non-linear systems, such as in the Duffing oscillator [119], the damped, driven Jaynes-Cummings model [120] and an SSET-resonator close to the JQP [46, 47].

In Fig. 5.14, we show the response for a drive strength appropriate for this. In the region where the low amplitude state becomes stable again, the numerical mean amplitude moves to a point between the two stable solutions, and the steady state is a mixture of the two solutions. This can be seen in Fig. 5.15, where we plot the position distribution as we pass through the bistability at the points labelled (a) and (b) in Fig. 5.14. In Fig. 5.15 (a), we see that most of the distribution is in the high amplitude state, with only a very low probability of being in the low state whereas in (b), on the other side of the bistability, most of the distribution is in the low amplitude state.

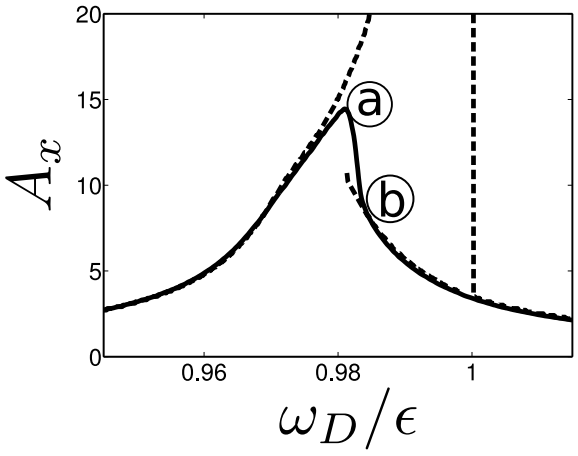

Figure 5.14.: Response of the system as a function of driving frequency, all parameters are the same as in Fig. 5.9, except $f_0 = 0.015$. The solid line shows the numerical response, the dashed line shows the analytically predicted stable solutions using the damping and frequency shift from Eqn. (5.78). The system shows a bistability in the region where the linear solution reappears. The dynamics at the points marked (a) and (b) are shown in Fig. 5.15.

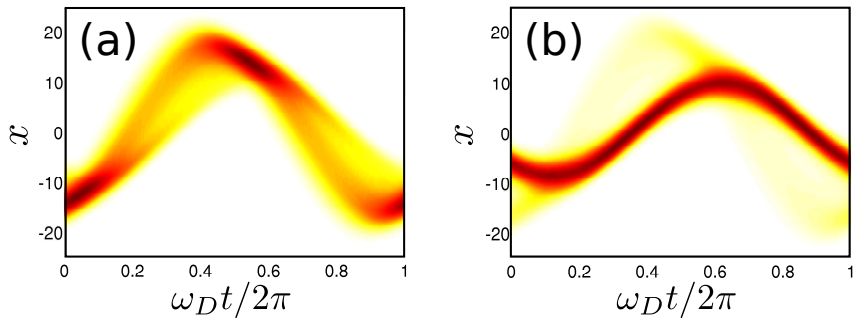

Figure 5.15.: Position distribution of the oscillator at the points labelled (a) and (b) in Fig. 5.14.

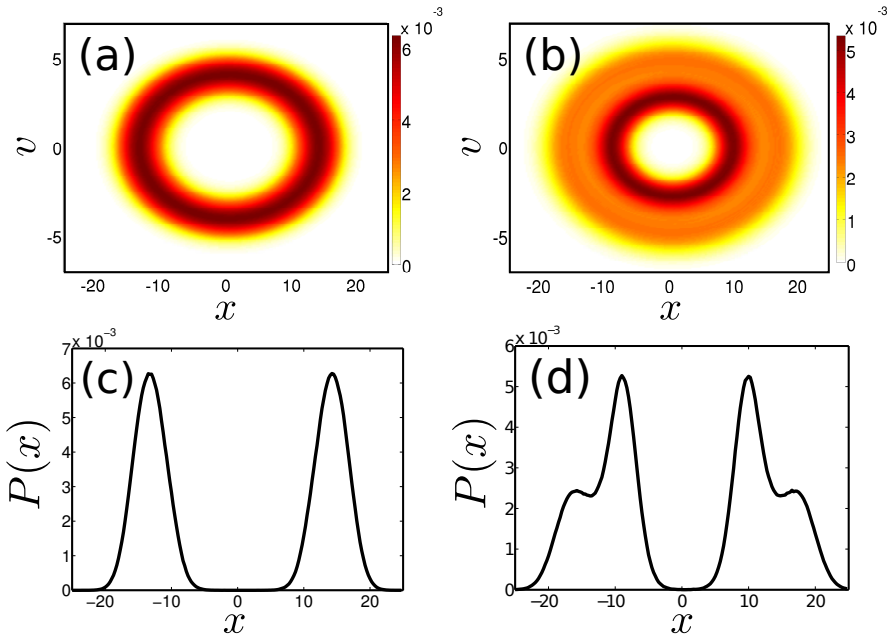

Figure 5.16.: $P(x, v)$ distributions. In (a) and (b) we show the full distribution far away from and at the bistability respectively. In (c) and (d) we show slices through these distributions at $v = 0$.

To check that the two states are indeed distinct, we need to make sure that they do not cross in phase-space [119]. To do this, we look at the probability distribution as a function of both the position and velocity of the resonator. This is shown in Fig. 5.16 (a) and (b), where we show results away from the bistability and in the bistable region. Both plots show rings in phase space, which means that the resonator oscillates in its steady state [46, 47]. Away from the bistability there is only one ring, which shows only one stable amplitude oscillation, while at the bistability we can see two rings; the system really does have two distinct stable orbits. To make this more apparent, in Fig. 5.16 (c) and (d) we show slices through the phase-space distribution at $v = 0$. We clearly see a double peaked structure in the bistable plot which is absent in the case where only one stable solution is present.

The two orbits at the bistability are linked by *noise*, the edges of the distributions around the rings overlap. The system is able to switch between the two states when fluctuations drive the high amplitude state to a lower orbit or vice-versa. This then leads to the steady state containing both stable solutions as seen in Fig. 5.15. If the amplitude of the two states is well separated, this cannot happen. For example, when the drive is larger, the fluctuations cannot take the system far enough towards the other state to get over the potential barrier. As a result, the system stays in one or the other of the states, depending on the choice of initial conditions.

The variance of the distribution is also a useful way of identifying the bistability. We show results for the variance of the x distribution,

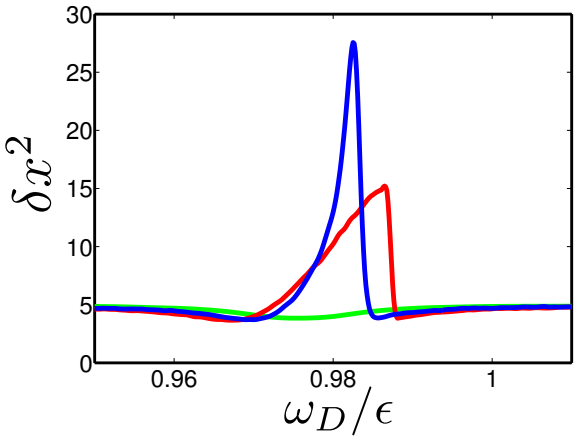

Figure 5.17.: Variance of the x distribution δx^2, averaged over one period of the drive for various drive strengths, the green curve is $f_0 = 0.01$ (linear), the blue curve is $f_0 = 0.015$ (bistable) and the red curve is $f_0 = 0.02$ (non-linear).

averaged over one period of the drive, for various drive strengths, in Fig. 5.17. The linear results, the green curve, show that the variance in this region is approximately constant, with a shallow dip near to the resonance. This dip occurs because the average temperature felt by the oscillator drops slightly when the amplitude of the oscillations increases, this decreases the variance. We also show an example of the variance in the high amplitude state as a red curve, this corresponds to the blue curve in Fig. 5.11 (the sweep from high to low frequency), in this case the variance increases away from the linear result. This can be understood by thinking about two trajectories which exit the linear boundary a small distance apart. As they are accelerated, deterministically, by the drive away from the damped region, the separation between the trajectories increases. This causes the variance to increase with the amplitude of the oscillations. The red curve in Fig. 5.17 shows the variance for the bistable system. We see a much larger peak coinciding with the region of the bistability, the two solutions with different amplitudes cause the variance to sharply increase.

5.5 THERMODYNAMICS

Much recent attention has focused on studying the thermodynamic properties of small systems [122, 123, 124, 117, 30]. As systems are made smaller, fluctuations become more important, and so events which apparently violate the second law of thermodynamics can become possible [30]. Questions about the distribution of thermodynamic variables of small systems are addressed by fluctuation relations [31, 32]. These relations are able to give detailed information about the properties of the distribution of thermodynamic quantites, such as the work done and heat transferrred in out-of-equilibrium

processes [117, 30]. These kinds of relations have very recently been used to examine the thermodynamics of transport in mesoscopic devices [33, 34, 35].

One simple way in which we can look at this type of behaviour, in the driven SET-resonator, is to examine the work done by the external force [117, 30]. The work done over a period, $\tau_n = 2\pi n/\omega_D$, corresponding to n periods of the driving force is given by,

$$W_n = \frac{1}{\tau_n}\int_{t_0}^{t_0+\tau_n} f(t)v(t)\,dt. \tag{5.79}$$

For macroscopic systems the work is a well defined quantity which only has one possible, positive, outcome. However, since the trajectory of the oscillator is stochastic, if we integrate over a finite time, then the work done can take on many different values and so has a *distribution*. In particular, if the drive strength is small enough, it is possible for the work done to be *negative*, apparently violating the second law of thermodynamics [30]. This effect has been observed in oscillators coupled to true thermal baths [124, 117, 30]. For the thermal case, many exact results about this distribution exist, we will discuss these in detail later. The work distribution provides another way in which we can look at how far the analogy between the SET and a thermal bath goes.

We begin by looking at the behaviour of the system in the linear regime. In this case, we expect that the distribution should be exactly Gaussian, as it is for a thermal environment [117, 30]. It is also straightforward to calculate the mean work done for the linear system. This is simply given by,

$$\langle W_n\rangle = \frac{1}{\tau_n}\int_0^{\tau_n} f(t)\langle v(t)\rangle\,dt. \tag{5.80}$$

Since we know $\langle v(t)\rangle$ from the time derivative of the linear ansatz, Eqn. (5.60), we find,

$$\langle W_n\rangle = \frac{f_0^2\omega_D^2\gamma_{\text{eff}}}{2(\omega_{\text{eff}}^2-\omega_D^2)^2+2\gamma_{\text{eff}}^2\omega_D^2}, \tag{5.81}$$

which is independent of integration time and, as required by the second law, always positive.

The stochastic nature of the dynamics then leads to fluctuations about this value. We show results for the work distribution, $P(W_n)$, for parameters in the linear region in Fig. 5.18, where we have used the same parameters as Fig. 5.4 and an approximately resonant drive frequency. The integration times used are $n = 1, 20, 50$. We see all of the features described above, the work distribution has a positive mean value which does not change with n, but the distribution gets narrower as the integration time increases. As n increases, the stochastic nature of the dynamics gets averaged out, suppressing the negative fluctuations in the work. This is the same behaviour as has been observed in a thermal harmonic oscillator [124, 117].

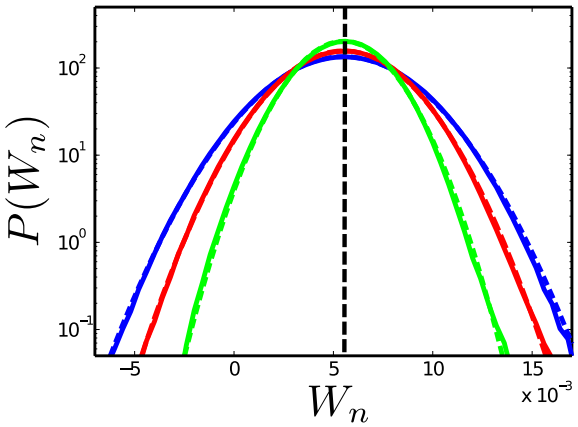

Figure 5.18.: Work distributions for $n = 1$ (blue), $n = 20$ (red) and $n = 50$ (green). The parameters used are the same as in Fig. 5.4, and the drive frequency is approximately resonant, $\omega_D/\epsilon = 0.98$. The coloured, dashed lines show Gaussian fits to the data. The vertical, black, dashed line shows $\langle W_n \rangle$ as calculated from Eqn. (5.81).

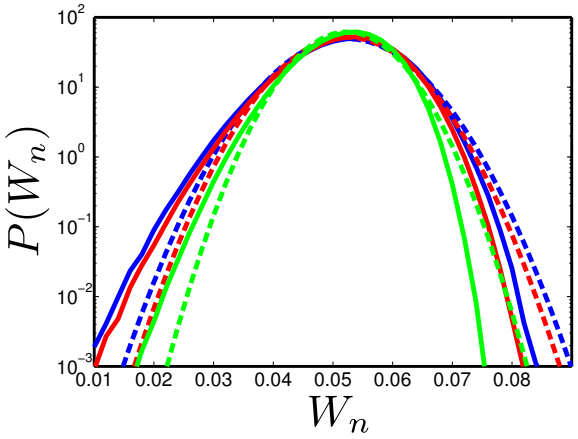

Figure 5.19.: Work distributions for $n = 1$ (blue), $n = 20$ (red) and $n = 50$ (green). The parameters used are the same as in Fig. 5.9, and the drive frequency, $\omega_D/\epsilon = 0.985$, and initial conditions were chosen so that the system is in the high amplitude state. The dashed lines show Gaussian fits to the data.

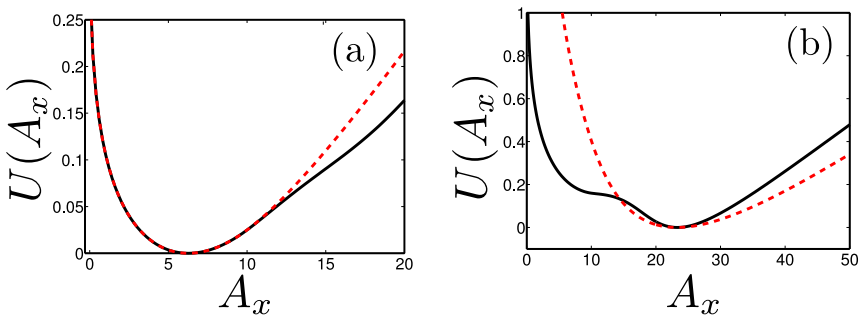

Figure 5.20.: Potential landscapes which correspond to (a) Fig. 5.18 and (b) 5.19. The black lines show the potential, while the red, dashed lines show the effective linear potentials.

If we look at a system which is oscillating in the high amplitude state, we find that the distribution looks slightly different. An example of this is shown in Fig. 5.19, where we see that the average work is much larger than for the linear case, because of the larger amplitude oscillations. We also see that the distribution is no longer Gaussian, trajectories with lower values of work occur more often than for a Gaussian distribution, whereas trajectories with larger values of work occur less often. To understand this, it is useful to look at the potential landscapes which correspond to Figs. 5.18 and 5.19. These potentials are plotted in Fig. 5.20, along with the potential for a linear system, with the value for γ_{eff} and ω_{eff} calculated at the stable amplitude. We note that these potentials are calculated using the more complex expressions for γ_{eff} and ω_{eff} from Eqn. (5.78). In the linear case, the potential follows the linear result at $A_x < A_c$, as expected, and since we know that the system does not fluctuate above this point, the behaviour is exactly linear and so has Gaussian fluctuations [117, 30]. For the non-linear potential, we see that the potential is not well approximated by the linear result, because of the amplitude dependence of γ_{eff} and ω_{eff}. The fluctuations in amplitude are larger than in the linear case, which can be seen in Fig. 5.17; the system has trajectories which reach into the shoulder in the potential in the linear region. This causes the non-Gaussian behaviour seen in the work distributions in Fig. 5.19.

We can also look at the work distribution around the bistability. Distributions for various values of n are shown in Fig. 5.21, where we can clearly see that the two different stable states give separate peaks in the distribution. As the integration time is increased, we see that the width of both subdistributions decreases. This is because we are examining the system on timescales much lower than the *switching time* of the system, where the switching time is the average time the system takes to get between to two stable states.

We can examine this switching time by integrating the system over longer periods. We expect that if the integral goes over a long enough

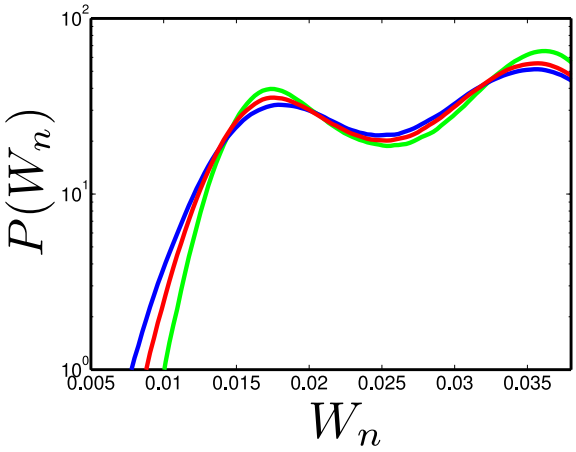

Figure 5.21.: Work distributions for $n = 1$ (blue), $n = 20$ (red) and $n = 50$ (green). The parameters used are the same as in Fig. 5.14 and the drive frequency chosen such that the system is bistable.

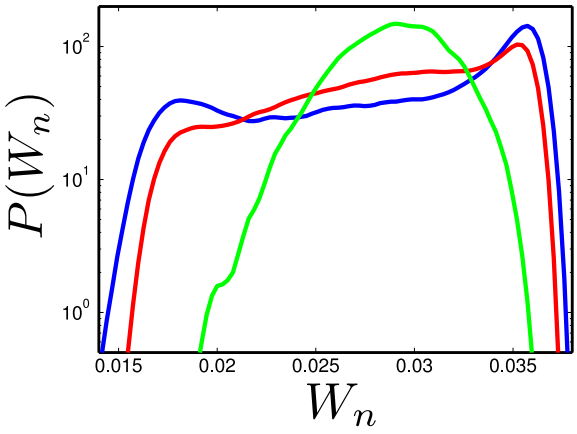

Figure 5.22.: Work distributions for long integrations in the bistable region. Same parameters as Fig. 5.21, but with $n = 500$ (blue), $n = 1000$ (red) and $n = 5000$ (green).

period the distribution should become unimodal. In the long time limit, all of the trajectories spend some time in both of the stable states. We can see this happening in Fig. 5.22. We note that obtaining good statistics for such long trajectories is difficult, and so these results have much less averaging than those presented previously. We see that, when we integrate over 500 periods, the distributions is still bimodal, the curve for $n = 1000$ shows the central part of the distribution becoming a peak. Finally, for 5000 periods, the distribution becomes unimodal, on this timescale most of the trajectories are able to explore enough phase-space to spend time in both stable states.

5.5.1 *Fluctuation relations*

Results have recently become available [31, 32] which are able to quantify the probability of observing rare events in small systems, such as fluctuations in the work done which lead to a negative value of W_n. These results give rise to *fluctuation relations* (see Ref. [30] for a review), which relate the relative probabilities of positive and negative energy fluctuations. To describe these fluctuation relations we introduce the *symmetry function* for the thermodynamic quantity X_n [30],

$$S(X_n) = \ln\left(\frac{P(+X_n)}{P(-X_n)}\right), \tag{5.82}$$

which relates the relative probabilities of trajectories with $X = X_n$, to those with $X = -X_n$. There are then two forms that the fluctuation relations can take. Firstly, the *transient* fluctuation relation describes systems which have been perturbed from their equilibrium state for a finite amount of time [117, 30], in this case the symmetry function obeys,

$$S(X_n) = \frac{X_n}{T}, \tag{5.83}$$

where T is the temperature of the external environment. This relation is valid for all integration times, n. Secondly, there is the *steady state* fluctuation relation, which is obeyed by systems in an out-of-equilibrium steady state, such as in the presence of periodic drive. In this case the fluctuation relation only holds for infinite integration times [30],

$$\lim_{n\to\infty} S(X_n) = \frac{X_n}{T}. \tag{5.84}$$

It is the steady state fluctuation relation which we make use of here.

We are able to test such relations for a limited range of parameters in the SET-resonator. Exact results are available for a harmonic oscillator driven by periodic force in a thermal environment [117, 30], and it is these results with which we make a comparison. To do this, we first introduce a slightly different definition of the work done

$$\bar{W}_n = \tau_n W_n \tag{5.85}$$

which matches the definition used in the derivation of the fluctuation relations [117, 30]. The symmetry function for the work done, integrated over n periods of the drive, is then,

$$S(\bar{W}_n) = \ln\left(\frac{P(+\bar{W}_n)}{P(-\bar{W}_n)}\right). \tag{5.86}$$

Then if the probability distribution is Gaussian, as it is for a harmonic oscillator in a true thermal environment [117, 30], we find that the symmetry function obeys,

$$S(\bar{W}_n) = \frac{2}{\delta\bar{W}_n^2}\bar{W}_n, \tag{5.87}$$

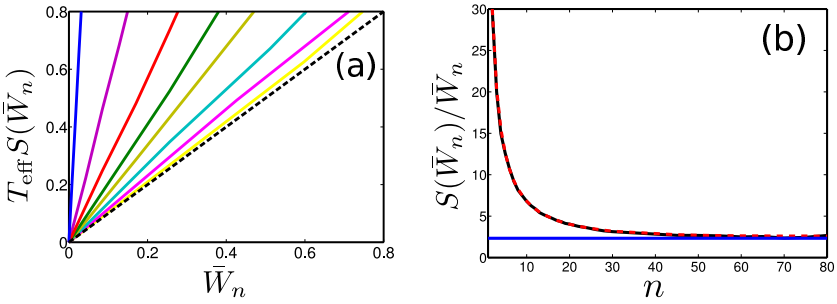

Figure 5.23.: The symmetry function in the linear regime, with $\kappa = 0.05$, $\epsilon = 0.3$, $f_0 = 0.01$, $\omega_D = 0.98\epsilon$. In (a) we show $S(\bar{W}_n)$ for $n = 1, 5, 10, 15, 20, 30, 50, 70$ as solid lines (n increases as the gradient decreases), the dashed line shows $T_{\rm eff}S(\bar{W}_n) = \bar{W}_n$ which is the long time limit prediction. In (b) we show the gradient of $S(\bar{W}_n)$ as a function of number of periods, n. The solid, black line is the direct numerical result, the red, dashed line is obtained from the numerical mean and variance, assuming the distribution is Gaussian. The blue line shows the prediction of the linear theory for the long time limit.

where $\delta\bar{W}_n^2$ is the variance of the work distribution. This shows that, for a Gaussian distribution, the symmetry function is linear, with a gradient given by $2/\delta\bar{W}_n^2$. Comparing with the fluctuation relation, Eqn. (5.84), we see that in the long time limit, this gradient obeys,

$$\lim_{n\to\infty} \frac{2}{\delta\bar{W}_n^2} = \frac{1}{T}, \tag{5.88}$$

where T is the temperature of the environment. This then provides us with a sensitive way of, not only examining how close the fluctuations are to Gaussian, but also of determining the temperature of the bath in contact with the system.

Unfortunately, the parameters with which we can numerically explore the symmetry function are limited. To calculate $S(\bar{W}_n)$, we need to have good statistics in the region $\bar{W}_n < 0$. This requires that the average work done is small compared to the variance of the distribution, even in the long integration time limit. This means that we cannot explore the way in which changing the drive frequency causes the system to explore the non-linear region, through resonance effects, as we did in the previous part of this chapter. This would make $\langle\bar{W}_n\rangle$ too large. Instead we choose to look at the way in which changing the strength of the electro-mechanical coupling, κ, affects the symmetry function, while keeping the drive strength weak enough to allow us to study the negative work fluctuations.

To begin with, we look at the results in the region where the linear theory holds. We plot the symmetry function for various integration times, n, in Fig. 5.23 (a), as solid lines, along with the result expected for the long time limit, as a dashed line, given by the effective temperature defined in Eqn. (5.48). As n is increased, the line moves

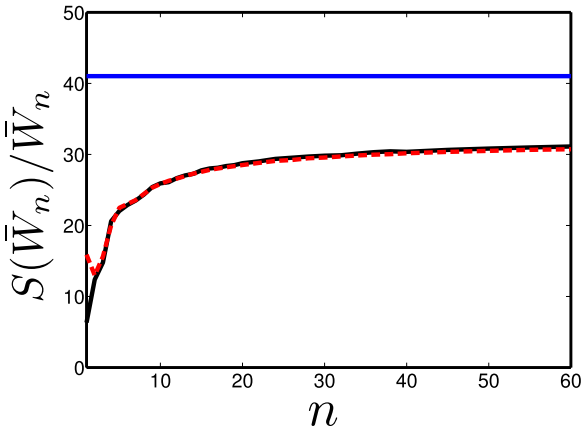

Figure 5.24.: Gradient of the symmetry function varying with integration time for the same parameters as Fig. 5.23, but with $\kappa = 0.5$. The solid, black line is the direct numerical result, the red, dashed line is obtained from the numerical mean and variance, assuming the distribution is Gaussian. The blue line shows the prediction of the linear theory for the long time limit.

towards the expected value, but the noise in the results increases. This increase in noise is because it becomes more difficult to find trajectories in which the work done is negative as the integration time increases. The scale of the fluctuations decrease with increasing n as the trajectories become closer to the mean when averaged over a large number of periods.

We can then look at how the gradient of the symmetry function varies with of the number of periods of integration, n. Results for this are shown in Fig. 5.23 (b). We show two methods of calculating this gradient. The first is using the direct numerical results to explicitly calculate $S(\bar{W}_n)$, and then the gradient is calculated directly from this. These results are shown as the solid, black line. Secondly, we can calculate the gradient by simply using the numerical value for the mean and variance and assuming the distribution is Gaussian, then Eqn. (5.87) gives direct access to the result. This calculation is shown as a red, dashed line in Fig. 5.23. We see that the two methods of calculating the gradient give the same result, since the distribution is Gaussian, except at very large n, where the noise in the direct numerical results increases. We can also see that, as n gets larger, the gradient converges on the effective temperature, as defined in the linear theory. There is a slight difference between the two results, which is because of the effect of finite coupling [110, 113].

We next go on to look at the behaviour as we change the coupling strength, κ. In Fig. 5.24, we show results for the same parameters as in Fig. 5.23, but for larger coupling, $\kappa = 0.5$. We see that the distribution is still well approximated by the Gaussian result at large n, but now the long time limit does not converge with the linear temperature.

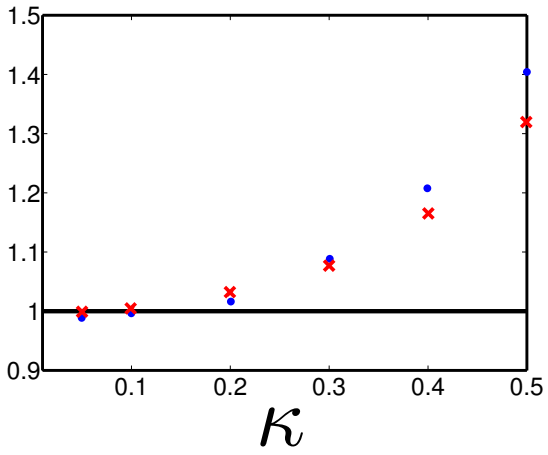

Figure 5.25.: Effective temperature as a function of κ, normalised by the linear result, T_{eff}. The solid, black line shows T_{eff}, the red crosses are the temperature calculated from the long integration time limit of the symmetry function, the blue dots show the temperature calculated from the variance of the steady state v distribution.

This is consistent with the results found for the variance of the steady state undriven system [110]. We see that the temperature found is higher than the linear result, this is expected since the fluctuations are amplified when the oscillator spends time in the uncoupled region.

In Fig. 5.25, we plot, as red crosses, the steady state temperature, calculated in this way compared to the linear response result, as a function of the electro-mechanical coupling, κ. As the coupling is increased, this temperature increases away from the linear result. As κ is increased, A_c decreases and so more and more of the resonator's trajectory lies in the region where the SET becomes stuck in one charge state (this is true, even without the drive [112]). This leads to an increase in the effective temperature as described above. As a comparison, we also plot, as the blue dots in Fig. 5.25, the variance of the corresponding steady state (undriven) velocity distribution. In the small κ limit, this also gives the effective temperature of the SET [110]. For $\kappa \to 0$, we see the linear result, the work distribution result and the variance calculation match. As the coupling is increased, the variance increases above the linear result, following the results from the work distribution quite closely. There is no significant difference in the sensitivity of the temperature calculated using either of these methods to the effects of finite coupling.

5.6 SUMMARY AND FUTURE WORK

In this chapter, we have examined the dynamics of the SET-resonator in the presence of a periodic drive. We have seen how a straightfor-

ward generalisation of the theory presented in Refs. [110, 112, 113] is able to accurately predict the behaviour for weak drive strengths, when the non-linear parts of the decay rates are not important. In this region, we found that the SET acts on the oscillator very much like a thermal bath, the only slight complication to this picture occurs in the limit $\omega_D \ll \gamma_{\text{eff}}$, when the temperature of the bath appears to be position dependent.

We then described the non-linear dynamics. We presented two techniques for calculating the amplitude dependent damping and frequency renormalisation experienced by the oscillator. The first of these allowed us to derive exact analytic results, but did not give good quantitative agreement with the numerical simulations, and so a more complex result was derived. Using these expressions we were able to find the amplitude of the stable solutions. We found regions where only one state is available to the oscillator, and others where two solutions are possible. For large drive strengths, the final state of the oscillator in this region depends on its initial conditions, the potential barrier between the two solutions is too large. For lower drive strength, it is possible to find regions where the system is bistable. The system switches between the two states on a short timescale compared to that of the numerical simulations.

The distribution of the work done by the force provides a further way of examining the dynamics. In the linear region, the distribution is Gaussian and satisfies the fluctuation relation for a thermal bath. In the large amplitude state, the distribution can become non-Gaussian when the effective potential no longer matches the linear result on the scale of the fluctuations. The work distribution also provides a useful tool for examining the timescale for switching between the stable solutions in the bistable region. The distribution has two peaks for integration times less than the switching time, but becomes unimodal for integration times longer than the switching time.

We also examined fluctuation relations for stronger electro-mechanical coupling. We found that, for large κ, the system can still have Gaussian fluctuations, but the effective temperature of these is smaller than predicted by the linear theory.

There are still many questions to be answered about the thermodynamics of the system. It would be interesting to examine the distributions of transferred heat and the change in internal energy, as exact results are also available for these in the case of harmonic oscillator coupled to a true thermal bath. We would also like to look at the symmetry function over a larger range of parameters. What happens to $S(W)$ as a function of drive frequency for different drive strengths? It would also be interesting to explore the other fluctuation relations, and to see how the system reacts to a different type of driving force.

Calculation of the current noise spectrum could also provide us with more insights into the dynamics, in particular, the timescales

which are important for the system. This would let us look in more detail at the switching time involved in the bistable behaviour.

Part IV.

Appendices

A

THE INTERACTION HAMILTONIAN FOR THE COOPER-PAIR RESONANCES

In this appendix we derive the coupling Hamiltonian between the SSET and its electromagnetic environment, Eqn. (2.62) from the main text. This is used to derive the Born-Markov description of the Cooper-pair resonances in Sec. 2.5.

We begin by finding the Hamiltonian for the SSET in the absence of coupling to the environment. The circuit diagram, along with our conventions for the direction of current and voltage, is given in Fig. A.1. We represent the Josephson junctions as capacitances, in parallel with pure Josephson elements. In this appendix, we obtain results for an asymmetric SSET, including the possibility of non-equivalent Josephson junctions and an asymmetric distribution of bias.

We begin by writing expressions for the different voltages and currents in the system using Kirchoff's laws. Loops 1 and 2, as labelled in Fig. A.1, respectively give for the voltages,

$$V_L + V_1 - V_g + \frac{Q_g}{C_g} = 0, \tag{A.1}$$

$$V_R + V_2 + V_g - \frac{Q_g}{C_g} = 0, \tag{A.2}$$

where V_1 and V_2 are the voltages across the left and right Josephson junctions and Q_g is the charge on the gate capacitor. While the nodes, labelled 1, 2 and 3, give for the currents,

$$I_L + I_g - I_R = 0, \tag{A.3}$$

$$I_L = -I_1 - C_L \dot{V}_1, \tag{A.4}$$

$$I_R = -I_2 - C_R \dot{V}_2. \tag{A.5}$$

We obtain expressions for V_1 and V_2 which will allow us to find the Hamiltonian of the system. To do this we will mostly work in Fourier space, since this allows us to write the differential equations which

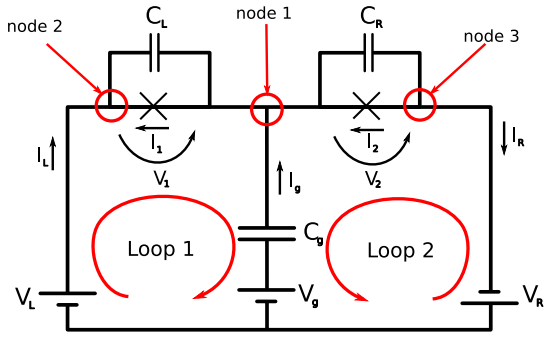

Figure A.1.: Circuit diagram of the SSET with no coupling to the environment. Our conventions for current and voltage are shown. The labelled loops and nodes are those to used in the Kirchoff's laws calculations (see text).

we derive as algebraic equations. To begin with we Fourier transform equations (A.1) and (A.2) [125, 126],

$$0 = 2\pi(V_L - V_g)\delta(\omega) + \tilde{V}_1 - \frac{1}{i\omega C_g}\left(\tilde{I}_1 - \tilde{I}_2 - i\omega(C_L\tilde{V}_1 - C_R\tilde{V}_2)\right), \tag{A.6}$$

$$0 = 2\pi(V_R + V_g)\delta(\omega) + \tilde{V}_2 + \frac{1}{i\omega C_g}\left(\tilde{I}_1 - \tilde{I}_2 - i\omega(C_L\tilde{V}_1 - C_R\tilde{V}_2)\right), \tag{A.7}$$

where the tilde indicates a Fourier transformed variable and we have eliminated I_g using equations (A.3)-(A.5). To find expressions for V_1 and V_2 separately we add the two Fourier space equations to find,

$$\tilde{V}_1 + \tilde{V}_2 = -2\pi(V_L + V_R)\delta(\omega), \tag{A.8}$$

which we can then use to eliminate V_2 from Eqn. A.6. Hence, we obtain,

$$\tilde{V}_1 = 2\pi\left(V_L - \frac{C_L V_L - C_R V_R + C_g V_g}{C_\Sigma}\right)\delta(\omega) + \frac{1}{-i\omega C_\Sigma}(\tilde{I}_1 - \tilde{I}_2), \tag{A.9}$$

where we have defined the total capacitance of the island, $C_\Sigma = C_L + C_R + C_g$. We can then use the same technique to find V_2 and convert back to the time domain,

$$V_1 = -V_L - \frac{C_L V_L - C_R V_R + C_g V_g}{C_\Sigma} - \frac{1}{C_\Sigma}(Q_1 - Q_2), \tag{A.10}$$

$$V_2 = -V_R + \frac{C_L V_L - C_R V_R + C_g V_g}{C_\Sigma} + \frac{1}{C_\Sigma}(Q_1 - Q_2). \tag{A.11}$$

We can then use these to construct the Hamiltonian of the system. The superconducting phase, ϕ_i, and number operators, N_i, for each of the Josephson junctions are our conjugate variables, here $i = 1, 2$ labels the left and right junction respectively. We can use the standard

Josephson relations [125, 127], and write down Hamilton's equations for the system,

$$\frac{\partial H_0}{\partial \phi_1} = \frac{\hbar}{2e}\dot{Q}_1 = -\hbar\dot{N}_1 = E_{J1}\sin\phi_1, \tag{A.12}$$

$$\frac{\partial H_0}{\partial \phi_2} = \frac{\hbar}{2e}\dot{Q}_2 = -\hbar\dot{N}_2 = E_{J2}\sin\phi_2, \tag{A.13}$$

$$\begin{aligned}\frac{\partial H_0}{\partial N_1} = \hbar\dot{\phi}_1 = 2eV_1 = -2eV_L - 2e\frac{C_L V_L - C_R V_R + C_g V_g}{C_\Sigma} \\ + \frac{4e^2}{C_\Sigma}(N_1 - N_2),\end{aligned} \tag{A.14}$$

$$\begin{aligned}\frac{\partial H_0}{\partial N_2} = \hbar\dot{\phi}_2 = 2eV_2 = -2eV_R + 2e\frac{C_L V_L - C_R V_R + C_g V_g}{C_\Sigma} \\ - \frac{4e^2}{C_\Sigma}(N_1 - N_2).\end{aligned} \tag{A.15}$$

From which we can construct the Hamiltonian of the system as a function which satisfies all of these relations,

$$\begin{aligned}H_0 = -E_{J1}\cos\phi_1 - E_{J2}\cos\phi_2 + \frac{2e^2}{C_\Sigma}(N_1 - N_2)^2 \\ + 4e^2\frac{N_0}{C_\Sigma}(N_1 - N_2) - 2e(V_L N_1 + V_R N_2),\end{aligned} \tag{A.16}$$

where we have defined $N_0 = -(C_L V_L - C_R V_R + C_g V_g)/2e$. By rearranging we can write this, up to an unimportant constant as,

$$H_0 = E_C(N_1 - N_2 + N_0)^2 - 2e(V_L N_1 + V_R N_2) - E_{J1}\cos\phi_1 - E_{J2}\cos\phi_2, \tag{A.17}$$

where we have defined the charging energy of the island, $E_C = (2e)^2/2C_\Sigma$.

The Hamiltonian is quantised by promoting the counting variables $\hat{N}_1$, $\hat{N}_2$ and phase variables $\hat{\phi}_1$, $\hat{\phi}_2$ to operators which obey the commutation relations,

$$[\hat{N}_1, \hat{\phi}_1] = i, \qquad [\hat{N}_2, \hat{\phi}_2] = i. \tag{A.18}$$

We can then reduce the Hamiltonian to the form which we use in the main text, given in Eqns. (2.60) and (2.61), by simplifying the circuit so that it is symmetric. We take $C_L = C_R = C_J$, $E_{J1} = E_{J2} = E_J$ and $V_L = V_R = V/2$, this means that $N_0 = C_g V_g/2e = n_g$. We also define the quantum numbers $\hat{n} = \hat{N}_2 - \hat{N}_1$, and $\hat{k} = (\hat{N}_1 + \hat{N}_2)/2$. Putting all of this together we obtain,

$$\begin{aligned}H_0 = \sum_{n,k}(E_C(n - n_g)^2 - 2eVk)\,|n,k\rangle\langle n,k| \\ - \frac{E_J}{2}(|n,k\rangle\langle n+1,k+1/2| + |n,k\rangle\langle n-1,k-1/2| + h.c.).\end{aligned} \tag{A.19}$$

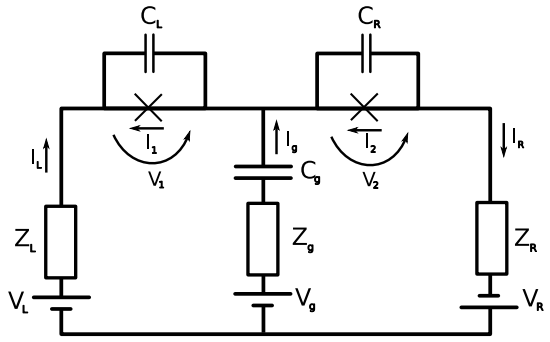

Figure A.2.: Circuit diagram of the SSET with impedances coupled to the leads and gate.

To understand the effects of adding an electromagnetic environment we introduce impedances in series with each of the leads [125, 67, 126]. The new circuit is shown in Fig. A.2.

We follow the same procedure as for the case without environment, this results in the same Fourier space equations as in equations A.6 and A.7, but with extra terms proportional to the impedances,

$$0 = 2\pi(V_L - V_g)\delta(\omega) + \tilde{V}_1 - Z_L(\omega)\tilde{I}_L + \left(Z_g(\omega) + \frac{1}{-i\omega C_g}\right)\left(\tilde{I}_1 - \tilde{I}_2 - i\omega(C_L\tilde{V}_1 - C_R\tilde{V}_2)\right), \quad \text{(A.20)}$$

$$0 = 2\pi(V_R + V_g)\delta(\omega) + \tilde{V}_2 - Z_R(\omega)\tilde{I}_R - \left(Z_g(\omega) + \frac{1}{-i\omega C_g}\right)\left(\tilde{I}_1 - \tilde{I}_2 - i\omega(C_L\tilde{V}_1 - C_R\tilde{V}_2)\right). \quad \text{(A.21)}$$

In this case we cannot immediately separate the equations for $\tilde{V}_1$ and $\tilde{V}_2$, and so we write the coupled equations [126],

$$\begin{pmatrix} i\omega C_L\hat{Z}_L - 1 & -i\omega C_R\hat{Z}_g \\ -i\omega C_L\hat{Z}_g & i\omega C_R\hat{Z}_R - 1 \end{pmatrix}\begin{pmatrix}\tilde{V}_1\\ \tilde{V}_2\end{pmatrix} = 2\pi\delta(\omega)\begin{pmatrix}V_L - V_g\\ V_g + V_R\end{pmatrix} + \begin{pmatrix}\hat{Z}_L & -\hat{Z}_g\\ -\hat{Z}_g & \hat{Z}_R\end{pmatrix}\begin{pmatrix}\tilde{I}_1\\ \tilde{I}_2\end{pmatrix}, \quad \text{(A.22)}$$

where we define $\hat{Z}_g = Z_g + 1/(-i\omega C_g)$ and $\hat{Z}_{L(R)} = Z_{L(R)} + \hat{Z}_g$. We then need to invert the matrix on the LHS to find expressions for the voltages. We can also simplify the term proportional to $\delta(\omega)$ in

the limit where the bare environment has no capacitive component, $\lim_{\omega\to 0}\omega Z_{L,R,g}(\omega) = 0$ [125, 67]. This then allows us to write,

$$\begin{aligned}\begin{pmatrix}\tilde{V}_1\\ \tilde{V}_2\end{pmatrix} &= -\frac{2\pi\delta(\omega)}{C_\Sigma}\begin{pmatrix}C_g+C_R & C_R\\ C_L & C_G+C_L\end{pmatrix}\begin{pmatrix}V_L-V_g\\ V_g+V_R\end{pmatrix}\\ &+\frac{1}{(i\omega C_L\hat{Z}_L-1)(i\omega C_R\hat{Z}_R-1)+\omega^2 C_R C_L\hat{Z}_g^2}\\ &\times\begin{pmatrix}i\omega C_R\hat{Z}_R-1 & i\omega C_R\hat{Z}_g\\ i\omega C_L\hat{Z}_g & i\omega C_L\hat{Z}_L-1\end{pmatrix}\begin{pmatrix}\hat{Z}_L & -\hat{Z}_g\\ -\hat{Z}_g & \hat{Z}_R\end{pmatrix}\begin{pmatrix}\tilde{I}_1\\ \tilde{I}_2\end{pmatrix}.\end{aligned} \tag{A.23}$$

We are interested in the effects of the environment on the system, and so we subtract off the terms which give rise to the system Hamiltonian H_0. To do this we define $\delta V_i = V_i - V_{i,0}$ where $V_{i,0}$ is the voltage with $Z_{L,R,g} = 0$. These are given by,

$$\begin{pmatrix}\tilde{V}_{1,0}\\ \tilde{V}_{2,0}\end{pmatrix} = -\frac{2\pi\delta(\omega)}{C_\Sigma}\begin{pmatrix}C_g+C_R & C_R\\ C_L & C_G+C_L\end{pmatrix}+\frac{1}{-i\omega C_\Sigma}\begin{pmatrix}-1 & 1\\ 1 & -1\end{pmatrix}\begin{pmatrix}\tilde{I}_1\\ \tilde{I}_2\end{pmatrix}. \tag{A.24}$$

We note that this is the same result as that obtained in the previous section. The relevant limit for our system is the case of weak coupling to the gate, $C_g \ll C_{L,R}$. In this limit we find that the fluctuating part of the voltages is given by,

$$\begin{pmatrix}\delta\tilde{V}_1\\ \delta\tilde{V}_2\end{pmatrix} = \frac{-(Z_L+Z_R)}{1-i\omega\frac{C_L C_R}{C_\Sigma}(Z_L+Z_R)}\begin{pmatrix}\frac{C_R^2}{C_\Sigma^2} & \frac{C_L C_R}{C_\Sigma^2}\\ \frac{C_L C_R}{C_\Sigma^2} & \frac{C_L^2}{C_\Sigma^2}\end{pmatrix}\begin{pmatrix}\tilde{I}_1\\ \tilde{I}_2\end{pmatrix}. \tag{A.25}$$

This contains the information about how the bath couples to the system operators. To see this we try to map the system onto the generic bath Hamiltonian [67],

$$H_{\text{env}} = \sum_n \frac{\Phi_n^2}{2L_n} + \frac{(Q_n - \alpha Q_1 - \beta Q_2)^2}{2C_n}, \tag{A.26}$$

where Q_n, Φ_n, C_n, L_n are the charge, phase, capacitance and inductance of the n^{th} mode of the environment and $Q_{1(2)}$ are the charge variables of the SSET. These couple to the environment with strength given by α and β. Physically, this environment corresponds to a set of harmonic oscillators modelled as inductors and capacitors to which the SSET is coupled [67]. We find that Hamilton's equations for the for the environment variables give,

$$\dot{Q}_n = \frac{\partial H_{\text{env}}}{\partial \Phi_n} = \frac{\Phi_n}{L_n}, \tag{A.27}$$

$$\dot{\Phi}_n = -\frac{\partial H_{\text{env}}}{\partial Q_n} = -\frac{Q_n - \alpha Q1 - \beta Q_2}{C_n}. \tag{A.28}$$

We can also define the parts of the voltages which fluctuate due to the interaction with the environment. These result in a fluctuation in the phase at each of the junctions of the SSET,

$$\delta\dot{\Phi}_1 = \delta V_1 = -\frac{\partial H_{\text{env}}}{\partial Q_1} = -\alpha \sum_n \frac{Q_n - \alpha Q_1 - \beta Q_2}{C_n}, \tag{A.29}$$

$$\delta\dot{\Phi}_2 = \delta V_2 = -\frac{\partial H_{\text{env}}}{\partial Q_2} = -\beta \sum_n \frac{Q_n - \alpha Q_1 - \beta Q_2}{C_n}. \tag{A.30}$$

We can then use the solution to equation (A.27), which in Fourier space takes the form,

$$\tilde{Q}_n = \frac{\omega_n^2}{\omega^2 - \omega_n^2}(\alpha\tilde{Q}_1 + \beta\tilde{Q}_2), \tag{A.31}$$

where $\omega_n = 1/\sqrt{C_n L_n}$. This lets us write,

$$\sum_n \frac{\tilde{Q}_n - \alpha\tilde{Q}_1 - \beta\tilde{Q}_2}{C_n} = \sum_n \frac{\omega^2}{\omega_n^2 - \omega^2}\frac{\alpha\tilde{Q}_1 + \beta\tilde{Q}_2}{C_n}, \tag{A.32}$$

which then allows us to find the current-voltage relation (noting that $\tilde{I} = -i\omega\tilde{Q}$),

$$\delta\tilde{V}_1 = -i\omega\alpha(\alpha\tilde{I}_1 + \beta\tilde{I}_2)\sum_n \frac{\omega^2}{\omega_n^2 - \omega^2}, \tag{A.33}$$

$$= Z_{\text{eff}}(\alpha^2\tilde{I}_1 + \alpha\beta\tilde{I}_2). \tag{A.34}$$

A similar expression can be obtained for $\delta\tilde{V}_2$, and hence we can write,

$$\begin{pmatrix}\delta\tilde{V}_1 \\ \delta\tilde{V}_2\end{pmatrix} = Z_{\text{eff}}\begin{pmatrix}\alpha^2 & \alpha\beta \\ \alpha\beta & \beta^2\end{pmatrix}\begin{pmatrix}\tilde{I}_1 \\ \tilde{I}_2\end{pmatrix}, \tag{A.35}$$

which then has the same form as equation (A.25). From this we can identify the coupling constants as

$$\alpha = \frac{C_R}{C_\Sigma}, \tag{A.36}$$

$$\beta = \frac{C_L}{C_\Sigma}. \tag{A.37}$$

For a symmetric SSET, $C_L = C_R$, hence $\alpha = \beta = 1/2$ and so we can write the interaction part of the environmental Hamiltonian as,

$$H_{\text{int}} = -\frac{Q_1 + Q_2}{2}\sum_n \frac{Q_n}{C_n}. \tag{A.38}$$

We can rewrite this in terms of the system operator $\hat{k} = -(Q_1+Q_2)/4e$ as,

$$H_{\text{int}} = -2e\hat{k}\delta\hat{V}, \tag{A.39}$$

where $\delta V = \sum_n Q_n/C_n$ is the environment operator which describes the fluctuation of the voltages [67]. This is the interaction Hamiltonian used in the main text, Eqn. (2.62).

B

TRANSFORMING THE COOPER-PAIR RESONANCES HAMILTONIAN

In the first part of this appendix we calculate the transformation to the Hamiltonian for the Cooper-pair resonances, used in Eqn. (2.64) of the main text, as a perturbative expansion in E_J. In the second part, we use this transformation to calculate series expansions for the operators $\hat{n}'$ and $\hat{k}'$ which are used throughout Secs. 2.5 and 3.7.

B.1 TRANSFORMING THE HAMILTONIAN

We begin with the system Hamiltonian, $H_S = H_{\text{ch}} + H_J$, as defined in Eqns. (2.60) and (2.61) in the main text. We find a unitary transformation, $H' = UHU^\dagger$ (we drop the subscript S in this appendix), such that H' only contains diagonal elements and those which couple resonant states. To do this we define the projector onto the k-th doublet as,

$$P_k = |0,k\rangle \langle 0,k| + |1,k+p+1/2\rangle \langle 1,k+p+1/2| \,. \tag{B.1}$$

Then the condition on H' above becomes $P_k H' P_{k''} = 0$ for $k \neq k''$. We then write the transformation as [69] $U = \mathrm{e}^{iS}$, with $S = S^\dagger$, and treat H_J as a perturbation. This allows us to write a series expansion for S in terms of J,

$$S = S^{(0)} + JS^{(1)} + J^2 S^{(2)} + \ldots . \tag{B.2}$$

There are infinitely many transformations which satisfy the condition on H', and so to uniquely specify U we choose that S should not have matrix elements within the doublet, $P_k S P_k = 0$. We note that $S^{(0)} = 0$, since for the case $J = 0$ we need no transformation. This then allows us to find the transformed form of the Hamiltonian as,

$$\begin{aligned} H' = H_{\text{ch}} + H_J + [iJS^{(1)}, H_{\text{ch}}] + [iJS^{(1)}, H_J] \\ + [iJ^2 S^{(2)}, H_{\text{ch}}] + \frac{1}{2!}\left[iJS^{(1)}, [iJS^{(1)}, H_{\text{ch}}]\right] + \ldots , \end{aligned} \tag{B.3}$$

which we can then write as a power series,

$$H' = H^{(0)} + H^{(1)} + H^{(2)} + \ldots , \tag{B.4}$$

where we have grouped terms by order in J;

$$H^{(0)} = H_{\text{ch}}, \tag{B.5a}$$

$$H^{(1)} = H_J + [iJS^{(1)}, H_{\text{ch}}], \tag{B.5b}$$

$$H^{(2)} = [iJS^{(1)}, H_J] + [iJ^2S^{(2)}, H_{\text{ch}}] + \frac{1}{2!}\left[iJS^{(1)}, [iJS^{(1)}, H_{\text{ch}}]\right]. \tag{B.5c}$$

These can then be used to construct the expression for S term by term, and so build up the effective Hamiltonian. As an example, we give the calculation of $S^{(1)}$. We begin by noting that $P_k H^{(n)} P_{k''} = 0$ for all n and $k \neq k''$ which gives,

$$0 = P_k H_J P_{k''} + P_k(iJS^{(1)}H_{\text{ch}} - H_{\text{ch}}iJS^{(1)})P_{k''}, \tag{B.6}$$

from which we can calculate the matrix elements of $iS^{(1)}$ as,

$$\langle 0,k|\, iS^{(1)}\, |1,k+1/2\rangle = -\frac{J}{2peV} = G_1, \tag{B.7}$$

$$\langle 0,k|\, iS^{(1)}\, |1,k-1/2\rangle = -\frac{J}{2(p+1)eV} = -G_2, \tag{B.8}$$

and the obvious conjugates. G_1 and G_2 become the natural small parameters of the perturbation theory. These expressions can be used to calculate $S^{(2)}$, and so on. This allows the transformed Hamiltonian to be found up to any order, for example we find that the second order corrections to the diagonal elements are given by,

$$\langle 0,k|\, H^{(2)}\, |0,k\rangle = -\frac{J^2}{eV}\frac{2q}{q^2-1}. \tag{B.9}$$

We also need to be able to calculate the off-diagonal coupling between resonant states, J_p. This appears to order $2p+1$ in the perturbation expansion. The method outlined above becomes very cumbersome at high orders and so, to calculate J_p for higher orders, we introduce the level-shift operator [69, 45],

$$R(z) = H_J + H_J\frac{Q_k}{z-H_{\text{ch}}}H_J + H_J\frac{Q_k}{z-H_{\text{ch}}}H_J\frac{Q_k}{z-H_{\text{ch}}}H_J + \ldots, \tag{B.10}$$

where $Q_k = 1 - P_k$. Which allows us to calculate the required matrix element, $J_p = \langle 0,k|\, R(\bar{E})\, |1,k+p+1/2\rangle$. This gives the expression found in Eq. (2.65). However, we have checked explicitly that this approach gives the same expression for $J_{p=1}$ (the highest order used in the main text) as that obtained using the perturbation expansion.

B.2 THE TRANSFORMED OPERATORS

We also need to transform the operators k and n. To illustrate the method we give an explicit calculation of k'. This is done in exact

analogy with the calculation of H'. We first write k' as a power series,

$$k' = k^{(0)} + k^{(1)} + k^{(2)} + \dots, \tag{B.11}$$

where,

$$k^{(0)} = k, \tag{B.12a}$$
$$k^{(1)} = [iJS^{(1)}, k], \tag{B.12b}$$
$$k^{(2)} = [iJ^2S^{(2)}, k] + \frac{1}{2!}\left[iJS^{(1)}, [iJS^{(1)}, k]\right]. \tag{B.12c}$$

This allows us to calculate $k^{(1)}$ as,

$$k^{(1)} = \frac{1}{2}\sum_k G_1 \left|0,k\right\rangle \left\langle 1,k+1/2\right| + G_2 \left|0,k\right\rangle \left\langle 1,k-1/2\right| + h.c.. \tag{B.13}$$

Also, $k^{(2)}$ is given by,

$$\begin{aligned} k^{(2)} = {} & \frac{(2p+1)G_1G_2}{2}\sum_k \left(\left|0,k\right\rangle \left\langle 0,k+1\right| - \left|0,k\right\rangle \left\langle 0,k-1\right| + h.c.\right) \\ & + (G_1^2+G_2^2)\sum_k (\left|1,k+1/2\right\rangle \left\langle 1,k+1/2\right| - \left|0,k\right\rangle \left\langle 0,k\right|). \end{aligned} \tag{B.14}$$

A similar calculation can be performed to calculate the power series for $n' = n^{(0)} + n^{(1)} + n^{(2)} + \dots$. We find $n^0 = n$,

$$n^{(1)} = \sum_k G_1 \left|0,k\right\rangle \left\langle 1,k+1/2\right| - G_2 \left|0,k\right\rangle \left\langle 1,k-1/2\right| + h.c., \tag{B.15}$$

$$\begin{aligned} n^{(2)} = {} & G_1G_2\sum_k \left(\left|0,k\right\rangle \left\langle 0,k+1\right| - \left|0,k\right\rangle \left\langle 0,k-1\right| + h.c\right) \\ & + (G_1^2+G_2^2)\sum_k (\left|1,k+1/2\right\rangle \left\langle 1,k+1/2\right| - \left|0,k\right\rangle \left\langle 0,k\right|). \end{aligned} \tag{B.16}$$

C

DERIVING THE CURRENT NOISE EXPRESSION

In this appendix we show how it possible to derive the general expression for the current noise, given in Eqn. (4.20), starting from the expression for the current-current correlation function, Eqn. (4.16),

$$S_I(t_1,t_2) = \partial_{t_1}\partial_{t_2}[\theta(t_1-t_2)f(t_1,t_2)+\theta(t_2-t_1)f(t_1,t_2)^*] - \langle I(t_1)\rangle\langle I(t_2)\rangle. \tag{C.1}$$

In Fourier space, the correlation function of the counting variable is given by,

$$f(t_1,t_2) = \langle\langle 0|\frac{\partial}{\partial i\chi}\left[e^{\mathcal{M}(\chi)(t_1-t_2)}\frac{\partial}{\partial i\chi}e^{\mathcal{M}(\chi)t_2}\right]|\rho_0\rangle\rangle\,. \tag{C.2}$$

The simplest term to calculate in Eqn. (C.1) is,

$$\partial_{t_1}\partial_{t_2}f(t_1,t_2) = \langle\langle 0|\,\partial_{i\chi}[\mathcal{M}e^{\mathcal{M}(t_1-t_2)}\partial_{i\chi}\mathcal{M}e^{\mathcal{M}t_2} - \mathcal{M}^2e^{\mathcal{M}(t_1-t_2)}\partial_{i\chi}e^{\mathcal{M}t_2}\Big]\,|\rho_0\rangle\rangle. \tag{C.3}$$

The terms with $\partial_{i\chi}e^{\mathcal{M}t_2}$ cancel and so, in the limit $t_2\to\infty$, we obtain,

$$\partial_{t_1}\partial_{t_2}f(t_1,t_2) = \langle\langle 0|\mathcal{M}'e^{\mathcal{M}(t_1-t_2)}\mathcal{M}'|0\rangle\rangle, \tag{C.4}$$

and similarly for the conjugate part,

$$\partial_{t_1}\partial_{t_2}f^*(t_2,t_1) = (\langle\langle 0|\mathcal{M}'e^{\mathcal{M}(t_2-t_1)}\mathcal{M}'|0\rangle\rangle)^*. \tag{C.5}$$

To calculate the derivatives of the step function, we introduce the piecewise continuous, differentiable function,

$$\theta_\epsilon(t) = \begin{cases} 0 & t<0 \\ \frac{1}{2}\left[1-\cos\left(\frac{t}{\epsilon}\right)\right] & 0\le x<\epsilon\pi \\ 1 & x\ge\epsilon\pi \end{cases}, \tag{C.6}$$

which corresponds to the Heaviside function in the limit $\lim_{\epsilon\to 0}\theta_\epsilon(t) = \theta(t)$. This has the advantage of always being zero for $t<0$ therefore, the fact that we only know the forward time evolution operator now

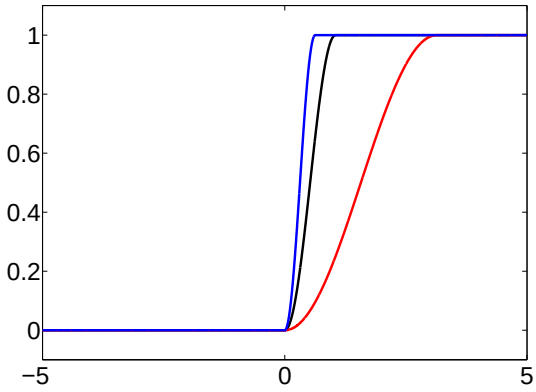

Figure C.1.: The approximation to the Heaviside function which we use, defined in Eqn. (C.6) for various values of ϵ.

presents no problems. This function is shown for various values of ϵ in Fig. C.1.

We next consider the terms in Eqn. (C.1) involving a single time derivative of the step function, $\theta'(t)$. We note that $\lim_{\epsilon\to 0}\theta'(t) = \delta(t)$ and so we can write these terms as,

$$\delta(t_1 - t_2)\left[\partial_{t_2} f(t_1, t_2) - \partial_{t_1} f(t_1, t_2) + \partial_{t_1} f^*(t_2, t_1) - \partial_{t_2} f^*(t_2, t_1)\right], \quad \text{(C.7)}$$

which, since the delta function only gives a contribution at $t_1 = t_2$, can be written,

$$2\delta(t_1 - t_2)\mathrm{Re}\left[\partial_{t_2} f(t_1, t_2) - \partial_{t_1} f(t_1, t_2)\right]. \quad \text{(C.8)}$$

We can then go on to calculate the relevant derivatives, and find,

$$\partial_{t_2} f(t_1, t_2)|_{t_1=t_2} = \langle\langle 0|\mathcal{M}''|0\rangle\rangle + \langle\langle 0|M'\partial_{i\chi} e^{\mathcal{M}t_2}|\rho_0\rangle\rangle, \quad \text{(C.9)}$$

$$\partial_{t_1} f(t_1, t_2)|_{t_1=t_2} = \langle\langle 0|M'\partial_{i\chi} e^{\mathcal{M}t_2}|\rho_0\rangle\rangle. \quad \text{(C.10)}$$

Finally we need to calculate the terms involving $\theta''(t)$,

$$-\theta''(t_1 - t_2)f(t_1, t_2) - \theta''(t_2 - t_1)f(t_2, t_1). \quad \text{(C.11)}$$

We show explicitly how to calculate $\theta''(t_1 - t_2)f(t_1, t_2)$. To do this we perform a trial integration, using a function $\Psi(t_1, t_2)$, which vanishes at the boundaries, ensuring convergence,

$$\int dt_1 \int dt_2 \theta''_\epsilon(t_1 - t_2)\Psi(t_1, t_2)f(t_1, t_2). \quad \text{(C.12)}$$

Making the change of variables, $\tau_1 = t_1 - t_2$, $\tau_2 = (t_1 + t_2)/2$, so that the Jacobian is unity we find, by integrating by parts,

$$\begin{aligned}\int d\tau_1 \int d\tau_2 \theta''_\epsilon(\tau_1)\Psi(\tau_1\tau_2)f(\tau_2 + \tau_1/2, \tau_2 - \tau_1/2) \\ = -\int d\tau_1 \int d\tau_2 \theta'_\epsilon(\tau_1)\partial_{\tau_1}\Psi(\tau_1\tau_2)f(\tau_2 + \tau_1/2, \tau_2 - \tau_1/2).\end{aligned} \quad \text{(C.13)}$$

Choosing Ψ such that $\partial_{\tau_1}\Psi(0,\tau_2)=0$ gives,

$$\int d\tau_1 \int d\tau_2 \theta''(\tau_1)\Psi(\tau_1\tau_2) f(\tau_2+\tau_1/2,\tau_2-\tau_1/2) \\ = -\int_0^\infty d\tau_1 \int d\tau_2 \theta'_\epsilon(\tau_1)\frac{1}{2}\left[\partial_{t_1} f(t_1,t_2)-\partial_{t_2}(t_1,t_2)\right]. \quad \text{(C.14)}$$

This then allows us to identify,

$$\theta''(t_1-t_2)f(t_1,t_2)=\theta'(t_1-t_2)\frac{1}{2}\left[\partial_{t_1} f(t_1,t_2)-\partial_{t_2} f(t_1,t_2)\right], \quad \text{(C.15)}$$

similarly we find,

$$\theta''(t_2-t_1)f^*(t_2,t_1)=\theta'(t_2-t_1)\frac{1}{2}\left[\partial_{t_2} f^*(t_1,t_1)-\partial_{t_1} f^*(t_2,t_1)\right], \quad \text{(C.16)}$$

and so we find for the full term,

$$-\theta''(t_1-t_2)f(t_1,t_2)-\theta''(t_2-t_1)f(t_2,t_1) \\ = -\delta(t_1-t_2)\mathrm{Re}\left[\partial_{t_2} f(t_1,t_2)-\partial_{t_1} f(t_1,t_2)\right]. \quad \text{(C.17)}$$

Putting all of this together we obtain an expression for the two time correlation function,

$$S_I(t)=\delta(t)\mathrm{Re}\langle\langle 0|\mathcal{M}''|0\rangle\rangle+\langle\langle 0|\mathcal{M}'\mathrm{e}^{\mathcal{M}t}\mathcal{M}'|0\rangle\rangle \\ +\langle\langle 0|\mathcal{M}'\mathrm{e}^{-\mathcal{M}t}\mathcal{M}'|0\rangle\rangle^*-\langle I\rangle^2, \quad \text{(C.18)}$$

which is the result used in the main text.

D

DOUBLE QUANTUM DOTS

In this appendix we consider the model of coherent transport through a double quantum dot, coupled to a thermal bath, discussed in Ref. [107]. In this paper, it was found that the zero-frequency current noise, calculated at different points along the system, took different values. This result is worrying, since it implies a violation of charge conservation through the device. Here we show that these quantities, calculated using the formalism presented in Chap. 4, do conserve charge.

D.1 MODEL

A schematic of the model which we use (following Refs. [88, 58, 107]), is shown in Fig. D.1. A potential difference is applied across the two dots, so that electron transport occurs across the system. Leads at the left and right provide reservoirs for the electrons, and a thermal environment is connected to the dots. This decoheres states which are superpositions of $|L, N_L\rangle$ and $|R, N_L\rangle$ where $L(R)$ labels states in which the left (right) dot is occupied, and N_L counts the number of electrons in the left reservoir, as for the SSET.

We begin by just considering the internal dynamics of the system (i.e. the $\chi = 0$ evolution), to do this we introduce the states $|i\rangle = \sum_{N_L} |i, N_L\rangle$ where $i = 0, L, R$. The Hamiltonian for the dots is then given by,

$$H_S = \frac{\epsilon}{2}(|L\rangle\langle L| - |R\rangle\langle R|) + \Omega(|L\rangle\langle R| + |R\rangle\langle L|), \tag{D.1}$$

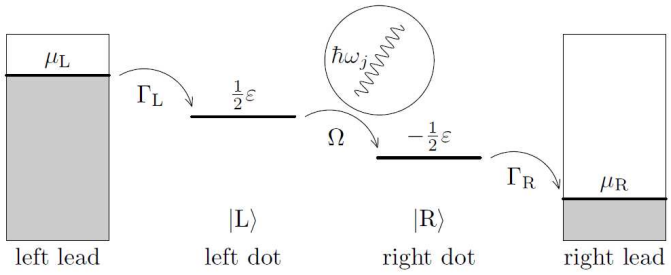

Figure D.1.: A schematic of the DQD system. (Reproduced from [107])

where we have assumed the charging energy of the state $|0\rangle$ is 0 and the $|L\rangle$ and $|R\rangle$ states are equally detuned from this, by an amount $\epsilon/2$. The dots are coherently coupled, with a strength described by Ω. This Hamiltonian then has eigenvalues given by,

$$E_{\pm} = \pm\frac{\Delta}{2}, \tag{D.2}$$

where $\Delta = \sqrt{4\Omega^2 + \epsilon^2}$. We follow the method of Ref. [107] to include the baths in our Born-Markov description. Using the basis,

$$|\rho\rangle\rangle = (\rho_{00}, \rho_{LL}, \rho_{RR}, \rho_{RL}, \rho_{LR})^T, \tag{D.3}$$

with $\rho_{ij} = \langle i|\,\rho\,|j\rangle$. We write the master equation,

$$\frac{d|\rho\rangle\rangle}{dt} = \mathcal{M}|\rho\rangle\rangle = \mathcal{M}_{\text{coh}}|\rho\rangle\rangle + \mathcal{M}_{\text{leads}}|\rho\rangle\rangle + \mathcal{M}_{\text{therm}}|\rho\rangle\rangle, \tag{D.4}$$

where $\mathcal{M}_{\text{coh}} = -i[H_S, \rho]$ gives the coherent evolution, $\mathcal{M}_{\text{leads}}$ includes the transitions into and out of the leads and $\mathcal{M}_{\text{therm}}$ is the dephasing and decoherence due to the thermal environment. Following [107] these have the forms,

$$\mathcal{M}_{\text{coh}} = \begin{pmatrix} 0 & 0 & 0 & 0 & 0 \\ 0 & 0 & 0 & -i\Omega & i\Omega \\ 0 & 0 & 0 & i\Omega & -i\Omega \\ 0 & -i\Omega & i\Omega & i\epsilon & 0 \\ 0 & i\Omega & -i\Omega & 0 & -i\epsilon \end{pmatrix}, \tag{D.5}$$

$$\mathcal{M}_{\text{leads}} = \begin{pmatrix} -\Gamma & 0 & \Gamma & 0 & 0 \\ \Gamma & 0 & 0 & 0 & 0 \\ 0 & 0 & -\Gamma & 0 & 0 \\ 0 & 0 & 0 & -\Gamma/2 & 0 \\ 0 & 0 & 0 & 0 & -\Gamma/2 \end{pmatrix}, \tag{D.6}$$

$$\mathcal{M}_{\text{therm}} = \begin{pmatrix} 0 & 0 & 0 & 0 & 0 \\ 0 & 0 & 0 & 0 & 0 \\ 0 & 0 & 0 & 0 & 0 \\ 0 & \gamma_+ & -\gamma_- & -\gamma_p & 0 \\ 0 & \gamma_+ & -\gamma_- & 0 & -\gamma_p \end{pmatrix}. \tag{D.7}$$

We have assumed the decay rates into and out of the bath are equal $\Gamma_L = \Gamma_R = \Gamma$. We have also introduced the quantities which describe the thermal bath [107],

$$\gamma_{\pm} = -\pi\frac{\Omega}{\Delta}J(\Delta)\left(\frac{\epsilon}{\Delta}\coth\left(\frac{\Delta}{2T}\right) \pm 1\right) \tag{D.8}$$

$$\gamma_p = 4\pi\frac{\Omega^2}{\Delta^2}J(\Delta)\coth\left(\frac{\Delta}{2T}\right), \tag{D.9}$$

where T is the temperature of the bath, and $J(\omega)$ its spectral density, which we take to be Ohmic and of the form,

$$J(\omega) = \frac{2\gamma\omega}{\pi} \mathrm{e}^{-\frac{\omega}{\omega_c}}. \tag{D.10}$$

Here, γ is the coupling strength between the dots and the environment and ω_c is a high frequency cut-off, introduced for regularisation, which we assume is much larger than any other scale in the problem.

To calculate the noise we consider two counting variables. As well as N_L, which counts electrons moving from the reservoir to the left dot (this is then a purely incoherent counting process), we will also consider N_C, which counts electrons moving from the left to right dot (this involves keeping track of coherences correctly). Counting at the left junction, we find that the Fourier transformed evolution matrix, $\mathcal{M}_L(\chi)$, simply picks up a phase on the term which corresponds to incoherent decays from the lead to the left dot,

$$\mathcal{M}_L = \begin{pmatrix} -\Gamma & 0 & \Gamma & 0 & 0 \\ \Gamma \mathrm{e}^{i\chi} & 0 & 0 & -i\Omega & i\Omega \\ 0 & 0 & -\Gamma & i\Omega & -i\Omega \\ 0 & -i\Omega + \gamma_+ & i\Omega - \gamma_- & i\epsilon - \Gamma/2 - \gamma_p & 0 \\ 0 & i\Omega + \gamma_+ & -i\Omega - \gamma_- & 0 & -i\epsilon - \Gamma/2 - \gamma_p \end{pmatrix}. \tag{D.11}$$

Calculating the matrix which counts electrons transferring from the left to the right dot is slightly more complicated. This involves coherences which can be dealt with in the same way as for SSET. As an example we introduce the notation $\rho_{ij,q}(\chi) = \sum_N \mathrm{e}^{i\chi N} \langle i, N| \rho |j, N+q\rangle$ and calculate the evolution of the population,

$$\rho_{LL,0}(\chi) = \sum_{N_C} \mathrm{e}^{i\chi N_C} \langle L, N_C| \rho |L, N_C\rangle, \tag{D.12}$$

this then has the equation of motion,

$$\dot{\rho}_{LL,0}(\chi) = \sum_{N_C} \mathrm{e}^{i\chi N_C} [\Gamma \langle 0, N_C| \rho |0, N_C\rangle - i\Omega(\langle R, N_C+1| \rho |L, N_C\rangle - \langle L, N_C| \rho |R, N_C+1\rangle)], \tag{D.13}$$

which gives,

$$\dot{\rho}_{LL,0}(\chi) = \Gamma\rho_{00,0}(\chi) - i\Omega \left(\mathrm{e}^{i\chi}\rho_{RL,-1}(\chi) - \rho_{LR,1}(\chi)\right). \tag{D.14}$$

We can do the same thing for the coherences and find, for example,

$$\dot{\rho}_{RL,-1}(\chi) = \mathrm{e}^{i\chi}(\gamma_+ - i\Omega)\rho_{LL,0}(\chi) - (\gamma_- - i\Omega)\rho_{RR,0}(\chi) - \left(-i\epsilon + \frac{\Gamma}{2} + \gamma_p\right)\rho_{RL,-1}(\chi). \tag{D.15}$$

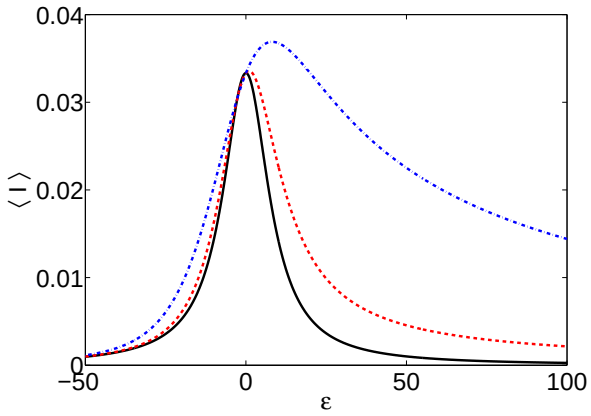

Figure D.2.: Current as a function of dot detuning, ϵ. For all curves the parameters are $\Omega = 5$, $\Gamma = 0.1$, $T = 10$. The curves show different couplings to the thermal bath. These are given by $\gamma = 0$ (black, solid line), $\gamma = 1 \times 10^{-3}$ (red, dashed line) and $\gamma = 1 \times 10^{-2}$ (blue, dotted line).

Combining all of these we find the evolution matrix,

$$\mathcal{M}_C = \begin{pmatrix} -\Gamma & 0 & \Gamma & 0 & 0 \\ \Gamma & 0 & 0 & -i\Omega e^{-i\chi} & i\Omega \\ 0 & 0 & -\Gamma & i\Omega & -i\Omega e^{i\chi} \\ 0 & (-i\Omega + \gamma_+)e^{i\chi} & i\Omega - \gamma_- & i\epsilon - \Gamma_p & 0 \\ 0 & i\Omega + \gamma_+ & (-i\Omega - \gamma_-)e^{-i\chi} & 0 & -i\epsilon - \Gamma_p \end{pmatrix}, \tag{D.16}$$

where $\Gamma_p = \Gamma/2 + \gamma_p$.

D.2 RESULTS

Now that we have $\mathcal{M}(\chi)$ for both counting positions we can use our formulae to calculate the current, noise and Fano factor.

To begin with we calculate the current, as a function of detuning of the dots, for different strengths of coupling to the thermal bath γ. These are shown in Fig. D.2. We find the same results as in Refs. [88, 107], the current is the same through the left junction as it is between the dots. We also see that coupling to the thermal environment makes the current increasing asymmetric with respect to ϵ.

We can also find the zero frequency Fano factor, $F(0) = S(0)/\langle I \rangle$. In Ref. [107] they find that, as γ is increased, $F(0)$ becomes dependent on where the current is measured, and eventually starts to give unphysical negative values when calculated between the dots. From our calculation, we find this is not the case. The noise is independent of where it is calculated and our results match those found in Refs. [88, 107], for the incoherent junction, as shown in Fig. D.3.

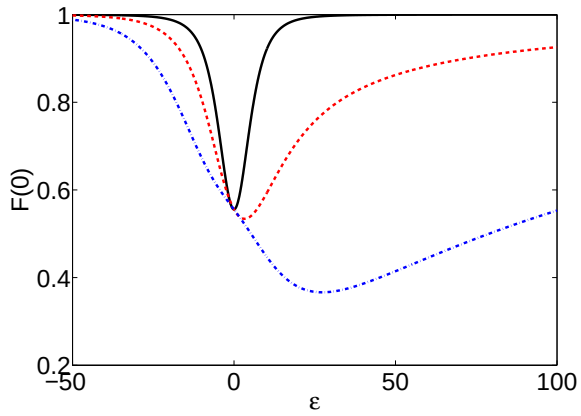

Figure D.3.: Zero frequency Fano factor as a function of dot detuning, ϵ. For all curves the parameters are $\Omega = 5$, $\Gamma = 0.1$, $T = 10$. The curves show different couplings to the thermal bath. These are given by $\gamma = 0$ (black, solid line), $\gamma = 1 \times 10^{-3}$ (red, dashed line) and $\gamma = 1 \times 10^{-2}$ (blue, dotted line).

We are also able to go beyond the calculation of Ref. [107], and find the full frequency dependent noise. In Fig. D.4, we show the effect of the bath coupling strength on the frequency dependent noise, at $\epsilon = 0$. We see that the noise through the central dots has peaks at $\omega = \pm 2\Omega$. These are exactly analogous to those found in the DJQP noise. At $\epsilon = 0$ and $\gamma = 0$ the peaks are symmetric, as expected. As the thermal environment is turned on, the peaks are gradually destroyed: the environment kills off the coherence, but it does this asymmetrically, and so the positive frequency peaks becomes larger than the negative frequency peak.

The noise through the left junction shows a much weaker dependence on the thermal environment. The thermal environment only destroys coherence between the dots, and so does not effect the incoherent transport, except at frequencies associated with coherent oscillations. We see that it only destroys the small features at $\omega = \pm 2\Omega$. A zoomed in version of this can be found in Fig. D.5. These results match those found in Ref. [88].

Detuning the system from resonance introduces asymmetries to $F_C(\omega)$, as for the resonances in the SSET. If we detune such that $\epsilon > 0$, as in Fig. D.6, we find that the negative frequency peak is enhanced, when the coupling to the thermal bath, $\gamma = 0$. As γ is increased the peaks in $F_C(\omega)$ become weaker, the coherent transport is destroyed. The negative frequency peak is more affected by the bath: the thermal environment prefers to take energy out of the system. This effect is similar to that seen for the position noise spectrum of a harmonic oscillator, calculated in Sec. 3.1. This means that, as the coupling to the thermal bath is increased, we go through a point where the spec-

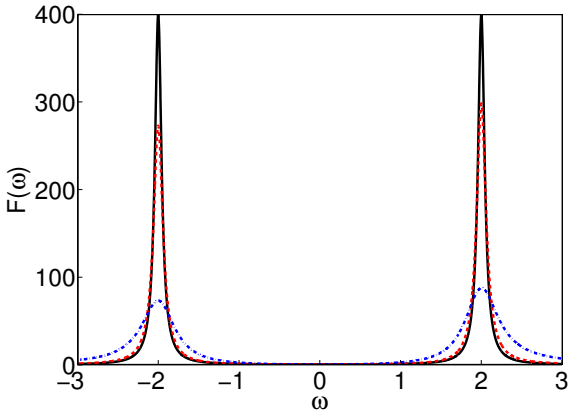

(a) $F_C(\omega)$

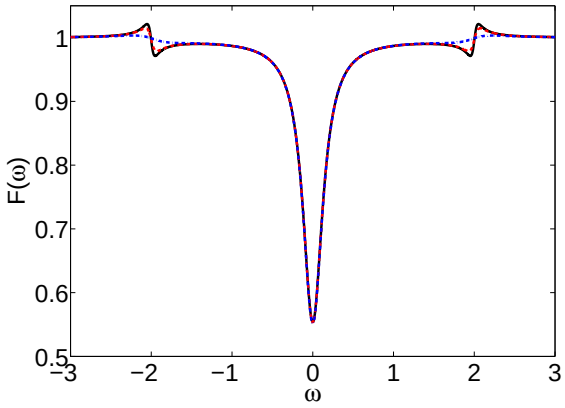

(b) $F_L(\omega)$

Figure D.4.: Frequency dependent Fano factor between the dots (a), and through the left junction (b). For all curves the parameters are $\epsilon = 0$, $\Omega = 1$, $\Gamma = 0.1$, $T = 10$. The curves show different couplings to the thermal bath. These are given by $\gamma = 0$ (black, solid line), $\gamma = 1 \times 10^{-3}$ (red, dashed line) and $\gamma = 1 \times 10^{-2}$ (blue, dotted line)

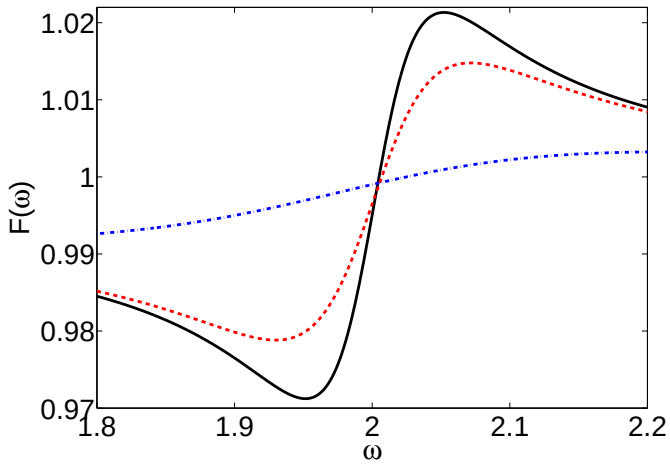

Figure D.5.: Zoomed in view of Fig. D.4 (b).

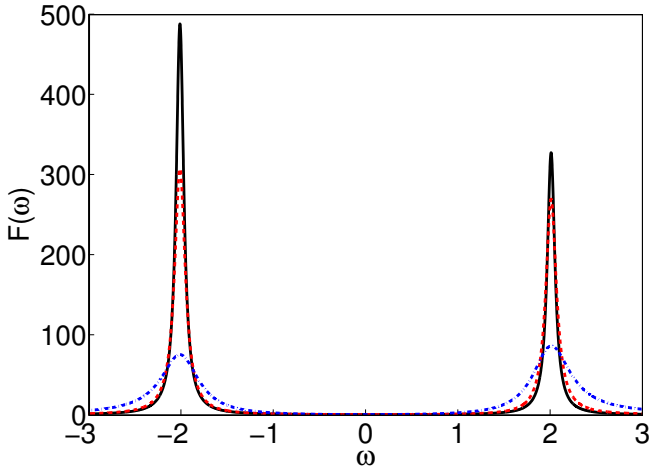

Figure D.6.: Frequency dependent Fano factor between the dots, $F_C(\omega)$. Same parameters as Fig. D.4 except $\epsilon = 0.2$

trum is symmetric, as the effect of the thermal environment exactly cancels the effect of the detuning.

D.3 DISCUSSION AND CONCLUSIONS

In Ref. [107] it was claimed that the issues with charge conservation, found in the zero frequency noise between the dots, are a problem with the quantum regression theorem. We have been able to provide a full, unambiguous calculation, of the correct value for this noise and obtained the same results as previously calculated for the incoherent junctions. This means that the problem encountered in Ref. [107] is one with the correct method of counting in the presence of coherence, and not the regression theorem.

We have also been able to use our technique to find the same results as [88] for the symmetrised finite frequency spectrum, at the incoherent junctions. As an extension we have also calculated the the finite frequency noise in the current between the dots, and found that the thermal environment, as well as detuning of the dots from resonance, are able to introduce asymmetries.

Measurement of finite frequency noise between the dots is difficult. This quantity would not show up in, for example, the behaviour of an oscillator coupled to the leads, since it does not give a contribution to the displacement current through the device. However, it may be possible to measure this quantity by coupling an oscillator to a different quantity, such as $\sigma_x = |L\rangle\langle R| + |L\rangle\langle R|$, as in Ref. [128], but this needs further investigation.

E

THE COHERENT EXPRESSION FOR THE CURRENT NOISE, NEAR THE CPRS

It is possible to derive an expression for the purely coherent contributions to the current noise close to the CPRs, which we use in Sec. 4.5. In this appendix, we calculate the noise using only the evolution under the action of the coherent Hamiltonian, ignoring all incoherent effects.

Counting at the left junction, the Hamiltonian for each block, in the basis $\{|0, N_L\rangle, |1, N_L - p - 1\rangle\}$, is given by,

$$H^{N_L} = \begin{pmatrix} -\Delta E & J_p \\ J_p & \Delta E \end{pmatrix}, \tag{E.1}$$

where the full Hamiltonian is simply, $H = \sum_{N_L} H^{N_L}$. The current operator can then be found as,

$$\hat{I}_L = -2e\frac{d\hat{N}_L}{dt} = -\frac{2ei}{\hbar}[H, \hat{N}_L], \tag{E.2}$$

which is given by,

$$\hat{I}_L = -\frac{2eiJ_p(p+1)}{\hbar}\sum_{N_L} |0, N_L\rangle \langle 1, N_L - p - 1| - h.c.. \tag{E.3}$$

It is convenient to work in a basis where H is diagonal, and so we introduce,

$$|a, N_L\rangle = \cos\alpha\, |0, N_L\rangle + \sin\alpha\, |1, N_L - p - 1\rangle, \tag{E.4}$$

$$|b, N_L\rangle = -\sin\alpha\, |0, N_L\rangle + \cos\alpha\, |1, N_L - p - 1\rangle. \tag{E.5}$$

In this basis the current operator is written as,

$$\hat{I}_L = -I^{(L)}_{ab}\sum_{N_L} |a, N_L\rangle \langle b, N_L| - h.c., \tag{E.6}$$

where the relevant matrix element is given by,

$$I^{(L)}_{ab} = -\frac{2eiJ_p(p+1)}{\hbar}. \tag{E.7}$$

We then write the two-time correlation function of the current as,

$$\lim_{t_2\to\infty}\langle \hat{I}_L(t_1)\hat{I}_L(t_2)\rangle = \mathrm{Tr}[\hat{I}_L e^{iH(t_1-t_2)}\hat{I}_L e^{iH(t_2)}\rho_0], \tag{E.8}$$

where ρ_0 is an arbitrary, initial density matrix of the full (dissipative) evolution. The correlation function can then be calculated, defining $t = t_1 - t_2$ as,

$$\langle \hat{I}_L(t)\hat{I}_L(0)\rangle = |I_{ab}^{(L)}|^2 \left[e^{i\omega_{ab}t}\rho_{aa} + e^{i\omega_{ba}t}\rho_{bb} \right]. \tag{E.9}$$

The noise spectrum which corresponds to this is simply two delta peaks at $\omega = \pm\omega_{ab}$. By analogy with the charge noise spectrum calculation, from Sec. 3.7, we make the ad-hoc assumption that the effect of the environment on these peaks will be to broaden them by Γ_{coh}, the decay rate of the coherences. This then gives the spectrum,

$$S_L(\omega) = |I_{ab}^{(L)}|^2 \left[\frac{\rho_{aa}\Gamma_{\text{coh}}}{(\omega - \omega_{ab})^2 + \Gamma_{\text{coh}}^2} + \frac{\rho_{bb}\Gamma_{\text{coh}}}{(\omega - \omega_{ba})^2 + \Gamma_{\text{coh}}^2} \right], \tag{E.10}$$

which shares many similarities with the coherent part of the charge noise (discussed in the main text).

A similar calculation can be performed for the noise at the right hand junction. The resulting spectrum is the same, but with the replacement $I_{ab}^{(L)} \to I_{ab}^{(R)}$, with,

$$I_{ab}^{(R)} = \frac{2eiJ_p p}{\hbar}. \tag{E.11}$$

F

NUMERICAL SIMULATIONS OF THE SET-RESONATOR SYSTEM

In this appendix we discuss the numerical techniques used to obtain results throughout chapter 5. We wish to simulate the behaviour of the differential equations, given in Eqn. (5.14), of the main text. These equations are stochastic, because the island charge, n, fluctuates according to the tunnel rates given by Eqns. (5.15) and (5.16). These lead to changes in n by the processes shown in Fig. 5.1.

We perform Monte Carlo simulations of the trajectory of the system, governed by these equations. We evolve time in discrete steps of length Δt. At each time step, a uniform random number, $r \in [0,1]$, is chosen. If r is in an interval $[0, \Gamma_L^- \Delta t]$ then the state of the SET island is changed accordingly, this test is then performed on all the other rates, so, for example, if $r \in [\Gamma_L^- \Delta t, \Gamma_L^+ \Delta t]$ the state is evolved according to Γ_L^+. Otherwise, the resonator is evolved according to Hamilton's equations for the position and velocity. To improve the efficiency of our simulations we evolve the ODEs in time with a slightly more sophisticated algorithm than Euler's method. We implement a version of Heun's algorithm [129] which, for the equation $dx/dt = f(x,t)$, has the update rule,

$$x(t+\Delta t) = x(t) + \frac{[f(x,t) + f(\tilde{x}, t+\Delta t)]dt}{2}, \tag{F.1}$$

with,

$$\tilde{x}(t+\Delta t) = x(t) + f(x,t)\Delta t. \tag{F.2}$$

This can then be used to calculate how the trajectory of the SET-resonator system evolves in time.

We are then able to produce all of the results of chapter 5 by appropriate averaging over this trajectory. A typical run goes as follows: firstly we evolve the equations from an arbitrary set of initial conditions for a long enough time, t_0, that the system has lost all memory of the initial condition (this is tested by ensuring that the results are not sensitive to changes in t_0). We then evolve the system along the trajectory recording the relevant quantity, for example the position and velocity distributions in Fig. 5.3 were obtained by binning the value of x and v at each timestep.

To calculate the work done by the driving force, as in Sec. 5.5, is more numerically intensive. The work is given by an integral over a part of the trajectory, as in Eqn. (5.79), which can be calculated by using a simple trapezium rule integration [129]. This then means that we only obtain one data point for each amount of time, τ_n, of our simulation as opposed to each Δt for simple quantities such as x and v.

BIBLIOGRAPHY

[1] Ya. M. Blanter and M. Büttiker. Shot noise in mesoscopic conductors. *Phys. Rep.*, 336:1, 2000.

[2] Yu .V. Nazarov and Ya .M. Blanter. *Quantum Transport*. Cambridge University press, 2009.

[3] A. A. Clerk, M. H. Devoret, S. M. Girvin, Florian Marquardt, and R. J. Schoelkopf. Introduction to quantum noise, measurement, and amplification. *Rev. Mod. Phys.*, 82:1155, 2010.

[4] M. S. Choi, F. Plastina, and R. Fazio. Charge and current fluctuations in a superconducting single-electron transistor near a cooper pair resonance. *Phys. Rev. B*, 67:045105, 2003.

[5] D. Marcos, C. Emary, T. Brandes, and R. Aguado. Finite-frequency counting statistics of electron transport: Markovian theory. *New J. Phys.*, 12:123009, 2010.

[6] D. V. Averin and K. K. Likharev. Coulomb-blockade of single-electron tunneling and coherent oscillations in small tunnel junctions. *J. Low Temp. Phys.*, 62:345, 1986.

[7] T. A. Fulton and G. J. Dolan. Observation of single-electron charging effects in small tunnel junctions. *Phys. Rev. Lett.*, 59:109, 1987.

[8] W. W Xue, Z. Ji, F. Pan, J. Stettenheim, M. P. Blencowe, and A. J. Rimberg. Measurement of quantum noise in a single-electron transistor near the quantum limit. *Nature Physics*, 5:660, 2009.

[9] P.-M. Billangeon, F. Pierre, H. Bouchiat, and R. Deblock. Very high frequency spectroscopy and tuning of a single-cooper-pair transistor with an on-chip generator. *Phys. Rev. Lett.*, 98:126802, 2007.

[10] A. Naik, O. Buu, M. D. LaHaye, A. D. Armour, A. A. Clerk, M. P. Blencowe, and K. C. Schwab. Cooling a nanomechanical resonator with quantum back-action. *Nature*, 443:193, 2006.

[11] G. A. Steele, A. K. Huettel, B. Witkamp, M. Poot, H. B. Meerwaldt, L. P. Kouwenhoven, and H. S. J. van der Zant. Strong coupling between single-electron tunneling and nano-mechanical motion. *Science*, 325:1103, 2009.

[12] T. A. Fulton, P. L. Gammel, D. J. Bishop, L. N. Dunkleberger, and G. J. Dolan. Observation of combined josephson and charging effects in small tunnel junction circuits. *Phys. Rev. Lett.*, 63:1307, 1989.

[13] P. Hadley, E. Delvigne, E. H. Visscher, S. Lähteenmäki, and J. E. Mooij. 3*e* tunneling processes in a superconducting single-electron tunneling transistor. *Phys. Rev. B*, 58:15317, 1998.

[14] A. A. Clerk, S. M. Girvin, A. K. Nguyen, and A. D. Stone. Resonant cooper-pair tunneling: Quantum noise and measurement characteristics. *Phys. Rev. Lett.*, 89:176804, 2002.

[15] A. A. Clerk and S. Bennett. Quantum nanoelectromechanics with electrons, quasi-particles and cooper pairs: effective bath descriptions and strong feedback effects. *New J. Phys.*, 7:238, 2005.

[16] D. R. Koenig, E. M. Weig, and J. P. Kotthaus. Ultrasonically driven nanomechanical single-electron shuttle. *Nature Nanotechnology*, 3:482, 2008.

[17] A. V. Moskalenko, S. N. Gordeev, O. F. Koentjoro, P. R. Raithby, R. W. French, F. Marken, and S. E. Savel'ev. Nanomechanical electron shuttle consisting of a gold nanoparticle embedded within the gap between two gold electrodes. *Phys. Rev. B*, 79:241403, 2009.

[18] S. D. Bennett, L. Cockins, Y. Miyahara, P. Grütter, and A. A. Clerk. Strong electromechanical coupling of an atomic force microscope cantilever to a quantum dot. *Phys. Rev. Lett.*, 104:017203, Jan 2010.

[19] D. Mozyrsky, M. B. Hastings, and I. Martin. Intermittent polaron dynamics: Born-oppenheimer approximation out of equilibrium. *Phys. Rev. B*, 73:035104, Jan 2006.

[20] B. Lassagne, Y. Tarakanov, J. Kinaret, D. Garcia-Sanchez, and A. Bachtold. Coupling mechanics to charge transport in carbon nanotube mechanical resonators. *Science*, 325:1107, 2009.

[21] R. J. Schoelkopf, P. Wahlgren, A. A. Kozhevnikov, P. Delsing, and D. E. Prober. The radio-frequency single-electron transistor (rf-set): A fast and ultrasensitive electrometer. *Science*, 280:5367, 1998.

[22] M. H. Devoret and R. J. Schoelkopf. Amplifying quantum signals with the single-electron transistor. *Nature*, 406:1039, 2000.

[23] K. W. Lehnert, K. Bladh, L. F. Spietz, D. Gunnarsson, D. I. Schuster, P. Delsing, and R. J. Schoelkopf. Measurement of the

excited-state lifetime of a microelectronic circuit. *Phys. Rev. Lett.*, 90:027002, 2003.

[24] M. P. Blencowe and M. N. Wybourne. Sensitivity of a micromechanical displacement detector based on the radio-frequency single-electron transistor. *App. Phys. Lett.*, 77:3845, 2000.

[25] R. G. Knobel and A. N. Cleland. Nanometre-scale displacement sensing using a single electron transistor. *Nature*, 424:291, 2003.

[26] M. V. Gustafsson, P. V. Santos, G. Johansson, and P. Delsing. Local probing of propagating acoustic waves in a gigahertz echo chamber. *Nature Physics*, 8:338, 2012.

[27] A. A. Clerk. Quantum phononics: To see a saw. *Nature Physics*, 8:256, 2012.

[28] O. Astafiev, K. Inomata, A. O. Niskanen, T. Yamamoto, Yu. A. Pashkin, Y. Nakamura, and J. S. Tsai. Single artificial-atom lasing. *Nature*, 449:588, 2007.

[29] N. Ubbelohde, C. Fricke, C. Flindt, F. Hohls, and R. J. Haug. Measurement of finite-frequency current statistics in a single-electron transistor. *Nature Commun.*, 3:612, 2012.

[30] S. Ciliberto, S. Joubaud, and A. Petrosyan. Fluctuations in out-of-equilibrium systems: from theory to experiment. *J. Stat. Mech.*, 12:P12003, 2010.

[31] C. Jarzynski. Nonequilibrium equality for free energy differences. *Phys. Rev. Lett.*, 78:2690, 1997.

[32] G. E. Crooks. Entropy production fluctuation theorem and the nonequilibrium work relation for free energy differences. *Phys. Rev. E*, 60:2721, 1999.

[33] A. Altland, A. De Martino, R. Egger, and B. Narozhny. Transient fluctuation relations for time-dependent particle transport. *Phys. Rev. B*, 82:115323, 2010.

[34] Y. Utsumi, D. S. Golubev, M. Marthaler, K. Saito, T. Fujisawa, and G. Schön. Bidirectional single-electron counting and the fluctuation theorem. *Phys. Rev. B*, 81:125331, 2010.

[35] D. V. Averin and J. P. Pekola. Statistics of the dissipated energy in driven single-electron transitions. *Europhys. Lett.*, 96:67004, 2011.

[36] P. G. Kirton, M. Houzet, F. Pistolesi, and A. D. Armour. Charge noise at cooper-pair resonances. *Phys. Rev. B*, 82:064519, 2010.

[37] P. G. Kirton, A. D. Armour, M. Houzet, and F. Pistolesi. Quantum current noise from a born-markov master equation. *ArXiv*, 1201.6238, 2012.

[38] Alexander N. Korotkov. Charge sensitivity of superconducting single-electron transistor. *App. Phys. Lett.*, 69:2593, 1996.

[39] M. D. LaHaye, O. Buu, B. Camarota, and K. C. Schwab. Approaching the quantum limit of a nanomechanical resonator. *Science*, 304:74, 2004.

[40] D. V. Averin and J. P. Pekola. Nonadiabatic charge pumping in a hybrid single-electron transistor. *Phys. Rev. Lett.*, 101:066801, 2008.

[41] G.-L. Ingold and Yu. V. Nazarov. *Single Charge Tunnelling*. Plenum, 1992.

[42] A. Shnirman and G. Schön. Quantum measurements performed with a single-electron transistor. *Phys. Rev. B*, 57:15400, 1998.

[43] Y. Makhlin, G. Schön, and A. Shnirman. Quantum-state engineering with josephson-junction devices. *Rev. Mod. Phys.*, 73:357, 2001.

[44] D. K. Ferry, S. M. Goodnick, and J. P. Bird. *Transport in nanostructures*. Cambridge University Press, 2nd edition, 2009.

[45] P. Joyez. *Le Transistor a une Paire de Cooper: Un Systeme Quantique Macroscopique*. PhD thesis, l'Universite Paris, 1995.

[46] D. A. Rodrigues, J. Imbers, and A. D. Armour. Quantum dynamics of a resonator driven by a superconducting single-electron transistor: A solid-state analogue of the micromaser. *Phys. Rev. Lett.*, 98:067204, 2007.

[47] D. A. Rodrigues, J. Imbers, T. J. Harvey, and A. D. Armour. Dynamical instabilities of a resonator driven by a superconducting single-electron transistor. *New J. Phys.*, 9:84, 2007.

[48] M.-S. Choi, R. Fazio, J. Siewert, and C. Bruder. Coherent oscillations in a cooper-pair box. *Europhys. Lett.*, 53:251, 2001.

[49] K. Blum. *Density Matrix Theory and Applications*. Plenum, 1996.

[50] H. Carmichael. *An Open Systems Approach to Quantum Optics*. Springer-Verlag, 1993.

[51] D. V. Averin and V. Ya. Aleshkin. Resonance tunneling of cooper pairs in a system of two small josephson junctions. *JETP Lett.*, 50:367, 1989.

[52] A. Maassen van den Brink, G. Schön, and L. J. Geerligs. Combined single-electron and coherent-cooper-pair tunneling in voltage-biased josephson junctions. *Phys. Rev. Lett.*, 67:3030, 1991.

[53] M.-S. Choi, F. Plastina, and R. Fazio. Shot noise for resonant cooper pair tunneling. *Phys. Rev. Lett.*, 87:116601, 2001.

[54] Y. Nakamura, A. N. Korotkov, C. D. Chen, and J. S. Tsai. Singularity-matching peaks in a superconducting single-electron transistor. *Phys. Rev. B*, 56:5116, 1997.

[55] A. A. Clerk. *New Directions in Mesoscopic Physics, NATO ASI*, 125:325, 2003.

[56] H. Schoeller and G. Schön. Mesoscopic quantum transport: Resonant tunneling in the presence of a strong coulomb interaction. *Phys. Rev. B*, 50:18436, 1994.

[57] M. P. Blencowe, J. Imbers, and A. D. Armour. Dynamics of a nanomechanical resonator coupled to a superconducting single-electron transistor. *New J. Phys.*, 7:236, 2005.

[58] C. Emary, D. Marcos, R. Aguado, and T. Brandes. Frequency-dependent counting statistics in interacting nanoscale conductors. *Phys. Rev. B*, 76:161404(R), 2007.

[59] T. Brandes. Waiting times and noise in single particle transport. *Ann. Phys.*, 17:477, 2008.

[60] G. Schaller, G. Kießlich, and T. Brandes. Transport statistics of interacting double dot systems: Coherent and non-markovian effects. *Phys. Rev. B*, 80:245107, 2009.

[61] Y. Nakamura, C. D. Chen, and J. S. Tsai. Quantitative analysis of josephson-quasiparticle current in superconducting single-electron transistors. *Phys. Rev. B*, 53:8234, 1996.

[62] M. Thalakulam, Z. Ji, and A. J. Rimberg. Resonant cooper-pair tunneling: Quantum noise and measurement characteristics. *Phys. Rev. Lett.*, 93:066804, 2004.

[63] D. B. Haviland, Y. Harada, P. Delsing, C. D. Chen, and T. Claeson. Observation of the resonant tunneling of cooper pairs. *Phys. Rev. Lett.*, 73:1541, 1994.

[64] J. Siewert and G. Schön. Charge transport in voltage-biased superconducting single-electron transistors. *Phys. Rev. B*, 54:7421, 1996.

[65] P.-M. Billangeon, F. Pierre, H. Bouchiat, and R. Deblock. ac josephson effect and resonant cooper pair tunneling emission of a single cooper pair transistor. *Phys. Rev. Lett.*, 98:216802, 2007.

[66] J. Leppäkangas and E. Thuneberg. Effect of decoherence on resonant cooper-pair tunneling in a voltage-biased single-cooper-pair transistor. *Phys. Rev. B*, 78:144518, 2008.

[67] Yu. Makhlin, G. Schön, and A. Shnirman. *New Directions in Mesoscopic Physics (Towards Nanoscience)*. Kluwer, Dordrecht, 2003.

[68] J. J. Toppari, T. Kühn, A. P. Halvari, J. Kinnunen, M. Leskinen, and G. S. Paraoanu. Cooper-pair resonances and subgap coulomb blockade in a superconducting single-electron transistor. *Phys. Rev. B*, 76:172505, 2007.

[69] C. Cohen-Tannoudji, J. Dupont-Roc, and G. Grynberg. *Atom-Photon Interactions*. Wiley-Interscience, 1992.

[70] A. Maassen van den Brink, A. A. Odinstov, P. A. Bobbert, and G. Schön. *Z. Phys. B: Condens. Matter*, 85:459, 1991.

[71] C.W. Gardiner and P. Zoller. *Quantum Noise: A Handbook Of Markovian And Non-Markovian Quantum Stochastic Methods With Applications To Quantum Optics*. Springer, 2004.

[72] D. S. Lemons. *An Introduction to Stocastic Processes*. John Hopkins University Press, 2002.

[73] R Aguado and L. P. Kouwenhoven. Double quantum dots as detectors of high-frequency quantum noise in mesoscopic conductors. *Phys. Rev. Lett.*, 84:1986, 2000.

[74] U. Gavish, Y. Levinson, and Y. Imry. Detection of quantum noise. *Phys. Rev. B*, 62:R10637, 2000.

[75] P.-M. Billangeon, F. Pierre, H. Bouchiat, and R. Deblock. Emission and absorption asymmetry in the quantum noise of a josephson junction. *Phys. Rev. Lett.*, 96:136804, 2006.

[76] J. Schwinger. Brownian motion of a quantum oscillator. *J. Math. Phys.*, 2:407, 1961.

[77] A. A. Clerk. Quantum-limited position detection and amplification: A linear response perspective. *Phys. Rev. B*, 70:245306, 2004.

[78] F. Marquardt, J. P. Chen, A. A. Clerk, and S. M. Girvin. Quantum theory of cavity-assisted sideband cooling of mechanical motion. *Phys. Rev. Lett.*, 99:093902, 2007.

[79] I. Wilson-Rae, N. Nooshi, W. Zwerger, and T. J. Kippenberg. Theory of ground state cooling of a mechanical oscillator using dynamical backaction. *Phys. Rev. Lett.*, 99:093901, 2007.

[80] K. Jaehne, K. Hammerer, and M. Wallquist. Ground-state cooling of a nanomechanical resonator via a cooper-pair box qubit. *New J. Phys.*, 10:095019, 2008.

[81] Melvin Lax. Formal theory of quantum fluctuations from a driven state. *Phys. Rev.*, 129:2342, 1963.

[82] Melvin Lax. Quantum noise. xi. multitime correspondence between quantum and classical stochastic processes. *Phys. Rev.*, 172:350, 1968.

[83] D.F. Walls and G.J. Milburn. *Quantum Optics*. Springer, 1994.

[84] F. Diedrich, J. C. Bergquist, Wayne M. Itano, and D. J. Wineland. Laser cooling to the zero-point energy of motion. *Phys. Rev. Lett.*, 62:403, 1989.

[85] A. Wallraff, D. I. Schuster, A. Blais, L. Frunzio, R.-S. Huang, J. Majer, S. Kumar, S. M. Girvin, and R. J. Schoelkopf. Strong coupling of a single photon to a superconducting qubit using circuit quantum electrodynamics. *Nature*, 431:162, 2004.

[86] Y. D. Wang, Y. Li, F. Xue, C. Bruder, and K. Semba. Cooling a micromechanical resonator by quantum back-action from a noisy qubit. *Phys. Rev. B*, 80:144508, 2009.

[87] O. Naaman and J. Aumentado. Narrow-band microwave radiation from a biased single-cooper-pair transistor. *Phys. Rev. Lett.*, 98:227001, M 2007.

[88] R. Aguado and T. Brandes. Shot noise spectrum of open dissipative quantum two-level systems. *Phys. Rev. Lett.*, 92:206601, 2004.

[89] M. Braun, J. König, and J. Martinek. Frequency-dependent current noise through quantum-dot spin valves. *Phys. Rev. B*, 74:075328, 2006.

[90] D. Marcos, C. Emary, T. Brandes, and R. Aguado. *Phys. Rev. B*, 83:125426, 2011.

[91] L. S. Levitov, H. Lee, and G. B. Lesovik. Electron counting statistics and coherent states of electric current. *J. Math. Phys.*, 37:4845, 1996.

[92] D. A. Bagrets and Yu. V. Nazarov. Full counting statistics of charge transfer in coulomb blockade systems. *Phys. Rev. B*, 67:085316, 2003.

[93] T. J. Harvey, D. A. Rodrigues, and A. D. Armour. Current noise of a superconducting single-electron transistor coupled to a resonator. *Phys. Rev. B*, 78:024513, 2008.

[94] Y. Makhlin, G. Schön, and A. Shnirman. Statistics and noise in a quantum measurement process. *Phys. Rev. Lett.*, 85:4578, 2000.

[95] T. J. Harvey, D. A. Rodrigues, and A. D. Armour. Spectral properties of a resonator driven by a superconducting single-electron transistor. *Phys. Rev. B*, 81:104514, 2010.

[96] W. Lu, Z. Ji, L. Pfeiffer, K. W. West, and A. J. Rimberg. Real-time detection of electron tunnelling in a quantum dot. *Nature*, 423:422, 2003.

[97] J. Bylander, T. Duty, and P. Delsing. Current measurement by real-time counting of single electrons. *Nature*, 434:361, 2005.

[98] S. Gustavsson, R. Leturcq, B. Simovic, R. Schleser, T. Ihn, P. Studerus, K. Ensslin, D. C. Driscoll, and A. C. Gossard. Counting statistics of single electron transport in a quantum dot. *Phys. Rev. Lett.*, 96:076605, 2006.

[99] H.-A. Engel and D. Loss. *Phys. Rev. Lett.*, 93:136602, 2004.

[100] C. Emary and R. Aguado. *Phys. Rev. B*, 84:085425, 2011.

[101] R. Deblock, E. Onac, L. Gurevich, and L. P. Kouwenhoven. Detection of quantum noise from an electrically driven two-level system. *Science*, 301:203, 2003.

[102] E. Onac, F. Balestro, L. H. Willems van Beveren, U. Hartmann, Y. V. Nazarov, and L. P. Kouwenhoven. Using a quantum dot as a high-frequency shot noise detector. *Phys. Rev. Lett.*, 96:176601, 2006.

[103] S. Gustavsson, M. Studer, R. Leturcq, T. Ihn, K. Ensslin, D. C. Driscoll, and A. C. Gossard. Frequency-selective single-photon detection using a double quantum dot. *Phys. Rev. Lett.*, 99:206804, 2007.

[104] J. Basset, A. Kasumov, P. Moca, G. Zarand, P. Simon, H. Bouchiat, and R. Deblock. Quantum noise measurement of a carbon nanotube quantum dot in the kondo regime. *Phys. Rev. Lett.*, 108:046802, 2012.

[105] C. Flindt, T. Novotný, and A.-P. Jauho. Current noise spectrum of a quantum shuttle. *Physica E*, 29:411, 2005.

[106] W. Belzig and Yu. V. Nazarov. *Phys. Rev. Lett.*, 87:067006, 2001.

[107] J. Prachar and T. Novotný. Charge conservation breaking within a generalized master equation description of electronic transport through dissipative double quantum dots. *Physica E*, 42:565, 2010.

[108] C. Flindt, T. Novotný, and A.-P. Jauho. Current noise in a vibrating quantum dot array. *Phys. Rev. B*, 70:205334, 2004.

[109] J. Gabelli and B. Reulet. High frequency dynamics and the third cumulant of quantum noise. *J. Stat. Mech.*, 2009:P01049, 2009.

[110] A. D. Armour, M. P. Blencowe, and Y. Zhang. Classical dynamics of a nanomechanical resonator coupled to a single-electron transistor. *Phys. Rev. B*, 69:125313, 2004.

[111] A. D. Armour. Current noise of a single-electron transistor coupled to a nanomechanical resonator. *Phys. Rev. B*, 70:165315, Oc 2004.

[112] C. B. Doiron, W. Belzig, and C. Bruder. Electrical transport through a single-electron transistor strongly coupled to an oscillator. *Phys. Rev. B*, 74:205336, 2006.

[113] C. Doiron. *Electronic transport in nanoelectromechanical systems: Noise, back-action and quantum measurement*. PhD thesis, Universität Basel, 2009.

[114] F. Pistolesi and S. Labarthe. Current blockade in classical single-electron nanomechanical resonator. *Phys. Rev. B*, 76:165317, 2007.

[115] N. M. Chtchelkatchev, W. Belzig, and C. Bruder. Charge transport through a single-electron transistor with a mechanically oscillating island. *Phys. Rev. B*, 70:193305, 2004.

[116] G. Labadze and Ya. M. Blanter. Current response of ac-driven nanoelectromechanical systems in single-electron tunneling regime. *ArXiv*, 1007.5186, 2010.

[117] S. Joubaud, N. B. Garnier, and S. Ciliberto. Fluctuation theorems for harmonic oscillators. *J. Stat. Mech.*, 2007:P09018, 2007.

[118] R. Zwanzig. *Nonequilibrium Statistical Mechanics*. Oxford university press, 2001.

[119] S. H. Strogatz. *Nonlinear Dynamics And Chaos*. Westview Press, 2001.

[120] M. A. Armen and H. Mabuchi. Low-lying bifurcations in cavity quantum electrodynamics. *Phys. Rev. A*, 73:063801, 2006.

[121] D. A. Rodrigues and G. J. Milburn. Noise in a superconducting single-electron transistor resonator driven by an external field. *Phys. Rev. B*, 78:104302, 2008.

[122] R. van Zon and E. G. D. Cohen. Stationary and transient work-fluctuation theorems for a dragged brownian particle. *Phys. Rev. E*, 67:046102, 2003.

[123] K. Feitosa and N. Menon. Fluidized granular medium as an instance of the fluctuation theorem. *Phys. Rev. Lett.*, 92:164301, 2004.

[124] F. Douarche, S. Joubaud, N. B. Garnier, A. Petrosyan, and S. Ciliberto. Work fluctuation theorems for harmonic oscillators. *Phys. Rev. Lett.*, 97:140603, 2006.

[125] M. H. Devoret. *Quantum Fluctuations, Volume 63 (Les Houches)*. Elsevier, 1997.

[126] M. Houzet. Private communication.

[127] M. Tinkham. *Introduction to Superconductivity*. Dover Publications, 2004.

[128] D. Mozyrsky and I. Martin. Quantum-classical transition induced by electrical measurement. *Phys. Rev. Lett.*, 89:018301, 2002.

[129] W. H. Press, S. A. Teukolsky, W. T. Vetterling, and B. P. Flannery. *Numerical Recipes*. Cambridge University Press, 3rd edition, 2007.